Aix*Marseille université
Socialement engagée

NNT : 2024AIXM0024

THÈSE DE DOCTORAT

Soutenue à Aix-Marseille Université
le 29 Février 2024 par

Dara MARIN

Photo–Excited Paramagnetic States and Cobalt Doping Effects in ZnO Nanoparticles : An EPR Study

Discipline
Physique et sciences de la matière

Spécialité
Matière condensée et nanosciences

École doctorale
Ecole Doctorale 352

Laboratoire/Partenaires de recherche
Institut Matériaux Microélectronique et Nanosciences de Provence UMR 7334

Composition du jury

Emre ERDEM Professeur, Sabanci University	Rapporteur
Dariya SAVCHENKO Professeure Assistante, Kyiv Politechnic	Rapporteure
Fabienne MICHELINI Professeure, Aix-Marseille université, IM2NP	Présidente du jury
Athanassios K. BOUDALIS Directeur de Recherche, CNRS, Institut de Chimie de Strasbourg	Examinateur
Adrien SAVOYANT Maître de conférence, Aix-Marseille Université, IM2NP	Co-Directeur de thèse
Sylvain BERTAINA Chargé de recherche, CNRS, IM2NP	Directeur de thèse

Institut Matériaux Microélectronique Nanosciences de Provence

cnrs

anr agence nationale de la recherche

Affidavit

I, undersigned, Dara Marin, hereby declare that the work presented in this manuscript is my own work, carried out under the scientific supervision of Adrien Savoyant and Sylvain Bertaina, in accordance with the principles of honesty, integrity and responsibility inherent to the research mission. The research work and the writing of this manuscript have been carried out in compliance with both the French national charter for Research Integrity and the Aix-Marseille University charter on the fight against plagiarism. This work has not been submitted previously either in this country or in another country in the same or in a similar version to any other examination body.

Marseille, December 14, 2023.



Cette œuvre est mise à disposition selon les termes de la Licence Creative Commons Attribution - Pas d'Utilisation Commerciale - Pas de Modification 4.0 International.

Liste de publications et participation aux conférences

Liste des publications réalisées dans le cadre du projet de thèse :

1. Jradi, Z., Marin, D., Campos, A., O'byrne, M., Margeat, O., Bertaina, S., Savoyant, A. Influence of Cobalt Doping on the Photogenerated Holes in ZnO NPs. *Phys. Status Solidi RRL*, 2300341 (2023).

2. Marin, D., Gerbaud, G., Margeat, O., Ziarelli, F., Ferrer, F., Ouari, O., Campos, A., Bertaina, S., Savoyant, A.. Magnetic functionalization of ZnO nanoparticles surfaces via optically generated methyl radicals. *J. Chem. Phys.* **158**, 184704 (2023).

3. Marin, D., Tiwari, S. K., Bertaina, S., Savoyant, A. Zero-field magnetic resonance of cobalt ion pairs in ZnO nanocrystals. *Phys. Rev. B* **105**, 035424 (2022).

Participation aux conférences et écoles d'été au cours de la période de thèse :

1. "Magnetic states in ZnO NPs : The interface between organic and inorganic materials" oral presentation in the European Conference Physics of Magnetism 2023 (PM's 23), 26-30 June 2023.

2. "Electron Paramagnetic Resonance for Spin-Detection in nano-objects" oral presentation in 12th Meeting on Nanoscience Advances. 13-15 September 2021.

3. "Zero-field magnetic resonance of confined cobalt pairs in ZnO NPs" poster presentation in ARPE summer school 2021. 14-18 June 2021. The presentation won the Poster prize.

4. "Photo-Induced Paramagnetic States In ZnO NPs" poster presentation in the International Summer School on Nanosciences and Nanotechnologies 19-24 June 2022.

5. "Photo-Induced Paramagnetic States In ZnO NPs" poster presentation in Journées de la Matière Condensée (JMC) 2022. 22-26 August 2022.

Résumé

Cette étude est dédié à l'investigation des états paramagnétiques exhibés par les nanoparticules de ZnO, en utilisant la Résonance Paramagnétique Électronique dans les régimes continue et pulsé. Nous explorons les caractéristiques des nanoparticules (NPs) non dopés, qui présentent des signaux paramagnétiques uniquement lorsqu'elles sont soumises à une excitation optique. Un signal à $g = 1.96$ d'une seule raie est identifié, associé à l'ionisation d'un défaut de cœur au sein du réseau de ZnO. De plus, un groupe de 4 raies est observé, attribué aux radicaux méthyle formés à la surface des NPs. En outre, un groupe de 3 raies est détecté près des raies de radicaux méthyle, proposé comme provenant de biradicaux méthyles formés par interaction d'échange et/ou dipolaire. Le mécanisme de formation de radicaux proposé dans cette étude suggère que l'ionisation du défaut de cœur libère une charge positive (un trou), qui migre vers la surface des NPs, initiant une réaction photo-Kolbe, entraînant la formation des radicaux méthyle. L'étude examine le comportement paramagnétique du système, y compris les temps de relaxation spin-réseau et de cohérence de spin en fonction de la température. Ensuite, des NPs de ZnO dopées au cobalt sont étudiées. Les résultats démontrent que la présence de cobalt inhibe l'ionisation des défauts de cœur, entravant ainsi la survenue de la réaction photo-Kolbe à la surface des NPs. De plus, l'augmentation des niveaux de dopage entraîne une interaction des ions cobalt via une interaction d'échange, conduisant à la formation de paires de cobalt présentant une transition EPR à champ quasi-nul.

Mots-clés: Résonance paramagnétique électronique, dynamique de spin, nanoparticules, ZnO, photoexcitation, radicaux méthyle, surface polaire, réaction photo-Kolbe.

Abstract

This study delves into the investigation of paramagnetic states exhibited by ZnO NPs (NPs), employing the Electron Paramagnetic Resonance in continuous and pulsed wave regimes. We explore the characteristics of undoped samples, that exhibit paramagnetic signals only when submitted to optical excitation. A single line at $g = 1.96$ is identified, associated with the ionization of a core-defect within the ZnO lattice. Additionally, a group of 4 lines is observed, attributed to methyl radicals formed on the NP surface. Furthermore, a 3-lines group is detected near those of the methyl radical, proposed to originate from methyl biradicals formed through exchange and/or dipolar interaction. The proposed mechanism in this study suggests that the ionization of the core-defect releases a positive charge (hole), that migrates to the NP surface, initiating a photo-Kolbe reaction and resulting in the formation of methyl radicals. The study examines the paramagnetic behavior of the system, including spin-lattice and spin coherence relaxation times at different temperatures. In a second moment, cobalt-doped ZnO NPs are investigated. The findings demonstrate that the presence of cobalt prevents the ionization of core-defects, hindering the occurrence of the photo-Kolbe reaction on the surface of the NP. Moreover, increasing doping levels leads to cobalt ions to interact via exchange interaction, leading to the formation of cobalt pairs, that present near-zero-field EPR transitions.

Keywords: Electron paramagnetic resonance, spin dynamics, ZnO, NPs, photoexcitation, methyl radicals, polar surface, photo-Kolbe reaction.

Résumé étendu

Le ZnO est un matériau polyvalent largement utilisé dans divers domaines scientifiques et technologiques, notamment en science des matériaux, en physique, en astronomie, en ingénierie et en chimie. Son attrait réside dans son prix abordable, sa stabilité robuste et ses propriétés physiques intrigantes, telles que la piézoélectricité et la présence d'excitons à température ambiante. Une particularité du ZnO réside dans sa forte interaction avec la lumière [1], entraînant des effets photo-induits tels que la photoconductivité [2; 3], la photocatalyse [4; 5; 6; 7] et la photoluminescence [8; 9].

Notamment, l'émergence d'une activité magnétique photo-induite positionne le ZnO comme un candidat prometteur pour les capteurs quantiques [10]. Les effets photo-induits présents dans ce matériau proviennent principalement des propriétés excitoniques et des défauts ponctuels, ainsi que de leurs interactions [11; 12; 13; 14; 15]. Dans les systèmes de ZnO à l'échelle nanométrique, les effets photo-induits peuvent être influencés par le rapport surface/volume substantiel et/ou par l'existence de défauts ponctuels spécifiques pouvant agir comme de nouveaux sites de recombinaison ou comme des centres donneurs/accepteurs de charges. L'étude de ces défauts induits par la taille revêt donc un intérêt significatif pour la réalisation de dispositifs efficaces à basse de nanostructures de ZnO.

Un outil puissant pour étudier les défauts ponctuels dans les semi-conducteurs est la Résonance Paramagnétique Électronique (RPE). La technique de la RPE offre une sensibilité élevée (jusqu'à 1000 fois plus sensible que la RMN) et une spécificité, permettant l'investigation des propriétés statiques et dynamiques dans divers matériaux, tels que les systèmes chimiques et biologiques [16]. Cette technique est utilisée depuis plus de cinquante ans pour analyser les défauts paramagnétiques intrinsèques et extrinsèques au sein du ZnO [17; 18; 19; 20; 21; 22]. En plus de la RPE en onde continue (CW), qui fournit des informations sur le spin électronique et ses interactions avec l'environnement, la technique de la RPE pulsée (PW) offre des informations crucials sur la dynamique des spins résonantes.

L'utilisation de la RPE pulsée permet d'accéder à des détails supplémentaires sur le système, notamment des caractéristiques telles que les noyaux faiblement couplés, l'amplification des transitions interdites et des informations sur les propriétés de relaxation du système de spins. Cela est réalisé en manipulant les spins à l'aide de séquences spécifiques d'impulsions micro-ondes.

Dans le ZnO volumique, les études RPE indiquent la présence d'un signal constant résonnant à $g = 1.96$, provenant de défauts dans le réseau cristallin. Néanmoins, et assez étonnamment, la nature précise de ce défaut reste sujet à débat. Dans les nanostructures, en plus du défaut central, un nouveau signal est observé à $g = 2.003$, qui a été démontré être lié à des défauts de surface [23], devenant relativement plus important dans les spectres à mesure que la taille des nanostructures diminue.

Des perspectives sur l'origine des raies EPR mentionnées dans les structures de ZnO

peuvent être obtenues en incorporant une excitation supplémentaire pendant l'expérience, telle qu'un faisceau lumineux optique ou un champ électrique appliqué. La lumière est capable d'ioniser des défauts ponctuels présents dans la structure cristalline, permettant l'émergence d'états dans la bande interdite, [24; 25] présentant éventuellement des propriétés paramagnétiques.

Dans ce contexte, ce travail vise d'abord à étudier les signaux paramagnétiques observés dans les nanoparticules de ZnO, lorsqu'elles sont soumises à une photo-excitation dans le domaine visible. Dans un deuxième temps, nous étudions des nanoparticules de ZnO dopées avec des ions de cobalt, montrant comment la présence de ces ions altère les propriétés magnétiques de ce matériau.

Pour aborder ce sujet, un bref chapitre sur la physique des semi-conducteurs, en particulier à l'échelle nanométrique, est présenté. La formation du cristal de ZnO résulte de l'hybridation sp^3 entre les atomes de zinc et d'oxygèn, avec un transfert de charge fort et prononcé conduisant à une presque totale ionisation du cation Zn^{2+} et de l'anion O^{2-}. Les états de liaison sp^3 donnent naissance à la bande de valence, tandis que les états anti-liants forment la bande de conduction. L'écart d'énergie ou la séparation entre ces bandes est d'environ 3,4 eV. Le caractère ionique et l'absence d'inversion de symétrie dans la structure du ZnO confèrent des propriétés piézoélectriques à ce matériau. Parmi tous les composés II-VI possédant une structure wurtzite, le ZnO présente le tenseur piézoélectrique le plus significatif et est également le composé le plus ionique de ce groupe.

De plus, le ZnO est reconnu pour sa conductivité de type n, associée à des défauts donneurs d'électrons dans le réseau cristallin. En plus de ce défaut, le ZnO possède d'autres défauts, chacun étant responsable de l'introduction d'un nouveau niveau d'énergie dans le matériau, situé à l'intérieur de la bande interdite.

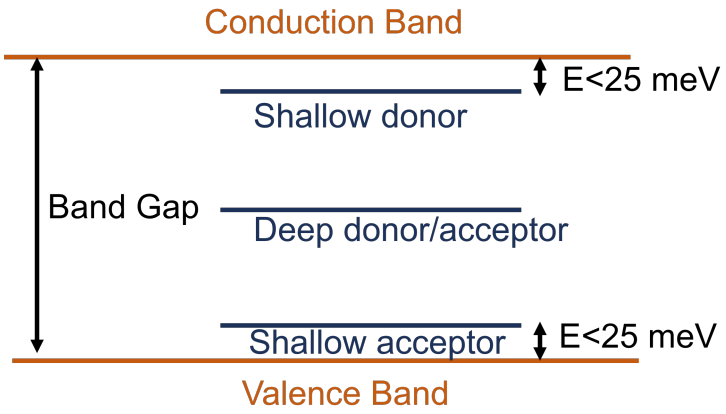

Figure 1: *Les impuretés introduisent de nouveaux niveaux d'énergie à l'intérieur de la bande interdite du semi-conducteur. Les donneurs peu profonds libèrent un électron dans la bande de conduction à température ambiante, tandis que les accepteurs peu profonds créent un trou dans la bande de valence. En revanche, les donneurs et accepteurs profonds sont positionnés plus en profondeur dans la bande interdite, ne contribuant donc pas de manière significative à la conductivité de type n ou p.*

Les défauts peuvent agir en tant que donneurs ou accepteurs de charge superficiels ou profonds et servir également de centres de recombinaison. Les donneurs superficiels introduisent un niveau d'énergie juste en dessous de la bande de conduction et sont généralement activés par l'énergie thermique présente à température ambiante (environ 25 meV).

Dans des conditions standards, le donneur superficiels transfère un électron vers la bande de conduction, contribuant à la conductivité du matériau. Les accepteurs superficiels, en revanche, sont situés juste au-dessus de la bande de valence, de sorte qu'un électron de la bande de valence peut être capturé par cette impureté à température ambiante, créant ainsi un trou dans la bande de valence. Les impuretés profondes (accepteurs ou donneurs) sont localisées bien loin des bandes d'énergie autorisées, typiquement à des énergies bien supérieures à 25 meV.

Les défauts dans les NPs de ZnO que nous étudions sont principalement analysés via la RPE. Pour interpréter efficacement les résultats, un bref chapitre sur les techniques de la RPE est présenté. Ce chapitre introduit le concept de magnétisation dans le cadre de la mécanique quantique et fournit des notions fondamentales sur l'analyse de la RPE, tant en régime CW et PW.

Dans la RPE CW, un champ magnétique statique est appliqué conjointement à une onde électromagnétique de fréquence fixe (généralement dans la plage des GHz) pour étudier les espèces paramagnétiques. La RPE fonctionne en mesurant l'absorption de puissance microonde nécessaire pour provoquer des transitions de spin chez les électrons non-appariés. Cette absorption d'énergie se produit lorsque les électrons absorbent des photons de la fréquence spécifique de l'onde électromagnétique appliquée et passent ainsi d'un état d'énergie à un autre. Ces transitions de spin sont sensibles aux champs magnétiques, ce qui permet d'identifier et de caractériser les espèces paramagnétiques présentes dans l'échantillon. En étudiant les variations de cette absorption d'énergie en fonction du champ magnétique appliqué, la RPE en CW fournit des données cruciales pour comprendre la nature et les propriétés des électrons non-appariés, contribuant ainsi à la caractérisation fine des matériaux et à la compréhension des phénomènes physiques à l'échelle microscopique.

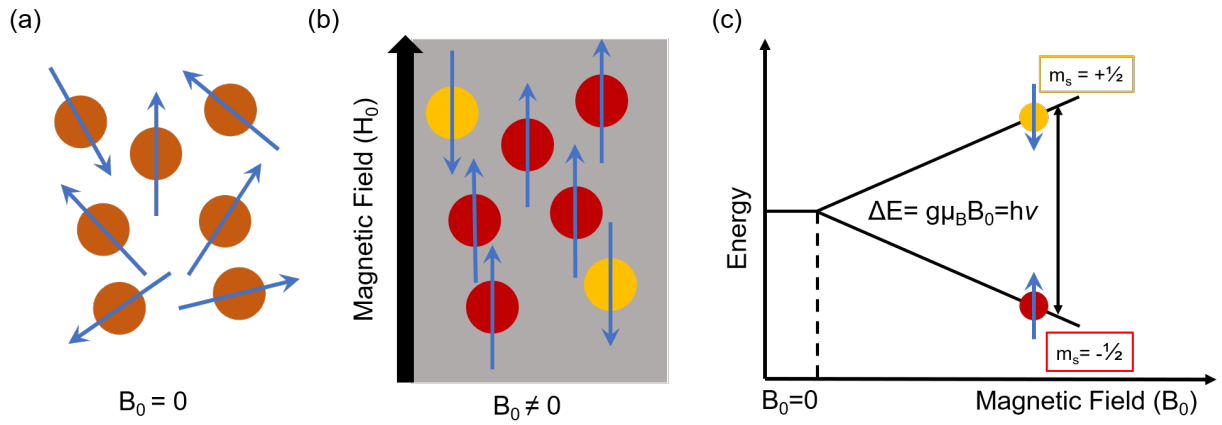

Figure 2: *(a) En l'absence de champ magnétique externe, les spins électroniques sont orientés de manière aléatoire dans l'espace. (b) Lorsque le champ magnétique est appliqué, la dégénérescence énergétique est levée et les spins s'alignent parallèlement ou antiparallèlement au champ magnétique. (c) Par l'énergie fournie par les photons, les spins peuvent basculer de l'état d'énergie inférieure à l'état d'énergie supérieure et l'absorption peut être mesurée.*

Cette technique est largement utilisée dans la caractérisation des espèces paramagnétiques telles que les radicaux libres, les ions de métaux de transition et les défauts cristallins. Elle est utile pour l'identification des structures chimiques et pour étudier la

réactivité des électrons.

La technique de RPE pulsée est une extension de la méthode en régime CW, fournissant des informations plus détaillées sur les interactions et la dynamique des spins électroniques dans les matériaux paramagnétiques. En RPE pulsée, les spins électroniques sont manipulés par des séquences d'impulsions de micro-ondes. Avec la capacité de contrôler et de moduler le temps des impulsions de micro-ondes et les intervalles entre elles, la RPE pulsée offre plus de informations sur les propriétés des spins électroniques et les interactions présentes dans les matériaux étudiés.

Après l'explication du principe de fonctionnement de la RPE, les échantillons étudiés au cours de la thèse sont présentés avec leurs modes de fabrication et leurs particularités. De plus, ce chapitre décrit les techniques expérimentales et les équipements utilisés pour obtenir les mesures.

Par la suite, les signaux paramagnétiques observés dans les NPs de ZnO sont présentés. Les signaux étudiés sont divisés en conditions "dark" et "light". Dans ce contexte, "dark" représente les échantillons qui n'ont pas été soumis à une photo-excitation avant la mesure de RPE. Sous les conditions "dark", il y a une faible illumination ambiante ; cependant, cela n'influence pas le système. En revanche, sous les conditions "light", les échantillons subissent une photo-excitation, et la longueur d'onde spécifique de l'excitation est toujours indiquée. Les signaux étudiés sont :

- Core-Defect : De nombreux auteurs ont identifié un signal paramagnétique caractérisé par une seule raie localisée à $g = 1,96$. Ce signal émerge soit par activation lumineuse, soit, dans certains cas, en l'absence d'excitation externe.

- Défaut de surface : Lorsque le core-defect est présent dans des conditions dark, le défaut de surface est également présent. Il provient d'un défaut à la surface de la NP et est caractérisé par une seule raie centrée à $g = 2,003$.

- Radicaux méthyles : Sous illumination, simultanément au core-defect, un signal composé de 4 raies espacées de 2,2 mT centrées à $g = 2,005$ a été observé dans les échantillons. Dans notre étude, nous démontrons que ce signal particulier provient des radicaux méthyles générés à la surface des NPs. Les raies de ce signal sont désignées comme L_1, L_2, L_3 et L_4, respectivement, progressant du champ faible au champ magnétique élevé.

- Système à 3 raies : En plus de la formation des radicaux méthyles, la présence de raies adjacentes est identifiée. Ces raies sont nomées L_5, L_6 et L_7, suivant la nomenclature donnée (du champ faible au champ élevé).

- Éléphant : Un signal distinctif est présent dans les NPs, caractérisé par un pic large et anisotrope centré autour de $g = 2,023$. Ce signal se superpose à ceux provenant des radicaux méthyles. Il apparaît également sous illumination à 405 nm, en même temps que les autres groupes.

Après l'identification des systèmes paramagnétiques coexistants dans le système, nous avons analysé les changements provoqués par le processus de deutération des échantillons, suivant une fonctionnalisation de surface. Dans ce cas, nous avons constaté que les atomes d'hydrogène du radical méthyle sont remplacés par du deutérium, provoquant d'importants changements dans le spectre RPE. Dans un second temps, nous avons soumis les échantillons à un traitement thermique à 500 °C et nous avons observé que la couche de

surface organique est éliminée, provoquant l'ionisation du core-defect dans des conditions "dark". Des analyses supplémentaires pour identifier les composés organiques présents dans les échantillons sont réalisées à l'aide des techniques RMN et FTIR. Des images TEM et SEM sont obtenues pour caractériser la morphologie des NPs.

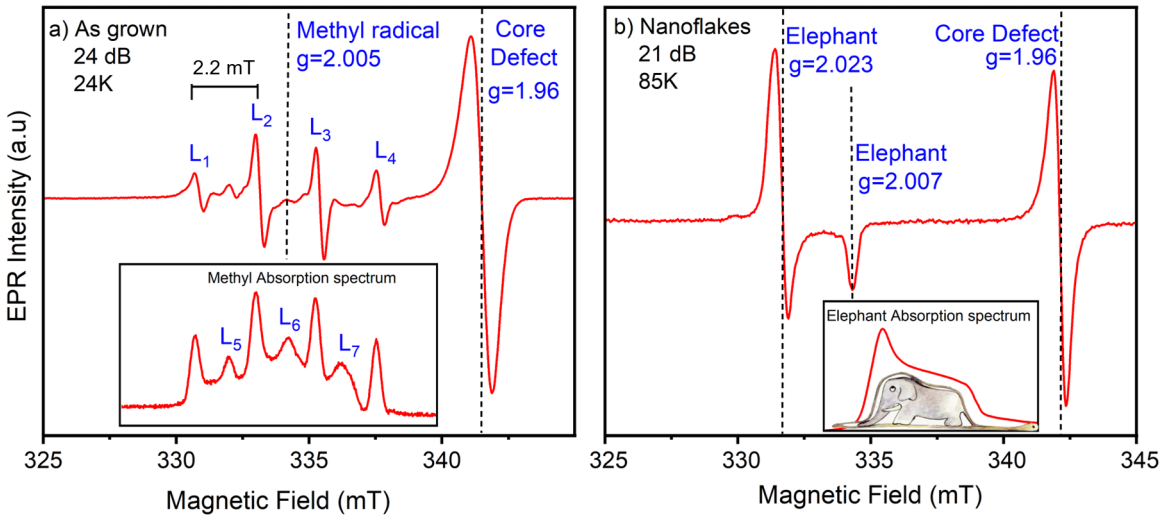

Figure 3: *Suite à une excitation optique, des réponses de RPE sont observées dans les nanoparticules de ZnO. Sur la Figure (a), l'illustration identifie quatre raies associées aux radicaux méthyle (désignées par L_1 à L_4), le système à 3 raies (identifié comme L_5 à L_7, indiquant possiblement la formation de biradicaux), et le défaut de cœur intrinsèque. L'identification du système à 3 raies est mise en évidence et simplifiée dans les spectres d'intégration, représentés dans la zone encadrée. Sur la Figure (b), le signal "éléphant" est identifié, avec les spectres d'intégration représentés dans la région encadrée. De manière amusante, nous attribuons humoristiquement la dénomination de ce signal au "Petit Prince" comme une source d'inspiration légère et humoristique.*

L'analyse RPE de ces systèmes est ensuite réalisée, étudiant la valeur du spin électronique à travers les oscillations de Rabi. Nous avons également identifié deux régimes de température dans le spectre lié au méthyle : tout d'abord, un régime lié à des changements réversibles dans le spectre RPE, associés à la saturation du système et au possible blocage de la rotation du méthyle (T<35K). Nous avons également identifié un régime où des réactions chimiques se produisent entre les radicaux méthyles, et nous avons observé la perte de ces spécimens (T>35K). La condition initiale du système est restaurée en laissant les échantillons se stabiliser dans des conditions ambiantes pendant environ 1 heure. Un état de RPE silencieux est observé lorsque les NPs sont soumises à un chauffage partiel (T < 120 K), indiquant l'existence d'une réaction chimique intermédiaire activée thermiquement.

Des expériences de RPE PW sont réalisées pour caractériser les temps de relaxation spin-réseau (T_1) de notre système et spin-spin (T_2). L'étude de l'intensité de signaux RPE avec la température du système montre qu'au-dessus de 30 K, le système subit une réaction chimique, réduisant la présence des radicaux méthyles. Ce phénomène induit des altérations dans le temps de cohérence (T_2), qui est intrinsèquement lié à la concentration des spins. Les analyses montrent que le core-defect présente des temps de relaxation plus courts, ce qui signifie une interaction plus forte avec les spins voisins et suggère une concentration plus élevée de cette espèce. La raie de RPE affichant un temps de cohérence

plus long est associée au système à 3-raies (L_5).

L'étude du temps de relaxation spin-réseau (T_1) suggère que la préservation de l'aimantation est plus efficace dans les groupes organiques par rapport au core-defect.

Après l'étude des NPs de ZnO non dopées, nous passons à l'étude des nanoparticules de ZnO dopées avec des ions de cobalt. L'avantage de l'incorporation d'un ion de métal de transition (TM) dans un cristal semi-conducteur réside dans la présence d'un état électronique à spin élevé intrinsèque, originaire de l'ion TM, qui réside dans la bande d'énergie située en dessous du niveau de Fermi (c'est-à-dire, occupé même lorsque $T \rightarrow 0$). Dans ce contexte, nous étudions deux types de NPs de ZnO dopées au cobalt. Les deux ensembles d'échantillons explorés dans ce chapitre sont :

1. ZnO:Co synthétisé par la méthode sol-gel.

2. ZnO:Co synthétisé à l'aide de méthodes à haute température.

Les NPs synthétisées par la méthode sol-gel présentent un diamètre moyen d'environ 15 nm. Le processus de dopage n'a pas d'impact sur la taille des nanoparticules. Cependant, soumettre les NPs à une procédure de recuit entraîne une augmentation du diamètre jusqu'à 50 nm. Les NPs produits par la méthode sol-gel sont nettement plus petits que ceux dopés par réaction à l'état solide (haute température), qui ont un diamètre moyen de 70 nm. Les deux techniques de fabrication donnent des NPs avec une cristallinité élevée. Le motif structural est conforme à la structure cristalline wurtzite, et il n'y a pas de formation discernable d'agrégats de cobalt dans le matériau.

L'incorporation de cobalt dans le réseau du ZnO entraîne l'élimination du core-defect ionisé, suggérant une relation concurrentielle entre ces deux systèmes. La génération de radicaux méthyles à la surface des NP, déclenchée par une réaction de photo-Kolbe, dépend notablement de la présence et de l'activation du core-defect. Dans les cas où le core-defect est absent, la formation de radicaux méthyle est inhibée. La quantité de trous photo-générés peut être contrôlée en augmentant la température et également par l'incorporation de cobalt dans les NPs de ZnO.

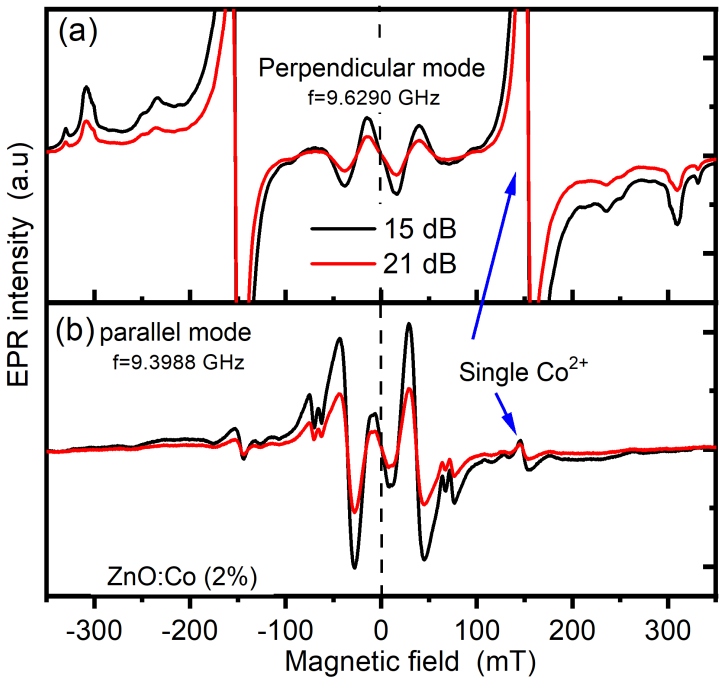

Figure 4: *(a) Spectres en mode perpendiculaire ($B_1 \perp B_0$) de ZnO/Co 2%. (b) Spectres de RPE enregistrés en utilisant le mode parallèle ($B_1 \parallel B_0$) de la cavité à double mode. Dans les deux cas, la transition à champ nul est présente.*

Lorsque la quantité de cobalt devient importante (plus de 1%), les ions de cobalt sont moins isolés et interagissent par l'intèraction d'échange, ce qui conduit à la formation de paires Co^{2+} détectables. Les valeurs des constantes de couplage J ont été déterminées et leur présence a été associée à deux paires ferromagnétiques et deux paires antiferromagnétiques dans les spectres de RPE, couvrant les bandes X et Q. Les valeurs estimées du couplage J varient de |0,137| à |0,378| K.

Dans le cas des paires Co^{2+}, leur grande anisotropie conduit à une relation parabolique dans les niveaux de résonance, permettre l'occurrence des transitions de RPE en mode parallèle. Enfin, les facteurs les plus limitants pour l'utilisation de ces spins appariés dans un contexte de technologie quantique sont la difficulté de contrôler leur nombre et leur nature.

Dans un dernier chapitre, visant à expliquer de manière concise les phénomènes décrits tout au long de la thèse, en indiquant le mécanisme qui génère la présence des composés organiques à la surface de la NP.

Nous commençons par une explication possible pour le système à 3 raies, indiquant qu'il peut provenir de la formation de biradicaux à travers l'interaction de deux radicaux méthyles. Nous simulons l'effet des interactions d'échange et dipolaires pour étayer cette théorie.

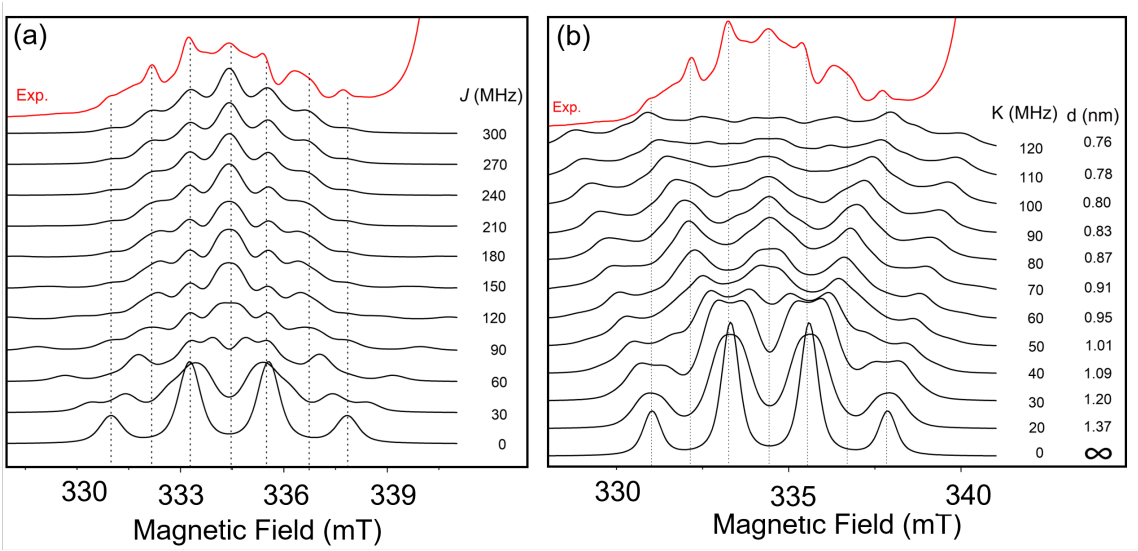

Figure 5: *Effet de l'interaction d'échange (a) et de l'interaction dipolaire (b) entre deux radicaux méthyle sur le spectre RPE du radical méthyle. En rouge, les résultats expérimentaux obtenus par relaxation optique de l'échantillon as-grown pendant 480 minutes sont présentés à titre de comparaison.*

Par la suite, nous avons analysé comment l'interaction de deux radicaux méthyles peut se produire via les interactions d'échange et dipolaires, ainsi que les effets que ces interactions peuvent avoir sur le spectre RPE. Sur la base des simulations réalisées avec EasySpin et des résultats expérimentaux obtenus, nous montrons que l'apparition du système à 3 raies pourrait être due à la formation de biradicaux.

Nous montrons qu'avec des valeurs appropriées d'interaction d'échange et dipolaire, les spectres expérimentaux sont presque exactement reproduits. Nous notons que des analyses futures doivent être effectuées pour des preuves concluantes de l'origine de ce système, où une distribution d'interactions devrait être considérée.

Enfin, une dernière partie est incluse afin d'associer tous les résultats obtenus avec les NPs dopées et non-dopées dans un modèle physique, expliquant la génération de radicaux méthyle à la surface de la NP. Ce modèle repose sur la propriété de polarisation du ZnO. La polarisation présente dans ce matériau induit des charges de surface fictives, et par conséquent, un potentiel électrique non constant à l'intérieur de la NP. Cela conduit le système hors de l'équilibre thermodynamique. La tendance du système est de revenir à l'équilibre, ce qui se fait par la passivation des surfaces polaires.

À température ambiante, la passivation de la surface est principalement réalisée par les défauts du réseau cristallin. Dans ce régime spécifique, la passivation des NPs implique principalement les défauts superficiels du réseau ZnO. Les défauts donneurs libèrent des électrons, qui agissent comme des passivateurs pour la surface chargée positivement. En revanche, le défaut ionisé (après libération de l'électron et devenant chargé positivement) est responsable de la passivation de la surface négative.

À basse température, le mécanisme change car la conductivité des NPs diminue, devenant plus isolante à mesure que la température est réduite. Dans ce régime, l'augmentation du potentiel électrique, une fois que les surfaces ne sont plus passivées, entraîne l'ionisation de l'acide acétique, identifié à la surface de la NP. Cette dissociation entraîne la production de CH_3COO^- (acétate) et la libération d'un proton H^+. À cette température, ces éléments sont responsables de la passivation.

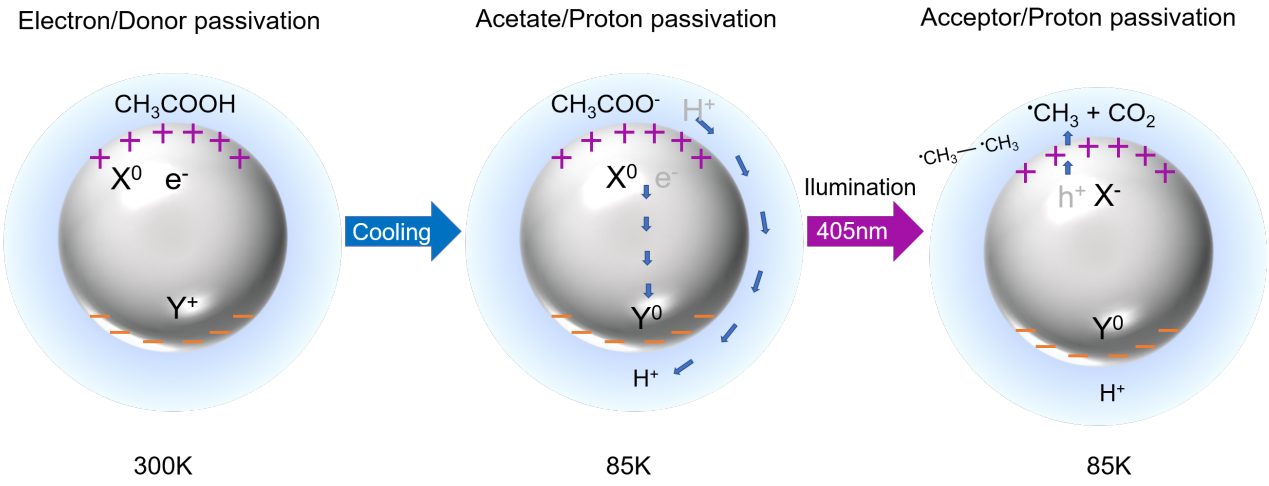

Figure 6: *À température ambiante, la surface des NP est passivée par des donneurs peu profonds. Avec la diminution de la température, les électrons reviennent à leurs centres d'origine, incitant la passivation de la surface par l'ionisation des molécules d'acide acétique situées à la surface des NP. Lors d'une excitation optique, la réaction de photo-Kolbe se produit, aboutissant à la formation de radicaux méthyle détectables par RPE.*

Cependant, lors de l'excitation optique des NPs, une énergie suffisante (3 eV) est fournie pour promouvoir un électron de la bande de valence vers un état intraband-gap créé par un défaut accepteur, laissant un trou dans la bande de valence.

$$\mathrm{X}^0 \xrightarrow{h\nu} \mathrm{X}^- + \mathrm{h}^+ \text{ (bulk)} \tag{1}$$

Ce défaut ionisé est associé au signal que nous observons en RPE, à $g = 1,96$, le core-defect. Ensuite, les trous photo-générés peuvent être transportés vers la surface de la NP :

$$\mathrm{h}^+ \text{ (bulk)} \rightarrow \mathrm{h}^+ \text{ (surface)} \ , \tag{2}$$

Les trous photo-générés sont des espèces oxydantes réactives potentielles et peuvent interagir avec les acétates présents en surface. Dans ce contexte, le trou est transféré de la NP à l'acétate, conduisant à la formation de radicaux méthyles et de CO_2 en tant que produits de la réaction.

$$\mathrm{h}^+ + \mathrm{CH_3COO}^- \rightarrow^{\cdot} \mathrm{CH_3} + \mathrm{COO} \text{ (surface)} \tag{3}$$

La formation de radicaux par ce processus a été observée par d'autres auteurs [26]. Désignée sous le nom de réaction photo-Kolbe, cette réaction a été largement documentée sur des surfaces oxydées.

L'ensemble de ces travaux trouve son intérêt dans la génération et la manipulation d'états de spin de surface sur des NPs de petite taille, entre 5 et 20 nm, avec des applications potentielles dans les domaines des mémores magnétiques, bits quantiques et des capteurs magnétiques à l'échelle nanométriques.

Acknowledgements

I was born in July 1996, and since then, I've navigated through numerous decisions — some good, some not so much. Throughout it all, I've been fortunate to have the unwavering support of my beloved sister, Bianca Marin. Therefore, during this incredibly special (albeit stressful) moment in my life, I want to express my heartfelt gratitude to her.

For being the guiding light throughout the arduous journey of my Ph.D., I extend my heartfelt thanks to Adrien Savoyant. Over these three years of collaboration, I had the pleasure of working alongside Adrien, who shared brilliant (and occasionally unconventional) ideas and imparted invaluable lessons on the proper practice of science. Beyond the humor and jokes, his influence inspired me to consistently strive for excellence, a phenomenon that I affectionately refer to as the "Savoyant effect".

I extend my gratitude to Sylvain Bertaina for his invaluable teachings, particularly in pulsed EPR techniques. It was a pleasure to collaborate with such a brilliant mind.

I express my gratitude to Guillaume Gerbaut, Guillaume Reinhart, Michael Texier, Hervé Vezin, Giuseppe Sicoli, Olivier Margeat, Fabio Ziarelli and Andrea Campos, for their patience in teaching me their respective specialized techniques and equipment, often taking the time to explain concepts multiple times. Additionally, I extend special thanks to Remy Dassoneville, who patiently taught me the fundamentals of Python programming and offered valuable tips for this thesis.

In Brazil we said that one swallow doesn't make a summer. For helping me to make this summer, I would like to thank all the swallows that helped me, my dear friends Loïc Soriano, Gueric Etesse, Martin O'Byrne, Zahraa Jradi, Jeremy Rebaud, Iago Modenez and Remy Dassoneville (again). Your support and assistance have been invaluable.

For love, the fuel of human souls, I thank Hans Beukes.

Abbreviations

- CB : Conduction Band
- CD : core-defect
- CW: Continuous Wave
- EPR : Electron Paramagnetic Resonance
- ESEEM : Electron Spin Echo Envelope Modulation
- FID : Free Induction Decay
- FTIR : Fourier Transform Infrared Spectroscopy
- HYSCORE : Hyperfine Sublevel Correlation
- HOMO : Highest Occupied Molecular Orbital
- LUMO :Lowest Unoccupied Molecular Orbital
- NMR : Nuclear Magnetic Resonance
- NP : NP
- PW : Pulsed Wave
- SEM : Scanning Electron Microscopy
- SOMO : Singly Occupied Molecular Orbital
- TEM : Transmission Electron Microscopy
- VB : Valence Band

Symbols and physical constants

- γ : gyromagnetic ratio
- ν_D : Deuterium nuclear frequency
- ν_H : Hydrogen nuclear frequency
- $h = 6.626.10^{-34}$ J.s : Planck constant
- $\hbar = 1.055.10^{-34}$ J.s : Reduced Planck constant
- B_0 : Static Magnetic Field
- c : Speed of light 3.10^8 m/s
- e : elementary charge $=1.602.10^{-19}$ C
- g : g-factor
- J : Exchange coupling constant
- $k_B = 1.380.10^{-23} J.K^{-1}$: Boltzmann Constant
- T_1 : Spin-lattice relaxation time
- T_2 : Coherence time
- μ : magnetic moment
- $\mu_B = 9.27.10^{-24}\ J.T^{-1}$: Bohr's magneton
- χ : Magnetic susceptibility

Contents

Liste de publications et participations aux conférences **IV**

Resumé **V**

Abstract **VI**

Résumé étendu **VII**

Abbreviations **XVII**

Symbols and physical constants **XVIII**

Introduction **1**

1 ZnO and Semiconductor Physics at the Nanoscale **5**
1.1 Semiconductors and molecular orbitals . . . 6
1.2 Properties of ZnO . . . 7
1.2.1 Crystalline structure . . . 7
1.2.2 Polarity . . . 8
1.2.3 Intrinsic defects . . . 9
1.3 Generation and recombination of carriers in semiconductors . . . 13

2 Introduction to Continuous Wave and Pulsed Wave EPR techniques **15**
2.1 Paramagnetism . . . 17
2.2 The g-factor . . . 18
2.2.1 g-factor anisotropy . . . 19
2.3 Measuring the Zeeman effect - Principles of EPR . . . 21
2.3.1 Homogeneous broadening . . . 23
2.3.2 Inhomogeneous broadening . . . 23
2.3.3 Static magnetic field and microwave frequency . . . 23
2.4 The interaction Hamiltonian . . . 24
2.4.1 Hyperfine interaction . . . 25
2.4.2 Superhyperfine interaction . . . 26
2.4.3 Zero-field splitting . . . 26
2.4.4 Exchange interactions . . . 27
2.4.5 Dipolar interaction . . . 28
2.5 The total Hamiltonian . . . 28
2.6 Magnetization evolution - Bloch equations . . . 29
2.7 Spin-lattice relaxation T_1 . . . 32
2.7.1 Direct process . . . 32

2.7.2 Raman process . . . 34
2.7.3 Orbach process . . . 34
2.8 Transversal relaxation time T_2 . . . 35
2.8.1 Instantaneous diffusion . . . 35
2.8.2 Spectral Diffusion . . . 36
2.9 Pulsed EPR . . . 37
2.10 Free Induction Decay (FID) . . . 39
2.11 Hahn's echo . . . 39
2.12 Rabi Oscillations . . . 40
2.13 Pulsed EPR techniques . . . 41
2.13.1 Inversion recovery (T_1) . . . 41
2.14 T_m measurements . . . 42
2.14.1 2-pulses echo decay . . . 42
2.15 ESEEM . . . 44
2.16 HYSCORE . . . 44
2.17 Nuclear effects investigated by double resonance techniques . . . 46
2.17.1 ELDOR detected NMR . . . 46

3 Experimental Procedures 48
3.1 Studied Samples - Fabrication methods . . . 49
3.1.1 ZnO synthesized via solid-gel method . . . 49
3.1.2 ZnO annealed . . . 49
3.1.3 ZnO aqueous coprecipitation . . . 50
3.1.4 ZnO:Co doped . . . 50
3.2 Nuclear Magnetic Resonance . . . 51
3.3 Fourier Transform Infrared spectroscopy(FTIR) . . . 51
3.4 Electron microscopy . . . 52
3.4.1 Scanning Electron Microscopy (SEM) . . . 52
3.4.2 Transmission Electron Microscopy (TEM) . . . 52
3.5 Electron Paramagnetic Resonance . . . 52
3.5.1 Continuous wave EPR . . . 52
3.5.2 Pulsed EPR . . . 53

4 Paramagnetic Behavior in Photo-Excited ZnO Nanoparticles 54
4.1 Identification of the different paramagnetic systems . . . 56
4.1.1 Dark condition . . . 57
4.1.2 Photo-activated elements . . . 57
4.2 ZnO as-grown and annealed . . . 59
4.2.1 Identification of organic compounds . . . 59
4.2.2 Morphological characterization . . . 61
4.3 EPR Study . . . 62
4.3.1 Core- and surface-defect . . . 63
4.3.2 Spin value . . . 66
4.4 Methyl radicals (4-lines system) . . . 67
4.4.1 Deuteration . . . 68
4.4.2 Analytical Approach . . . 71
4.4.3 Identification of the electronic spins . . . 73
4.4.4 Saturation phenomena . . . 74
4.5 Chemical stability over time . . . 77

4.5.1 Changing the synthesis reagent and solvent . . . 79
4.6 Relaxation from the optically excited state . . . 80
4.6.1 Irreversible regime . . . 83
4.6.2 Reversible regime . . . 86
4.7 3-lines signal . . . 87
4.8 Relaxation phenomena - core-defect, Methyl radicals and 3-lines system . . . 90
4.9 Spin lattice relaxation time (T_1) . . . 91
4.10 Coherence time (T_2) . . . 94
4.10.1 2-pulses echo decay . . . 95
4.11 Electron Spin Echo Envelope Modulation (ESEEM) . . . 99
4.12 HYSCORE . . . 102
4.13 Q-band EPR analysis . . . 104
4.14 Correlation between EPR lines - ELDOR detected NMR . . . 106
4.15 Partial conclusions . . . 108

5 Co-doped ZnO 112
5.1 ZnO:Co nanoparticles wet fabrication method . . . 114
5.2 Nanoparticle's characterization . . . 115
5.3 EPR Study . . . 117
5.4 ZnO:Co high-temperature method . . . 120
5.4.1 Nanoparticle's characterization . . . 120
5.4.2 EPR study . . . 123
5.5 Analytical and simulation approaches . . . 129
5.5.1 Matrix interaction . . . 129
5.5.2 Eigenenergies and eigenstates . . . 132
5.5.3 Perturbational treatment of the Zeeman interaction . . . 133
5.5.4 EPR transitions . . . 134
5.5.5 Simulations . . . 135
5.6 Partial conclusions . . . 137

6 Physical modelling 139
6.1 Origin of the 3-lines system . . . 140
6.2 Polar nanoparticles . . . 148
6.2.1 Non-passivated nanoparticles . . . 150
6.2.2 Passivated nanoparticles . . . 152

Conclusion 161

Future Perspectives 166

A ZnO NP synthesis 167

B Fourier Transform Infrared Spectroscopy (FTIR) 168

C Raising and lowering operators formalism 172

D "Elephant" signal 173

E Orientation of an anisotropic crystal in EPR 175

F Analytical coefficients **177**

Bibliographie **178**

Introduction

> Nothing is absolute. Everything changes, everything moves, everything revolves, everything flies and goes away.
>
> *Frida Kahlo*

Quantum technologies exploit quantum properties of matter, like superposition, tunneling, and entanglement, for their operations. The beginning of the quantum era was marked by the first quantum revolution, a period that delineated the discovery of the quantum properties of matter and established the distinctions between quantum and classical phenomena.

In the contemporary age, we are witnessing the unfolding of what is often termed as the second quantum revolution. This phase is propelled by progress in efficient technologies based on the quantum properties of matter, leading to advancements in quantum information, quantum sensing, quantum optics, and associated fields [27]. One notable hurdle in realizing functional systems of this nature involves temperature demands. Maintaining extremely low temperatures is often imperative to prevent thermal fluctuations that can disrupt the coherence of the system. Consequently, temperatures on the order of millikelvin (mK) are typically necessary. There is considerable interest in developing functional systems capable of preserving coherence even at higher temperatures, as they would significantly expand the potential applications and usability of quantum technologies in various scientific and practical domains.

As potential candidates for this evolutionary leap, various elements are considered, including polarized photons [28], ionic traps [29], and both nuclear and electronic spins [30]. In recent times, special attention has been directed towards localized spins within semiconductors, once that these spins possess the potential to encode fundamental units of quantum information [31; 32; 33] and can act as a two-level system [34]. Advancements in this field also consider the prospect of employing molecular spin qubits. Stable organic radicals and biradicals, in particular, are being considered for their potential role in adiabatic quantum computation [35].

This engineering achievement demonstrates that the presence of defects expands the utility of semiconductors beyond materials with well-defined band-gaps and p- or n- type conductivity, opening up an entirely new realm of investigation. Over the past 50 years, extensive research into this extrinsic behavior has resulted in the multitude of applications seen in today's semiconductor materials [36].

In this context, zinc oxide (ZnO) stands out as a versatile material widely employed across various scientific and technological domains, such as Material Science, Physics, Astronomy, Engineering, and Chemistry. Its appeal lies in the affordability, robust sta-

bility, and intriguing physical properties, such as piezoelectricity and stable excitons at room temperature. Another distinguishing feature of ZnO is its strong interaction with light, leading to various photo-induced effects observed in numerous studies. These effects include phenomena like photo-conductivity [1; 2; 3], photocatalysis [4; 5; 6; 7], and photo-luminescence [8; 9]. The compound's response to light enables applications across different fields and continues to be an area of active research due to its potential in various technological advancements.

Notably, the observation of photo-induced magnetic activity in ZnO positions this material as a promising candidate for applications in quantum sensors [10] or magnetic memories. The observed photo-induced effects are mainly driven from excitonic and point defects related properties, along with their interplay [11; 12; 13; 14; 15]. Light exposure has the ability to ionize point defects within the ZnO lattice, resulting in the emergence of intraband-gap states [24; 25], potentially demonstrating paramagnetic characteristics. The ionization of point defects can provide an electron in the conduction band or a hole in the valence band of the semiconductor. These delocalized state can then propagate throughout the crystal and recombine or react far from their generating centers.

Particularly in nanostructured ZnO systems, the photo-induced effects may be influenced by a substantial surface-to-volume ratio and the presence of specific point defects that can serve as recombination sites or charge donor/acceptor centers. Exploring and understanding these properties in nanoscale ZnO systems is of great interest for tailoring efficient devices based on ZnO nanostructures.

A powerful tool for studying point defects in semiconductors is the Electron Paramagnetic Resonance (EPR). This technique offers as its principal advantages, high sensitivity (up to 1000 times more sensitive than NMR) and specificity (capability of distinguishing and characterizing different properties or types of defects with precision), allowing for the investigation of static and dynamic properties in various materials, such as chemical and biological systems [16]. This technique has the capability to differentiate between different types of point defects, including impurities, atomic vacancies, or other defects within the crystal structure. EPR can provide detailed insights into the nature of these defects, their location in the crystal lattice, and even how they interact with their environment. The ability to specifically identify and characterize these defects is crucial for understanding the structure and properties of materials, as well as for the development of more advanced electronic devices. The EPR technique has been employed for over fifty years to analyze intrinsic and extrinsic paramagnetic defects within ZnO [17; 18; 19; 20; 21; 22]. The EPR spectroscopy is based on the Zeeman interaction, which involves the property of unpaired electrons to align themselves with a static magnetic field and undergo state transitions (flips) when energy is provided via photons. The operational wavelength of EPR is in the microwave domain (approximately 3 cm in the X-band). This wavelength corresponds to a photon with energy of approximately 10^{-5} eV.

Aside from the conventional continuous wave (CW) EPR technique, which provides information regarding the electronic spin and its interactions with the environment, the pulsed wave (PW) EPR method offers additional insights into its dynamics. PW EPR techniques provides access to additional information about the system, including the elucidation of weakly coupled nuclei, the enhancement between forbidden transitions, and direct insights into the relaxation properties of the electronic spins. The fundamental concept behind PW EPR involves the manipulation of spins through specific sequences of microwave pulses. This manipulation enables to align the spins in specific directions, allowing the observation of subsequent relaxation processes. Furthermore, double reso-

nance techniques offer the capability to excite simultaneously different transitions and subsequently observe the correlation between them.

In bulk ZnO, EPR studies have consistently identified a signal at g=1.96, originating from defects within the crystal lattice. Despite numerous investigations, the precise nature of this defect remains an ongoing challenge in the field. In nanostructures, as the size of the structure decreases, surface-related signal gains prominence in the EPR spectra. In this domain, a signal emerges at g = 2.003, that has been demonstrated to be related to surface defects [23], indicating the amplified influence of the surface in smaller structures.

The combination of characteristics originating from the bulk of the NP together with the properties arising from the surface constitutes the core-shell model for NPs [37]. This model serves as a conceptual framework to comprehend the intricate interplay and collective influence of the distinct characteristics exhibited by the interior core (rather stable and characteristic of the material) and the shell (more versatile and environment dependent) of the system.

Insights into the aspects of the before mentioned EPR signals observed in ZnO can be attained by introducing additional excitation during the experiment, such as an optical light beam. This approach aids in deciphering the well-documented interactions of ZnO with light. In bulk ZnO single crystal, photo-EPR experiments have shown that the signal of the core-defect (g=1.96) is highly sensitive to photo illumination [38; 39; 40]. In NPs, studies have shown that altering the synthesis method or subjecting the samples to annealing can alter the state of the core-defect, that can be present even in the absence of photo-excitation [41]. Surprisingly, applying photo-excitation EPR techniques, additional states (not related to the well known core-defect neither to the surface state situated at g=2.003) are detected [1; 42]. Careful analysis reveals that these newly observed photo-induced states are associated with a complex shell that encapsulates the ZnO nanostructures when specific synthesis methods are employed for the NPs production [**?**]. It has been observed that these photo-activated states can remain stable for several hours after excitation removal, indicating promising prospects for encoding information at a very low scale in these semiconducting NPs[42].

The current thesis is centered on studying the paramagnetic states present in ZnO NPs, originating from internal structural defects, external doping with transition ions, and organic compounds that caps the surface. Furthermore, this study aims to elucidate how these elements interact with light. As the material's properties strongly correlate with the fabrication method of the NPs [43; 44], a meticulous study encompassing various samples synthesized by different methods is carried out, in order to attribute each EPR signal to its precise origin. Investigating the origin of magnetism in these NPs involves examining different combinations of coexisting mechanisms within this system. After identifying the signals, we characteriz each one of them, considering variations in the environment, such as temperature and microwave excitation power, to better understand the present phenomena. To comprehensively address all aspects, this thesis is structured as follows:

1. An initial introductory chapter provides an overview of the essential characteristics exhibited by ZnO at the nanoscale. This chapter aims to lay the foundational groundwork necessary for constructing the physical model that explain the presence of the various paramagnetic states present in ZnO NPs.

2. A second introductory chapter is dedicated to elucidate the Electron Paramagnetic

Resonance (EPR) technique, encompassing both CW and PW regimes. This chapter is essential as EPR constitutes the primary technique employed for characterizing the system under study, and its interpretation can be complex and nuanced.

3. A third chapter is formulated to present the experimental aspects of the work, encompassing the fabrication of the NPs and the equipment used for acquiring the measurements.

4. The fourth chapter delineates the diverse coexisting subsystems inherent in undoped ZnO NPs exposed to photo-excitation. This chapter investigates the paramagnetic states existing in these samples and endeavors to elucidate their inherent nature and characteristics. It presents the main investigations and findings of this thesis.

5. The fifth chapter presents our results obtained on ZnO:Co doped samples. This chapter outlines samples produced by two distinct methods and discusses the properties associated with each of them.

6. A final chapter is included, with the presentation of a physical model, developed in order to explain coherently the results previously presented in the other chapters.

Chapter 1

ZnO and Semiconductor Physics at the Nanoscale

Contents

1.1 Semiconductors and molecular orbitals 6

1.2 Properties of ZnO 7

1.2.1 Crystalline structure 7

1.2.2 Polarity 8

1.2.3 Intrinsic defects 9

1.3 Generation and recombination of carriers in semiconductors 13

Nanomaterials have garnered significant attention in the recent decades. The advancement of electron microscopy has made it possible to directly observe and manipulate materials at the nanoscale. Intriguingly, the properties and phenomena exhibited by nanoparticles smaller than 100 nm have led to the discovery of new and unique characteristics [45].

The emergence of novel properties in these materials can be attributed to two distinct factors: Firstly, there are phenomena that exhibit a smooth scalability. These phenomena are closely associated with the proportion of atoms located on the material's surface, which becomes increasingly significant as the scale is reduced.

Secondly, quantum effects become more pronounced, displaying discontinuous behavior as a result of electron shells being filled in systems with delocalized electrons [46]. In simpler terms, confinement effects take place [47].

Zinc Oxide (ZnO), like other wide band gap semiconductors, has been considered for application in the field of microelectronics but discarded once that its properties aren't so easy-manipulated as silicon-based materials. In particular, the absence of stable and reproducible p-type doping prevent the fabrication of p-n junctions, imposing limitations to its technological applications. A reassessment has begun in recent years due to its intriguing properties and potential applications in various technological fields. This has raised expectations for the development of new materials that combine the semiconductor properties of ZnO and the possibility for quantum manipulation.

ZnO possesses a unique combination of a high bandgap energy (approximately 3.4 eV) and remarkable excitonic stability (around 60 meV). These characteristics make this material and related structures promising for potential applications in the fields of optoelectronics, spintronics, and UV light emission and detection [48].

Preliminary results point to the possibility of achieving both n-type[1] and p-type [2] conduction in ZnO [49]. While n-type conductivity is readily attainable in this material, obtaining p-type conductivity remains a challenge.

In this chapter, we will provide a brief overview of the properties of ZnO, with a specific focus on nano-sized crystals. This foundational knowledge will be essential for understanding the experimental results presented in the next chapters.

1.1 Semiconductors and molecular orbitals

When molecules are formed, the atomic orbitals associated with each of the atoms merge, creating a new orbital that encompasses the entire molecule. A simplified modeling that described this process is achieved through the calculation of the linear combination of the atomic orbitals.

If $|\Phi_1\rangle$ represents the wave function of the valence electron in atom 1, and $|\Phi_2\rangle$ represents the wave function of the valence electron in atom 2 (assuming that these atoms possess only one electron in the valence band each), then the wave functions for the electrons that belong to the molecule formed by atoms 1 and 2 are constructed through a linear combination [50]:

$$|\Psi\rangle = C_1 |\Phi_1\rangle + C_2 |\Phi_2\rangle \tag{1.1}$$

[1]Semiconductor that possess donor impurities. In other words, it gives to the semiconductor a free electron, that is available in the material, increasing the conduction.

[2]Semiconductor that possess acceptors impurities. The conduction is made by means of holes.

In this context, the wave function of the electrons, represented as $|\Psi\rangle$, undergoes modifications that lead to the formation of both bonding and antibonding orbitals. These changes in the wave function describe the reorganization of the electron distribution in the molecule. Bonding orbitals result from constructive interference between the atomic orbitals, leading to increased electron density between the nuclei and a stabilizing effect. Conversely, antibonding orbitals arise from destructive interference, causing reduced electron density between the nuclei and resulting in a higher energy state for the molecule. In semiconductors, the bonding and antibonding states play a pivotal role in determining the allowed energy levels for electrons, which collectively form what is known as energy bands.

It is worth to note that the defining characteristic of a semiconductor primarily stands on the size of its constituent atoms and the interatomic spacing. Together with the number of "free" electrons, these variables will define the conductivity of the material. In some cases, the conductivity can vary depending on the direction within the crystal lattice. This directional dependence of conductivity is a direct consequence of the crystal's structure, with some directions allowing for more efficient electron flow. The presence of conductivity in a semiconductor is contingent upon the availability of electrons and energy states within a band that allow electrons to move. Maximum conductivity is achieved when a band is filled to approximately 50% of its total electron capacity.

At absolute zero temperature, a semiconductor exhibits a completely filled valence band (VB) and an entirely empty conduction band (CB), making it behave as an insulator. However, as thermal energy is introduced, some electrons gain sufficient energy to transition from the VB to the CB, leading to an increase in conductivity. This rise in conductivity is attributed to the greater number of charge carriers—electrons—in the CB, which can move and participate in electrical conduction. Additionally, the presence of defects in the semiconductor can introduce new energy levels inside the band gap, facilitating the conductivity. This combination yields intriguing properties, which will be explored in the following sections, with a particular focus on ZnO.

1.2 Properties of ZnO

1.2.1 Crystalline structure

The formation of the ZnO crystal is a result of the ionic sp^3 hybridization between Zn and O atoms with strong and pronounced charge transfer leading to almost fully ionized cation Zn^{2+} and anion O^{2-}. The bonding sp^3 states give rise to the VB, while the antibonding states form the CB. The energy gap, or separation between these bands, is approximately 3.4 eV [51] and it's characterized as being a direct bandgap [3][52].

ZnO is classified as a II-VI direct wide-band gap semiconductor and can adopt different crystal structures, including zincblende, rocksalt, and wurtzite. The most common phase is wurtzite[4], which is thermodynamically more stable. The wurtzite structure is illustrated in Figure 1.1, where the planes and directions are represented considering the hexagonal structure.

[3]The maximum of the VB and the minimum of the CB lies in the same value of k, so no phonon is needed to promote a transition.

[4]Basic hexagonal symmetry in P63mc space group

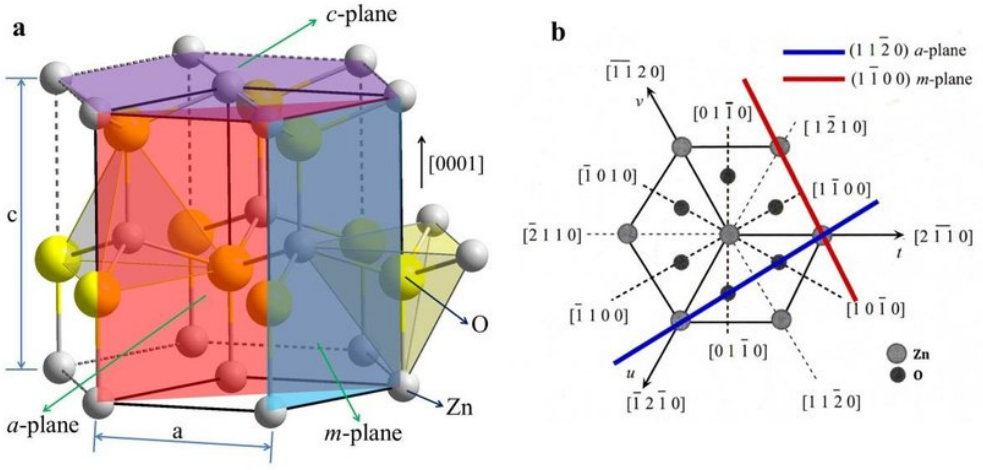

Figure 1.1: *Wurtzite structure. Image extracted from reference [53]*

The standard lattice parameters at room temperature determined by experimental measurements (usually X-ray diffraction) and theoretical calculations (ab initio method) are presented in the table below [54]:

Experimental [55]			Theoretical [56]		
a (Å)	c (Å)	c/a	a (Å)	c (Å)	c/a
3.2496	5.2042	1.6018	3.286	5.241	1.595

Table 1.1: *Standard values for the a, c and c/a parameter for ZnO presented in Wurtzite structure.*

Possible deviations from these parameters can occur due to lattice instability, residual stress or finite size effect in nanostructured materials. The presence of point defects (0D), dislocations (1D), grain boundaries (2D) or secondary phase (3D) can also modify the lattice parameters.

1.2.2 Polarity

The ionic character and the absense of symmetry inversion in the structure of ZnO imparts piezoelectric properties to this material[5] [57]. Among all II-VI compounds possessing a wurtzite structure, ZnO demonstrates the most significant piezoelectric tensor [58] and is also the most ionic compound within this group. This phenomenon arises from the symmetry and the electronegativity of the elements that compound the ZnO lattice. The electronegativity disparity between Zn and O atoms, coupled with the lower structural symmetry in comparison to cubic lattices, results in ZnO having non-coincident centers of positive and negative charges. Consequently, a self-induced electrostatic dipole emerges along the c-axis, present even in the absence of an external field.

[5]Piezoelectricity is a reversible physical process that occurs in some materials whereby an electric moment is generated upon the application of a stress.

The crystal is formed of dipoles $\vec{d}$, that occupies a volume V. The collective effect of these dipoles contributes to a spontaneous macroscopic electrostatic polarization ($\vec{P}$):

$$\vec{P} = \vec{d}/V \tag{1.2}$$

If a material has a polarization, then it induces fictive surface charges, defined as

$$\rho_S = \vec{n} \cdot \vec{P} \tag{1.3}$$

Where $\vec{n}$ is the vector normal to the considered surface. Note that surfaces perpendicular to the polarization present no fictive charges. This mechanism is represented in Figure 1.2.

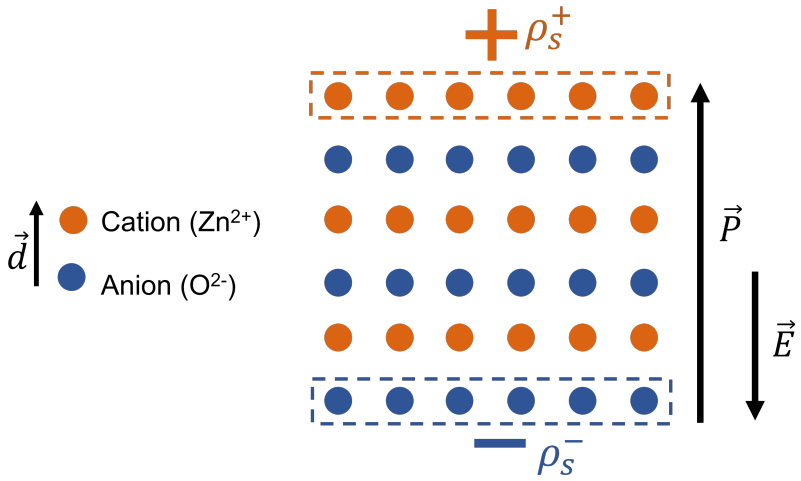

Figure 1.2: *Creation of fictive polar surfaces in an ionic solid.*

With these definitions applied to the wurtzite structure, the c-axis is termed a polar axis, and the c-plane is a polar surface. The presence of these polar surfaces plays a crucial role in the restructuring of the crystal, once that they generally exhibit massive surface reconstructions, as a mechanism for surface stabilization [59]. An interesting characteristic of ZnO is the divergence of theoretical and experimental results concerning the surface restructuration, indicating the presence of charge transfer mechanisms for its stabilization [60].

When polar molecules are present during the synthesis of the crystal, the electric field generated by the surfaces attracts polar molecules, as a mechanism for surface stabilization. This phenomenon results in the creation of a solvation shell that surrounds the particle, maintaining its stability even after the synthesis is complete.

In nanosystems, the solvation shell can significantly influence the properties of the system, especially in the case of small NPs, where the solvation shell can be as large as the nanoparticle itself (for NP's smaller than 5 nm) [61].

1.2.3 Intrinsic defects

The CB of ZnO is essentially made of Zn 4s orbitals and the upper VB from the O 2p and Zn 3d levels [62]. Imperfections in the crystalline lattice, such as interstitial elements and vacancies, lead to the disruption of symmetry within the crystal, creating missing bonds. This disruption introduces energy levels within the band gap of the semiconductor

[63] and a shift in the Fermi level, thereby contributing to an increase in the material's conductivity. In pure semiconductors, the Fermi level is exactly at the center of the band gap.

Defects can act as either shallow or deep donors or acceptors [6] and also serve as recombination centers. Shallow donors introduce an energy level just below the CB, and are typically activated with the thermal energy present at room temperature (approximately 25 meV). At standard conditions, the shallow donor transfers one electron to the CB, contributing to the material's conductivity. Shallow acceptors, on the other hand, are situated just above the VB, so that an electron of the VB can be captured by this impurity at room temperature, leading to a hole in the VB. Deep impurities (acceptors or donors) are localized far away from the allowed energy bands, typically at energies far higher than 25 meV. For this kind of impurity, even when they are present, they don't contribute significantly to the n- or p- conductivity of the material. The representation of the energy levels introduced in a semiconductor band gap through the presence of impurities is shown in Figure 1.3:

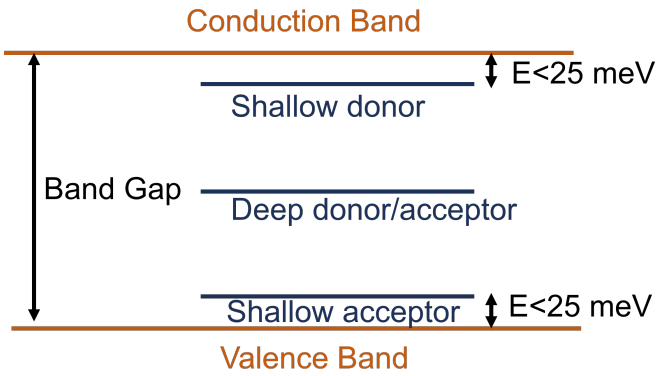

Figure 1.3: *Impurities introduce new energy levels within the semiconductor band gap. Shallow donors release an electron into the CB at room temperature, whereas shallow acceptors create a hole in the VB. On the other hand, deep donors and acceptors are positioned deeper within the band gap, thereby not significantly contributing to either n or p-type conductivity.*

In most of the cases, the ground state of the defects are non-magnetic and so, EPR silent. However, this situation can be altered by applying radiation to change the charge state of the defect. In such cases, EPR can be a valuable tool for determining the origin of the defect, as well as its symmetry and interactions with the surroundings.

When referring to a defect, we will use the Kröger–Vink notation :

$$M_S^C \tag{1.4}$$

Where M corresponds to the species (atoms, vacancies, interstitials), S indicates the lattice site that the species occupies and C corresponds to the electronic charge. It's important

[6] A straightforward definition distinguishes between shallow and deep states based on their ionization energy. Shallow states have ionization energies that are close to the valence or CB (within a few kT), while deep states are located deeper within the band gap. A more comprehensive definition involves the behavior of the wave function. Shallow states exhibit wave functions resembling that of a hydrogen atom, allowing for the calculation of binding energy using the effective mass approximation. In contrast, centers with binding energies that cannot be computed using the effective mass approximation are referred to as deep centers [64].

to note that in this notation, the charge value doesn't stand for the actual charge carried by the site. Instead, it indicates the relative charge concerning the normal charge state in the absence of a defect. For instance, the neutral oxygen vacancy (V_O^0) contains two excess electrons (charge -2) at the site, rendering it neutral relative to the standard O^{2-} site.

It has been demonstrated that the presence of defects in ZnO modify its optical properties [65] and the primary intrinsic defects of interest in ZnO include zinc interstitials (Zn_i), oxygen interstitials (O_i), zinc vacancies(V_{Zn}), and oxygen vacancies (V_O). The native defects present in ZnO are illustrated in Figure 1.4

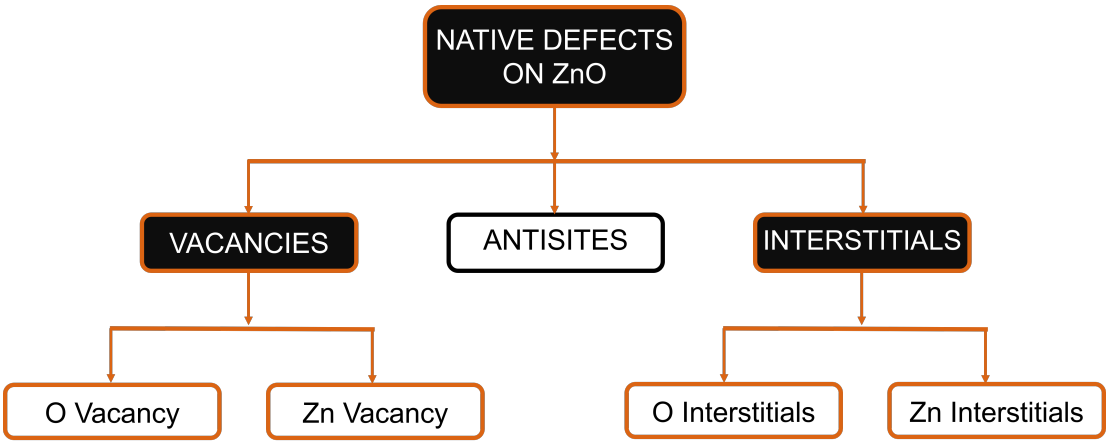

Figure 1.4: *Native defects present in ZnO lattice. Figure adapted from reference [43]*

Oxygen vacancies (V_O)

According to ab initio calculations, oxygen vacancies are classified as deep donor defects. These vacancies can manifest in multiple charge states, including the neutral state V_O^0, where the site contains two electrons, the positively charged state V_O^+, characterized by a single electron at the site, and the negatively charged state V_O^-, with no electrons in the site. Previous studies suggest that the energy needed to ionize a neutral oxygen vacancy to a charged state ($V_O^0 \rightarrow V_o^+$) is approximately 2 eV [66]. In this charged state, these vacancies are associate to a characteristic g-factor = 1.99. Furthermore, an electron from the Zn site remains unattached to the oxygen vacancy, contributing to the population of the CB, thus enhancing the material's conductivity.

Oxygen vacancies possess a relatively low formation energy, and some researchers have indicated these defects as the primary source of n-type conductivity in ZnO [67]. However, other studies suggest that they function as deep donor defects and remain stable in their neutral form, without adding any electrons to the CB. As a result, they may not produce a high concentration of carrier electrons [68].

Nonetheless, V_O can act as recombination centers for charge carriers, influencing both radiative and non-radiative recombination processes in ZnO. For example, a neutral oxygen vacancy can capture a photogenerated hole (which may originate from an exciton), resulting in a single ionized vacancy:

$$V_O^0 + e^- h^+ \rightarrow V_O^+ + e^-(CB) \tag{1.5}$$

The hole from the exciton recombines with one of the two electrons on the neutral vacancy, and the remaining electron from the exciton is free to join the CB.

Zinc vacancies (V_{Zn})

The absence of a zinc atom at its normal site in the crystalline lattice introduces partially occupied states within the band gap, resulting from the missing bonds that would ordinarily form between the zinc atom and its four nearest oxygen neighbors.

Zinc vacancies are theoretically linked to p-type conductivity, enhancing the mobility of positively charged carriers, or "holes". These vacancies are deemed as deep electron acceptors. Theoretically, zinc vacancies are proposed to be the primary acceptor-type defects in ZnO [66; 68].

Zinc Interstitial (Zn_i)

The wurtzite crystal structure accommodates interstitial atoms in two distinct sites: the tetrahedral site and the octahedral site. The tetrahedral site imposes stringent geometric constraints on interstitial zinc, while the octahedral site, forming a channel along the c-axis, presents fewer constraints.

Due to the more favorable conditions, interstitial zinc atoms are expected to be more abundant in the octahedral site. However, even in this preferred location, Zn_i still possesses a notably high formation energy. Consequently, they are not considered the primary contributors to ZnO conductivity, as indicated by previous research [66], however, it is important to note that zinc interstitials are classified as shallow donors in the material.

Oxygen Interstitial (O_i)

Lastly, we turn our attention to Oxygen Interstitial defects. It is worth noting that the formation energy for this particular defect is considerably high, leading us to anticipate that the presence of oxygen interstitials in significant concentrations is not likely under equilibrium conditions.

The presence of interstitial oxygen at the octahedral site introduces states in the lower section of the band gap, capable of accommodating two electrons. These states are derived from oxygen p orbitals, giving rise to deep acceptor transition levels [66].

Complex defects

The presence of green luminescence in ZnO points to the existence of complex defects formed in the ZnO lattice [69; 70]. It was reported in previous studies that complexes defects act as nonradiative recombination centers in ZnO [71; 72]. These complex can involve intentionally doped hydrogen atoms that are added to the lattice during the NPs syntheses and are commonly present in association with the defects mentioned before. More specifically, $V_{Zn} - H_i$, $O - H$ and $Zn - H_O$. The combination of interstitial and vacancies elements is also a source of new energy levels, and are characterized by the formation of defects type $V_{Zn} - Zn_i$ and $V_{Zn} - V_O$ [73].

The existence of such intricate defects results in complexity concerning the energy levels introduced by the point defects within the band gap. The precise values are often based on approximations that may not consistently align with the real scenario, thereby leading to conflicting outcomes in the literature.

1.3 Generation and recombination of carriers in semiconductors

The connection between the VB and the CB in a semiconductor can be made through optical excitation, that gives the necessary energy to overcome the band gap present in the material. In a first moment, a photon of energy $h\nu$ (with energy higher than the band gap) is absorbed, generating an electron-hole pair. In a second moment, the material tends to return to its lower energy state by recombining the electron-hole pair, releasing energy in either a radiative or non-radiative manner. During this relaxation process, the system emits phonons (heat) and/or photons (light). The most straightforward mechanisms for creating electron-hole pairs are those that do not rely on phonons, typically observed in semiconductors with a direct band-gap. In such cases, the most common recombination pathways for electrons and holes include:

Band to band recombination

When the energy supplied by a photon is sufficient to excite an electron beyond the band gap energy value (e.g., 3.37 eV for ZnO), the electron can transit directly from the VB to the CB in the case of direct band semiconductors. In the case of indirect band semiconductors, the transition may involve the assistance of a phonon with appropriate k-vector.

Conversely, the reverse process leads to the recombination of the electron-hole pair, resulting in the emission of a photon through either spontaneous or stimulated emission.[2].

Trap centers - Intermediate states

Traps within the band gap can be created through defects or impurities in the semiconductor lattice. In this scenario, an electron in the VB may transit to an intermediate state associated with the trap before migrate to the CB. The energy required for this process is lower than the energy needed for a direct transition from the VB to the CB.

On the other hand, defects also play a significant role in the recombination rate, as they facilitate the relaxation of the excited state. When a defect attracts an electron through electrostatic interaction, it can also attract a hole. As a result, the defect functions as a recombination center, encouraging the recombination of electron-hole pairs. It is important to note that this process can be thermally activated [74].

Traps play a crucial role as they temporarily reduce the number of free carriers, thereby altering the conductivity of the semiconductor. The process involving the generation and recombination of electrons and holes in semiconductors through trapping mechanisms is commonly referred to as the Shockley-Read-Hall effect, which primarily involves non-radiative processes [75].

Excitons

Excitons are composite entities formed when a free electron and a free hole become bound to each other. The excitons have the ability to diffuse through the semiconductor medium.

[2]Stimulated emission is a process where an excited electron interacts with a photon in a manner that prompts the electron to recombine with it, leading to the emission of a photon with identical properties to the incident one.

Several types of excitons exist, including Frenkel[7] , Wannier [8], Mott [9] , and charge transfer excitons.

In the context of Frenkel excitons, electrons within the VB are excited, becoming detached from the atoms in the lattice while remaining bound to their respective holes. Under the influence of external factors such as an electric field, these excitons can give rise to free electron-hole pairs.

When a sample contains a limited number of donors or acceptors, impurities within the lattice attract excitons through van der Waals interactions. In this scenario, the exciton becomes trapped by the impurity and is referred to as a bound exciton. In ZnO, the exciton binding energy is well-established at 60 meV. In high-quality ZnO crystals at cryogenic temperatures, direct radiative recombination of shallow donor-bound excitons typically dominates in photoluminescence, as discussed in [76]. At temperatures below cryogenic levels, excitons may become bound to impurities in the lattice. Photoluminescence analysis of ZnO has revealed the presence of numerous bound excitons emitting at low temperatures, as discussed in [77; 78].

The three principal mechanisms for the generation of electron-hole pairs are depicted in Figure 1.5:

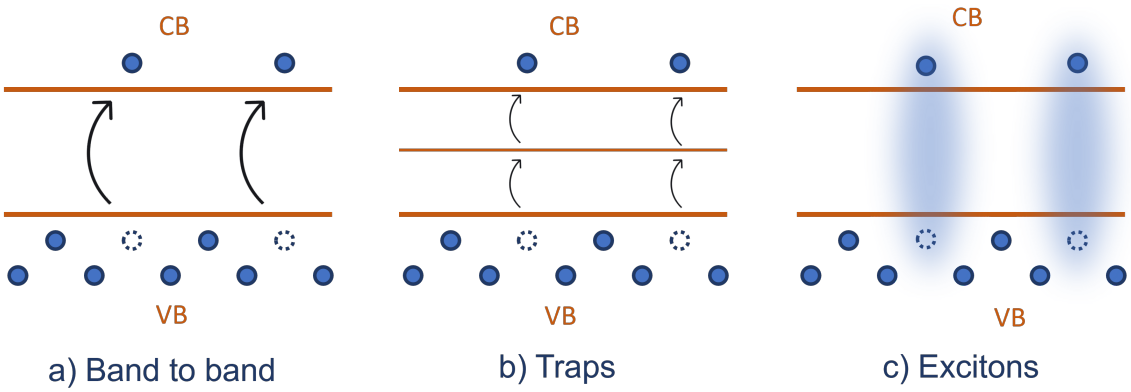

Figure 1.5: *Principal mechanismsn for the generation of electron-hole pairs in semiconductors.*

The characteristics mentioned above will be of fundamental interest when analyzing ZnO nanoparticles through EPR. In this context, the paramagnetism of the system arises from defects present in the lattice. Therefore, the fabrication method of the crystal is crucial, as it defines the quantity and nature of these defects.

[7]Frenkel Excitons: These excitons occur when the electron and hole are localized on the same molecule or ion within a crystal lattice. They are common in molecular crystals or materials with tightly confined units.

[8]Wannier-Mott Excitons: Wannier excitons arise when the electron and hole are spatially separated but still bound together due to electrostatic attraction. This can happen in materials with lower dielectric constants or when the electron-hole pair is localized in adjacent lattice sites.

[9]Mott Excitons: Mott excitons form due to strong Coulomb interactions between electrons and holes, particularly in materials with a high concentration of charge carriers. They appear when the binding energy of the exciton is comparable to or greater than the energy gap between the conduction and valence bands. Mott excitons are characteristic of strongly correlated electron systems and are influenced by band structures and many-body effects.

Chapter 2

Introduction to Continuous Wave and Pulsed Wave EPR techniques

Contents

2.1 Paramagnetism . . . 17
2.2 The g-factor . . . 18
2.2.1 g-factor anisotropy . . . 19
2.3 Measuring the Zeeman effect - Principles of EPR . . . 21
2.3.1 Homogeneous broadening . . . 23
2.3.2 Inhomogeneous broadening . . . 23
2.3.3 Static magnetic field and microwave frequency . . . 23
2.4 The interaction Hamiltonian . . . 24
2.4.1 Hyperfine interaction . . . 25
2.4.2 Superhyperfine interaction . . . 26
2.4.3 Zero-field splitting . . . 26
2.4.4 Exchange interactions . . . 27
2.4.5 Dipolar interaction . . . 28
2.5 The total Hamiltonian . . . 28
2.6 Magnetization evolution - Bloch equations . . . 29
2.7 Spin-lattice relaxation T_1 . . . 32
2.7.1 Direct process . . . 32
2.7.2 Raman process . . . 34
2.7.3 Orbach process . . . 34
2.8 Transversal relaxation time T_2 . . . 35
2.8.1 Instantaneous diffusion . . . 35
2.8.2 Spectral Diffusion . . . 36
2.9 Pulsed EPR . . . 37
2.10 Free Induction Decay (FID) . . . 39
2.11 Hahn's echo . . . 39

2.12 Rabi Oscillations 40
2.13 Pulsed EPR techniques 41
2.13.1 Inversion recovery (T_1) 41
2.14 T_m measurements 42
2.14.1 2-pulses echo decay 42
2.15 ESEEM 44
2.16 HYSCORE 44
2.17 Nuclear effects investigated by double resonance techniques . 46
2.17.1 ELDOR detected NMR 46

To effectively interpret the EPR results presented in the upcoming chapters and relate them to the underlying physical phenomena occurring inside and on the surface of the NPs, thus deriving meaningful insights about our system, we introduce a concise chapter presenting the EPR techniques. This chapter introduces the concept of magnetization within the framework of quantum mechanics and provides fundamental insights into the EPR analysis, both in continuous wave (CW) and pulsed wave (PW) regimes.

Readers who have a comprehensive understanding of EPR principles may choose to skip this specific chapter, as its content may already be familiar to them.

2.1 Paramagnetism

Paramagnetism is a magnetic phenomenon occurring in materials, where individual magnetic moments do not strongly interact with each other. In the absence of magnetic field, the magnetic moments are randomly oriented [79]. When an external magnetic field is applied, the magnetic moments tend to align in the direction of the field, resulting in weak induced magnetisation. This alignment disappears when the external magnetic field is removed. Paramagnetism is observed in materials containing atoms or ions with unpaired electrons, such as certain transition metals and molecular magnets.

At the atomic scale, the phenomenon of paramagnetism is explained through the concept of total angular momentum, denoted $\vec{J}$, which is the sum of both orbital momentum ($\vec{L}$), and intrinsic spin angular momentum ($\vec{S}$), henceforth, we are resulted with the equation

$$\vec{J} = \vec{L} + \vec{S}. \tag{2.1}$$

Under many circumstances, $\vec{L}$ can be zero, particularly in the ground state, due to crystal field effect (the so-called orbital momentum quenching). Consequently, the primary source of magnetism stems from $\vec{S}$ in this case. The total angular momentum can also possess degenerate values, and in such cases, distinct quantum states can be separated by the application of an external magnetic field, through the *Zeeman effect*, that affects particles that possess magnetic moment.

Considering atomic physics in a classical view, electrons trace their orbits around the central nucleus. This movement, analogous to a current loop, gives rise to the emergence of a magnetic moment, symbolized as $\vec{M}$, intricately entwined with the electron's orbital momentum. However, this definition alone is insufficient to describe the behavior of particles lacking orbital momentum when submitted to an external magnetic field. In this scenario, a second contribution needs to be taken into account. This contribution relates to the magnetic moment arising from the spin, giving rise to the general expression.

$$\vec{M} = -\mu_B(\vec{L} + g_e\vec{S}) \tag{2.2}$$

where $\vec{L}$ and $\vec{S}$ are given in units of $\hbar$. The term g_e corresponds to a dimensionless value known as the free electron "g-factor". The g-factor is better described in section 2.2.

In this context, the above-mentioned Zeeman effect splits degenerated states (Kramer degeneracy) through the application of an external magnetic field, with energy

$$E = -\vec{M} \cdot \vec{B} \tag{2.3}$$

The energies, once degenerated, are split in levels, following a relation that is proportional to the applied magnetic field and the magnetic quantum number:

$$E = -\mu_B B_0(m_L + g_e m_s). \tag{2.4}$$

In the above equation, m_L is the magnetic orbital quantum number (the orbital angular momentum projection) and m_s is the spin angular momentum projection.

The relation 2.4 is the true Zeeman interaction. However, if both $\vec{L}$ and $\vec{S}$ are present and are coupled by spin-orbit interaction ($\vec{L}$ - $\vec{S}$), the Zeeman interaction can be recast as a function of the total angular moment projection m. This representation is true if the multiplet belonging to different $\vec{J}$ are sufficiently separated. In this case, there's the apparition of a rescale (or effective) g-factor, the so called Landé factor (g_J):

$$E(J, m) = \mu_B g_J m B_0. \tag{2.5}$$

This Landé factor depends on the quantum numbers J, L and S of a particular multiplet.

2.2 The g-factor

One of the most significant physical quantities obtained through electron paramagnetic resonance is the g-factor, which is profoundly influenced by the environment in which electrons are situated. Paul Dirac made its initial prediction , employing it as a crucial demonstration of the applicability of the theory of relativity in explaining atomic interactions [80].

The magnetic moment associated with the spin degree of freedom was primarily introduced by Dirac, in his work called "The quantum theory of Electron", in which Dirac considers the relativistic Hamiltonian of an electron moving in an arbitrary electromagnetic field to deduce the relativistic wave function of the electron [81]. In this scenario, the g-factor appears as the dimensionless constant that relates the ratio of the electron's magnetic moment to its angular momentum:

$$\frac{M}{L} = -g\frac{e}{mc}, \tag{2.6}$$

For a free electron, this values was correctly predicted as $g_e = 2(1 + \alpha/2\pi) = 2.0023$, where α is the fine structure constant, that quantifies the strength of the electromagnetic interaction between elementary charged particles.

From an experimental point of view, The magnetic field is responsible for splitting a pair of energy levels and the g-factor determines the slope of the splitting [80]. An EPR transition occur at a given B-field, denoted resonant field (B_R), that corresponds to the condition $h\nu = \Delta E$, where the electromagnetic wave energy $h\nu$ match the energy difference between two levels ΔE. Modelling the two levels as an effective spin 1/2, the resonant condition is

$$h\nu = g\mu_B B_R \tag{2.7}$$

However, the resonant field depend on the electromagnetic wave frequency ν, so the relevant value is rather the ratio ν/B_R, which is completely characteristic of a given transition:

$$g = \frac{h\nu}{\mu_B B_R} \tag{2.8}$$

In semiconductor materials, such as ZnO, the g-factor is primarily influenced by the spin-orbit coupling of the valence electrons and the presence of closed electron shells below these valence states [82]. The effective value of the g-factor can be described by the following expression:

$$g = 2 - \frac{2E_p\Delta}{3E_g(E_g + \Delta)}, \tag{2.9}$$

where E_p is the Kane energy [1], E_g is the band gap and Δ is the spin orbit coupling [83]. When conduction electrons are considered, the problem becomes more complicated, as there exists a quasi-continuum series of levels that participates on the phenomena.

2.2.1 g-factor anisotropy

Comparing to the g-value of a free electron, bound electrons can present positive or negative shifts. If a paired electron is promoted to a single occupied molecular orbital (SOMO), the shift is positive. On the other hand, if an unpaired electron is promoted to a previous unoccupied orbital, the shift have negative values. The both cases are represented in Figure 2.1.

Since that the spin-orbit coupling and orbital anisotropy can be present in determined systems, it is reasonable to expect that the g-factor value and symmetry depend on the orbital in which the unpaired electron resides. In systems exhibiting isotropy, the g-value remains isotropic. However, in more complex systems, such as transitions ions, free radicals and point defects, the g-factor can present anisotropy, indicating the disruption of symmetry in these systems.

Given these scenarios, the g-factor can no longer be viewed as a straightforward scalar quantity. Instead, it becomes essential to represent it as a matrix, containing values corresponding to each directional aspect of the system. This matrix can be represented in its diagonal form, with the three main values corresponding to the three directions in the x-y-z coordinate system:

[1] The Kane energy is associated to the Kane model for semiconductors. For more details, reference [82] is recommended

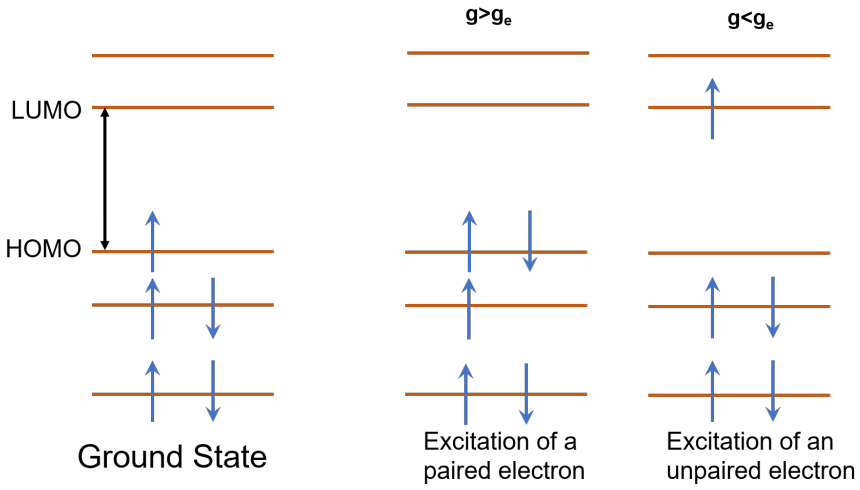

Figure 2.1: *Representation of the highest occupied molecular orbital (HOMO) and lowest unoccupied molecular orbital (LUMO). The value of g depends on the final orbital occupied by the excited unpaired electron*

$$\mathbf{g}=\begin{pmatrix} g_x & 0 & 0 \\ 0 & g_y & 0 \\ 0 & 0 & g_z \end{pmatrix} \tag{2.10}$$

which leads to the matrix representation of the magnetic moment :

$$\begin{pmatrix} M_x \\ M_y \\ M_z \end{pmatrix} = -\mu_B \begin{pmatrix} g_x & 0 & 0 \\ 0 & g_y & 0 \\ 0 & 0 & g_z \end{pmatrix} \begin{pmatrix} S_x \\ S_y \\ S_z \end{pmatrix} \tag{2.11}$$

Considering a Zeeman Hamiltonian H_{Zeeman}=-$\vec{M}$ $\cdot\vec{B}$, the degenerate energy states associated with the spin can be resolved by applying an external magnetic field $\vec{B} = B_x x + B_y y + B_z z$ and following the Schrödinger equation $H\left|\Psi\right\rangle = E\Psi$. For an arbitrary system, the Zeeman Hamiltonian can be written as

$$H_{zeeman} = \mu_B[g_x B_x S_x + g_y B_y S_y + g_z B_z S_z] \tag{2.12}$$

If axial symmetry is present, the g-factor can be simplified as:

$$g_x = g_y = g_\perp,\ g_z = g_\parallel, \tag{2.13}$$

which leads to a representation where the angle θ, that associates the applied magnetic field $\mathbf{B}$ and the symmetry axis z of the system is considered:

$$g' = [g_\perp^2 \sin^2\theta + g_\parallel^2 \cos^2\theta]^{1/2}. \tag{2.14}$$

In the case of a powder sample, the effective g-factor (or the one observed by spectroscopy) is a superposition of $g_\parallel$ and $g_\perp$. By probability, we have that the states belonging to the plane are more abundant, and $g_\perp$ are more prominent in relation to $g_\parallel$, once that few are the randomly oriented crystals that contribute to the z direction. The distribution of states is represented in Figure 2.2.

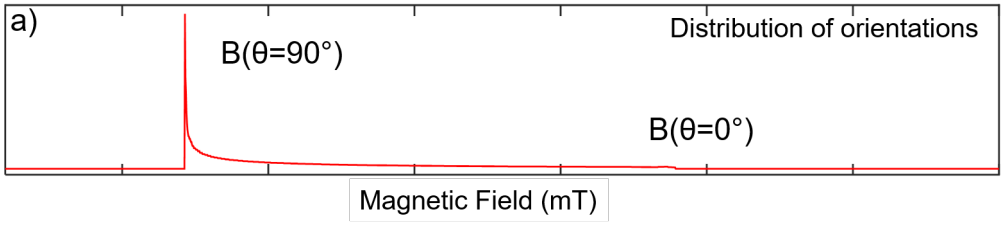

Figure 2.2: *Representation of the distribution of orientations for a powder sample.*

It can happen that these different values are very similar, so that give rise to a splitting weaker than the line width: In this case, the anisotropy is manifested as a non-symmetric behavior of the line shape.

2.3 Measuring the Zeeman effect - Principles of EPR

As we have seen in the section before, the Zeeman splitting is responsible for removing the energy degeneracy of the system. Applying a static magnetic field, the spin states can be separated in different energy levels. For a spin 1/2, the possible states are $m_s = +1/2$ and $m_s = -1/2$, associated to the energy values $E_+ = +g\mu_B B_0/2$ and $E_- = -g\mu_B B_0/2$, respectively. The transition between these levels can be achieved through a quantized amount of energy, that is responsible to promote a spin from the lower state of energy to the upper state. This energy is given by electromagnetic radiation with wavelength ν. The condition for such transition is that the energy of the photon is the same of the difference between levels [84]:

$$\Delta E = \mu_B g B_0 = h\nu, \tag{2.15}$$

where h is the Planck constant ($h = 6.63 \cdot 10^{-34} Js$). The term $h\nu$ represents the electromagnetic radiation energy, corresponding to the oscillating magnetic field B_1. For electronic spins and static B_0-field of about 1 T, the necessary wavelength is in the range of microwaves (MW). It is interesting to note that high values of g resonate at low magnetic fields and vice versa.

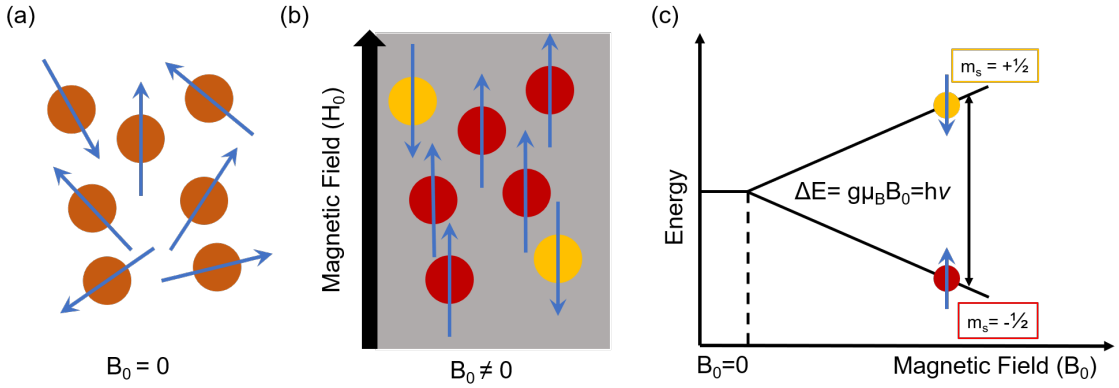

Figure 2.3: *(a) In the absence of external magnetic field, the electronic spins are randomly oriented in space. (b) When the magnetic field is applied, the energy degeneracy is solved and the spins are aligned parallel or antiparallel to the magnetic field. (c) With energy given by photons, the spins can flip from the state of lower energy to the state of upper energy and the absorption can be measured.*

EPR transitions in a spectrometer are typically detected indirectly by measuring the radiation absorbed by the system and the subsequent change in the Q-factor. For having a net energy difference between absorbed and emitted radiation, a difference of population between upper and lower states must hold. In this scenario, the three fundamental conditions for having EPR transitions are:

1. The energy provided by the microwave matches the energy difference between two levels (Equation 2.15);
2. The system possesses a net population difference between lower and higher state;
3. the selection rules $\Delta m_s = \pm 1$, $\Delta m_i = 0$ are satisfied. (The microwave flips the electronic spin but does not affect the nucleus).

Applying the Boltzmann statistics, valid in the thermal equilibrium, it follows that the ratio of population between upper and lower states (condition 2) is given by

$$\frac{N_u}{N_l} = e^{-\frac{\Delta E}{kT}}, \tag{2.16}$$

where $k = 1.38 \cdot 10^{-23} m^2 kg\ s^{-2} K^{-1}$ is the Boltzmann constant and T is Temperature (K).

When the radiation B_1 is applied, it flips the spins and the population difference is reduced. In the time right after the excitation (t_0), the system possesses an extra amount of energy (E_0). As a simple thermodynamic system, after the excitation, the system interacts with the surroundings loosing energy to the environment and recovers equilibrium. This phenomenon follows an exponential decay [84]:

$$E = E_0\ exp(-(t - t_0)/T_1), \tag{2.17}$$

where the relaxation time T_1 defines the flow of energy from the system to the environment and its characteristic for each material. T_1 is related to the mean lifetime in which the spin remains in the upper state. More details about this exchange is described in section 2.7.

It also can be associated a transition probability W, responsible to take the lower state to the upper state:

$$W_{l \Rightarrow u} = \frac{2\pi}{\hbar} |\langle u| g\mu_B \vec{B_1} \cdot \vec{S} |l\rangle|^2 \delta(\omega - \omega_0), \tag{2.18}$$

where the term given by the Kronecker delta restricts the expression just for the case where the microwave frequency ω is in resonance with the Larmor frequency ω_0 of the excited states. The Larmor frequency depend on the static field B_0[1]:

$$\omega_0 = \gamma B_0 \tag{2.19}$$

where γ is the electron gyromagnetic factor. $\gamma = -1.76 \cdot 10^{11}$ rad $s^{-1} \cdot$ T $^{-1}$

[1] In the presence of a static magnetic field, the electronic magnetic moment precess around the direction of the magnetic field. This is called *Larmor precession*. The frequency in which the magnetic moment precess is proportional to the applied field and is called *Larmor frequency* :$\omega_0 = (ge/2m_e)B_0$

2.3.1 Homogeneous broadening

As all quantum system, the lifetime of an excitation possesses a broadening, related to the uncertainty principle, that attests to the fitness of the excite state. The uncertainty in lifetime causes an uncertainty in the energy of the system ($|E| = \hbar/T_1$).

From an experimental point of view, it corresponds to the fact that the absorption lines are not infinitely sharp but have a width, associated to spontaneous emission and/or other relaxation mechanisms when these are present.

In EPR, the spectra are analyzed in the frequency space, so the line shape is the Fourier transform of the exponential decay behavior, situated in the energy space. The result of this operation is a Lorentzian shape. For this kind of broadening, the spins have an identical collective behavior and when this condition is not fulfilled, the system is under the influence of *inhomogeneous broadening* phenomenon.

2.3.2 Inhomogeneous broadening

When spin packets have different Larmor frequencies, due to a distribution in interaction and environment, inhomogeneous broadening happens in the spectral lines. Each spin packet possesses its own homogeneous broadened Lorentzian line. When the contribution of all the spin packets is considered, the total line shape is the superposition of all the homogeneous lines and the resultant behavior approaches a Gaussian shape.

The principal sources of inhomogeneous broadening are a change in the Zeeman frequencies across the sample due to a non-intentional external magnetic field, the anisotropy of the tensors contained in the interaction Hamiltonian and unsolved hyperfine interactions. The effect of the inhomogeneous broadening is to reduce the global coherence time of the spins by defocusing their transverse magnetization. However, this drawback can be avoided by refocusing the spins with a MW pulse, thus producing a spin echo [85].

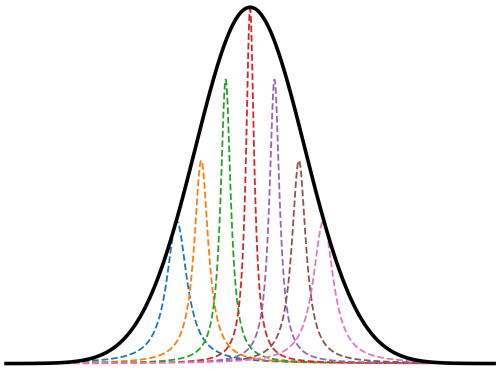

Figure 2.4: *Inhomogeneous broadening (in black). Each colored line corresponds to the homogeneous line of a spin packet.*

2.3.3 Static magnetic field and microwave frequency

As an extension of the theory developed for NMR analysis, the first literatures about EPR are conceived adopting the sweep in the frequency and maintaining the magnetic field unchanged. From an experimental point of view, this approach is not very suitable because, differently from NMR, that uses coils for detection, EPR uses a cavity, projected

to a specific wavelength. Changing the microwave frequency would imply a change in the cavity's dimensions.

To overcome this issue, the EPR experiment is conceived for a fixed frequency and the magnetic field varies by varying the electric current in an electromagnet. Attention must be paid not to vary the magnetic field too fast, once it may lead to passage effects. The adiabatic passage condition must hold

$$\frac{dB_0}{dt} \ll \gamma B_1^2 \tag{2.20}$$

Achieving this condition can be challenging in systems with long spin-lattice relaxation times and very narrow lines. To attenuate this feature and also increase sensitivity, it is usual to measure the derivative of the absorption. For this, a small oscillating field is superimposed in the z-axis. This process is known as "field modulation", an application of the "lock-in detection" concept.

Another factor influencing experimental sensitivity is the frequency range in which the sample is placed. As indicated by Equation 2.16, it becomes evident that raising the frequency (resulting in a higher ΔE), the population difference between levels is increased.

In this context, different frequency ranges spectrometers have been conceived to increase sensitivity and reveal hidden features of physical systems. The range of frequencies used to perform EPR analysis is represented below, with a focus on the more prevalent bands (X, Q, and W) and their commonly utilized frequencies [86]. Column 3 illustrates the magnetic field at which a free electron resonates in accordance with each band:

Band	Frequency (GHz)	Resonant Field (mT) ($g = 2$ spin)
L	1.1	39
S	4	143
X	9.4-10 **(9.75)**	348
Q	33-50 **(34)**	1210
W	75-110 **(94)**	3350

Table 2.1: *Frequencies Bands in EPR. Frequencies highlighted in bold represent the most commonly used values. In the right, the resonating field for free electrons.*

Besides the sensitivity, access to hidden anisotropy of the g-factor can be extracted by changing the frequency band, once that the resonant fields changes.

2.4 The interaction Hamiltonian

In the previous sections, we explored the characteristics of the electronic Zeeman interaction, and investigated the g-factor, the finger-print of the resonant-spins system. Nevertheless, quantum systems can exhibit significantly greater complexity due to the potential presence of additional interactions.

If nuclei with non-zero spin are also present in the vicinity of the system, the nuclear spin will also interact with the magnetic field, by the **nuclear Zeeman interaction**. This interaction is not detectable by EPR because of the selection rule ($\Delta m_s = \pm 1, \Delta m_i = 0$), but is the scope of NMR technique.

Additional interactions can indeed be present, and they can profoundly alter the spectra observed in EPR, providing valuable insights into the surrounding environment of the electrons. Here, we discuss some of the more significant interactions:

2.4.1 Hyperfine interaction

The unpaired electrons are susceptible to interacts with nuclear spins, when the latter are present in their vicinity. This interaction is sensitive to anisotropy, meaning that its strength and nature can vary depending on the orientation of the electron's magnetic moment with respect to the nuclear magnetic field.

Understanding and characterizing this interaction is crucial in EPR and nuclear magnetic resonance (NMR) spectroscopy, as it provides valuable information about the local environment and molecular structure in which the unpaired electrons are situated.

The hyperfine interaction is described by the Hyperfine Hamiltonian:

$$H_{HF} = \vec{S} \cdot \tilde{A} \cdot \vec{I}, \tag{2.21}$$

where the $\vec{S}$ and $\vec{I}$ term stand for electronic and nuclear spin, respectively. $\tilde{A}$ is the hyperfine tensor, describing the coupling between $\vec{S}$ and $\vec{I}$.

Considering an s orbital, the unpaired electron has finite probability density for being at the nucleus of the atom, at zero distance from the nuclear spin. It leads to a singularity of the dipole-dipole interaction, once that the interaction scales proportionally to $1/r^3$. This singularity has been unraveled by Fermi and gives origin to the isotropic term of the Hyperfine Hamiltonian, also known as *Fermi contact interaction*.

The contribution of adjacent orbitals p,d,f (for which l is different of zero) implies the need of an averaging of the dipole-dipole interaction in the space of these orbitals. This leads to an anisotropic contribution to the hyperfine interaction. The hyperfine operator can then be written with these two contributions considered apart:

$$\tilde{A} = \tilde{\mathbf{A}}_{\mathbf{iso}} + \tilde{\mathbf{T}}_{\mathbf{an}}, \tag{2.22}$$

where $\tilde{A}_{iso}$ contains the isotropic terms and $\tilde{\mathbf{T}}_{\mathbf{an}}$ the anisotropic contribution.

Considering an electronic spin 1/2, when several nuclei with spin I interact identically with the electron, the effect in the EPR lines is a splitting, generating a total number of lines equal to $n = (2I + 1)$.

When $I = 1/2$, the ratio of the corresponding lines follows the pattern of Pascal's triangle, illustrated in Figure 2.5. In the case where one electron interacts with three nuclei (the case of methyl radical), this specific situation is highlighted.

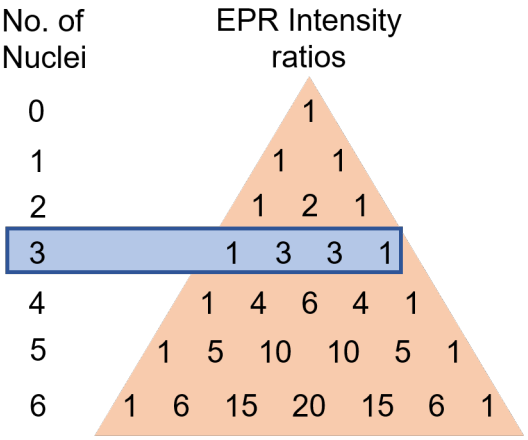

Figure 2.5: *Pascal triangle showing the number of lines and respective intensity ratio for an electronic spin coupled with several nuclei with* $I = 1/2$.

2.4.2 Superhyperfine interaction

When the unpaired electron interacts with the nuclei of adjacent atoms that compose the molecule, this interaction is called superhyperfine or ligand hyperfine. It is termed "superhyperfine" because it provides even finer details about the electron's environment compared to the standard hyperfine interactions, involving only the first set of nuclei. This interaction is substantially weaker than the hyperfine interaction. In other words, the superhyperfine Hamiltonian is an extension of the hyperfine one, where the interaction with distant nuclei is considered [87]:

$$H_{SHF} = \sum_i (\vec{S} \cdot \tilde{A} \cdot \vec{I}_i) \tag{2.23}$$

The central nucleus play a pivotal role, strongly interacting with the unpaired electron (HF). In this scenario, the second order interactions (SHF) split the HF lines, giving rise to multiple closely spaced lines around all the HF peaks.

However, in some cases, the SHF splitting may be relatively small, which means that the additional lines created by the interaction are very closely spaced and thus are hidden by the HF line width.

2.4.3 Zero-field splitting

The zero-field splitting, often referred to as fine structure, is an interaction that manifests in systems with electronic spins higher than $1/2$.

This is the case for certain organic compounds, exhibiting a triplet state, and inumerous transition metal ion complexes [88]. The fine structure originates from the interaction between the unpaired electron and the anisotropic environment induced by the electrical crystal field. This interaction is mediated through spin-orbit and dipolar interactions, and notably, it is present even in the absence of an external magnetic field.

The spin Hamiltonian of the fine structure is thus, independent of the external magnetic field:

$$H_{FS} = \vec{S} \cdot \tilde{D} \cdot \vec{S} \tag{2.24}$$

For transition ions, the splitting generated by the fine structure is mostly due to spin-orbit coupling and the $\tilde{D}$ matrix can be approximated to a diagonal form, where each matrix component is associated with the crystal axis:

$$H_{FS} = D_X S_X^2 + D_Y S_Y^2 + D_Z S_Z^2. \tag{2.25}$$

When $|D_Z| \geq |D_X|, |D_Y|$, the simplification $D = 3D_Z/2$ and $E = (D_X - D_Y)/2$ is made. In this approach, the D term represents the anisotropy along the z axis and E the anisotropy present in the $x-y$ plane. In the important case of axial symmetry ($D_X = D_Y$) the Hamiltonian is reduced to

$$H_{FS} = DS_z^2 \tag{2.26}$$

2.4.4 Exchange interactions

The exchange interaction emerges as a result of the quantum properties of electrons and is a consequence of the Coulomb interaction due to the overlap between orbitals occupied by unpaired electrons [88]. This interaction was first introduced by Heisenberg and for this is also known as "Heisenberg interaction". The concept of the exchange interaction as an observable feature in EPR was initially introduced by Gorter and Van Vleck [89]. It was subsequently mathematically demonstrated by Van Vleck [90] and further refined by Anderson's theory [91].

Considering a scenario where two centers, A and B, of a transition metal ion, are situated in a diamagnetic environment, the localization of the electrons, which would typically be expected to be confined separately to each center, needs to be adjusted. This adjustment takes into account that the electron "belonging" to the center A can become partially delocalized onto B, and vice versa [92]. In other words, the exchange interaction arises from the fact that the spatial distribution of electrons are not strictly confined to individual centers, but can exhibit a degree of delocalization and overlap between neighboring sites.

If the wavefunction of two identical particles overlap, these particles become indistinguishable[2] at atomic scales. The consequence is that the total wave function for the system possess a symmetrical and an antisymmetric component (for fermions, like electrons, the function must be strictly antisymmetric). The physical consequences of these two possible states is an energy difference between parallel (J different of zero) and antiparallel ($J = 0$) states. The sign of J will define which state is the ground state, with negative values standing for ferromagnetic coupling (or singlet state), and positive values standing for ferromagnetic couplings (triplet states).

Considering an isotropic system, i.e, discharging the spin-orbit influence in the operator (not considering $\vec{L}$), the exchange interaction can be written as a Heisenberg operator that associates the electronic spin $\vec{S_1}$ with the electronic spin $\vec{S_2}$, generating the Hamiltonian

$$H_{EX} = \vec{S_1} \cdot \tilde{J} \cdot \vec{S_2} = J(\vec{S_1} \cdot \vec{S_2}) \tag{2.27}$$

[2]In quantum mechanics, indistinguishable particles are particles that can not be uniquely identify or label individually, because their quantum states are identical. It has profound implications in how electrons behaves in atoms and molecules, and it plays a crucial role in many quantum phenomena, including the Pauli exclusion principle and the formation of quantum states like Bose-Einstein condensates and Fermi gases.

By Anderson's theory, some basic rules were stipulated to understand the magnetic behavior of transition ions [93]:

- When two ions have lobes of magnetic orbitals (which contain unpaired electrons) oriented towards each other in a manner that allows the existence of a significant overlap integral between the orbitals, the resulting exchange interaction is antiferromagnetic.
- When the orbitals are configured in a manner where they appear to be in proximity but lack any significant overlap integral, the interaction becomes ferromagnetic.
- When a magnetic orbital overlaps with an empty orbital, the interaction between the two ions becomes ferromagnetic.

2.4.5 Dipolar interaction

When the distance between centers exceeds the extension of the orbitals occupied by these electrons, the overlap of the wave function is no more present and the interaction between centers is in the form of an electric dipole. Contrary to the exchange interaction, the dipolar interaction is purely magnetic in nature, and has the same form as its classical counterpart. The dipolar interaction Hamiltonian can be written in terms of the distance r between centers. For two spins 1/2, with same isotropic g-factor, the interaction is given by

$$H_{DIP} = \frac{\mu_0 {\mu_B}^2 g^2}{4\pi r^3}\left[\vec{S_1}\cdot\vec{S_2} - 3(\vec{S_1}\cdot\vec{e_{12}})(\vec{S_2}\cdot\vec{e_{12}})\right] \tag{2.28}$$

The pre-factor can be written as $K(r)$, where

$$K(r) = \frac{\mu_0 {\mu_B}^2 g^2}{4\pi r^3} = \frac{52}{r^3}\ \text{MHz} \tag{2.29}$$

with r given in nm. The effects on EPR spectra become more significant with increasing concentration of materials, that can interact by exchange. When the concentration reaches a significant level, both exchange and dipolar interactions can lead to a loss of spectral resolution.

2.5 The total Hamiltonian

Incorporating all the interactions discussed in the previous sections, we have access to a comprehensive Hamiltonian that takes into account all of these interactions. This Hamiltonian is composed by the sum:

$$H_{TOTAL} = H_{Zeeman} + H_{HF} + H_{SHF} + H_{FS} + H_{EX} + H_{DIP} \tag{2.30}$$

These principal interactions are represented in Figure 2.6:

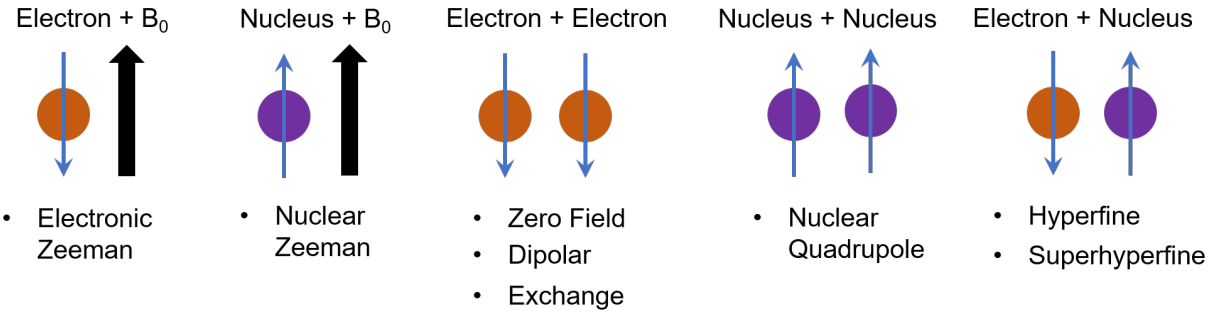

Figure 2.6: *The principal interactions that can be present in a paramagnetic system.*

2.6 Magnetization evolution - Bloch equations

Until this point, we have described the characteristics that cause a system to exhibit magnetization. The next step is to understand how the magnetization evolves when the system is driven out of equilibrium.

The motion of a macroscopic magnetization $\mathbf{M_S}$ in a classical magnetic field $\mathbf{B} = \mathbf{B_0} + \mathbf{B_1}(t)$, composed of a static magnetic field $\mathbf{B_0}$ and a time-dependent magnetic field $\mathbf{B_1}(t)$, is described by :

$$\frac{d\mathbf{M_S}}{dt} = \gamma(\mathbf{M_S} \times \mathbf{B}), \tag{2.31}$$

where no losses of magnetization were assumed.

To fully describe the mechanisms that induce a temporal evolution in the magnetization, two relaxation times should be considered:

- T_1, an inelastic process, related to the loss of energy in the system, and responsible for decreasing the magnetization along the z-axis.
- T_2, associated with the loss of coherence in the x-y plane, in which elastic processes may be included. This relaxation time conserves energy, as no energy is exchanged with the lattice.

In solids, the consideration $T_2 \ll T_1$ is typically valid, and the temporal evolution for each axis can be described [87]:

$$\frac{dM_x}{dt} = -\frac{M_x}{T_2} + \gamma M_y B_0 \tag{2.32}$$

$$\frac{dM_y}{dt} = -\frac{M_y}{T_2} + \gamma(M_z B_1 - M_x B_0) \tag{2.33}$$

$$\frac{dM_z}{dt} = -\frac{M_0 - M_z}{T_1} - \gamma M_y B_1 \tag{2.34}$$

Introducting the concept of the rotating frame , where the axes are rotating at the same frequency as the microwave (figure 2.7),the equation for the magnetization becomes

$$\frac{d\mathbf{M'}}{dt} = \gamma \mathbf{M'} \times \mathbf{B_{eff}} \tag{2.35}$$

with $\mathbf{B_{eff}}$ accommodates the frequency of the microwave field (ω):

$$\mathbf{B_{eff}} = \begin{pmatrix} B_1 \\ 0 \\ B0 + (\omega/\gamma) \end{pmatrix} \tag{2.36}$$

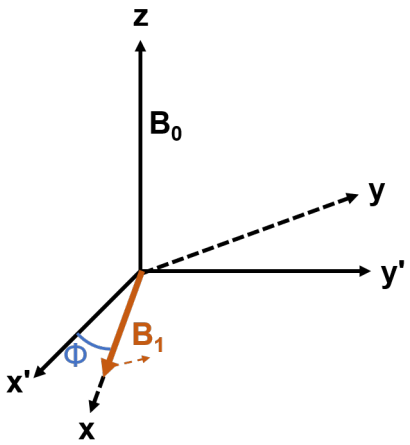

Figure 2.7: *Representation of the rotating frame. The static magnetic field is aligned with the z axis, and the oscillating magnetic field B_1 turns around the z axis with frequency ω. The new referential turns with the same frequency, and it's represented by dashed lines. The full lines represent the laboratory frame.*

Without loss of generality, we can assume that the field produced by the microwave $\mathbf{B_1}(t)$ is a cosine function given by $\mathbf{B_1}(t) = 2B_1\cos(\omega t)$. This lineary polarized microwave field that drives the magnetic dipole transitions can be decomposed into right and left circular polarization:

$$\mathbf{B_1}(t) = \begin{pmatrix} B_1 cos(\omega t) \\ B_1 sin(\omega t) \\ 0 \end{pmatrix} + \begin{pmatrix} B_1 cos(\omega t) \\ -B_1 sin(\omega t) \\ 0 \end{pmatrix} \tag{2.37}$$

In the rotating frame, the first term represents a rotation in the opposite direction of the Larmor frequency, having no effect on the spin system and, therefore, being disregarded. On the other hand, the second term has the same sense of rotation of the Larmor precession.

Rewriting the magnetization equations in the rotating frame x', y', and z':

$$\frac{dM'_x}{dt} = (\omega - \omega_0)M'_y - \frac{M'_x}{T_2} \tag{2.38}$$

$$\frac{dM'_y}{dt} = -(\omega - \omega_0)M'_x - \frac{M'_y}{T_2} + \gamma B_1 M'_z \tag{2.39}$$

$$\frac{dM'_z}{dt} = -\gamma M'_y B_1 + \frac{M_0 - M'_z}{T_1} \tag{2.40}$$

The term $\omega_0 = -\gamma B_0$ represents the *Larmor* frequency, which indicates the frequency at which the spins are rotating around the quantification axis z, proportional to the static applied field B_0. In the stationary state, the magnetization is given by:

$$M'_x = \frac{\gamma B_1(\omega_0 - \omega)T_2^2}{1 + (\omega_0 - \omega)^2 T_2^2 + \gamma^2 B_1^2 T_1 T_2} M_0 \tag{2.41}$$

$$M'_y = \frac{\gamma B_1 T_2}{1 + (\omega_0 - \omega)^2 T_2^2 + \gamma^2 B_1^2 T_1 T_2} M_0 \tag{2.42}$$

$$M'_z = \frac{1 + (\omega_0 - \omega)^2 T_2^2}{1 + (\omega_0 - \omega)^2 T_2^2 + \gamma^2 B_1^2 T_1 T_2} M_0 \tag{2.43}$$

When $\gamma^2 B_1^2 T_1 T_2$ is much smaller than 1, the system is considered non-saturated, leading to the simplification of the magnetization in the z direction as $M'_z = M_0$. In this regime, the loss of magnetization is entirely governed by T_2. The complex form of the magnetic susceptibility is characterized by the following terms:

$$\chi = \frac{M'_x}{2B_1} - i\frac{M'_y}{2B_1} \tag{2.44}$$

From these equations, two different situations arise:

- Non-saturated regime:

  When the saturation factor $s = \gamma^2 B_1^2 T_1 T_2 \ll 1$, equations 2.41, 2.42, and 2.43 will no longer have a T_1 dependence. As a result, the line assumes a *Lorentzian* shape with the form $f(x) = 1/(1 + x^2)$, which, in its half-width, represents the direct dependence of the spin-spin relaxation: $\Delta_{\omega_{1/2}} = 2/T_2$.

- Saturated regime: The continuous absorption of microwaves depends on the system's ability to dissipate its energy into the lattice. When the microwave power is too intense, causing the system to deviate from thermal equilibrium, it is said to be saturated [88].

Identifying $\frac{M'_x}{2B_1} = \chi'$ in Equation 2.44 as the dispersive part of the susceptibility and $i\frac{M'_y}{2B_1} = \chi''$ as the absorptive part, the susceptibility can be rewrite as:

$$\chi = \chi' + \chi'', \tag{2.45}$$

where χ'' satisfies the relation

$$\int_{-\infty}^{\infty} \chi'' d\omega = \frac{1}{4}\omega_0 \chi_0. \tag{2.46}$$

The expression $\chi_0 = \frac{M_0}{B_0}$ denotes the maximum susceptibility of the system, which is directly proportional to the total number of spins within the system. One implication of Equation 2.46 is that in a non-saturated regime, the area under the curve will provide a measurement of the total number of spins or paramagnetic species within the system. This area corresponds to the integrated susceptibility and can serve as a quantitative measure of the paramagnetic content.

The average power absorbed by the system is determined, after some calculation, as:

$$P = 2\omega B_1^2 \chi'' \tag{2.47}$$

This relation allows to easily identify the power level at which the system begins to saturate, as the relationship between P and B_1^2 is no longer linear. If the power of the mW is too strong and the system is saturated, the measurement becomes less reliable.

A simple way to verify the non-saturation of the system is to reduce the attenuation of the microwave power by 6 dB. If the system is in the linear regime, this adjustment should result in the doubling of the spectral intensity [86].

2.7 Spin-lattice relaxation T_1

The spin-lattice relaxation time, T_1, is defined as the time required for a spin system to return to thermal equilibrium after a perturbation is applied [94]. Considering a two-levels system, with energy levels $m_s = \pm\frac{1}{2}$, which are split by a Zeeman interaction and possess a difference in occupation states defined by N_0 in the absence of excitation (equilibrium) and N after the excitation has been applied and removed. The relaxation process can be mathematically represented by a first order differential equation:

$$\frac{dN}{dt} = -\frac{(N - N_0)}{T_1} \tag{2.48}$$

The spin polarization resulting from the Zeeman splitting generates magnetization along the z axis. As a result, T_1 is associated with the so-called longitudinal relaxation.

Considering a crystal with a non-zero temperature, the difference in occupation states is reduced by electron-phonon interaction [87]. The system reaches equilibrium toward the Boltzmann distribution. The oscillation of neighboring atoms in proximity to the resonant electron induces transitions that cause the system to relax. These transitions can be attributed to dipole-dipole interactions, where the lattice vibrations modulate internal dipolar fields. This phenomenon is referred to as *Waller relaxation* .

Alternatively, longitudinal relaxation can also occur due to spin-orbit interaction, leading to *Van Vleck relaxation* . The longitudinal relaxation may also depend on the crystal orientation, once that the interaction with the lattice may be anisotropic. In the particular case of powders, the measured longitudinal relaxation time is an average of the different directional relaxation times.

In summary, the relaxation time T_1 is a result of how the solid-state environment influences the spin degrees of freedom. In an ideal system, without hyperfine splitting, where all spins in the ensemble can be excited simultaneously, the measured T_1 can be considered "pure" and provides the absolute value of the spin-lattice interaction. Indeed, this interaction is strongly temperature-dependent because the phonon density increases as temperature rises. The prominent mechanisms responsible for longitudinal relaxation and that will be subsequently used for explaining the relaxation of the studied system are:

2.7.1 Direct process

Considering a two-level ($|a\rangle$ and $|b\rangle$) magnetic system, where the energy separation between the levels is given through the interaction with a static magnetic field, i.e., considering the Zeeman splitting, $E = \mu_B g B_0$. The direct relaxation process arises from the absorption and emission of a phonon from the crystalline lattice, whose energy equals the difference of energy promoted by the Zeeman effect, that is, $\delta = \hbar\omega = \mu_B g B_0$. In this scenario, the population of spins occupying level $|a\rangle$ is given by n_a, and the population

in the level $|b\rangle$ by n_b. Associated with the population of each state, there is a probability of transition between these two levels, defined by $W_{a\to b}$ for transitions from level $|a\rangle$ to level $|b\rangle$, and a probability $W_{b\to a}$ representing the reverse path. Therefore, the evolution of the population of each level with respect to time is given by:

$$\frac{dn_b}{dt} = -\frac{dn_a}{dt} = W_{a\to b} - W_{b\to a} \tag{2.49}$$

The phonon spectral density, $\rho(\omega)$, is given by the relation

$$\rho(\omega)d\omega = g_D(\omega)\bar{p_0}(\omega)d\omega \tag{2.50}$$

where $g_D(\omega)$ represents the Debye density of states [3], dependent on the speed of sound v in the medium:

$$g_D(\omega) = \frac{3\omega^2}{2\pi^2 v^3} \tag{2.51}$$

and

$$\bar{p_0}(\omega) = \frac{1}{e^{\hbar\omega/k_B T_0} - 1} \tag{2.52}$$

Introducing the temperature-independent factor K for describing the transition between states, the transition probabilities are given by

$$W_{b\to a} = K[1 + \bar{p_0}(\omega)] \quad ; \quad W_{a\to b} = K\bar{p_0}(\omega) \tag{2.53}$$

Considering the difference between the population of spins (N), the variation of this difference is expresses as

$$\frac{dN}{dt} = K[(1 + 2\bar{p_0}(\omega))N - n_t] \tag{2.54}$$

where n_t is the total population of spins. In the equilibrium (T=T_0),

$$N = N_0 = n_t \tanh\left(\frac{\hbar\omega}{2k_B T_0}\right). \tag{2.55}$$

Using the relation 2.48, the relation with the temperature for the direct process, for a Kramers doublet is given by the relation [95]:

$$\frac{1}{T_{1D}} = \alpha_D g^3 B_0^5 \coth\left(\frac{\hbar\omega}{2k_B T}\right) \tag{2.56}$$

The parameter α_D is a constant that incorporates and synthesizes various physical effects and relevant constants for the specific system studied. This constant is determined experimentally or theoretically, and its value may vary depending on the material, experimental conditions, and properties of the system under investigation. Note that for the condition $2k_B T \gg \hbar\omega$, the simplification

$$\frac{1}{T_{1D}} = \alpha_D g^3 B_0^5 \left(\frac{2k_B T}{\hbar\omega}\right) \tag{2.57}$$

is valid.

[3] Applying the Debye model, which assumes a three-dimensional solid lattice behaving as a continuum for sound waves. It simplifies the vibrations of atoms into acoustic phonons. The Debye density of states provides a way to estimate the number of states per frequency unit at a specific frequency in the material.

2.7.2 Raman process

The Raman relaxation is a process with two phonons in which a phonon is scattered at the spin system, making it gain or loss energy.

In this process, a phonon of energy δ_1 is absorbed simultaneously to the emission of a phonon with energy $\delta_2 = \delta_1 + \delta$, promoting the flip from $|b\rangle$ to $|a\rangle$. This mechanism happens by means of an intermediate virtual state, allowing access to an entire spectrum of phonon energies (lower than the Debye temperature) for the state transition. The equation describing the return to equilibrium for this mechanism is given by:

$$\frac{1}{T_{1R}} = K' \int_0^{\theta_D} \frac{\delta_1^6 e^{\delta_1/k_B T}}{(e^{\delta_1/k_B T} - 1)^2} \tag{2.58}$$

Considering that the temperature T is much smaller than the Debye temperature θ_D, the integral simplifies. And the relation

$$\frac{1}{T_{1R}} = \alpha_R T^9 \tag{2.59}$$

is obtained. Depending on the system and temperature range, the proportionality to T^9 may no longer be suitable for characterizing the system. This is particularly the case in molecular magnets, where multiple exponent values can be observed to describe the system [96].

2.7.3 Orbach process

In the Orbach process, the relaxation happens by mean of a real intermediate state. A phonon is absorbed, leading the spin state to an excited state, where it loses memory and then is relaxed to another spin state by emitting another phonon.

In this process, relaxation is constrained by the existence of the supplementary energy level $|c\rangle$, separated from the excited level $|b\rangle$ by an energy amount of energy Δ_0. The transition through this process can only occur if the condition $\Delta_O < k)B\theta_D$ is verified. Considering these conditions and performing the calculation, analogously to the other processes [97], the temperature dependence for the Orbach process is found [98]:

$$\frac{1}{T_{1O}} = \alpha_o \Delta_O^3 e^{-\Delta_O/T} \tag{2.60}$$

The Orbach process becomes less and less important as the temperature goes down due to the lack of thermally available phonons able to initiate the process [99].

At very low temperature (below 10K), the predominant relaxation mechanism is expected to be the direct process. Figure 2.8 illustrates the mechanism of these three processes:

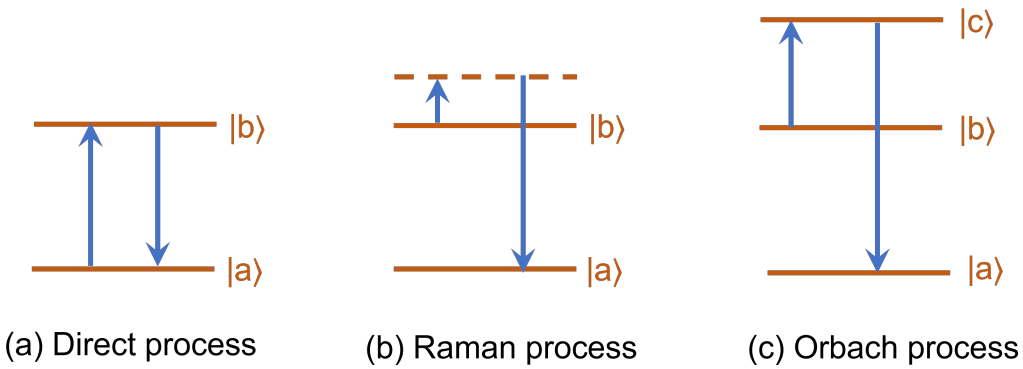

Figure 2.8: *Mechanisms that lead to longitudinal relaxation. In (a) Direct process, in (b) Raman process and in (c) Orbach process. The processes can coexist in a system depending on the geometry and temperature range.*

2.8 Transversal relaxation time T_2

In contrast to the longitudinal relaxation, the transverse relaxation does not involve energy exchange with the environment. Nevertheless, the system interacts with the spins present in the environment and loses coherence, related to an increase of entropy within the spin system. Several techniques have been developed in an attempt to disentangle the various mechanisms responsible for inducing decoherence, but this often necessitates a significant volume of data, the manipulation of multiple experimental parameters, and even then, the results can still pose challenges for analysis [100].

Given these limitations, the analyses carried in this work hasn't in scope the absolute study of the different decoherence mechanisms. Instead, the focus is on developing an understanding of the overall behavior of the transverse relaxation process. In this context, the relaxation time is treated as an experimental parameter, understand as a "phase memory time". The technique used for having access to the phase memory time is the 2-pulses Hahn's echo decay.

When examining the transverse relaxation time, two distinct phenomena come into play: spin defocusing and decoherence. Spin defocusing is linked to minor variations in the Larmor frequency among different spin packets. It can be corrected by an inversion pulse. On the other hand, decoherence stems from spin-spin interactions. In this scenario, the inherent randomness of this phenomenon prevents spin refocusing, causing the loss of coherence or information. The loss of coherence can impose restrictions to the usability of the system, particularly in the context of qubits. The internal process that influence the decoherence mechanisms are:

2.8.1 Instantaneous diffusion

The interaction between electron spins must be considered even in low concentration of paramagnetic species. In the context of pulsed EPR, after a $\pi/2$ pulse is applied, the ensemble of spins evolves in time due to the local field created by the excited spins. When a second pulse is applied, the spins are inverted almost instantly, which generates an abrupt change in the local field. It induces dephasing in the precession frequency, thus resulting in less efficient echo refocusing and shorter observed phase-memory.

It is considered as an instantaneous phenomenon because the duration of the pulse can be considered as negligible when compared to the relaxation time of the system. This phenomenon depends on the flip angle promoted by the pulse and also on the excitation bandwidth, which is intrinsically associated to the pulse duration.

2.8.2 Spectral Diffusion

The spins excited by the pulse aren't isolated from the spins that weren't touched, and any change in the environment distribution will lead to a perturbation in the local field . Each entity that possess a spin (electronic or nuclear) can change the spin state by means of flips or flip-flops.

In the case of indirect electron spin flip-flops, a dipolar electron pair close to the excited spin change its quantum state. Both spins belonging to the pair change its state simultaneously, promoting a fluctuation in the local magnetic field. This phenomenon is also known as **Spectral diffusion**.

Spectral diffusion depends on paramagnetic species concentration, once that this relaxation phenomena is due to the interaction between the excited spins and those that are not resonating. The relaxation occurs due to fluctuations in the local magnetic field experienced by the resonating spins, which leads to a change in their Larmor frequency.

The primary cause of these variations is associated with spin-spin flips and spin-lattice flips [101]. This results in a scenario where each spin-package interacts with the microwave pulse uniquely. In other words, when radiation is applied to promote a specific transition, it does not uniformly excite the entire line. Instead, a rapid spectral diffusion mechanism comes into play, efficiently spreading the excitation through the line at a rate comparable to the lattice relaxation.

In scenarios where the flip-flops involve the measured spin (those that have been excited by the MW pulse), this phenomenon is referred to as Spin diffusion. Considering the rate at which these flip-flops occur, denoted as W, it can be associated with a diffusion coefficient D. The spatial-temporal evolution of the polarization $p(x,t)$ follows a diffusion equation [100].

This diffusion equation has as intrinsic principle the stochastic interactions taking place within the system:

$$-\frac{\partial p(x,t)}{\partial t} = D\frac{\partial^2 p}{\partial x^2}, \tag{2.61}$$

where the relation $W = Da^2$ is true. Information about the flip-flop rate can be obtained by measuring the diffusion coefficient D, when the interspin distance a is known.

The figure below represents the mechanisms that lead the system to lose coherence.

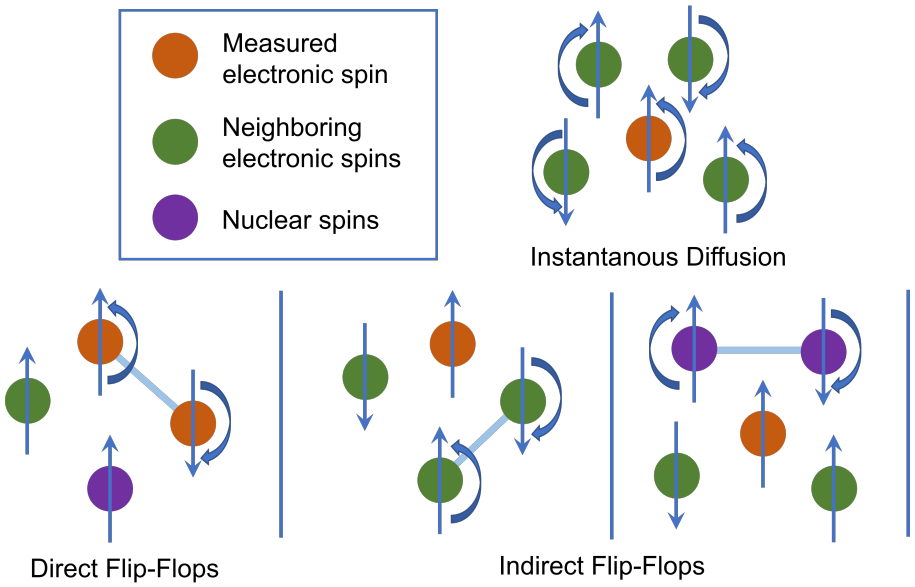

Figure 2.9: *Different mechanisms that influence the loss of spin coherence.*

A direct measure of the T_2 can be obtained in CW EPR, if the line presented by the system is homogeneous. In this case, T_2 can be associated to the half-widht at half-height by the relation

$$\Gamma_0 = \frac{1}{\pi T_2}. \tag{2.62}$$

Otherwise, pulsed EPR techniques must be applied to have access to T_2 relaxation times.

2.9 Pulsed EPR

In the presence of a magnetic field, the spins are oriented either in a parallel configuration (b state) or in an antiparallel configuration (a state). The difference of population between the a state (lower in energy and more populated) and the b state creates a magnetization along the axis of the static magnetic field.

Using the concept of the rotating referential, as introduced in the section 2.6, we set the system to be rotating with the same frequency of the microwave, in such a way that the magnetization becomes time independent. In other words, pulsed EPR is the technique that allows to measure the magnetization evolution as described by the Bloch equations.

The principle of pulsed EPR is to apply a short and intense MW pulse designed to rotate the magnetization by an angle β. This rotation is governed by the following relation:

$$\beta = F\frac{g\mu_B B_1}{\hbar}t_p, \tag{2.63}$$

Here, t_p represents the duration for which the pulse is applied, and F depends on the value of the total electronic spin:

- $F = 1$ for species with electronic spin $S = 1/2$;

- $F = 1$, if the pulse excites all transitions of a spin $S > 1/2$ simultaneously;
- $F = \sqrt{S(S+1) - m_s(m_s+1)}$ for $S > 1/2$ when specific transitions are excited.

The more interesting scenarios are found when the flip angles are set to $\beta = \frac{\pi}{2}$ or $\beta = \pi$, as illustrated in the figure below. These angles either project the magnetization onto the x-y plane or result in a complete inversion along the z-axis, as shown in the figure below:

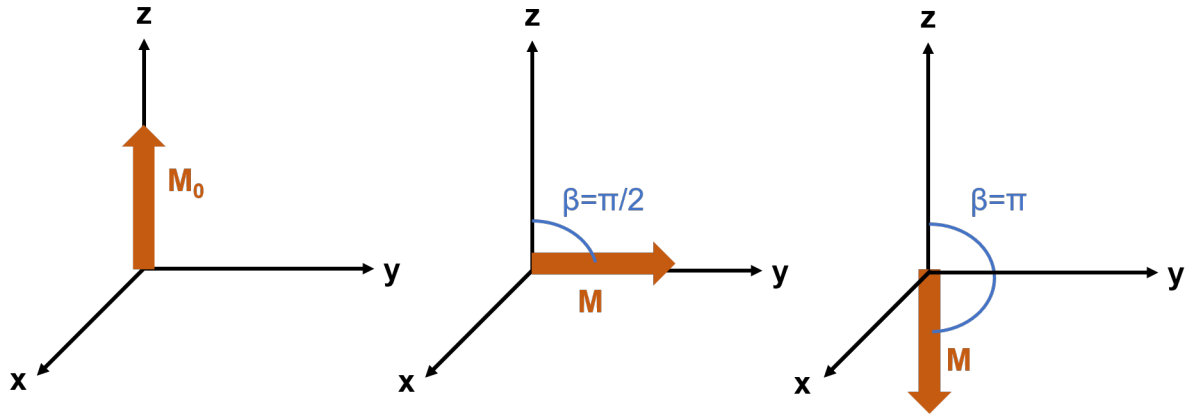

Figure 2.10: *Representation of the magnetization in the presence of magnetic field and after flip $\beta = \pi/2$ and $\beta = \pi$, respectively.*

The bandwidth of excitation is inversely proportional to the duration of the pulses. Shorter is the pulse duration, bigger is the bandwidth excited. The following approximation can be used to relate the excitation bandwidth Δv_e and the duration of the pulse [102]:

$$\Delta v_e \approx \frac{1.2}{t_p} \tag{2.64}$$

To exemplify, a pulse of 12 ns leads to an excitation bandwidth of 100 MHz. In a field scale, it corresponds to ≈ 3.6 mT.

When a pulse excites multiple transitions simultaneously, it is referred to as a *non-selective pulse*. However, when a pulse excites only one specific transition, it is termed a *selective pulse*. It is important to note that the number of transitions excited depends on the bandwidth of the pulse and, consequently, on the duration of the pulse.

In the presence of hyperfine interaction, achieving the selective excitation of a single transition becomes more delicate. The bandwidth of the pulse should be narrower than the separation between adjacent transitions:

$$t_p > 2\pi/A_s, \tag{2.65}$$

where A_s is the hyperfine splitting.

During an pulsed EPR experiment, the system passes by the periods:

Preparation ⇒	**Evolution** ⇒	**Mixing** ⇒	**Evolution** ⇒	**Detection**

In the preparation phase, the initial conditions are set and the spins are aligned. Subsequent to preparation, the system is allowed to evolve freely without external interactions.

During this period, the inherent dynamics of the spins unfold, leading to changes in their quantum states. Then the system passes by the mixing phase. In this intermediate stage, various interactions or manipulations are applied to the system. These interactions can include the application of pulses, external fields, or other forms of controlled perturbations. The mixing period is of crucial importance to nuclear detected techniques, because in this period, electron polarization is transfer to nuclear coherence. The second evolution happens after the mixing phase, where the system continues to evolve, but now with the influence of the introduced perturbations. Finally, the echo(s) signal is detected.

2.10 Free Induction Decay (FID)

After a pulse is applied and the spins, originally along the z axis, are flipped to the $x-y$ plane, the system is taken out of equilibrium. Considering an inhomogeneous line, formed by several spin packets, each spin packet has an intrinsic frequency that deviates from the frequency of the reference frame in which the turning pulse was applied.

At time $t = 0$ immediately following the pulse application, all the spins find themselves at the same location in the plane. However, as time progresses, these spin packets start to lose coherence due to the variations in their intrinsic frequencies. Consequently, the magnetization of the system begins to decrease, following an exponential law [4]:

$$M_x = M_0 \; exp(-t/T_2^*) \tag{2.66}$$

The FID encounters an experimental challenge during measurement. Once that pulses with high power are injected in the cavity, the detector must close while still reminiscent radiation for avoiding equipment damage or overheating.

When the major part of the radiation is dissipated, and the detector can finally be open, system has already undergone partial relaxation, resulting in the loss of information about the initial state. To overcome this issue, pulsed EPR uses the production of spin echos for measurements.

2.11 Hahn's echo

The decay of the FID can be reversed in a phenomenon called *Echo*. It was first described by Hahn in the context of Nuclear Resonance [103]. The principle is quite simple:

Considering a pulse $\pi/2$ applied in the system. If the broadening of the FID is inhomogeneous, it means that the spin packets have a frequency decaling from the central one. During the evolution period τ, this decaling is more and more evidenced. The trick is to apply another pulse π responsible to invert the phase of the spin packets. In this way, the packets that were distancing from the central one, will inverse phase and come back until in the time 2τ they will coincide with the central package and produce a peak of magnetization, or, an Echo.

From a mathematical point of view, this operation is similar to perform a temporal regression in the spin system. This is the simplest way of measuring T_m by a *primary echo*.

Further development brings new sequences with more than one refocusing pulses. In this case we have also the presence of secondary echos, that are a consequence of the

[4] T_2^* is inversely proportional to the EPR linewidht

refocalization of the FID produced by the first echo, these secondaries echos are called *stimulated echos*.

2.12 Rabi Oscillations

The oscillation between two energies levels was firstly observed by Isidor Isaac Rabi, who won the Nobel prize in physics in 1944 for " his resonance method for recording the magnetic properties of atomic nuclei" [104].

Considering a two level system, its state can be expanded in the state basis $\{|a\rangle, |b\rangle\}$:

$$|\Psi(t)\rangle = \gamma_a(t)\,|a\rangle + \gamma_b(t)e^{-i\omega_0 t}\,|b\rangle\,, \tag{2.67}$$

where ω_0 is the Larmor frequency and the exponential term accounts for the free evolution.

Applying the Schrodinger equation to describe the evolution of the system, we can evaluate the probability that an electron originally in the state $|a\rangle$ have passed after e time t to the state $|b\rangle$, due to the interaction with an electromagnetic wave, that for general reasons can detune from the Larmor frequency by the amount δ:

$$P_{a\Rightarrow b} = \frac{\omega_R^2}{\omega_R^2 + \delta^2} sin^2(\frac{\omega_0}{2}(t - t_0)) \tag{2.68}$$

Note that the equation presents an oscillating term that presents a minimum when t is a multiple of $2\pi/\omega_0$. The value of ω_0 depends on g, which means that systems that possess strong spin-orbit coupling will have a frequency that differs remarkably from the free electron (pure state 1/2).

The measurement of Rabi oscillations, also known as a nutation experiment, provides information about the frequency at which a particular spin S undergoes forced oscillations. This occurs when the spin is exposed to microwave radiation with a frequency that matches the Zeeman splitting between two projections of this spin, m_s, and $m_s \pm 1$.

The sequence employed to measure Rabi oscillations involves the application of a pulse with a variable duration, denoted as t, which rotates the magnetization by an angle θ. Subsequently, a waiting time of 5 T_2 is introduced to allow for the complete cancellation of transverse magnetization due to decoherence, leaving only the longitudinal magnetization. Following this, a standard sequence, $\pi/2 - \tau - \pi$, is applied. By varying the duration of the initial pulse, the magnetization can be rotated through multiple tours. The Rabi frequency is expressed in terms of the electronic spin value S, making this technique very useful for determining the electronic spin, when its value is unknown:

$$f = K\sqrt{P}\frac{g\mu_B}{h}\sqrt{S(S+1) - m_s(m_s \pm 1)} \tag{2.69}$$

K is an experimental constant that relates the microwave field and the microwave power $B_1 = K\sqrt{P}$.

2.13 Pulsed EPR techniques

2.13.1 Inversion recovery (T_1)

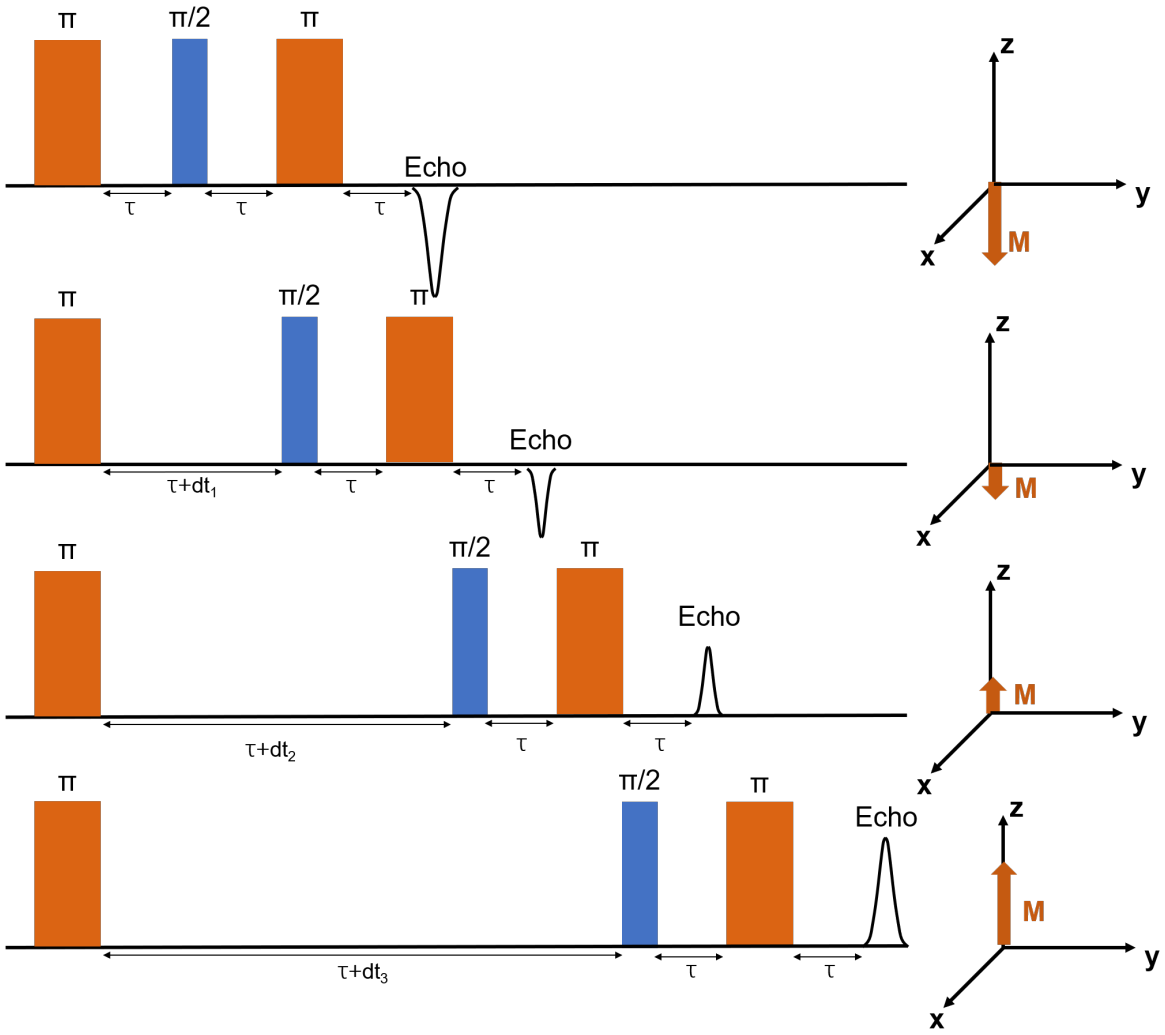

Figure 2.11: *Sequence that originates the Inversion Recovery echo. The representation of the measured echo at each moment of the sequence is represented in the axial system. The negative echo is obtained when the time t is short and the magnetization has negative composant.*

One of the simplest ways to measure the longitudinal relaxation time is by applying the inversion recovery sequence. This sequence is structured following the pattern of pulses: $\pi - t - \frac{\pi}{2} - \tau - \pi - \tau -$ Echo. Initially, the π pulse is utilized to invert the magnetization from z to $-z$. Then, the system is allowed to relax during the time t and a new sequence $\pi/2 - \tau - \pi$ is applied in order to generate a spin echo that allows the measurement of the residual z magnetization. The value of t is variated during the experiment, and the relative magnetization values are measured in relation to the magnetization acquired by the simple sequence $\pi/2 - \tau - \pi$.

In the absence of additional sources of decoherence, the magnetization returns to equilibrium following an exponential law:

$$M(t) = -M_0(1 - exp(-t/T_1)) \tag{2.70}$$

The pulse sequence and the Magnetization vector is illustrated in Figure 2.11:

2.14 T_m measurements

Due to the phenomena that leads the system to lose coherence besides the intrinsic spin-spin interaction, the experimental transverse relaxation time, is account as a phase memory time T_m. The simpler sequence employed for measuring the phase memory time is the 2-pulses echo decay.

2.14.1 2-pulses echo decay

The 2-pulses sequence involves the application of a $\pi/2$ pulse to the system, in order to transfer the magnetization to the plane. Subsequently, due to the inhomogeneous broadening, the system starts to lose coherence. Following a time interval τ after the initial pulse, an inversion pulse π is applied, in order to refocuse the different spin packets. After a time τ after the second pulse is applied, it is observable a spin echo.

The transverse relaxation through this technique time is determined by varying the time delay τ between successive repetitions of the sequence. Employing this method enables the tracking of the echo's intensity decay concerning τ, that usually follows an exponential decay. The schematic representation of the 2-pulse sequence is illustrated in Figure 2.12.

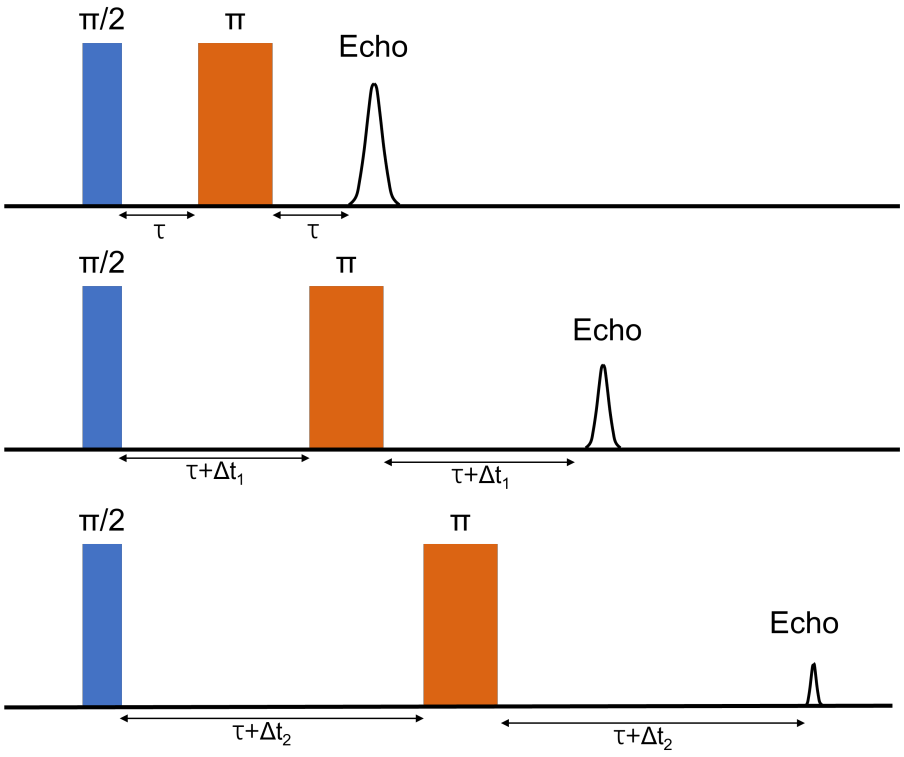

Figure 2.12: *2-pulses echo decay*

2.14.1. 2-pulses echo decay

The interesting phenomenon that can arise from the 2-pulses sequence is the transfer of polarization to nucleus that are surrounding the excited electronic spins. It gives origin to a series of experiments that allows the identification of nuclei interacting with the unpaired electron. Furthermore, these experiments provide a quantitative measurement of the strength of this interaction.

To gain insight into the process of polarization transfer, let's consider a system with an electronic spin S=1/2 and a nuclear spin I=1/2. In this system, the electron and nucleus interact through hyperfine coupling. In this scenario, we have four possible states for the system. Considering that the hyperfine tensor can have anisotropy, the mixing of states is represented by the matrix

$$|e,n\rangle = \begin{array}{c} \\ |\alpha\alpha\rangle \\ |\alpha\beta\rangle \\ |\beta\alpha\rangle \\ |\beta\beta\rangle \end{array} \begin{array}{c} \begin{array}{cccc} |\alpha\alpha\rangle & |\alpha\beta\rangle & |\beta\alpha\rangle & |\beta\beta\rangle \end{array} \\ \begin{bmatrix} T_{ZZ}, A_{iso} & T_{ZX}, T_{ZY} & T_{XZ}, T_{YZ} & T_{XX}, T_{YY}, T_{XY}, \\ T_{ZX}, T_{ZY} & T_{ZZ}, A_{iso} & T_{XX}, T_{YY} & T_{XZ}, T_{YZ} \\ T_{XZ}, T_{YZ} & T_{XX}, T_{YY} & T_{ZZ}, A_{iso} & T_{ZX}, T_{ZY} \\ T_{XX}, T_{YY}, T_{XY}, & T_{XZ}, T_{YZ} & T_{ZX}, T_{ZY} & T_{ZZ}, A_{iso} \end{bmatrix} \end{array}$$

Figure 2.13: *Mixing of states.*

The terms represented in black, that occupy the diagonal line, are the secular terms, where there's no change in the state of the system. The terms represented in blue are those where the electron spin is changed, but not the nuclear spin. They are responsible for the standard EPR measurements. The red ones are the pseudo secular terms, that are the key for ESEEM and ELDOR detected NMR techniques, where the electronic spin is maintained unchanged but the nuclear spin is flipped. Lastly, the green terms involve simultaneous flips of both electronic and nuclear spins. These non-secular terms are typically negligible.

In standard EPR techniques, the condition for a transition be allowed is $\Delta_{m_S} = 1$ and $\Delta_{m_I} = 0$. It forbid the nuclear transitions and is valid in the high field approximation, where $\omega_I >> A, B$, where A stands for the isotropic coupling constant in the hyperfine Hamiltonian and B, the anysotropic term, responsible for coupling $S_z I_x$.

When this condition is not fullfilled, the pseudo-secular terms make formally forbidden transition partially allowed. The presence of the B terms induce a tilt in the effective field at the nuclear spins, and this tilt is opposite for interaction with electronic spins in state α or $\beta>$ The frequencies presented by nuclei interacting with these states is given by:

$$\omega_\alpha = \sqrt{(\omega_I + A/2)^2 + B^2/4} \tag{2.71}$$

$$\omega_\beta = \sqrt{(\omega_I - A/2)^2 + B^2/4} \tag{2.72}$$

For $|\omega_I| > 2|A|$ (weak coupling), the nuclear frequency doublet is centered in $(\omega_\alpha + \omega_\beta)/2$ and for $|\omega_I| < 2|A|$ (strong coupling), the center represents $(|\omega_\alpha - \omega_\beta|)/2$ and can be recognized as the hyperfine coupling.

2.15 ESEEM

Electron Spin Echo Envelope Modulation allows the observation of electrons weakly coupled to nuclear spins [105]. These interactions influence the behavior of the electron's spin, causing variations in the echo's intensity over time. It results in an observable modulation in the echo intensity caused by the anisotropic hyperfine or superhyperfine interactions [106].

By applying a short pulse $\pi/2$, all the transitions are excited simultaneously, and the magnetization vector is carried to the -y-axis. Subsequently, during the period of free evolution, this magnetization vector precess in the x-y plane. As it precesses, it accumulates phase information. Once that the nuclear spins are turning with their Larmor frequency around the quantization axis, the field felt by the electronic spins change. The ESEEM change the time between pulses, which means that when this time is a multiple of the Larmor frequency, the effect felt by the electronic spins, is like no changes in the effective magnetic field happened. It creates a modulation. In this sense, the modulation is a consequence of the nuclear Zeeman interaction

The modulation depth k is connected to the Larmor frequency of the nucleus ω_I:

$$k = \left(\frac{B\omega_I}{\omega_a\omega_b}\right)^2 \tag{2.73}$$

Without anisotropy ($B = 0$), the modulation depht ($k = 0$) and no ESEEM signal is present. This coefficient is connected also to the distance between the electron and nuclear spin r:

$$k = \left(\frac{3\mu_0 g\beta_e}{8\pi B_0}\right)^2 \frac{sin^2 2\theta}{r^6} \tag{2.74}$$

For weak couplings $k \approx (B/\omega_I)^2$. The general modulation form for n interacting nuclei is given by the product,

$$v'_{2p} = exp\left(\frac{-2\tau}{T_m}\right)\prod_{I=1}^{n} V_{2p}(\tau) \tag{2.75}$$

where the term in the exponential describes the lost of magnetization in the plane, a consequence of the interactions experienced by the electrons. Additionally, the term V_{2p} characterizes the modulation arising from interactions with a singular nucleus, in its expanded form:

$$V_{2p}(\tau) = 1 - \frac{k}{4}\left[2 - 2cos(\omega_a\tau) - 2cos(\omega_b\tau) + cos((\omega_a - \omega_b)\tau) + cos((\omega_a + \omega_b)\tau)\right] \tag{2.76}$$

In high fields, ESEEM doesn't work so well because the probability of having forbidden transitions is smaller (high field approximation). We can see by the equations 2.76 that the 2-pulses ESEEM pattern contains modulations related to the SHF frequencies, but to their sums and differences as well [107].

2.16 HYSCORE

Besides the 2-pulses experiment, echo modulation can also be observed in 3-pulses experiment, that takes the form $\pi/2 - \tau - \pi/2 - T - \pi$. The advantage of this third pulse is the

increasing in the resolution of the modulation, once that the system relax slower, once that relaxation is due to spin-lattice interactions and not spin-spin interaction in this case [108]. The dependence of the modulation now assumes a form that does not depend on the sum and difference of the transitions, but depend on the two evolution times τ and T:

$$v_{3p}(\tau,T) = C[cos(\omega_a\tau) + cos(\omega_b\tau) + 2sin^2(\omega_a\tau/2)cos(\omega_b(\tau+T)) + 2sin^2(\omega_b\tau/2)cos(\omega_a(\tau+T))]. \quad (2.77)$$

In 1979, R.P.J. Merks and R. DeBeer had the idea to use the sinusoidal dependence of the stimulated echo to produce a 2-D experiment [109] varying the times τ and T. In this way, the experiment should present the appearance of cross peaks related to (ω_a, ω_b) and (ω_b, ω_a) that belonged to the same hyperfine interaction.

This technique has been enhanced, given origin to the 4-pulses Hyperfine Sublevel Correlation (HYSCORE) Spectroscopy [110]. In this technique, the time T is split in two times t_1 and t_2 and correlate hyperfine sublevels that belong to the same electron-nuclear coupling interaction. Because the relaxation time of electron spin-lattice significantly impacts the decay of the four-pulse echo in both the t_1 and t_2 domains, cross peak intensities, (ω_a, ω_b) and (ω_b, ω_a) are present, symmetrically arranged around the frequency diagonal.

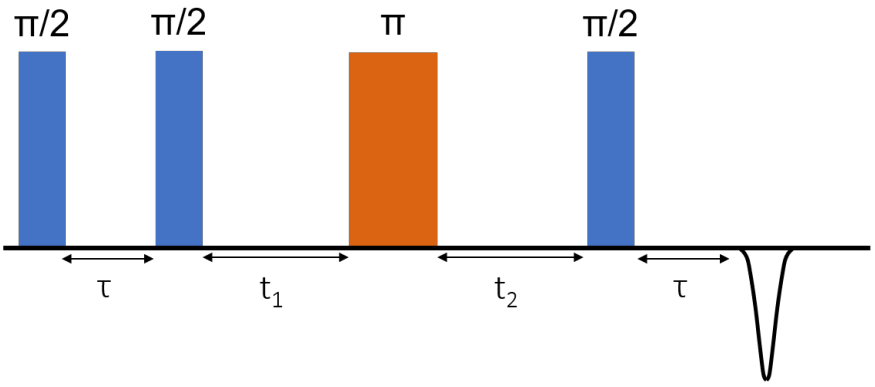

Figure 2.14: *HYSCORE sequence*

Peaks appearing in the upper right of the 2D spectra typically arise from nuclei in which the hyperfine coupling is smaller than the Larmor frequency and are centered in the Larmor frequency, separated by the hyperfine coupling. Peaks from nuclei in which the hyperfine interaction is bigger than the Larmor frequency appear in the upper left quadrant of the spectra.

Some of the more abundant nuclei and its respective Larmor frequency are expressed in the table below:

Nucleus	Nuclear Spin (I)	Larmor frequency (MHz/T)
^{1}H	1/2	42.6
^{2}H	1	6.5
^{3}H	1/2	45.4
^{13}C	1/2	10.7
^{15}N	1/2	4.31
^{23}Na	1/2	11.3

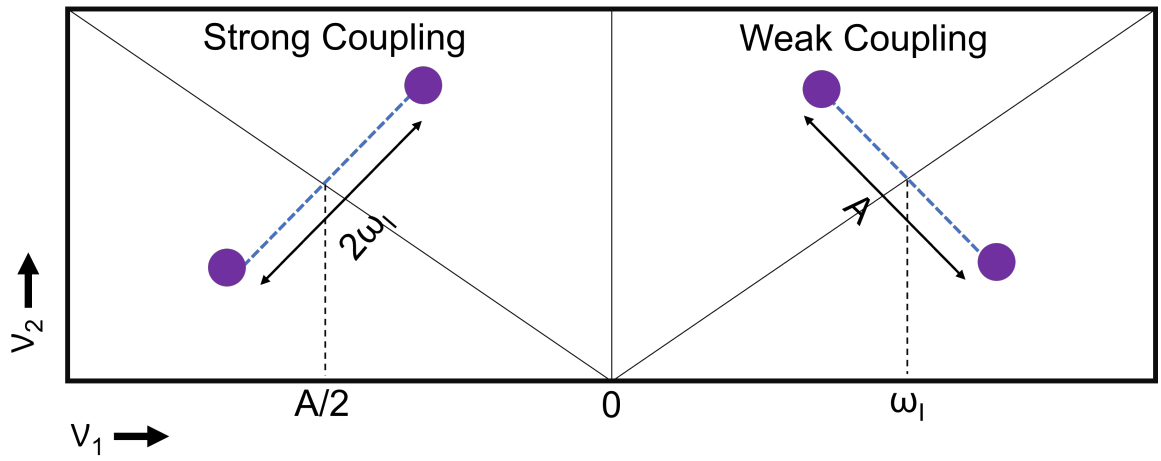

Figure 2.15: *Representation of the case of strong coupling,* $|\omega_I| < 2|A|$ *(left) and weak coupling,* $|\omega_I| > 2|A|$ *(right) in a HYSCORE spectra*

2.17 Nuclear effects investigated by double resonance techniques

In double resonance techniques, the system is being pumped by two different sources of radiation. The first pump is responsible to inverse the population by standard EPR transitions. The second radiation is in resonance with a target transition. In this sense, the second source of radiation can be in the MW range (for exciting direct forbidden transitions) or in the RF range (to promote nuclear transitions).

2.17.1 ELDOR detected NMR

This technique use the artifact of a hole burning, and has as advantage more sensitivity and less artifacts of dead time. The ELDOR experiment starts by exciting the paramagnetic system with a selective $\pi/2$ pumping pulse, with variable sequence. After the $\pi/2$ pumping pulse, there is a period of evolution, of average 5 T_m. During this time, the electron spins evolve and interact with their surroundings, leading to a total in-plane dephasing. The evolution time is crucial for allowing forbidden interactions to take place and influence the electron spins states. Following the evolution phase, a classic spin echo sequence is applied. This sequence consists of two pulses: a $\pi/2$ pulse followed by a π pulse. These pulses are applied at a specific magnetic field corresponding to one transition in the EPR spectrum.

The frequency between the first pulse (that is sweepted) and the second is characterized by Δf. At high detuning, the first pulse does not correspond to any transition, neither allowed or forbidden, and the echo generated from the entire sequence is the classic one of a 2-pulses experiment.

At exactly zero detuning ($\Delta f = 0$), the first pulse completely saturates the target transition so that the following detecting sequence gives no echo intensity (hole burning).

When the detuning is equal to the value of another close transition, the pumping pulse saturates it, and a new hole burning is achieved (less intense from the one of the zero detuning). It indicates the correlation between these transitions.

Care must be taken when the system posses $S > 1/2$, once this echo-intensity lowering is commonly due to a depopulating effect occurring when the two transitions of different $|m_s|$ share a common level.

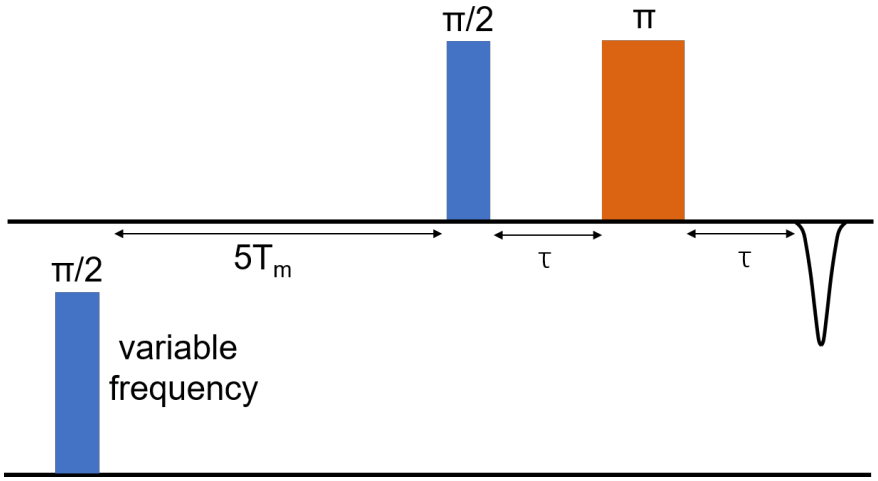

Figure 2.16: *ELDOR sequence*

Chapter 3

Experimental Procedures

Contents

3.1 Studied Samples - Fabrication methods 49
3.1.1 ZnO synthesized via solid-gel method 49
3.1.2 ZnO annealed 49
3.1.3 ZnO aqueous coprecipitation 50
3.1.4 ZnO:Co doped 50
3.2 Nuclear Magnetic Resonance 51
3.3 Fourier Transform Infrared spectroscopy(FTIR) 51
3.4 Electron microscopy 52
3.4.1 Scanning Electron Microscopy (SEM) 52
3.4.2 Transmission Electron Microscopy (TEM) 52
3.5 Electron Paramagnetic Resonance 52
3.5.1 Continuous wave EPR 52
3.5.2 Pulsed EPR 53

The objective of this chapter is to present, succinctly, the samples and the experimental techniques and equipments used for the acquisition of the experimental data discussed in the next chapters. Due to the high dependency of the experimental results on the sample fabrication methods, a greater emphasis is placed on this subject. A color code is adopted for each sample, making it easier for the reader to reference to each sample through the text.

3.1 Studied Samples - Fabrication methods

3.1.1 ZnO synthesized via solid-gel method

Zinc oxide nanoparticles (ZnO NPs) were synthesized using the method described by Pacholski *et al.* [111] and referred to as sol-gel method [112]. Initially, 2.0694 g of zinc acetate [$Zn(Ac)_2$], (Aldrich Chemicals,99.99%) was solubilized in 105 ml of methanol and 0.625 ml of distilled water. A second solution with 1.1236 g of potassium hydroxide (KOH, Aldrich Chemicals, 99.99%) and 57.5 ml of methanol was added dropwise at 60°C under magnetic stirring. After 3 h 15 min, the solution was removed from the thermal bath and submitted to centrifugation for 12 min at 7800 rpm. The precipitate was washed with the solvent and centrifuged once more. The white solid was dried in an oven at 100 °C and named to as the as-grown sample. The detailed step-by-step procedure is described in annex A.

An equivalent sample was synthesized by substituting methanol with ethanol as the solvent. This particular sample was used for comparative purposes and is further elaborated in the text. This sample is named *sample-ethanol*.

A third sample was prepared by substituting KOH with NaOH in the synthesis, adjusting the appropriate stoichiometric quantities accordingly. This sample is also detailed in the text and named *sample-NaOH*.

Surface functionalization - Deuterated sample

For the surface functionalization process, 5 mg of sodium acetate-d3 (Aldrich Chemicals, 99.99%) were introduced to a solution containing 50 mg of the as-grown sample, which was diluted in 2 ml of methanol.

The solution underwent centrifugation, and the supernatant was discarded. Subsequently, the functionalizing component and solvent were added once more to the remaining precipitate. This procedure was iterated three times, ultimately resulting in the formation of the solid referred to as the deuterated sample.

3.1.2 ZnO annealed

The as-grown sample underwent annealing for 4 min in a laboratory oven at 500 °C . Subsequently, the sample was removed from the oven and rest to cool at room temperature. The remaining powder was macerated to avoid the presence of agglomerates. This sample is defined as annealed.

All the samples presented before were produced by the author in the AMU facilities.

3.1.3 ZnO aqueous coprecipitation

Alternatively to the solid-gel method, ZnO nanostructures were produced by aqueous coprecipitation.

In this process, 100 ml of cationic solution was obtained by dissolving $Zn(NO_3)_2$,6-H2O (Aldrich 99.99%) in demineralized water. Precipitation was made by the dropwise addition of 125 ml of NaOH solution at 1 mol/l (NaOH solid from Scharlau (99%)) during 25 min. The precipitate obtained was centrifuged at 4000 rpm during 5 min and washed with demineralized water. This step was repeated five times. The solid was finally dried at 80 °C [113].

The samples produced through this method are referenced as *nanoflakes* and were not synthesized by the author.

3.1.4 ZnO:Co doped

ZnO:Co was prepared using two distinct techniques:

Wet reaction

The identical procedure employed for synthesizing the as-grown sample was employed, with the exception of substituting an appropriate quantity of Zinc Acetate with Cobalt Acetate ($C_4H_6CoO_4$). The nominal concentrations targeted are 1%, 0.5%, 0.1%, and 0.01% of cobalt acetate. Throughout the text, the samples are consistently referenced according to their respective doping concentrations.

The annealing process for these samples followed the same protocol as that employed for the as-grown sample. These samples were synthesized by the authors in the AMU facilities.

Solid-state reaction

For the dopping procedure, ZnO powder was combined with high-purity CoO. Quantities equivalent to nominal doping concentrations of 1%, 2%, 4%, 6%, and 8% were utilized for the doping. The materials were meticulously mixed and ground in a mortar for a duration of 3 hours. Subsequently, the mixture was annealed at 1100 degrees Celsius for 2 hours. These samples were not produced by the author.

All the aforementioned samples are illustrated in Table 3.1 to facilitate access to important information regarding each sample.

Sample	Production method	Precursors	Dopping	Fabricated by the author	Comments
As grown	Sol-gel method	$Zn(Ac)_2$ + KOH + H_2O In MeOH	None	Yes	The substitution of MeOH with EtOH and KOH with NaOH does not alter the properties of the sample.
Deuterated	Surface functionalization	As grown + CD_3CO_2Na	None	Yes	
Annealed	Heat at 500 °C for 4 minutes	As grown	None	Yes	
Nanoflakes	Aqueous precipitation	$Zn(NO_3)_2$ +NaOH+H_2O	None	No	
ZnO:Co wet	Sol-gel method	$Zn(Ac)_2$ + KOH + H_2O+$C_4H_6CoO_4$ In MeOH	0.01% , 0.1%, 0.5% and 1%	Yes	
ZnO:Co Solid state			1%, 2%, 4%, 6% and 8%.	No	

Figure 3.1: *Samples studied in this thesis*

3.2 Nuclear Magnetic Resonance

The solid-state ^{13}C spectra were acquired using a Bruker Avance-400 MHz nuclear magnetic resonance (NMR) spectrometer with a magnetic field of 9.4 T. A double-channel Bruker probe was employed for the measurements. Approximately 10 mg of the sample was loaded into a zirconium dioxide rotor with a 4 mm outer diameter and spun at a magic angle spinning rate of 10 kHz.

The ^{1}H–^{13}C Cross-Polarization Magic Angle Spinning (CPMAS) technique was applied, featuring a ramped ^{1}H-pulse that started at 100% power and gradually decreased to 50% during the 2 ms contact time to circumvent Hartmann–Hahn mismatches. To enhance the signal-to-noise ratio in the ^{13}C CPMAS experiment, 15000 scans were accumulated with a 2.2-second delay. The ^{13}C chemical shifts were referenced to tetramethylsilane and calibrated using the glycine carbonyl signal, set at 176.03 ppm.

3.3 Fourier Transform Infrared spectroscopy(FTIR)

The transmission of infrared light was quantified using a PerkinElmer Spectrum Two+ FT-IR spectrometer. To prepare the samples, the ZnO powder was dissolved in methanol (MeOH), resulting in a homogeneous solution. This solution was then deposited on silicon, which is transparent to infrared light, using a spin-coating technique. To enhance the signal-to-noise ratio, 15 layers of the ZnO solution were sequentially deposited.

Subsequently, the same samples were subjected to an annealing procedure while still deposited on silicon, after the initial measurements were taken. Fore more details about the technique and the identification of the organic bonds, the reader is conducted to annex B.

3.4 Electron microscopy

To overcome the limitations of optical microscopy and improve the resolution, electron microscopy was employed. This technique involves the liberation of electrons through thermionic emission, also known as thermal electron emission. Tungsten is commonly used as the material for this purpose. The liberated electrons are then accelerated by an electrical potential. With an accelerating voltage of 100 keV, the electrons achieve a wavelength of 0.037 angstroms. These electrons are subsequently scattered by the atomic potential of the sample. The diffracted and scattered electrons can be analyzed and interpreted to serve as the foundation for conventional imaging techniques.

Two distinct approaches were employed to produce the images showcased in the subsequent chapters:

3.4.1 Scanning Electron Microscopy (SEM)

This technique, which relies on the detection of low-energy secondary electrons (< 50 eV), is highly valuable for determining the surface morphology of crystals.

SEM imaging was conducted using a Gemini 500 ultra-high resolution field emission electron microscope equipped with an in-lens secondary electron (SE) detector, which is ideal for visualizing surface structures. SEM images were captured at a low accelerating voltage (2 kV) to enhance topographic contrast.

3.4.2 Transmission Electron Microscopy (TEM)

In an analogous technique, the transmitted electrons are collected and subsequently transformed into an image using magnetic lenses. The resulting image provides a projection of the structure along the direction of the electron beam. In fact, with a high-quality microscope, it is possible to achieve atomic resolutions. However, to attain such precision, it is imperative to employ extremely thin crystals with a thickness of less than 500 Å. This requirement is due to the electron's limited penetration depth into the sample.

A disadvantage of this technique is that sensitive samples may not resist to the conditions required for TEM, which include a high vacuum environment and potential damage caused by the high-energy electrons used in the imaging process [114].

Transmission Electron Microscopy (TEM) imaging was conducted using an FEI TITAN 80-300 electron microscope equipped with an image aberration corrector. The TEM was operated at an acceleration voltage of 200 kV.

3.5 Electron Paramagnetic Resonance

In optically excited EPR experiments, the samples were optically excited via the solid state laser beam of the OBIS Coherent LX series at 405 nm at a specific optical power (20 and 30 mW), focused on the sample within the EPR cavity. More details about the EPR technique are presented in chapter 2.

3.5.1 Continuous wave EPR

The Continuous wave (CW) EPR experiments were performed in a Bruker EMX spectrometer operating at X-band (9.39 GHz) equipped with a standard TE_{102} cavity allowing

for external optical excitation. A second cavity for experiments comparing perpendicular and parallel modes was employed, with respective frequencies $\nu_{\perp} = 9.629$ GHz and $\nu_{\parallel} = 9.399$ GHz.

The power of the microwave is attenuated following the relation $At = 10 \ \ log(P_0/P)$,where P_0 is the maximal MW power (200 mW).

Temperature control was made by two different cooling systems: For temperatures higher than 85K, liquid-nitrogen flux and an intelligent temperature controller (Oxford, ITC 503) were employed. Lower temperatures (down to 7K) were reached using a Brukers Cryocooler. All the measurements in pulsed EPR use the second method of cooling.

3.5.2 Pulsed EPR

Pulsed EPR technique were performed in two different spectrometers:

(1) Spectrometer from BIP (Marseille, FR): X-band (9.73 GHz) and Q-band (33.73 GHz) pulsed-EPR experiments were carried out on a Bruker Elexsys E580 spectrometer equipped with a standard dielectric ring resonator (ER4118X-MD5) and an optical helium flow cryostat (Oxford CF935O), allowing for external optical excitation. The microwave pulses were amplified with a 1 kW TWT, which gives a typical $\Pi/2$ pulse of 16 ns.

Lower temperatures were reached using a Brukers Cryocooler. Due to an experimental issue in obtaining temperatures lower than 15K with the cryostat (Oxford CF935O), the measurements for T_1 were obtained through another spectrometer:

(2) Spectrometer from LASIRE (Lille, FR): X-band (9.73 GHz) pulsed-EPR experiments were carried out on a Bruker Elexsys E580 spectrometer equipped with a standard resonator (ER4118X-MS5) and an optical cryostat from ColdEdge, allowing for external optical excitation. The microwave pulses were amplified with a 1 kW TWT, which gives a typical $\pi/2$ pulse of 16 ns.

Lower temperatures were reached using a Brukers Cryocooler. In this spectrometer, temperatures down to 7K were obtained.

Chapter 4

Paramagnetic Behavior in Photo-Excited ZnO Nanoparticles

Contents

4.1 Identification of the different paramagnetic systems 56
4.1.1 Dark condition 57
4.1.2 Photo-activated elements 57
4.2 ZnO as-grown and annealed 59
4.2.1 Identification of organic compounds 59
4.2.2 Morphological characterization 61
4.3 EPR Study 62
4.3.1 Core- and surface-defect 63
4.3.2 Spin value 66
4.4 Methyl radicals (4-lines system) 67
4.4.1 Deuteration 68
4.4.2 Analytical Approach 71
4.4.3 Identification of the electronic spins 73
4.4.4 Saturation phenomena 74
4.5 Chemical stability over time 77
4.5.1 Changing the synthesis reagent and solvent 79
4.6 Relaxation from the optically excited state 80
4.6.1 Irreversible regime 83
4.6.2 Reversible regime 86
4.7 3-lines signal 87
4.8 Relaxation phenomena - core-defect, Methyl radicals and 3-lines system 90
4.9 Spin lattice relaxation time (T_1) 91
4.10 Coherence time (T_2) 94
4.10.1 2-pulses echo decay 95
4.11 Electron Spin Echo Envelope Modulation (ESEEM) 99

4.12 HYSCORE 102
4.13 Q-band EPR analysis 104
4.14 Correlation between EPR lines - ELDOR detected NMR . . 106
4.15 Partial conclusions 108

The manipulation of magnetic defects in semiconductors is a prominent area of research for the advancement of innovative optical and magnetic devices [43], such as spin-polarized solar cells [115], spin light-emitting diodes (LEDs) [116], and magneto-optical switches [117].

In this context, ZnO emerges as a promising candidate due to its intrinsic defects that contribute to its n-type conductivity [118]. While the control of defects in ZnO has been extensively studied, novel features have arisen with the reduction of device size to the nanoscale. In this regime, interesting phenomena take place, once that the states belonging to the crystal are susceptible to confinement restrictions. Furthermore, the significant surface-to-volume ratio in nanostructures accentuates the prevalence of surface-related phenomena.

The connection between bulk and surface-defects presents new opportunities in nanotechnology, enabling the control of both bulk and surface magnetic properties. These nanostructures pave the way for the development of nanoscale spin-switches, characterized by highly localized and monitorable magnetization. Such advancements hold significant potential for applications in quantum computing, small-scale magnetic memories, and sensors [119]. The presence of catalytic activity in these nanostructures is also remarkable [120].

The ultimate state achieved, which results from the combination of bulk and surface properties, is greatly influenced by the surrounding environment and the fabrication process involved. This dependency arises because the stabilization and passivation mechanisms of polar nanostructures are significantly reliant on the particular fabrication methods employed.

The primary goal of this chapter is to identify the paramagnetic states present in ZnO nanoparticles under photo-excitation. Following this, the characterization of these states is conducted to establish a connection between them and their physical origin. For this purpose, we present the results obtained from nanoparticles synthesized via the sol-gel method using various reagents and solvents. A comparative analysis is performed between as-grown, deuterated and annealed samples.

4.1 Identification of the different paramagnetic systems

Over the years, various groups of paramagnetic signals have been observed in ZnO NPs, contingent upon the specific production techniques utilized for the fabrication of the NPs. Throughout the text, the characteristics and physical explanations related to the EPR observed signals will be examined and discussed. The final objective is to delve into the nature of the phenomenon, shedding light on its characteristics and providing a comprehensive understanding of its origins.

Throughout this text, we will make references to “dark” and “light” conditions. In this context, “dark” stands for samples that were not subjected to photo-excitation before EPR measurement. Under dark conditions, there is ambient illumination; however, it does not exert influence on the system. Conversely, in light conditions, the samples undergo photo-excitation with a laser of 405 nm wavelength. A concise summary of all the systems analyzed in this chapter is presented below.

4.1.1 Dark condition

core-defect

Numerous authors have identified a paramagnetic signal characterized by a single EPR line centered at $g = 1.96$. This signal emerges either through photo activation or, in certain instances, without the requirement of external excitation. The precise conditions leading to the appearance of this signal have remained unclear thus far, but has been proved to arise from the bulk part of the NPs [121; 23]. We have demonstrated that this signal originates from ionized defects within the ZnO lattice, emerging from the core of the NP, following the core-shell model. This signal consistently appears in all the samples studied, and its presence, together with the other systems, can be observed in Figure 4.1.

This signal is present in all the studied samples (in some in dark conditions and in other under light condition).

surface-defect

When the core-defect is present under dark conditions, the surface-defect is also present. It arises from a defect on the nanoparticle's surface and is characterized by a single line centered at g=2.003.

This signal is present in the annealed sample.

4.1.2 Photo-activated elements

Certain paramagnetic signals are only detected when submitted to photo-excitation. The source of photons used during this work is a laser with wavelength 405 nm (violet). All the observed signals observed under photo-excitation are:

core-defect

In some samples, as the as-grown, the core-defect only appears in the presence of photo-excitation.

Methyl radicals

Simultaneously to the core-defect, a signal composed by 4-lines spaced by 2.2 mT centered at $g = 2.005$ has been observed in the as-grown samples. This signal has sparked contradictory attributions among researchers. Some authors [122; 123] have associated it to Na impurities, yet this model fails to elucidate the presence of the signal in Na-free conditions. Other authors assigned this signal to a high-spin state within the ZnO lattice [1; 42]. However, this model also encounters limitations in explaining its absence in samples produced using high-temperature methods.

In our investigation, we demonstrate that this particular signal originates from methyl radicals generated on the NP's surface, constituting a shell state. The lines associated to this element are named as L_1, L_2, L_3 and L_4, respectively, progressing from low to high magnetic field.

This signal is present in the as-grown samples.

3-lines system

Along with the formation of methyl radicals, the presence of adjacent lines is identified. These lines are labeled L_5, L_6 and L_7, following the given nomenclature (low field to high field). These additional lines become more apparent when examining the absorption spectrum, as depicted in figure 4.1 and in this work will be tentatively assigned to the formation of methyl pairs on the NP surface.

This signal is present in samples where the methyl radical is observed.

Elephant

A distinctive signal is present in the NPs, characterized by an anisotropic large peak centered around $g = 2.023$. This signal is overlaid with those originating from methyl radical. It also appears under 405 nm light illumination, together with the other groups. Due to its resemblance in shape to the depiction of an elephant swallowed by a snake in the book "Le Petit Prince", we colloquially refer to this signal as the "elephant". The presence of this signal has been consistently identified in various EPR studies conducted in ZnO and was previously associated with surface ionized O^- atoms [70].

Although this signal is present in all samples, it also appears in NP lacking the organic shell (nanoflakes).

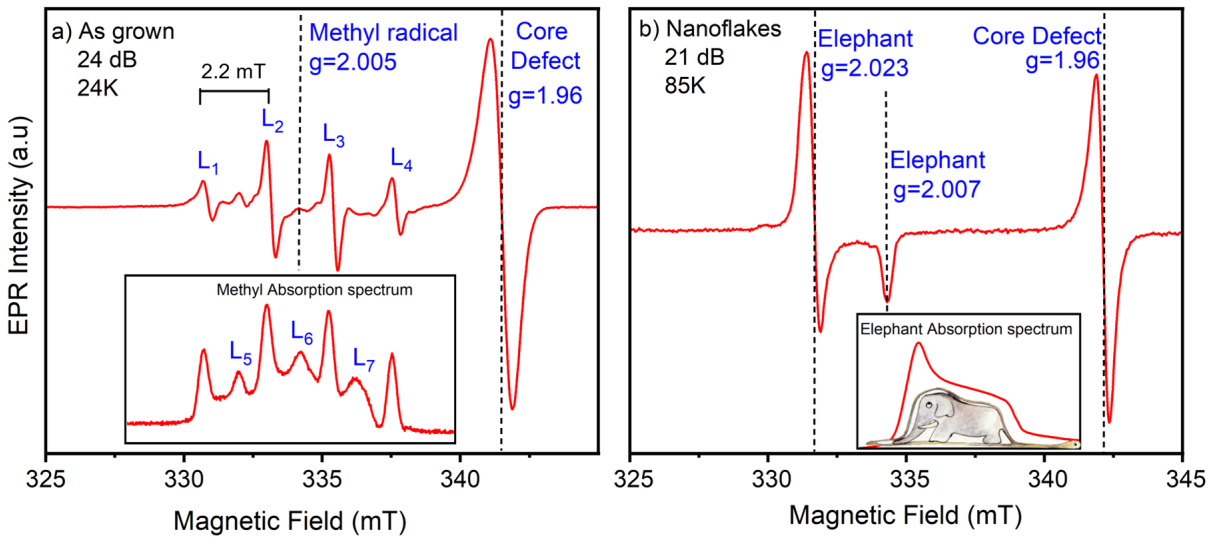

Figure 4.1: *Following optical excitation with a 405 nm wavelength laser, EPR responses are observed in ZnO nanoparticles. In Figure (a), the four lines associated with methyl radicals (referred to as L_1, L_2, L_3 and L_4) are presented, together with the 3-lines system (L_5, L_6 and L_7) and the intrinsic core-defect. The identification of the 3-lines system is simplified in the integration spectra, represented within the boxed area. In Figure (b), the "elephant" signal is identified in nanoflakes (another kind of sample, whithout the organic shell), with the integration spectra depicted within the boxed region. Amusingly, we humorously attribute the nomenclature of this signal to "Le Petit Prince" as a lighthearted source of inspiration.*

The photo-generated states are produced using the same wavelength (405nm), aligning with prior findings obtained for nanoparticles synthesized under comparable conditions [42]. This observation suggests that all the centers are generated by the same quantum of

light, i.e., the same photon. Nonetheless, the sequence of excitation appears to be critically significant, and the core-defect emerges as the initiator for the other observed centers. The additional groups (methyl radicals, 3-lines system and elephant) are only detected in the presence of the core-defect. Conversely, the existence of the core-defect does not rely on the presence of the other signals. For a better understanding of the systems, a general analysis is primarily carried, in order to morphologically characterize the NPs. In a second moment, all the paramagnetic signals are individually and collectively examined.

4.2 ZnO as-grown and annealed

The initial sample under analysis is the as-grown sample. The procedure detailing the synthesis of the NPs is presented in Section 3.1.1. These nanoparticles were synthesized using a wet method and may contain organic compounds adhered to their surface.

A portion of the as-grown samples underwent annealing at 500°C, following the methodology outlined in Section 3.1.1. The primary objective of this procedure is to eliminate the organic elements possibly present within the NPs. Samples submitted to this procedure are named as annealed samples.

4.2.1 Identification of organic compounds

Fourier Transform Infrared Spectroscopy (FTIR) analysis

The presence of organic compounds incoming from the NPs synthesis was investigated through Fourier Transform Infrared Spectroscopy (FTIR) for as-grown and annealed samples. The results are displayed in Figure 4.2. Additional information regarding FTIR spectroscopy is presented in Annex B.

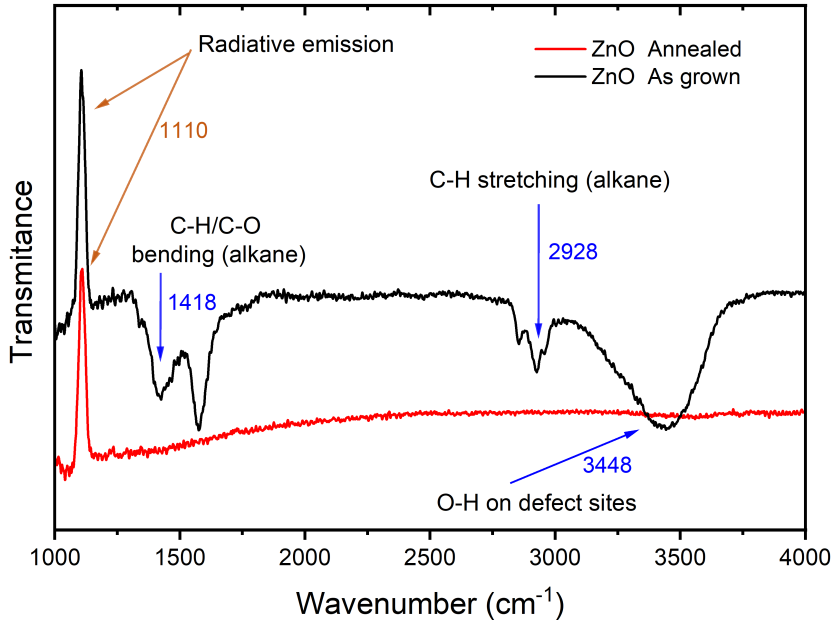

Figure 4.2: *Fourier Transform Infrared Spectroscopy (FTIR) of the as-grown (dark) and annealed (red) ZnO samples.*

The FTIR results reveal the presence of several organic bonds in the as-grown samples. The presence of O-H present in defect sites is identified through a decrease in the

transmittance at wavenumber 3448 cm^{-1} [124]. The peaks around 1418 cm^{-1} are related to the bending vibration mode of C-H and C-O in alkanes [1]. Lastly, peaks around 2928 cm^{-1} are observed, and are identified as the stretching vibrational mode of C-H bonds also in alkanes. A table for FTIR identification is provided in the end of Annex B. In the case of the annealed samples, it is observed that the high-temperature treatment effectively eliminates the organic compounds, as indicated by the absence of any signals in the FTIR analysis.

Additionally, a positive peak is observed at 1110 cm^{-1}. This peak is present in both samples (annealed and as-grown) and is more likely associated with radiative defect recombination occurring in the ZnO lattice. It has been demonstrated that the peak decreases when extrinsic impurities (such as cobalt) are incorporated into the ZnO lattice. These results are discussed in Section 5.2.

^{1}H–^{13}C NMR CPMAS analysis

Additional analyses were conducted using ^{1}H-^{13}C cross-polarization solid-state NMR spectroscopy (CPMAS) in the as-grown sample, in order to identify the molecular groups present in the NPs. It's worth noting that the results from FTIR and NMR analyses complement each other [125]. Both NMR and FTIR analyses were conducted at room temperature and under dark conditions.

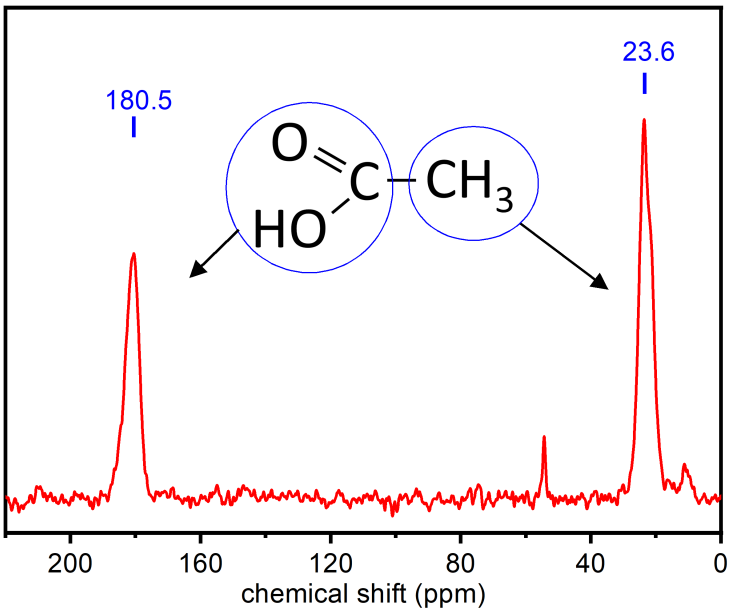

Figure 4.3: *^{1}H–^{13}C NMR CPMAS performed in the as-grown sample. The results allow the identification of methyl and carboxylate groups in the NP's*

The as-grown sample presented two principal peaks in the CPMAS analysis. First, a peak is observed at 23.6 ppm, corresponding to a methyl group. The second peak is observed at 180.5 ppm and is associate to a carboxylate group of an acetate molecule [41]. The global signature is that of an ethanoic acid (acetic acid) molecule (CH_3COOH).

[1] Alkanes are organic compounds that consist entirely of single-bonded carbon and hydrogen atoms.

These organic groups are most likely originating from the Zn-$(acetate)_2$ precursor used in the synthesis process, which is involved in the passivation of the ZnO polar surface during growth. The details about the passivation mechanism are discussed in Chapter 6.

4.2.2 Morphological characterization

The influence of the surface on the NPs properties becomes increasingly significant as the NP size decreases. The detection of organic groups on the surface is only efficient in systems with reduced sizes, specifically at the nanometric scale. No similar behavior is identified in bulk ZnO. In this way, the characterization of the NP's size, distribution, and structure is of fundamental importance.

Electronic Microscopy and X-Ray diffraction characterization

The NPs are presented in powder form, and an initial analysis is conducted to observe the homogeneity of the ensemble. As depicted in Figure 4.4, the images obtained through Scanning Electron Microscopy (a and b) and Transmission Electron Microscopy (c and d) reveal the distribution of NPs for both the as-grown and annealed samples. In both cases, the NPs exhibit an almost spherical shape with hexagonal facets.

In the case of the as-grown samples, the NPs showcase an average diameter of 15 nm. However, in the annealed samples, there is a substantial increase in size, with the NPs displaying an average diameter of 50 nm. These observations align with previous studies that have established a correlation between NP size and annealing temperature [126].

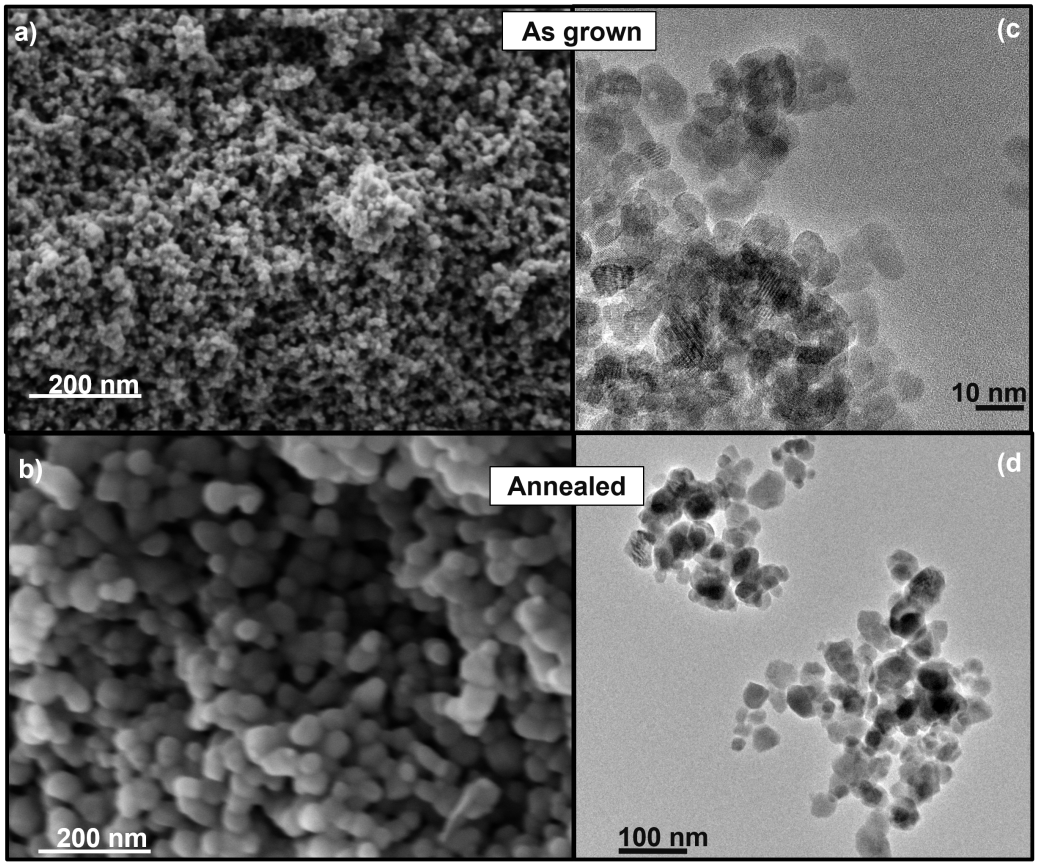

Figure 4.4: *ZnO NPs observed by SEM (a and b) and TEM (c and d) techniques. The NP's present average diameter of 15 nm before annealing and 50 nm after annealing.*

As expected, the crystal structure remains unaltered as the particle size increases, with both the as-grown and annealed samples exhibiting a hexagonal wurtzite structure. The crystalline planes can be observed by Fourier transform of TEM images (Figure 4.5).

The X-ray diffraction (XRD) technique supports the TEM results, and the identification of the crystalline planes is presented in Figure 4.5.

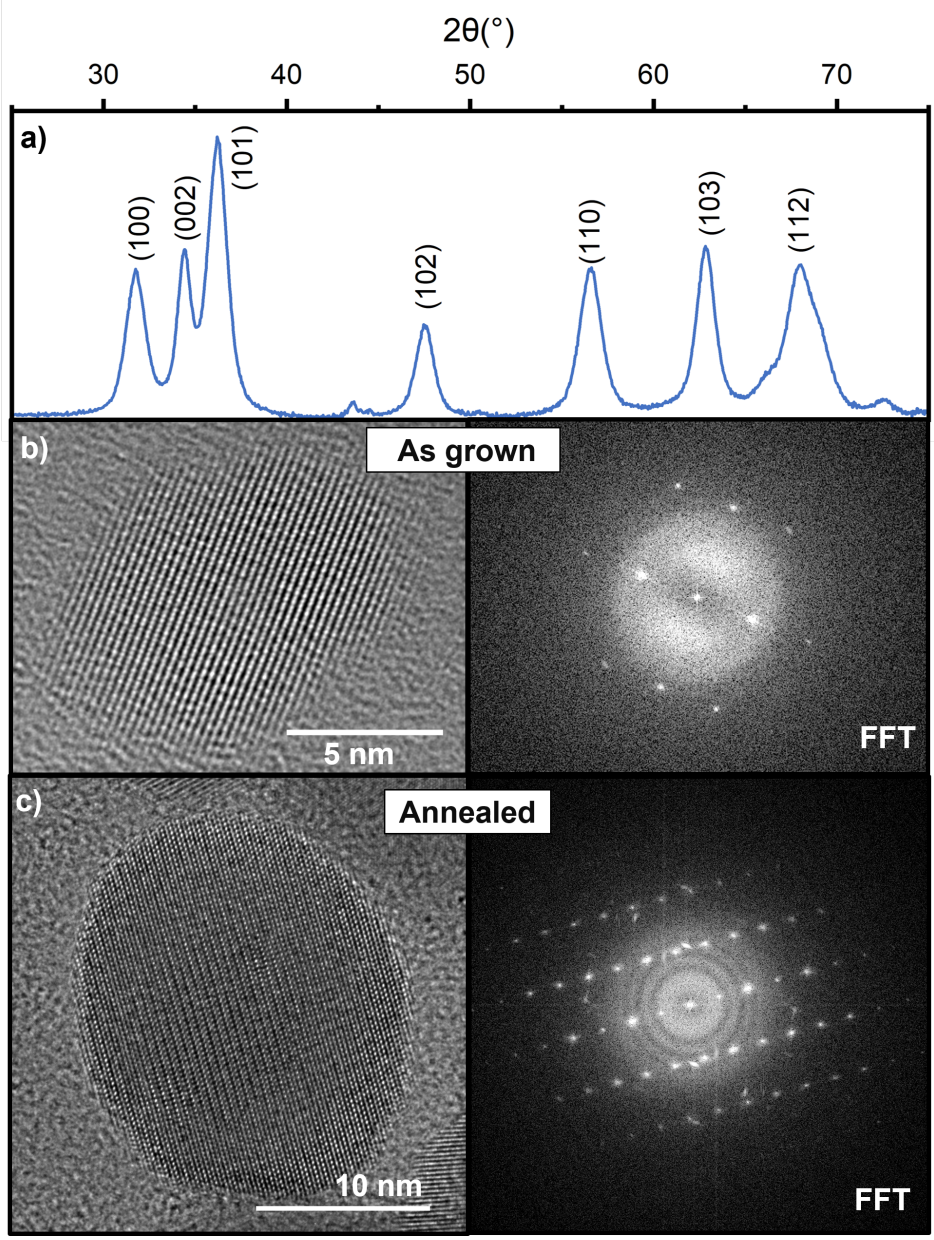

Figure 4.5: *(a) XRD spectroscopy for the as-grown samples, showcasing the identification of the planes of the wurtzite structure. (b) TEM microscopy image and the corresponding Fourier transform (on the right) for the as-grown sample. (c) Similar to (b), but representing the annealed sample.*

4.3 EPR Study

Performing EPR spectroscopy on the as-grown sample, no signal is observed under dark conditions, as shown in Figure 4.6 (a). However, when the 405 nm wavelength laser excite

the system, the appearance of different paramagnetic systems is observed, as showed in figure (b). The more prominent lines are those related to the core-defect ($g = 1.96$) and those related to methyl radicals (4-lines centered at $g = 2.005$).

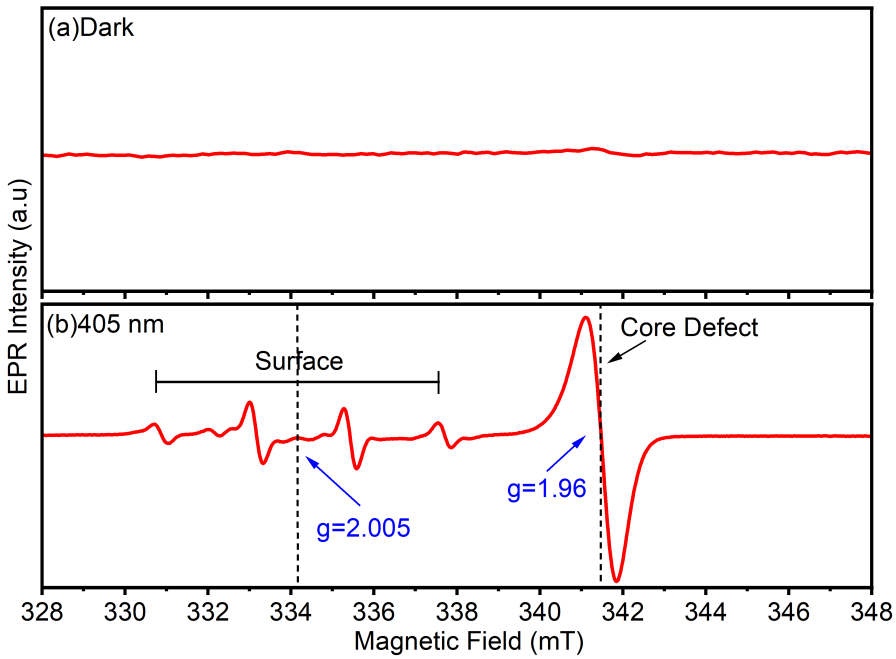

Figure 4.6: *EPR spectra of the as-grown sample in (a) dark condition and (b) illumination with 405 nm laser. The spectra were recorded with MW power attenuation of 15dB, modulation of 0.1 mT and T=36K.*

4.3.1 Core- and surface-defect

In the as-grown samples, the core-defect is exclusively observed under optical excitation. This distinctive signal is produced using a 3.06 eV excitation source, corresponding to a 405 nm violet laser. This signal is assigned to a defect present in the core of the NP, following the core-shell model. Furthermore, studies show that the intensity of this signal decreases with decreasing NP size [23].

The origin the core-defect remains a topic of debate in the scientific literature. Some authors attribute it to negatively charged zinc vacancies (V^{-}_{Zn})[127; 128; 129], while others link it to oxygen vacancies (V_o) [130]. Regardless of the specific entity responsible for the generation of the signal at $g = 1.96$, it is evident that it arises from a defect within the crystal [127]. The analyses of the signal response to different wavelengths shows that the maximum of intensity for the core-defect is achieved with light whose wavelength is between 400 and 420 nm [131].

After annealing, the core-defect is present under dark conditions. This phenomenon has also been observed in NPs synthesized through high-temperature methods [128]. In chapter 6, this property will be discussed, associating the presence of the core-defect with a surface passivation mechanism.

The annealing procedure vanish the lines associated with the methyl radicals, indicating the elimination of the organic compounds from the surface. However, after annealing,

a new line appears, centered at g=2.003. This signal emerges from a surface-defect caused in the nanoparticle by the heating procedure.

The identification of the core and surface-defect is in agreement with the core-shell model, where the surface/volume ratio has an impact in the sort of defects incorporated in ZnO [129]. The application of the core-shell model is only effective when applied to NPs with size inferior to 500 nm.

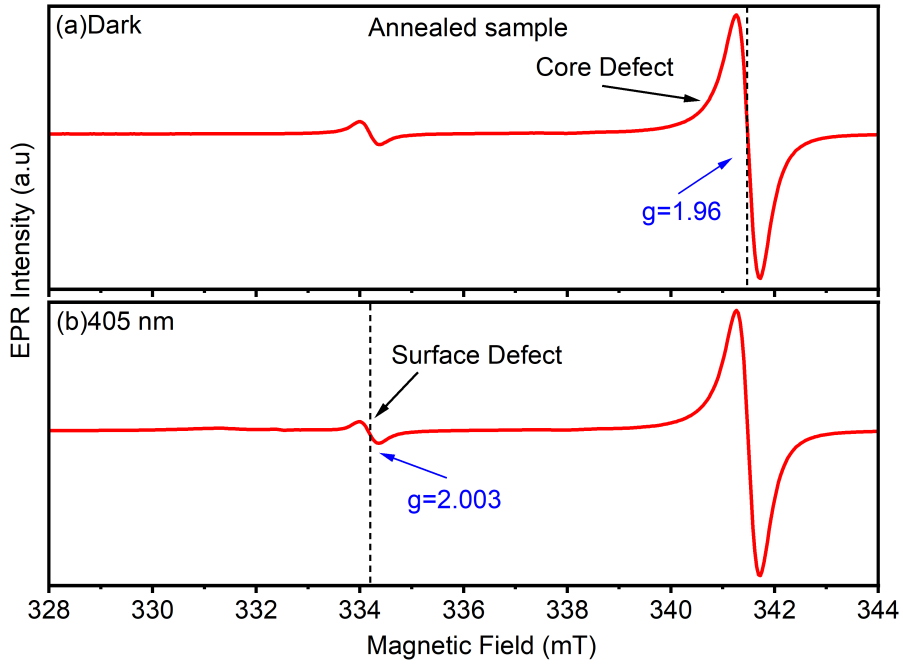

Figure 4.7: *The EPR spectra of the annealed sample are depicted under (a) dark conditions and (b) illumination with the 405nm laser. Following the annealing process, the methyl radicals have completely disappeared. The core and surface-defect are present in dark conditions and no longer exhibit photosensitivity. Consequently, the EPR spectra remain identical in both the presence and absence of light. The spectra were recorded with MW power attenuation of 15dB, modulation of 0.1 mT and T=35K.*

In the annealed sample, the "elephant" signal was observed under illumination, but its intensity is very small compared to the other signals. However, this observation indicates that the "elephant" signal is not related to the organic compounds situated in the NPs surface. It is expected to be originated from a more stable element, potentially a kind of defect in the ZnO crystalline lattice.

Saturation analysis

As discussed in section 2.6, achieving clear EPR results necessitates operating within a non-saturated regime of the system. To determine the optimal conditions for quantitative EPR measurements, a preliminary study was conducted by recording EPR spectra at different temperatures. For each temperature, different MW power attenuation were used. The relationship between attenuation (A_t) in dB and the microwave power (P) is determined by the equation:

$$A_t = 10\ log\ (P_0/P) \tag{4.1}$$

The parameter P denotes the maximum MW power achieved in the spectrometer, corresponding to 200 mW in our system. The response of the core-defect with increasing MW power at different temperatures is illustrated in Figure 4.8.

The function used for the fit is

$$I(p) = \frac{A * p}{1 + sp^2} \tag{4.2}$$

where $p = \sqrt{P}$

In this scenario, the parameter A denotes the non-saturated EPR intensity. In the X-band, where Curie's law holds true for a constant number of spins ($h\nu << kT$), the magnetic susceptibility varies inversely with the temperature for paramagnetic materials [132], i.e.,

$$\chi = \frac{C}{T} \tag{4.3}$$

where C is the Curie constant for the material. Following this approach, the parameter A is expected to be proportional to 1/T. The curves presented in Figure 4.8 are normalized by the A parameter.

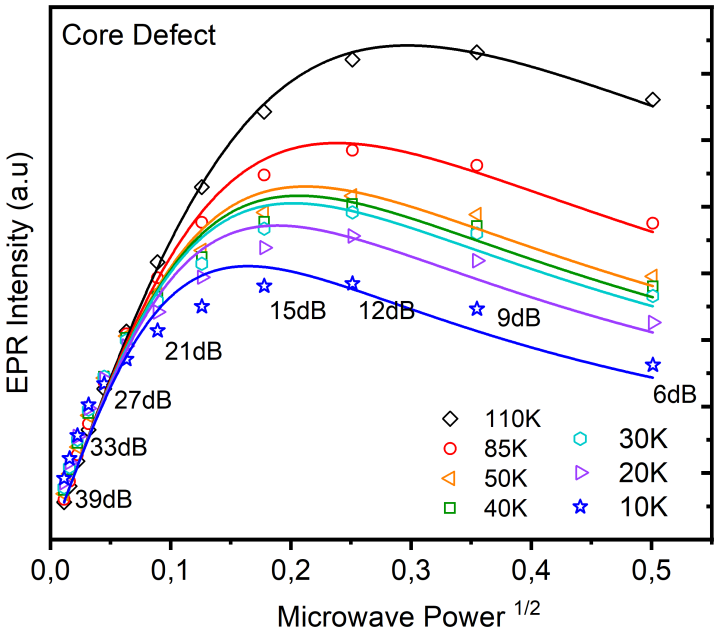

Figure 4.8: *Saturation curves for the core-defect at various temperatures, normalized by the A parameter.*

The parameter s, on the other hand, is directly related to the product of T_1 with T_2 ($s \propto T_1 \cdot T_2$) and is associated with the saturation effects within the system. A higher value of s indicates increased saturation effects. Since T_2 corresponds to the spin-spin interaction and is not expected to be highly influenced by temperature, measuring the s parameter indirectly provides insights into the behavior of the relaxation time T_1, associated with the spin-lattice interaction. The behavior of the A and s parameters with increasing temperature is depicted in Figure 4.9. In (a), the behavior of 1/A is presented, in such a way that the Curie law is manifested by an increasing straight line.

At higher temperatures, the linear regime (non-saturated) can be sustained at attenuation values higher than 18 dB. However, when decreasing the temperature, saturation effects become noticeable even at attenuation higher than 30 dB. This behavior is indicated by the deviation of the experimental points from the fit. In qualitative analyses, when the signal is considerably weak, operating at 15 dB can be advantageous. At this point, saturation begins to affect the system, but the EPR intensity reaches its maximum, providing a better signal-to-noise ratio. It's worth noting that the s parameter approaches zero as temperature increases, indicating that the temperature has the effect of impeding the saturation of the system. On the other hand, s tends toward higher values as the temperature approaches zero.

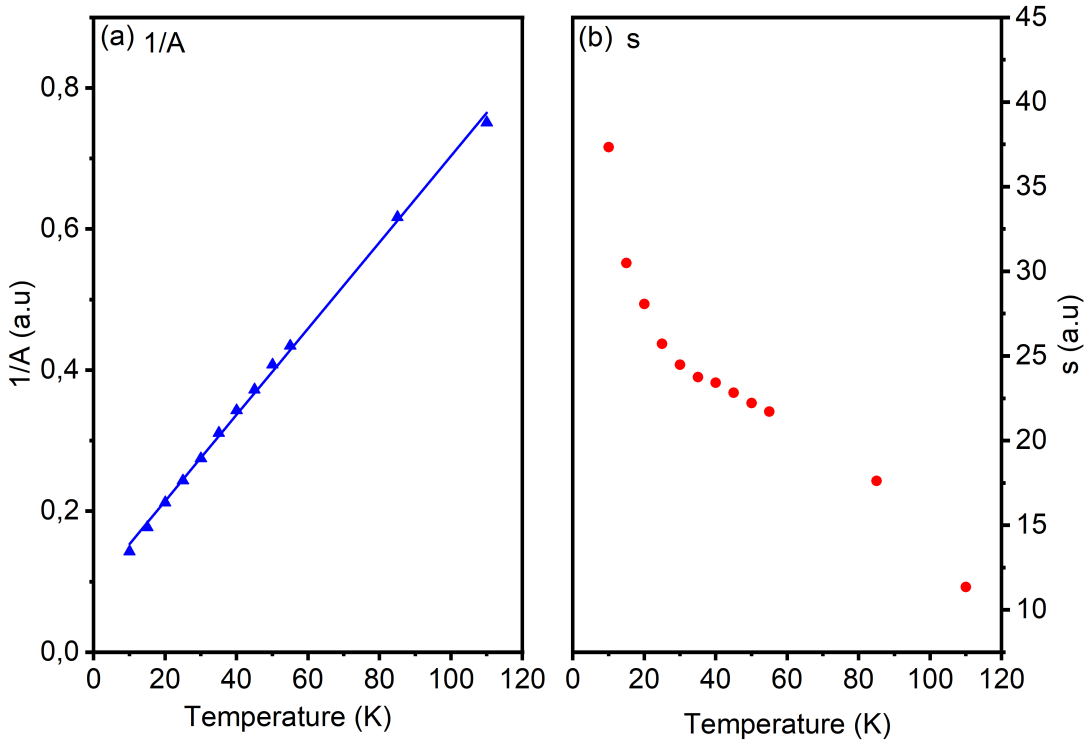

Figure 4.9: *Behavior of the parameters 1/A (a) and s (b) with increasing temperature. While A is associated to the EPR Intensity, thus expected to follow the Curie's law for paramagnetic materials, s is the coefficient that indicates the saturation of the system, where a higher value implies a greater susceptibility to saturation artifacts.*

4.3.2 Spin value

Applying the Rabi sequence at the core-defect line, it is observable the transition between the two resonant levels over time, which indicates the possibility to perform coherent spin manipulations. The used microwave attenuation that provided best results was 3 dB, providing the oscillations depicted in Figure 4.10.

The frequency of the Rabi oscillation depends on the applied oscillatory field B_1 and the spin value of the center, as described in section 2.12:

$$f = K\sqrt{P}\frac{g\mu_B}{h}\sqrt{S(S+1) - m_s(m_s \pm 1)} \tag{4.4}$$

The MW field B_1 at the center of the cavity (where the electric field is null) is associated

with the EPR power through the relation

$$B_1 = K\sqrt{P} \tag{4.5}$$

For a spin 1/2, the term inside the square root is equal to 1, leading to:

$$f = K\sqrt{P}\frac{g\mu_B}{h} \tag{4.6}$$

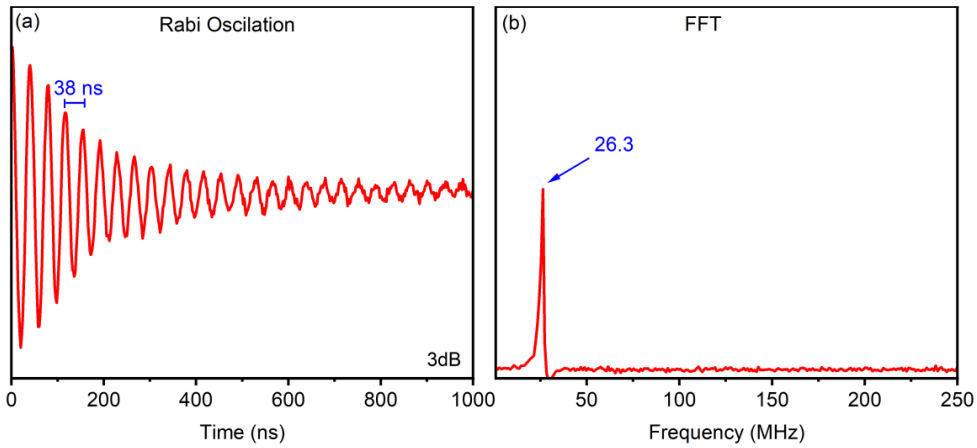

Figure 4.10: *Rabi oscillations measured over the core-defect. In (a) the temporal spectrum is presented, in (b) the Fourier Transform of (a). A single frequency of 26.3MHz is observed. The used MW attenuation was 3dB. T=25K.*

The Fourier transform of the Rabi oscilations indicates the oscillation frequency (Figure 4.10) of the core-defect. With the power attenuation set at 3dB, the identified frequency is 26.3MHz. Rabi oscillations were also conducted on other lines (linked to methyl radicals and the 3-lines system) within the same spectrometer. Interestingly, the same oscillation frequency was observed for all these lines, indicating that all systems possess the same electronic spin which, by comparison to a reference sample, is concluded to be a spin of value 1/2.

Then, measuring the Rabi oscillation, we have access to the K factor, which relates the MW power and the effective B_1 field at the sample location. This factor depends on many experimental parameters (filling factor, ...) and is otherwise almost impossible to be calculated or measured.

4.4 Methyl radicals (4-lines system)

The second signal to be analyzed consists of four lines centered at g=2.005. These lines are separated by a distance of 2.2 mT and have an intensity ratio of approximately 1:3:3:1. They are labeled, from left to right, as L_1, L_2, L_3, and L_4. This line distribution suggests a hyperfine coupling of electronic spin 1/2 with three nuclei possessing a nuclear spin 1/2, as highlighted in Figure 2.5.

Interesting, neither zinc[2] nor oxygen[3] possesses a nuclear spin 1/2, indicating that this interaction cannot arise from the interaction with atoms that form the lattice. However,

[2]Zinc possesses five stable isotopes. Four of them have a nuclear spin 0, and one has a nuclear spin 5/2.

[3]Oxygen possesses three stable isotopes. Two of them have a nuclear spin 0, and one has a nuclear spin 5/2.

the presence of organic acetates identified by FTIR and NMR suggests a possible surface state originating from these organic materials.

In this context, the EPR spectrum combined with the FTIR and NMR results, indicates that we are measuring signals from elements formed on the NP surface due to a catalytic reaction initiated by the core excitation. We suggest that this photocatalytic process relies on an initial photoinduced charge separation (resulting in the observed core-defect).

Following the charge separation process, the hole h^+ (created by capturing an electron from the valence band through the core-defect), moves towards the surface and interacts with adsorbed molecules. This type of reaction, characterized by an increase in catalytic activity among molecules adsorbed on surfaces due to the reduction in energy required to activate chemical reactions facilitated by the solid surface, has been previously documented [133; 134] occurring in oxide surfaces.

In this context, the molecule that corresponds to the organic groups identified by NMR and FTIR and that possess the hyperfine interaction observed in EPR, is that of methyl radical. The dissociation of methyl radicals via a hole is recognized as the photo-Kolbe reaction. The comprehensive details of this reaction, encompassing all its steps, are presented in Chapter 6. The energy level associated to methyl radical transitions are illustrated in Figure 4.11, together with the observed EPR spectrum.

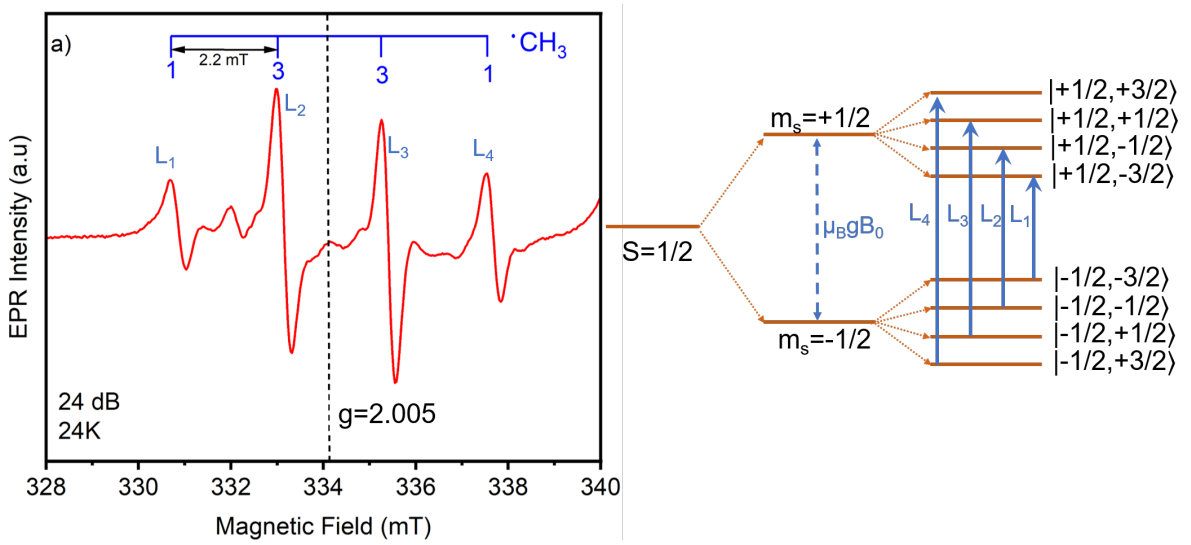

Figure 4.11: *Methyl radical trapped in the ZnO surface: (a) displays the experimental results of photo-irradiated ZnO nanoparticles (as-grown sample), while (b) illustrates the corresponding transitions of methyl radical indicated in an energy diagram.*

4.4.1 Deuteration

To provide conclusive evidence that the paramagnetic signal characterized by the 4- lines group arises from methyl radicals formed on the surface, a surface functionalization process was undertaken. Further details of this procedure are given in section 3.1.1. The key aspect of this process is to replace, at least partially, the adsorbed acetates (nuclear spin 1/2) with their deuterated counterparts (nuclear spin 1), i.e.

$$(CH_3COO)_2\text{-}Zn \rightarrow (CD_3COO)_2\text{-}Na \tag{4.7}$$

Consequently, after illumination, the resulting methyl radicals should contain a certain number of deuterium atoms, which can be discerned using EPR. The change in nuclear spin is expected to produce variations in the hyperfine structure, and the 4-line pattern should be replaced by a 7-line pattern with relative intensity ratios 1:3:6:7:6:3:1, as illustrated by the energy level diagram presented Figure 4.12. The experimental results indicate a successful substitution of hydrogen by deuterium, forming a deuterated radical when the NPs are submitted to photo-excitation.

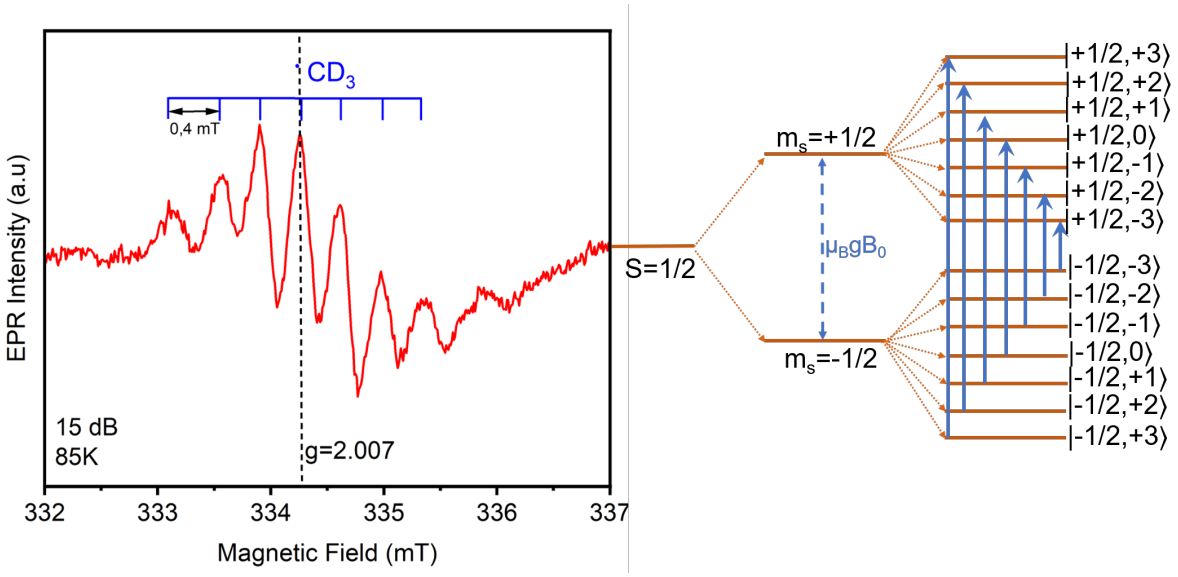

Figure 4.12: *$^{\bullet}CD_3$ trapped in the ZnO surface: (a) displays the experimental results of photo-irradiated ZnO nanoparticles (deuterated sample). Experimental conditions: A_t=15dB, modulation = 0.06mT, T=85K. (b) illustrates the corresponding transitions in an energy diagram.*

Simulations carried out using the EasySpin [135] software validate these findings. Figure 4.13 illustrates the simulations for $^{\bullet}CH_3$ and $^{\bullet}CD_3$, providing a comparison with the experimental measurements.

In Figure 4.13, we present a comparison between samples, showing the effect of the deuteration in the EPR spectrum. Under dark conditions (black lines), neither the as-grown (in (a) and (b)) either the deuterated (in (c) and (d)) samples present paramagnetic behavior. With optical excitation, the core-defect appears for both samples, unchanged by deuteration. In the deuterated samples, the four lines associated with the hyperfine structure of methyl radicals are replaced by seven lines corresponding to deuterated radicals. Simulations performed for both scenarios are presented in blue, confirming the successful replacement.

In the deuterated sample, an additional line is identified at $g = 1.984$. In the as-grown sample, it is possible to observe a disturbance in the line L_4, probably associated to the superposition with this signal. The g-value of this signal is exactly the middle between the core-defect and the $^{\bullet}CH_3$ or $^{\bullet}CD_3$ gravity center, so that the line can be attributed to some coupling between these two kinds of centers. This intermediate line has also been observed in Ref. [136] and in our analysis in Q-band EPR (see Section 4.13).

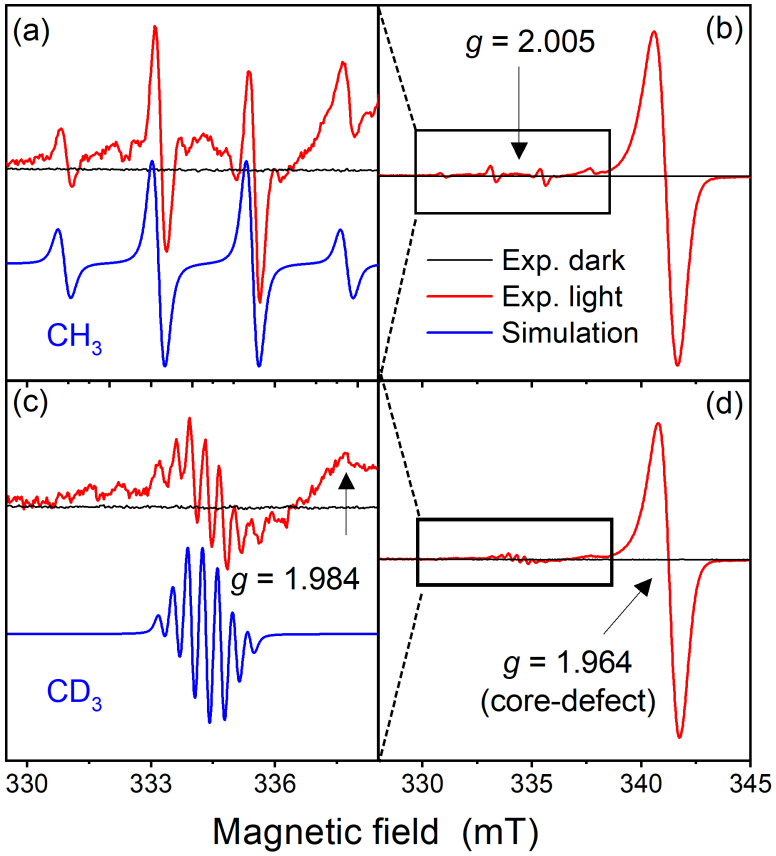

Figure 4.13: *EPR spectra of ZnO nanoparticles at 85 K under dark (black) and 405 nm illumination (red) conditions. In (a) and (b), the spectrum of the as-grown sample is presented. The red lines represent the experimental results, while the blue lines correspond to simulations performed in EasySpin for methyl radicals ($^{\bullet}CH_3$). In (c) and (d), the same procedure is applied to the deuterated sample and the simulation for ($^{\bullet}CD_3$) is presented in blue. The left panels display a magnified view of the surface signal for each case. The experimental data were acquired at temperature T=85K. Figure from ref [41]*

The ^{1}H-^{13}C cross-polarization solid-state NMR spectroscopy (CPMAS) was also realized in the deuterated samples and the comparison with the as-grown sample are depicted in Figure 4.14. While for the carboxylate group no significant changes are observed, for the methyl group, an important decrease in the intensity peak is identified for the deuterated sample. This result corroborates the hypothesis that the observed methyl radicals observed under photo-excitation arise from the dissociation of acetic acid molecules aggregated to the NPs surface.

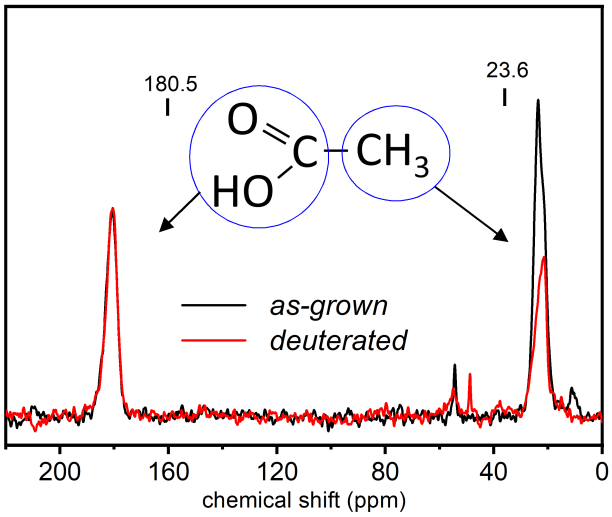

Figure 4.14: *Comparison of the ^{1}H-^{13}C cross-polarization solid-state NMR spectroscopy (CPMAS) results for the as-grown and deuterated samples.*

4.4.2 Analytical Approach

Considering the methyl radical $^{\bullet}CH_3$, characterized by one unpaired electron interacting with three nuclei of spin 1/2, the following Hamiltonian describes the interactions of the unpaired electron:

$$H = g\mu_B(\vec{S}\cdot\vec{B_0}) + \vec{S}\cdot(\tilde{A_1}\cdot\vec{I_1} + \tilde{A_2}\cdot\vec{I_2} + \tilde{A_3}\cdot\vec{I_3}) \tag{4.8}$$

With the first contribution being associated to the Zeeman effect and the others representing the hyperfine interaction with each nucleus. Assuming that the hyperfine tensor is isotropic and identical for the three nuclei, $\tilde{A_1} = \tilde{A_2} = \tilde{A_3} = \tilde{A}$ [137], and rewriting the Hamiltonian in terms of the "raising" and "lowering" operators (see Annex C) we obtain:

$$H = g\mu_B B_0 S_z + \frac{A}{2}S^+(I_1^- + I_2^- + I_3^-) + \frac{A}{2}S^-(I_1^+ + I_2^+ + I_3^+) + AS_z(I_1^z + I_2^z + I_3^z) \tag{4.9}$$

The electronic spin quantum number m_s can assume the values $+1/2$ and $-1/2$, while the nuclear one accounts the interaction of the three nuclei ($m_I = \pm 1/2, \pm 3/2$). Each combination of electronic and nuclear spin represents a possible state for the system. It creates a 16-dimensional space:

m_s	m_{I1}	m_{I2}	m_{I3}	m_I	state
+	+	+	+	+3/2	$\|1\rangle$
+	+	+	-	+1/2	$\|2\rangle$
+	+	-	+	+1/2	$\|3\rangle$
+	-	+	+	+1/2	$\|4\rangle$
+	+	-	-	−1/2	$\|5\rangle$
+	-	+	-	−1/2	$\|6\rangle$
+	-	-	+	−1/2	$\|7\rangle$
+	-	-	-	−3/2	$\|8\rangle$
-	+	+	+	+3/2	$\|9\rangle$
-	+	+	-	+1/2	$\|10\rangle$
-	+	-	+	+1/2	$\|11\rangle$
-	-	+	+	+1/2	$\|12\rangle$
-	+	-	-	−1/2	$\|13\rangle$
-	-	+	-	−1/2	$\|14\rangle$
-	-	-	+	−1/2	$\|15\rangle$
-	-	-	-	−3/2	$\|16\rangle$

The energy associated to each of these states is found by diagonalizing the correspondent 16x16 matrix composed by the Hamiltonian applied in these states. The terms outside the diagonal are disregarded, once that these terms can be considered as perturbations. The matrix terms are composed of

$$\begin{aligned}
\langle i|\, H\, |i\rangle &= \frac{3A}{4} + \frac{1}{2}\mu_B g B_0 \qquad \text{for i=1,16} \\
\langle i|\, H\, |i\rangle &= \frac{A}{4} + \frac{1}{2}\mu_B g B_0 \qquad \text{for i=2,3,4} \\
\langle i|\, H\, |i\rangle &= \frac{-A}{4} + \frac{1}{2}\mu_B g B_0 \qquad \text{for i=5,6,7} \\
\langle i|\, H\, |i\rangle &= \frac{-3A}{4} + \frac{1}{2}\mu_B g B_0 \qquad \text{for i=7,8} \\
\langle i|\, H\, |i\rangle &= \frac{-A}{4} - \frac{1}{2}\mu_B g B_0 \qquad \text{for i=10,11} \\
\langle i|\, H\, |i\rangle &= \frac{A}{4} - \frac{1}{2}\mu_B g B_0 \qquad \text{for i=12,13,14}
\end{aligned} \tag{4.10}$$

The EPR transitions occur by given energy for changing the electronic spin projection following the selection rules ($\Delta m_s = \pm 1$ and $\Delta m_I = 0$). This condition implies that each of the lower spin projection $m_s = -1/2$ is connected to one of the upper states, as showed in Figure 4.11.

The projections $m_I = \pm 1/2$ are 3-times degenerated, originating a theoretical ratio 1:3:3:1. for the EPR transitions intensities. The energy necessary to promote these transitions can be calculated. Considering the energy supplied by the MW photon, $E = h\nu$, matching the energy difference between two levels with the same nuclear projection, the resonant field (B_{Ri}) for each transition is explicit:

$$
\begin{aligned}
B_{R1} &= \frac{1}{\mu_B g}(\Delta E - \frac{3A}{4}) \\
B_{R2} &= \frac{1}{\mu_B g}(\Delta E - \frac{A}{2}) \\
B_{R3} &= \frac{1}{\mu_B g}(\Delta E + \frac{A}{2}) \\
B_{R4} &= \frac{1}{\mu_B g}(\Delta E + \frac{3A}{2})
\end{aligned}
\tag{4.11}
$$

With $\Delta E = g\mu_B B_0$. The difference of the resonant fields for adjacent transitions is directly related to the hyperfine coupling:

$$
\Delta B_R = \frac{A}{\mu_B g} \tag{4.12}
$$

The experimental findings, including the depicted energy levels representing the transitions linked to methyl radicals (Figure 4.11), align with the experimental observations. Previous studies have documented a 1:3:3:1 ratio among the methyl lines and a field separation of 2.2 mT [138], supporting the proposed model.

4.4.3 Identification of the electronic spins

Rabi Oscillations

The sequence for generating Rabi oscillations was executed on both the as-grown and deuterated samples, as described in section 2.12. In this investigation, the Rabi oscillations were recorded in 2D, simultaneously varying the magnetic field and time. Employing this method allowed for the extraction of Rabi oscillations for all the lines simultaneously, enabling the identification of any variation in electronic spin through changes in the oscillation frequency.

Figure 4.15 show the Rabi oscillations and its respective Fourier Transform for all the range of magnetic field where the transitions are observed. Due to the high relaxation presented by the core-defect (smaller echo), the Rabi oscillations were conducted in two different power attenuation. In the higher attenuation (15 dB), the core-defect does not present observable oscillations. By lowering the attenuation to 3 dB, the core-defect oscillations are observed.

All the oscillations correspond to electronic spins 1/2, as can be seen by the perfect match of frequencies among different systems. Using lower MW power (higher attenuation), the oscillations are slower (period $\approx$ 200 ns) while for higher MW power the oscillations are faster ($\approx$ 50 ns).

The recorded Rabi frequencies are as follows: 7.1 MHz for the four lines of $^{\bullet}CH_3$ (measured with A_t = 15 dB), 25.7 MHz for $^{\bullet}CD_3$ (measured with attenuation = 3 dB), and 25.2 MHz for the core-defect of the deuterated sample (also measured with attenuation = 3 dB). These results are in agreement to those measured in the as-grown samples 4.10 for the same attenuation. When normalized by MW power, the frequencies become 39.9 MHz, 35.6 MHz, and 36.3 MHz, respectively.

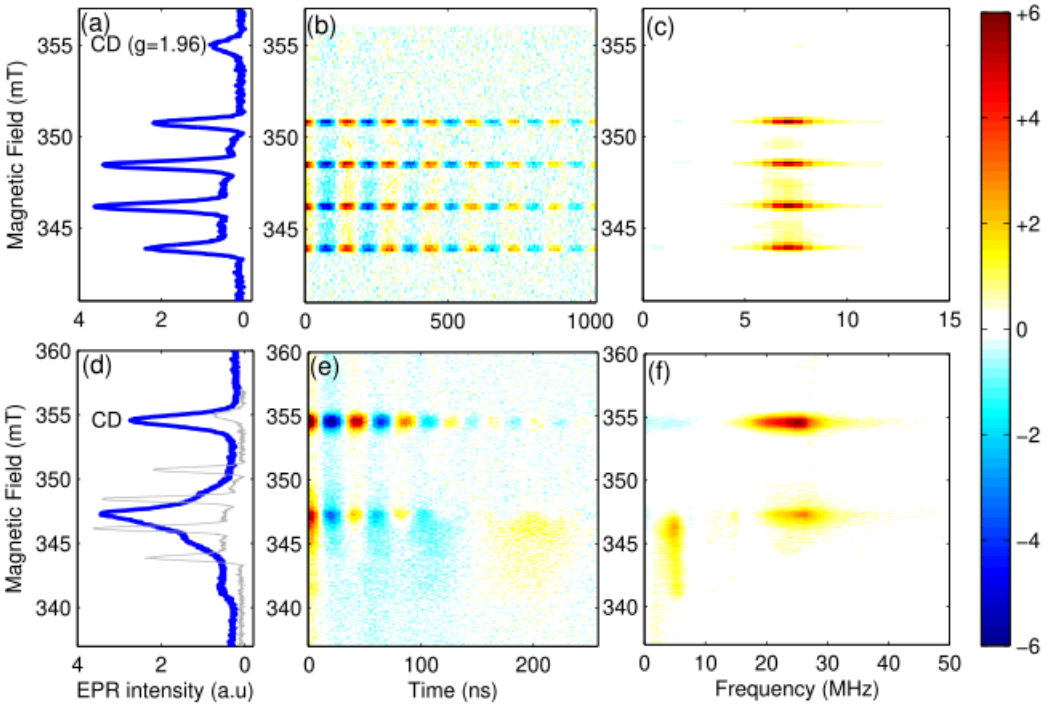

Figure 4.15: *Rabi oscillations measured in as-grown (upper panels) and deuterated (lower panels) samples. In (a) the field sweep for the as-grown sample, in (b) the Rabi oscillations and in c the frequency oscillation for $^{\bullet}CH_3$= 7MHz. The attenuation used was 15dB. In (d) the field sweep for deuterated sample, in (e) its respective Rabi oscillations and (f) the frequency for $^{\bullet}CD_3$= 26MHz. The attenuation used was 3dB. With lower attenuation, the core-defect frequency is also recognized at 26 MHz, in agreement with previous results. Figure extracted from ref [41].*

From these results, it can be deduced that all these transitions arise from 1/2 spins, with a slightly different experimental constant between the two samples. This variation is expected, as the experiment is known to depend on factors such as the sample filling factor and coupling parameters between the sample and the cavity.

4.4.4 Saturation phenomena

In order to characterize the response of the system to different MW power in different temperatures, measurements were conducted specifically on L_2 (the second line of the methyl group). Its higher intensity facilitated a superior signal-to-noise ratio. The method used is identical to that applied for characterizing the core-defect (subsection 4.3.1).

The line L_2 may exhibit contributions from other systems, including the 3-lines system and the "elephant" signal. This overlap could result in a modification of the relaxation time. In this scenario, the measured parameters (A and s) represent an average comprising the behavior of each individual system [139]. This phenomenon can explain the observed significant discrepancy from the model, as observed in Figure 4.16, where the experimental points diverge from the fit. This characteristic is more prominent in low temperatures.

As for the core-defect, the function used for the fit is

$$I(p) = \frac{Ap}{(1 + sp^2)} \tag{4.13}$$

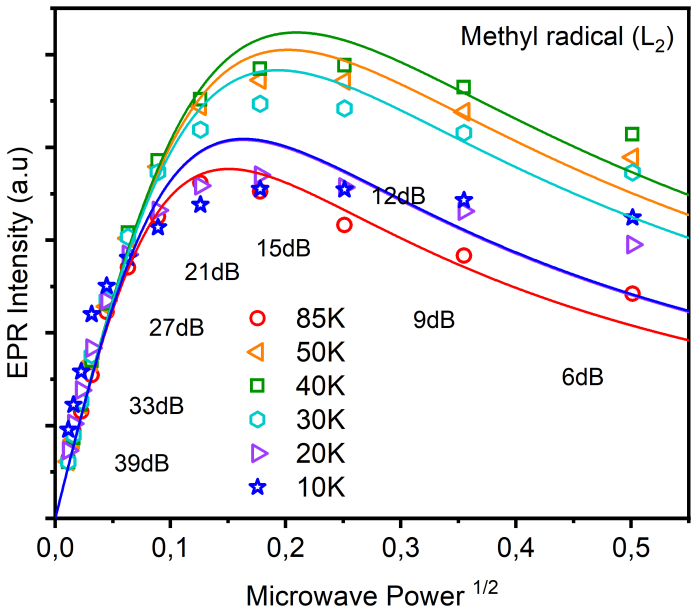

Figure 4.16: *Saturation curves for the L_2 line, belonging to methyl radical group. Several MW power attenuation and temperatures are considered. The fit is made through the function $I(p) = Ap/(1 + sp^2)$*

where $p = \sqrt{P/P_0}$

The behavior of the saturation factor s is plotted as a variable of temperature. As discussed in the subsection 4.3.1, the parameter s is proportional to the product of T_1 with T_2 (s $\propto T_1T_2$). The saturation curves exhibit distortions that are increased by lowering the temperature, and proper fit with the Bloch equation are only obtained at temperatures higher than 50K. When the discrepancy from the model is significant, the interpretation of the s parameter becomes less accurate. The behavior of the A and s parameters as the temperature increase are depicted in Figure 4.17.

For the methyl radicals, the unexpected rise in the s parameter as temperature decreases might be associated with the species disappearance at higher temperatures, caused by chemical reactions involving the methyl radicals. In Figure 4.17, the comparison of 1/A and the s parameter of the methyl radical and the core-defect is displayed. Observing the behavior of 1/A, the core-defect presents a typical behavior, following the Curies law, expressed by the linear behavior with increasing temperature. It suggests that T_2 does not exhibit significant variability with increasing temperature, indicating that the concentration of spins do not change with increasing temperature. Consequently, the product $T_1T_2 \propto s$ decreases because of the decline in T_1 due to faster spin-lattice relaxation at higher temperatures.

For the methyl radical, the presented behavior differs from the model for paramagnetic materials. It indicates a variation of the concentration of spins at this temperature range, causing a change in the relaxation time T_2. The variability of the T_2 parameter with

increasing temperature is explored in details by means with PW EPR, and the results are presented in section 4.10.

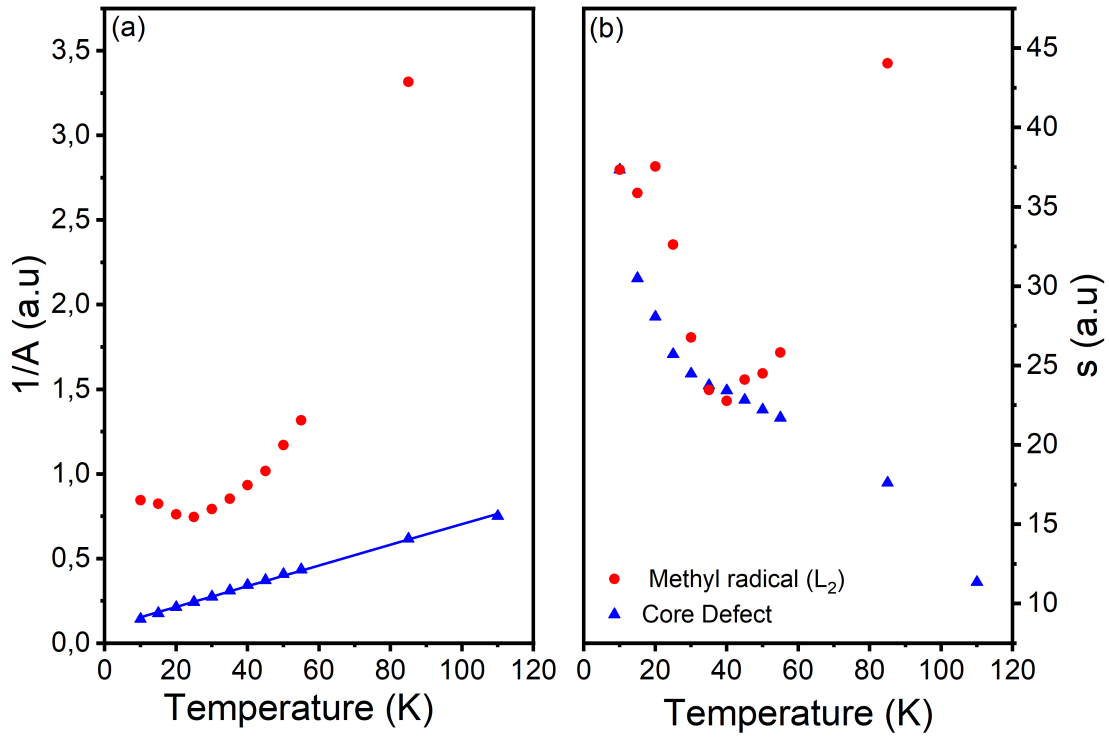

Figure 4.17: *Behavior of 1/A (a) and s (b) with increasing temperature for the core-defect (blue) and methyl radicals (red). While 1/A is associated to the EPR Intensity, thus expected to follow the Curie's law for paramagnetic materials, s is the coefficient that indicates the saturation of the system, where a higher value implies a greater susceptibility to saturation artifacts.*

Alternatively to the measurement of the parameter A, the EPR intensity's behavior was evaluated by considering the peak-to-peak intensity multiplied by the linewidth for each system. For the methyl radical, the measurements were taken considering the line L_2, due to its higher intensity. This method accounts for the linewidth broadening as the temperature decreases, a feature that was not accounted in the previous results and that could explain the discrepancy from the Curies law. To mitigate saturation effects, the data were acquired at 39dB attenuation, where the EPR transitions are not saturated (refer to Figures 4.16 and 4.8).

The experimental procedure began with illumination at 7K, using the 405nm laser. Subsequently, after allowing the sample to be fully optically excited, the laser was turned off. The measurements were then conducted while increasing the temperature up to 85K. The behavior of the inverse of the EPR intensity is depicted in Figure 4.18 to provide a clearer understanding of the system's adherence to the Curie model ($1/I \propto T$).

While the core-defect aligns closely with the model, the behavior of the methyl radicals demonstrates once again a substantial deviation. The crossed results indicates that this behavior is probably a consequence of changes in the T_2 relaxation time, directly associated to the concentration of spins. Interestingly, the behavior presented by the inverse of the EPR intensity for the methyl radicals is well described by an exponential function.

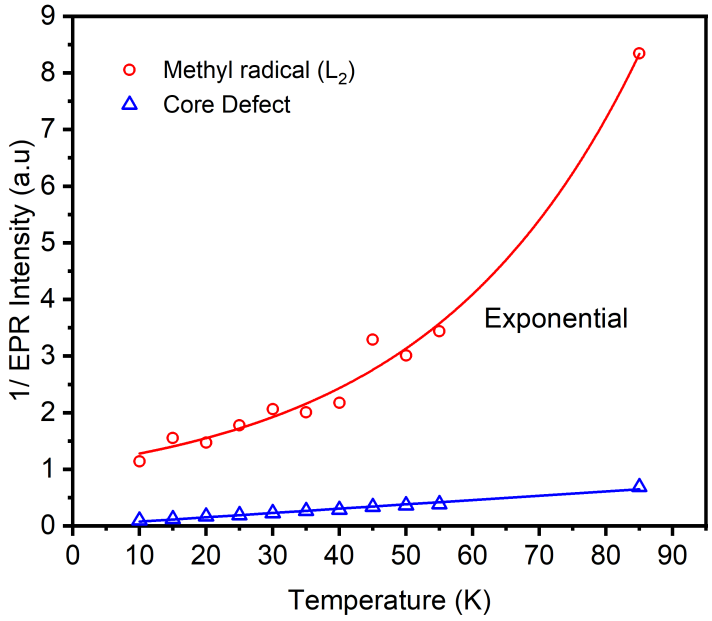

Figure 4.18: *The EPR intensity measured by peak-to-peak multiplied by the line width indicates that the core-defect adheres to the Curie model for paramagnetic materials. However, the methyl radicals exhibit a high discrepancy from this model, following an exponential behavior. This discrepancy is probably caused by chemical reactions that decrease the concentration of spins as the temperature increases.*

4.5 Chemical stability over time

An EPR study conducted over several months has been performed in order to characterize the chemical stability of ZnO NPs with time when the NPs are submitted to different gaseous environment. The analysis involved distinct samples of ZnO obtained from the same synthesis but exposed to varied atmospheric conditions. In the first tube, an inert gas (Argon) was introduced, and the tube was then sealed using a flame. The second tube followed a similar procedure, but the environment was filled with H_2 gas. In the third tube, the selected environment was air.

Subsequently, EPR spectra were recorded weekly and bi-weekly under identical conditions. The tubes were stored in a dark environment at room temperature between the measurements, and ultrasonic agitation was utilized before each measurement to reduce NP aggregation.

The measurements were conducted by placing the samples in the EPR cavity, cooling them to 85K, and illuminating them with a 405 nm laser with 30 mW power. To ensure an optimal exposure of the entire sample to the laser light, the tube was slowly rotated during illumination, until maximal EPR intensity was reached. The experimental parameters remained constant throughout the measurements, including the field modulation (0.1 mT) and attenuation (15dB). Investigations pertaining to methyl were specifically conducted on the L_2 line, chosen for its behavior similar to other lines but with notably higher EPR signal intensity. The behavior of the core-defect was measured and compared to that of the methyl radical. Continual monitoring ensured the consistent quality factor of the cavity,

that did not present significant discrepancies. The linewidths did not present discrepancy between experiments and for this, the EPR intensity was measured considering the peak-to-peak of the EPR signal.

The study began on day 0 after the synthesis and sealing of the tubes. During the first weeks, the signal of the methyl radical increased significantly, reaching levels 5-7 times higher than the starting point, normalized to one in each sample. This suggests that in the first few days, the nanoparticles undergo a stabilization process that is independent of the surrounding environment. This is evident as samples sealed in highly reactive gases (H_2), behave similarly to those in inert environments (Ar). Following this initial phase, the paramagnetic behavior approached a more stable phase, displaying less significant changes thereafter. The obtained results are depicted in Figure 4.19.

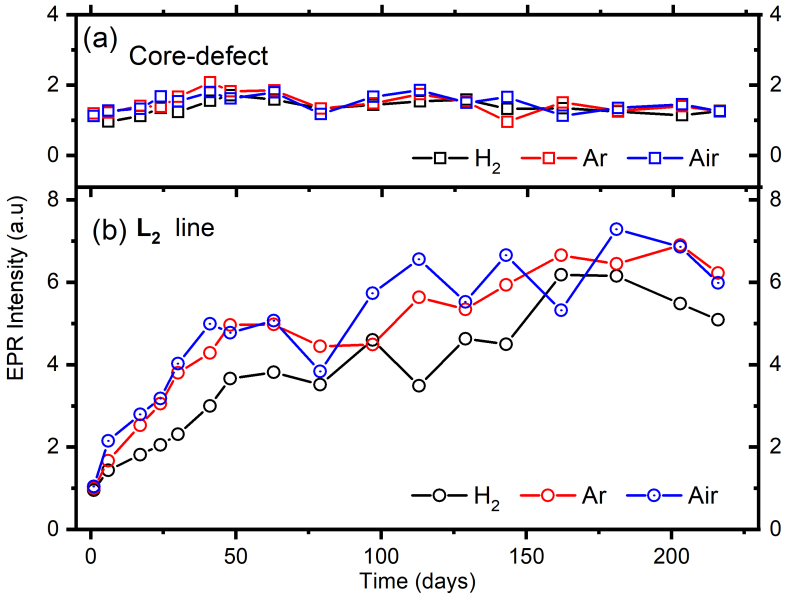

Figure 4.19: *Paramagnetic behavior of photo-excited ZnO nanoparticles over time. Panel (a) depicts the core-defect, while Panel (b) showcases the line L_2, representing the methyl group. Figure from ref [41].*

In Figure 4.19, the behavior of NPs submitted to different atmospheres is presented. It is observed that the surrounding atmosphere does not present important influence on the stabilization of the NPs.

It is interesting to observe that the methyl radical behavior differs from that of the core-defect, which is located in the bulk of the nanoparticles and maintains its magnetic behavior from day 0 onwards. The results present great variability, attributed to variations in the amount of illuminated defects between different experiments. However, the trends are meaningful. The key point is that after being illuminated several times, the NPs do not cease to produce the signal associated to the methyl radicals, as could be expected from a non-reversible reaction. On the contrary, the results show the increase of the photo-activation of these centers. This investigation demonstrates the reproducibility of methyl radical formation on the ZnO surface.

The production of methyl radicals is dependent on the ionization of the core-defect. A consistent increase in generated methyl radicals is observed as time progresses and the

nanoparticle stabilizes. This indicates that the photo-Kolbe reaction (better discussed in chapter 6) is more and more efficient, probably related to a progressive diminution of the hole-defect recombination mechanisms.

4.5.1 Changing the synthesis reagent and solvent

The dependence of the EPR observed signals on the synthesis precursors and/or solvents was investigated. For this purpose, two supplementary samples were synthesized. Each of them was synthesized by changing one of the chemicals used in the standard reaction (the standard reaction gives origin to the as-grown sample). The chemicals used for producing the new samples are:

1. Zinc acetate + NaOH + MeOH
2. Zinc acetate + KOH + EtOH
3. Zinc acetate + KOH + MeOH (Standard - used as a reference)

Sample (3) represents the standard synthesis and is presented as a reference.

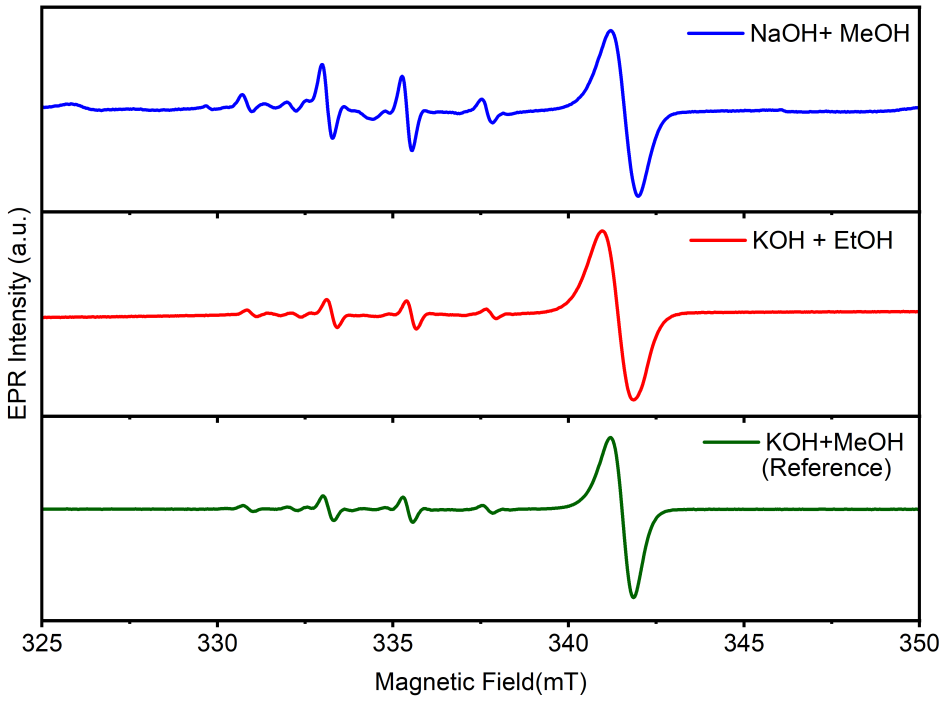

Figure 4.20: *EPR photo-activated signals in ZnO NPs samples produced with different reagents and solvents. The spectra were recorded at 85K.*

Figure 4.20 illustrates the signal pattern observed after illumination at 85K with a 405nm wavelength for the two supplementary samples. In the lower panel, the reference is also present. Sample (1), containing sodium hydroxide as precursor, presented an additional weak signal at dark conditions. This signal remained unchanged by photoexcitation. These additional lines have been observed before by other authors and were

associated to Mn^{2+} impurities that unintentionally doped the sample [140]. Interestingly, this signal does not impact the behavior of the photoexcited states.

For sample (2), altering the solvent from MeOH to EtOH did not induce any changes in the EPR reponse. This observation, combined with the CPMAS on deuterated samples, suggests that the methyl radical detected by EPR originates from the zinc acetate precursor and not from any product associated with MeOH or EtOH. It's important to note that the system consisting of three lines (L_5 to L_7) is identically present in both additional samples, but its observation is masked by the intense signal presented by the methyl radical.

In Chapter 1, it was discussed that ZnO is a polar ionic solid with a significant internal electrical field, leading to the generation of fictive charges on the NP surface. To neutralize these charges, acetates present in the solution may aggregate on the surface and remain connected even after the solution is dried. The stabilization provided by these acetates on the surface prevents the further growth of the nanoparticle. Studies conducted using Raman spectroscopy indicate that these acetates can exist in the form of free zinc acetates and potassium acetates [141]. A theoretical study performed by Hartree-Fock method indicates that the oxygen present in the carboxylic group is responsible to form bonds with the Zn surface atoms [142]. In this sense, the negatively charged oxygen, belonging to the carboxylic group, aggregates to the positively charged surface, composed by the Zn atoms. When the organic shell is removed through annealing, the system seeks an alternative stabilization method. In this scenario, the pre-existing defects within the crystalline lattice tend to become ionized, carrying charges to the surface and effectively facilitating electrical stabilization. This phenomenon is observed in Figure 4.7, where the core-defect became paramagnetic even in the absence of optical excitation. The complete model, accounting all these mechanisms, is discussed in chapter 6.

The subsequent phase of the analysis aims to assess information about the reproducibility of methyl radical formation. These radicals are recognized for their high reactivity, potentially leading to irreversible chemical reactions post-creation, rendering the nanoparticles EPR silent.

4.6 Relaxation from the optically excited state

After the system is optically excited, it is crucial to investigate the amount of time that the system remains in this excited state, i.e the lifetime that the methyl radical remains stable at the NP surface and the mechanisms responsible for the energy dissipation.

The applied optical excitation is responsible to change the system from its silent state (where the electrons are paired) to the paramagnetic state. This transition of states is provided by a photon with energy $E = h\nu \approx 3$ eV (laser 405 nm) :

$$\overrightarrow{S} = 0 \overset{h\nu}{\rightarrow} \vec{S} \neq 0 \tag{4.14}$$

It is assumed that a reverse phenomenon drives the system back to its ground state. To analyze the recovery of the initial state, the following procedure was employed:

In the as-grown sample, an initial EPR measurement was conducted under dark conditions at 85 K, revealing no observable EPR signal. Subsequently, the system was illuminated with 405 nm light (Figure 4.21 blue line). Photo-excited EPR signals were observed. The sample was then removed from the cavity and left to rest for 1 hour at room temperature in the absence of light to allow for relaxation. After the resting period,

the sample was returned to the cavity and measured under dark conditions at 85K (Figure 4.21 dark line). The EPR lines present under illumination were completely vanished and no EPR signal was observable. Subsequently, the system was illuminated again under identical conditions to the first optical excitation (red line). The signals obtained from the first and second illuminations (after the resting time) were then compared to evaluate any changes or irreversibility in the excited state. The results are presented in Figure 4.21, where a comparison between dark and light conditions is also depicted.

The results obtained with this approach suggest that following the 1-hour resting period at room temperature, the system fully returns to its initial state. First, note that the core-defect intensity is exactly the same after the first and second illumination. However, the methyl signal intensity demonstrates a degree of variability in the quantity of centers formed on the surface. This variability is also observed in the results presented in Figure 4.19.

The second aspect is to understand the decay of the signal over time once the photo-excitation is removed. At temperatures below 30 K, the system remained stable after optical excitation removal for over 24 hours. However, as the temperature surpassed 30K, the excited state became less stable, resulting in a gradual loss of intensity over time. To delve into this mechanism, the as-grown sample was subjected to in situ illumination at 85K using the 405 nm laser. Following this, the laser was switched off, and the initial measurement of the EPR intensity was recorded as the starting point. Subsequently, a new spectrum was obtained every 10 minutes during 8 hours, the results of this experiment are presented in Figure 4.22. It's worth noting that the laser power, whether 10 mW or 40 mW, did not influence the relaxation behavior, consistent with expectations. The laser power only influences the time that the system takes to reach a completely saturated excited state.

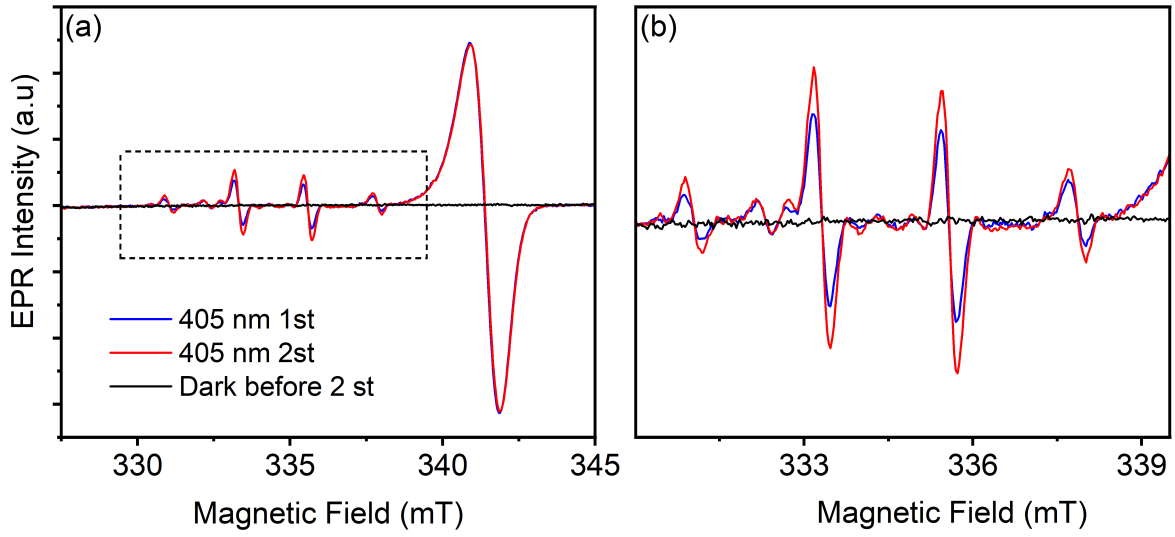

Figure 4.21: *EPR spectra recorded after first illumination (blue line). The system was then kept in dark conditions at room temperature for relaxation. Subsequently, a spectrum was recorded in dark conditions at 85 K (dark line). Finally, the sample was exposed to illumination under the same conditions as the initial photo-excitation (red line). Figure (b) focuses the methyl radical signal*

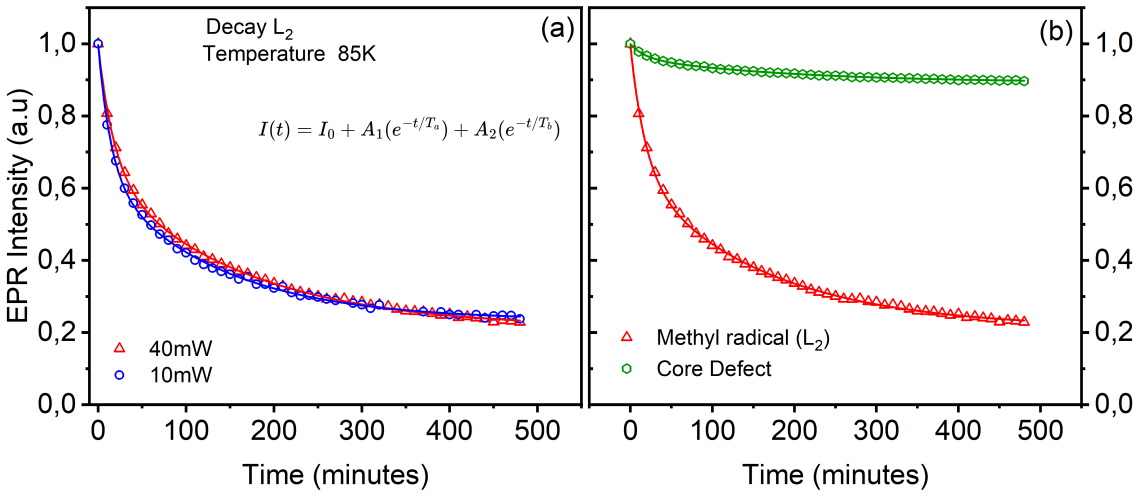

Figure 4.22: *Optical decay of the ZnO excited state. In (a), a comparison was made between two different excitation laser powers for the line L_2, belonging to the methyl radical group. In (b), the decay behavior of the methyl radical and the core-defect is compared.*

The decay behavior is accurately described by a biexponential model, featuring both short and long-term relaxation mechanisms. The parameters that fit the decay for the methyl radicals and the core-defect are presented in the table below:

-	I_0	A_1	T_a (min)	A_2	T_b (min)
L_2 (40mW)	0.21187	0.3485	18.20492	0.4341	159.4968
L_2 (10mW)	0.2333	0.36169	14.47428	0.40146	132.75074
core-defect L_2 (40mW)	0.89207	0.03847	17.73059	0.06895	194.05712

Table 4.1: *Values for the biexponential fit presented in Figure 4.22*

It is noteworthy that the core-defect exhibits a slower relaxation mechanism, suggesting that the decrease in intensity observed in the methyl radical is not attributed to the recombination of centers. Instead, it indicates a chemical reaction of the radicals that does not involve the core-defect. Interestingly, upon re-illumination of the system at this temperature, the EPR signal is not fully recovered. This implies that the disappeared methyl radicals did not revert to their acetate state, but rather transformed into an intermediate state that is EPR silent. Investigating radicals at this temperature poses challenges due to the potential occurrence of secondary reactions, such as methyl recombination [143].

The absence of signal recovery upon re-illumination when the system is partially heated, compared to full recovery when the sample is left at room temperature, suggests the presence of an intermediate EPR silent state. To better explore the properties of the system, two distinct regimes are studied:

1. **Reversible regime** : At temperatures below 30 K, the system demonstrates complete reversibility. Changes in temperature do not affect the system's stability. When the laser is turned off, the system doesn't suffer any losses.

2. **Irreversible regime**: Above 30 K, the methyl radicals enter an irreversible regime, transitioning to an intermediate silent state. Under these conditions, the initial state

can only be recovered after the system is allowed to remain at room conditions for approximately one hour.

Each one of the regimes is treated in details in the following sections.

4.6.1 Irreversible regime

To study the irreversible pathway that the system undergoes when partially heated (temperatures below 120 K), we choose the as-grown sample in argon atmosphere due to its inert nature. This ensures that the reactions occurring on the surface are not influenced by interactions with the environment. The sample was exposed to a 30 mW laser for optical excitation. The experimental parameters were set with an EPR MW attenuation of 15 dB and an illumination temperature of 8 K. The laser remained active as the sample was gradually heated up to 110 K. Subsequently, the system was cooled back down to 8 K while keeping the laser operating.

After the heating process, the lines associated with methyl radicals underwent transformation, while the core-defect increased in intensity. The entire heating process, which involved raising the temperature from 8 K to 110 K and back, was referred to as a "cycle". To understand the limit of transformation of the system, several cycles were executed, starting from an initial measurement.

The results are depicted in Figure 4.23, where the black line represents the initial spectrum recorded at 8K, the dotted lines represent intermediate cycles, and the red line represents the final state achieved through this procedure.

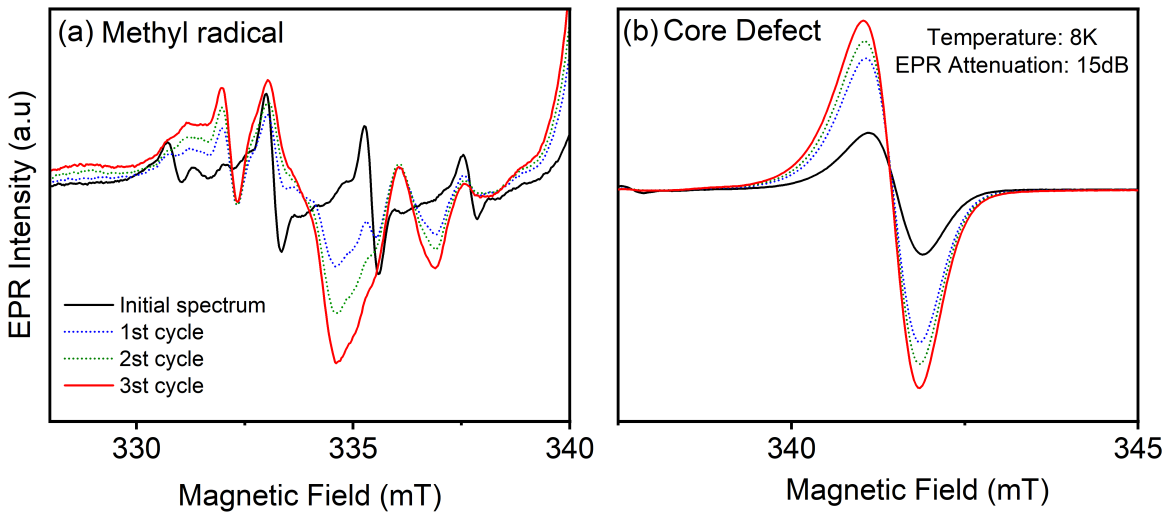

Figure 4.23: *Transformation in the EPR spectrum of the methyl radical and core-defect by heating the system under optical excitation.*

It is observable that the system experiences an irreversible process within this temperature range. In Figure 4.23, panel (b), the core-defect exhibits an increase in intensity, which might be attributed to the ionization of additional core-defect centers. On the other hand, the organic system appears to undergo a chemical reaction that transforms methyl radicals into other compounds, leading to alterations in its EPR signal. The exact mechanisms responsible for these behaviors likely involve complex thermally induced processes.

4.6.1. Irreversible regime

Once that the sample was under continuous illumination, the system simultaneously generated methyl radicals through a photo-Kolbe reaction while existing methyl radicals were being extinct due to thermal energy. To better understand the extinction of the methyl radicals separately, a new experiment was conducted with the heating conducted without optical excitation (laser off).

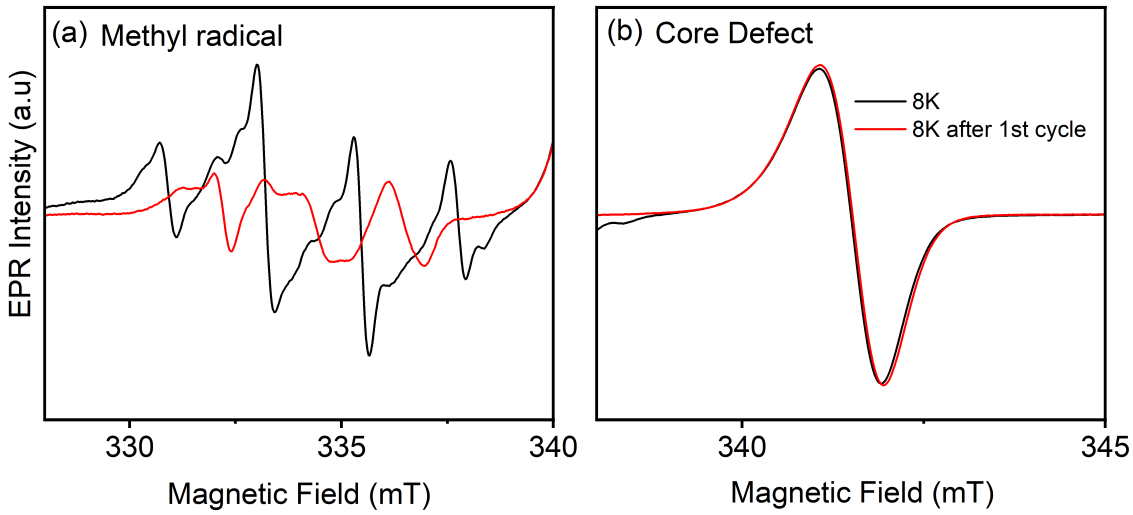

Figure 4.24: *Extinction of methyl radicals through increasing temperature*

In this new experiment, the sample was illuminated at 8K, the laser was subsequently turned off, and the sample was heated up to 110K. Following this, the sample was cooled back down to 8K, and a new spectrum was recorded. The results are presented in Figure 4.24.

In Figure 4.24 (b), we observe that the core-defect, even after undergoing the same heating cycle, maintains its intensity unchanged, indicating that the quantity of active centers (or ionized defects) remained constant. These results confirm again that the creation of methyl radicals is related to the core-defect, but the destruction of the methyl radicals is not. Without illumination, the methyl radicals disappear towards an intermediate state and the CD remains constant.

Making the subtraction of the spectrum after heating (red) from the initial one (black), it is observed that the specie that disappeared upon heating is the methyl radical. The result of applying this procedure is depicted in Figure 4.25

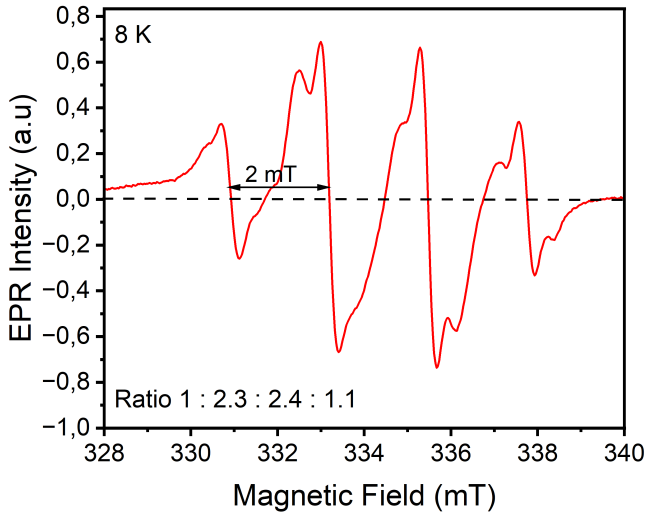

Figure 4.25: *Subtraction of the spectrum after heating from the initial spectrum. The difference between spectra correspond to the methyl radical, which undergoes a chemical reaction under the influence of thermal energy.*

In Figure 4.23, continuous exposure to the laser resulted in a competitive mechanism, where some methyl radicals underwent transformation due to the temperature increase, while others were generated through optical excitation.

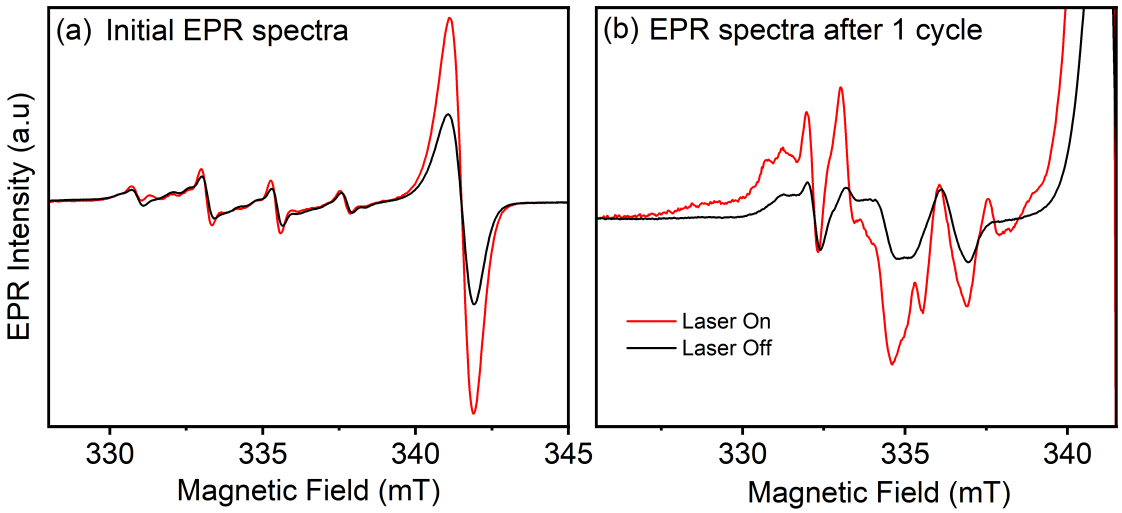

Figure 4.26: *(a)Initial EPR spectra for both experiments. the spectra were normalized through the line L_4, presuming identical quantities of generated methyl radicals after the initial illumination. In (b), the response of the methyl radical to heating is demonstrated, showing comparisons between samples heated with (red) and without (dark) simultaneous optical excitation.*

Conversely, in Figure 4.24, this concurrent process was circumvented, enabling the monitoring of the initial methyl radicals' evolution without interference from newly generated ones. Interestingly, in the latter scenario, the signal corresponding to methyl rad-

icals vanished almost entirely. The comparison between these experiments is illustrated in Figure 4.26.

At temperatures above 30K, the system undergoes chemical reactions. These observations indicate a complex interplay of chemical processes occurring within the material as it is exposed to varying temperatures.

4.6.2 Reversible regime

Interestingly, upon comparing the spectra obtained at 8 K and 36 K in the initial cycle, it's observed that the signal attributed to methyl radicals increases in intensity with rising temperatures within this range, even in the absence of optical excitation. This trend is illustrated in Figure 4.27. Notably, the core-defect exhibits a typical behavior where the EPR intensity decreases as the temperature increases.

In Figure 4.27, the behavior of both methyl radicals and the core-defect is examined. It is noticeable that at 8K, the methyl lines appear broader and less intense. Their respective ratios are measured as 1:2.6:2.3:1.2. As the temperature rises to 36 K, the ratio changes to 1:3.1:3:1.3, nearing the theoretically predicted 1:3:3:1 ratio expected for methyl radicals.

At temperatures above the rotational barrier, the methyl radicals present classical stochastic reorientation. At sufficiently low temperatures, they behave as quantum rotors and possess only the ground rotational state populated, being manifested for the decrease of the theoretical ratio between lines 1:3:3:1 [144]. However, due to the Heisenberg uncertainty, the rotational tunneling takes place [145; 146]. This phenomenon explains the broadening of the lines and the decrease in the intensity of methyl radical at temperatures below 36K. Methyl radicals are highly sensitive molecules, strongly influenced by their immediate environment. The reorientation of $^{\bullet}CH_3$ in molecular nanocrystals involves complex rotational motion around the molecular axis and quantum tunneling [147]. When the molecule interacts with a host crystal, its rotational movement can be hindered [148]. These results align with previous studies by other researchers, which have shown that above 45 K, the orientational order decreases [147]. This effect is also identified by the change in the 1:3:3:1 ratio of the free methyl radical, indicating that the ground vibrational state becomes more occupied, and the methyl radicals become rigid rotors [149; 150]. In resume, it is expected that at low temperatures, the states belonging to the projection $m_s = 3/2$ are less occupied.

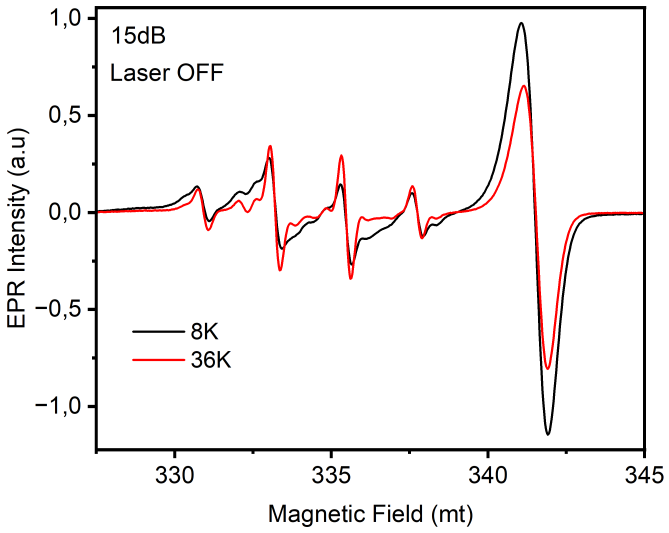

Figure 4.27: *Between 8K and 36 K, the lines attributed to methyl radicals show an increase in intensity as the temperature rises. Notably, this phenomenon occurs even in the absence of optical excitation. Conversely, the core-defect demonstrates an opposite behavior, where the signal decreases in intensity with increasing temperature.*

Furthermore, the stability of these elements within the matrix suggests that they are not entirely free in the environment. Instead, they interact with the ZnO structure, preventing rapid recombination [134].

In contrast to the behavior exhibited by the methyl radical, the core-defect demonstrates a more predictable trend, showing higher EPR intensity at lower temperatures and a gradual decrease as temperature increases. Upon simultaneous analysis of the methyl radicals and the core-defect, it becomes conclusive that the system undergoes a change of behavior around 40K.

4.7 3-lines signal

The presence of the 3-lines system alongside the photo-excited methyl radicals in all the samples emphasizes the necessity for a comprehensive analysis of this system. This analysis should consider the potential association between the 3-lines system and either the methyl radicals or secondary reactions taking place in the NPs surface.

A preliminary analysis was conducted to determine the value of the electronic spin of the 3-lines system. Rabi oscillations were induced with an EPR attenuation of 3 dB in the EPR spectrometer, following a procedure similar to that adopted in Figure 4.15.

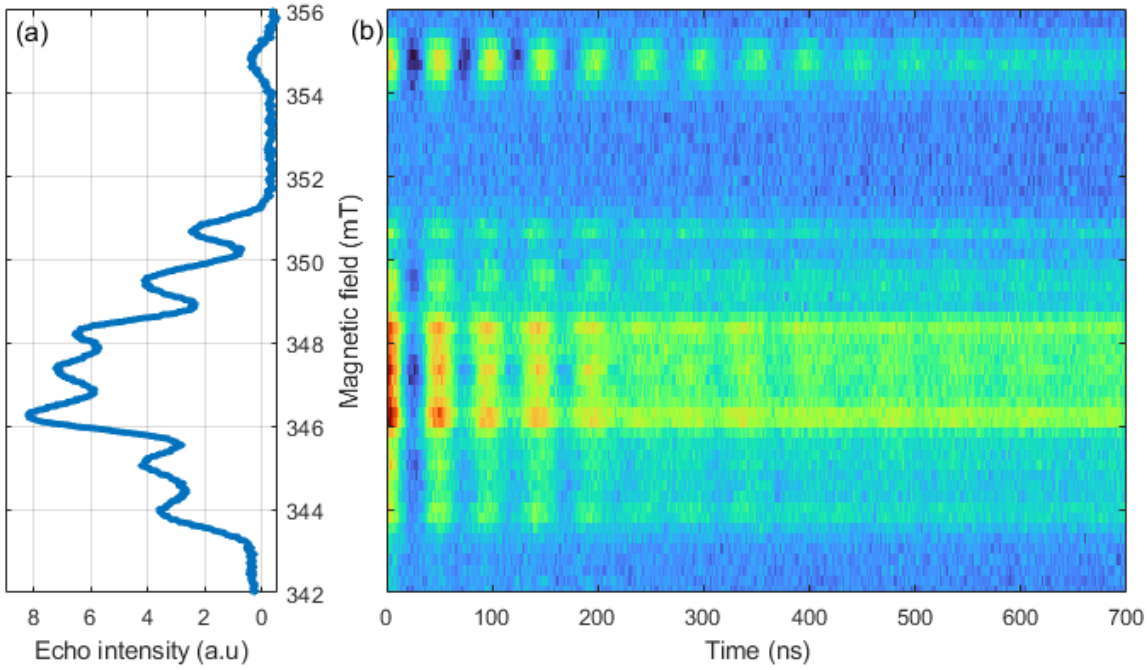

Figure 4.28: *Rabi oscillations in the time domain for all the lines studied in this chapter. On the left, the absorption spectrum corresponding to each line is presented. The spin value associated with the 3-lines system matches that of the methyl radicals and core-defect, which is s=1/2. This similarity is evidenced by the identical oscillations demonstrated by these systems.*

Figure 4.28 illustrates the Rabi oscillations observed for all the investigated lines in this chapter. The left side of the figure presents the absorption spectrum corresponding to each line, aligning with the Rabi oscillation. Particularly, noteworthy is the identical oscillation observed in both the methyl radical, core-defect and the 3-line system, suggesting that they share the same spin value (s=1/2).

It is intriguing that the 3-line system consistently manifests only in conjunction with methyl radicals and has never been observed independently. Notably, upon the elimination of methyl radicals, the 3-line system also disappears. This observation strongly suggests a close correlation between this system and the presence of methyl radicals. It is plausible that these lines arise from a secondary group of radicals generated during or after the charge transfer from the nanoparticles to the organic shell. Alternatively, they might emerge from the formation of methyl biradicals interacting via Heisenberg exchange. The exploration of these two scenarios is more thoroughly addressed in Chapter 6.

Concerning the stability in the optical excited state, the 3-lines group showed to present high stability at 85K. While the other lines (methyl radical and core-defect) decay through a biexponential decay behavior, the 3-lines stay unchanged over time. This result is presented in Figure 4.29, where the comparison of the decay of the three systems is presented. The initial value of the EPR intensity for all the systems was normalized to 1.

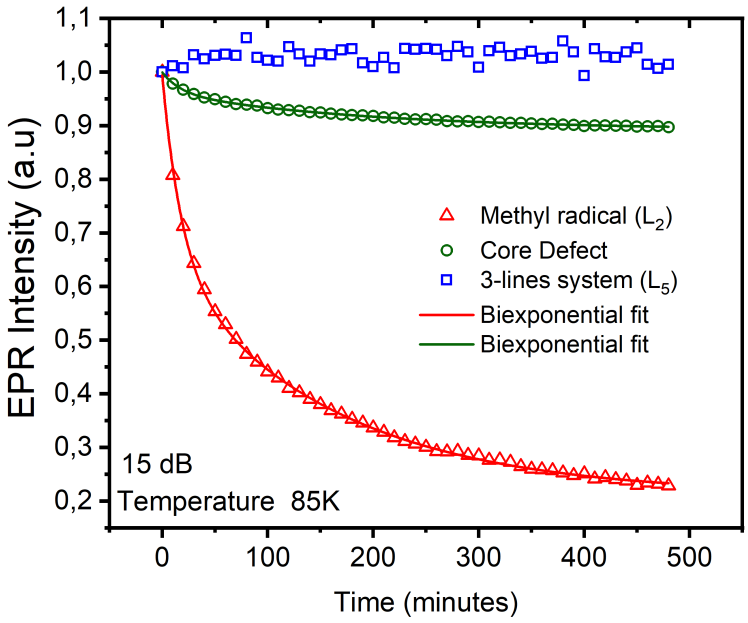

Figure 4.29: *The analysis of the stability of the optically excited state shows that the 3-lines stay unchangeable over time at 85K. Same data as Figure 4.22 with the 3-lines system included.*

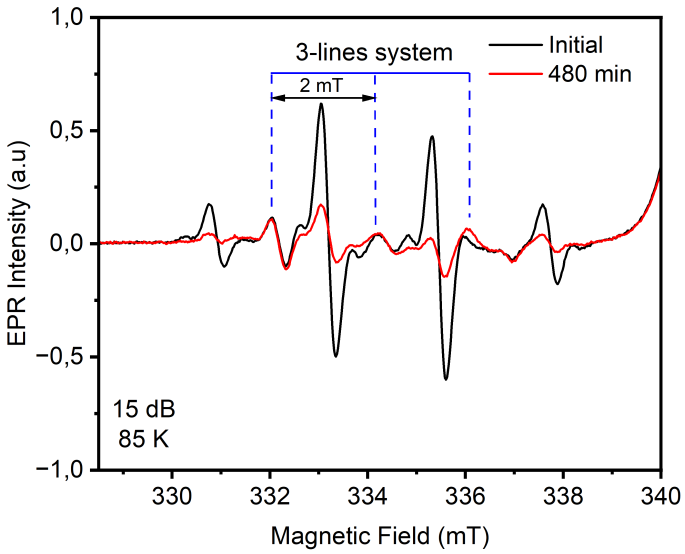

Figure 4.30: *Comparison of the EPR spectra acquired for photo-excited ZnO nanoparticles after the cessation of photo-excitation. The black line represents the data obtained at the initial stage of the experiment, following the cessation of optical excitation. The red line illustrates the data after 480 minutes without optical excitation. Both spectra were recorded under identical EPR conditions.*

In the initial stages following the start of the experiment, the lines associated with the

methyl radical are significantly more pronounced than the 3-lines system. However, in the final stages, they possess nearly the same EPR intensity. This behavior is illustrated in Figure 4.30.

The stability of the 3-lines system after photo-excitation removal at 85K indicates that this system should be associated to a less reactive chemical. In the context of technologies, this property gains interest, once that the system remains stable at conditions that can be more easily achieved (higher temperatures and without constant photo-excitation).

In the next sections, we present the spin dynamics associated to each system.

4.8 Relaxation phenomena - core-defect, Methyl radicals and 3-lines system

The considerable potential for spin-based quantum information, particularly focusing on impurities present in direct band-gap semiconductors that facilitate spin-photon interfaces, has sparked an increasing interest in understanding the fundamental mechanisms of spin relaxation in these materials [151].

In this context, understanding the mechanisms behind the system's loss of magnetization is crucially significant. This is because the longer the system stays in its excited state, the larger the window available for conducting spin manipulations. Moreover, comprehending the alterations in properties and relaxation times as temperature increases is fundamental in determining the temperature range within the system remains useful.

In accordance with the Bloch equations outlined in Chapter 2, two distinct relaxation times are established to elucidate the loss of magnetization within the material. The first, associated with longitudinal relaxation, is defined as T_1, while the second, linked to transverse relaxation, is denoted as T_2. Due to the influence of various intertwined mechanisms on T_2, making it challenging to isolate and analyze independently, we ultimately arrive at a phase-memory time, an experimentally measured parameter denoted as T_m. To access information of the relaxation times T_1 and T_m of the presented system, PW EPR techniques were used. For more details about this technique, see Section 2.9.

Before implementing the pulse sequences, a field sweep echo intensity was conducted across the system to monitor its temperature-dependent evolution. Note that before illumination, no echo is presented by the samples. The results of the field sweep for two distinct temperatures are depicted in Figure 4.31.

A notable observation is the significant alteration in the ratio between subsystem lines. At 5K, the methyl lines exhibit significantly greater prominence, whereas at 22K, the intensities of both methyl radicals and the 3-line system are comparable. This characteristic is attributed to the temperature-dependent behavior of the phase memory time T_m, which remains considerably more stable for the 3-line system. In other words, the echo intensity for the 3-line system remains nearly unchanged despite the temperature increase from 5K to 22K, whereas the group consisting of methyl radicals experiences a considerable loss in echo intensity.

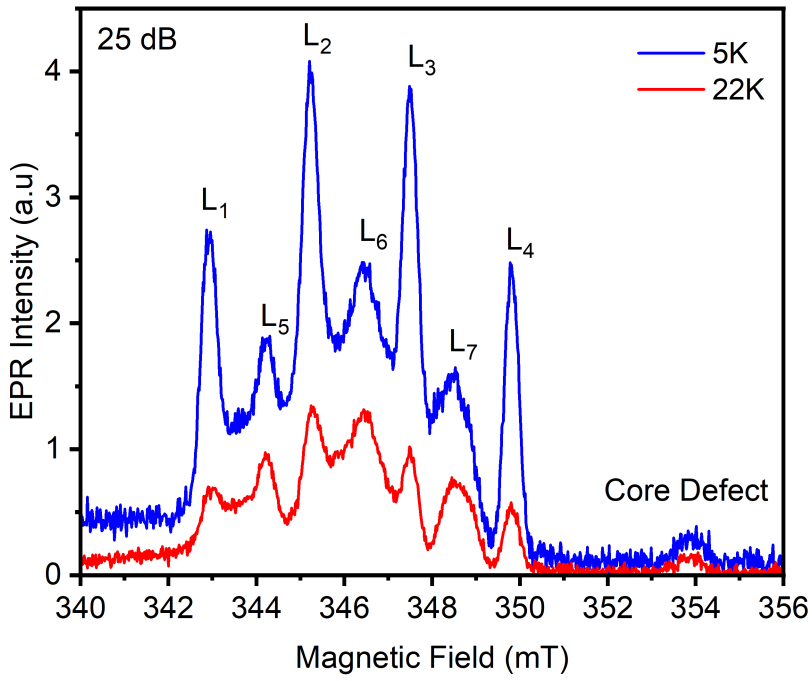

Figure 4.31: *EPR absorption spectra in pulsed EPR band X at 5K (in blue) and 22K (in red). The Intensity ratio between different subsystems change abruptly with increasing temperature.*

In pulse EPR, the detection of the echo is heavily reliant on the relaxation times. The results presented in this section indicate that methyl radicals are significantly more sensitive to temperature changes compared to the other species characterized by the 3-lines group, suggesting that the latter might be more suitable for quantum manipulations. Moreover, in pulsed EPR, measurements are based on pulse echoes, and any significant loss of information in the time between the initial pulse and the echo measurement (averaging about 400 ns) can lead to poor echo intensity. This characteristic is evident in Figure 4.31, where the core-defect, typically much more intense in CW EPR, demonstrates poor intensity in the pulsed regime. In other words, after a pulse is applied in the system, the phase memory time T_m for the core-defect is so short that almost all the transverse magnetization dissipates before the echo refocusing occurs.

4.9 Spin lattice relaxation time (T_1)

For all the following measurements, the attenuation was set as 6 dB and the shot repetition time as 1000ns, due to high values of T_1 observed. The values in nanoseconds that correspond to the angles $\pi/2$ and π radians are 16 and 32 ns, respectively.

To quantify longitudinal spin relaxation, which correlates with the dissipation of energy to the lattice, the inversion recovery technique was employed. This method consist in reversing the spin population and subsequently measuring its restoration to the equilibrium. The description of the sequence is presented in Section 2.13.1.

The technique revealed that for the methyl radical, approximately 75% of the spin population was inverted (at the lower temperature achieved, T= 7 K), signifying that some spins were not impacted by the inversion pulse. Consequently, this incomplete

inversion results in a reduced T_1 value due to spectral diffusion. This phenomenon has been documented in radical studies [152]. As measure the temperature increased, less efficient was the inversion pulse. The objective of the present study is not to offer absolute T_1 values, but to identify temperature-related patterns and the difference of behaviors presented between systems.

In Figure 4.32, we present the return to equilibrium of the magnetization, measured through the inversion recovery technique for the 3-lines system (line L_5). The measurement was performed at 31 K.

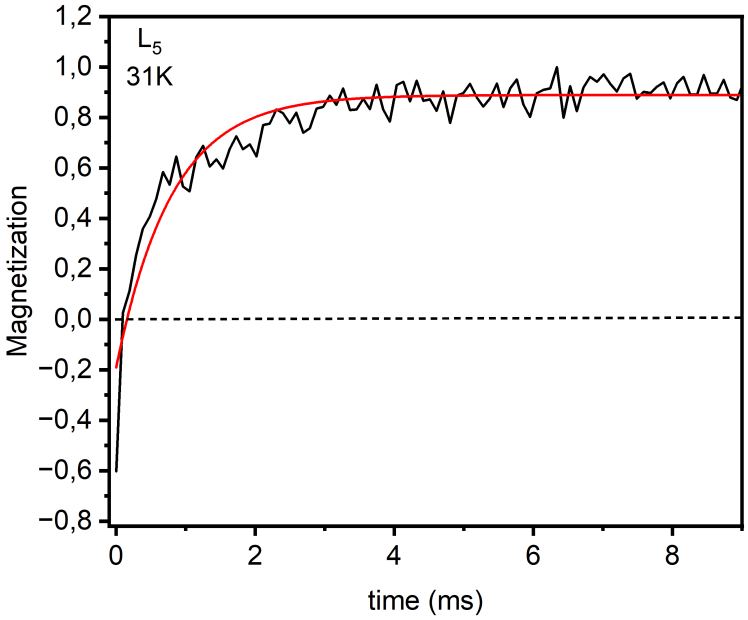

Figure 4.32: *The return to the equilibrium after the application of an inversion pulse. The target line is the L_5, corresponding to the 3-lines group. T= 31 K.*

The presented fit presented corresponds to a monoexponential function, defined by the equation;

$$M = M_0 + A\ exp(-t/T_1)) \tag{4.15}$$

where M_0 is the initial magnetization (measured after the return to equilibrium is completed). The investigation of the temperature-dependence of the system was carried out by fitting each return to the equilibrium with a monoexponential fit, obtaining the T_1 values for each system at each temperature.

In the limit $t \to \infty$ the original magnetization M_0 is recovered and for simplicity was normalized to 1. A is a negative constant that determine the quantity of spins that were able to suffer inversion. In the ideal case, $A = -2M_0$, representing that in the time 0 all the magnetization is $M = -M_0$. For the methyl radical, the experiments were conducted over the line L_2 while for the 3-lines system over L_5.

The behavior of the longitudinal relaxation time T_1 with increasing temperature is illustrated in Figure 4.33. According to Section 2.7, where we introduce that leads the system to loss energy to the environment, the expected behavior is described by the Direct

or Raman process, or a combination of both. For this, to describe the system's behavior, the employed fit was given by the equation

$$T_1(T) = \frac{A}{T^n} \tag{4.16}$$

where A is a constant and the parameter n is the parameter that determines the behavior of the system. Note that $n = 1$ represents the Direct process. However, for the Raman process, different values of n are allowed. Moreover, once that the organic shell does not constitute a bulk, this parameter is not restricted to those of the bulk (n=5,7 or 9). Note that in th observed temperature range (T from 7 to 31K), the chemical reaction is not expected to interfere in the relaxation phenomena.

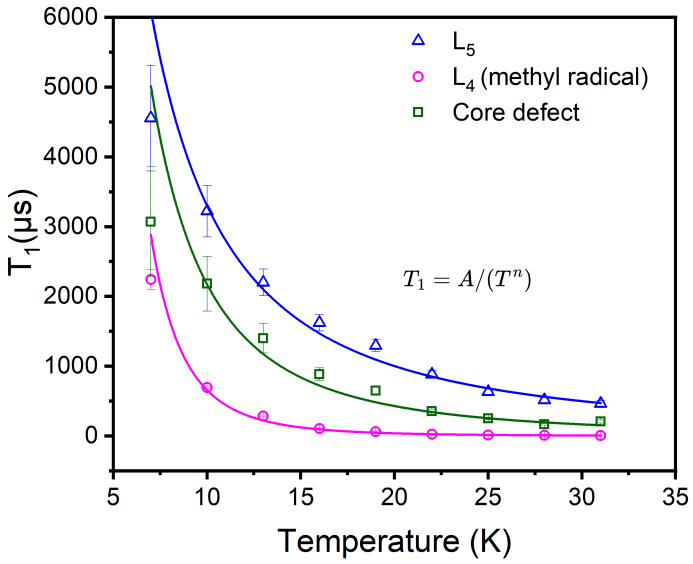

Figure 4.33: *Behavior of the longitudinal relaxation time T_1 with temperature.*

The obtained values of A and n for each system is presented in the table 4.2.

-	A ($K^n\mu s$)	n
methyl radical (L_4)	91.5 $*10^5$	4.14
3-lines system (L_5)	1.73 $*10^5$	1.80
core-defect	4.8 $*10^5$	2.34

Table 4.2: *Values for the fit constants presented in Figure 4.33*

To provide a better visualization of possible changes of behavior within the system, the obtained results are presented in the log-log scale. In this approach, the inverse of the relaxation time T_1 is plotted as function of T. The results are presented in Figure 4.34.

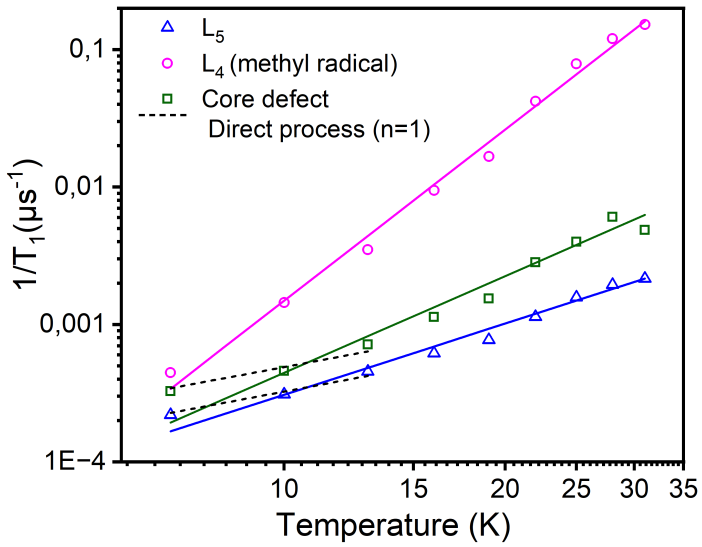

Figure 4.34: *Behavior of the inverse of T_1 with temperature in log-log scale. The slope of the solid lines present the exponent n obtained by the fit performed in Figure 4.33. The dashed lines present n=1, the direct process. The fit of the direct process was made considering the 3 first points for each system.*

At low temperatures, the expected predominant relaxation mechanism is the direct process (n=1) [153]. The curve representing the direct process is presented in dashed line for the core-defect and 3-lines system. This model seems to describe accurately the relaxation mechanism at temperatures below 15 K. At higher temperatures, the behavior of the system diverges from the direct process, probably due to the contribution of the Raman process, that becomes more pronounced in the measure that more phonons are available due to the increase of the thermal energy [154].

For the methyl radical, even at lowest temperatures, the direct process is not the principal mechanism of relaxation. This system present a Raman process with n=≈ 4. The discrepancy from the standard Raman process is expected, once that the relaxation is not happening in a bulk material. This change in behavior has already been observed in single molecule magnets [96].

This work remains a first insight into the relaxation mechanisms presented by the different systems. Further analysis, employing different pulse sequences, as saturation recovery are envisioned for comparing the results here obtained and thus, have a conclusive analysis about the phenomena of relaxation presented by each system. Moreover, more experimental points are required for a more complete analysis.

4.10 Coherence time (T_2)

The maximum value achievable by the coherence time is theoretically constrained by the spin-lattice relaxation, stating that $T_2 < 2T_1$. However, in real scenarios, this limit is rarely observed due to several factors that induce decoherence in the system. The inhomogeneity present due to the difference in the Larmor frequency of different spin packets (that is a source of decoherence) can be avoided by refocusing the spins with an inversion pulse. Applying this technique, the spins are refocused, producing an echo.

Nevertheless, certain dephasing processes are unavoidable. Some of these processes are intrinsic to the system, such as spins flip-flops, that changes the local field perceived by the spins and, thus, dephasing the spins in an irreversible way [101]. The method used to measure the coherence time also influence in the decoherence process. This is the case of instantaneous diffusion [155]. In this context, the measured coherence time will be set as a phase memory time (T_m), that accounts effects of decoherence intrinsic and extrinsic to the system. The phase memory time (T_m) for the different systems was measured through the 2-pulses Hahn's echo decay sequence.

4.10.1 2-pulses echo decay

The two-pulse echo decay method was utilized to analyze the phase memory time (T_m) of the system. Through this method, T_m is obtained by fitting the exponential decay of the Hahn echo over time. Details of this technique are presented in Section 2.14.1.

It is important to emphasize that the measured T_m does not represent an absolute physical property of the system, as it can be significantly influenced by the experimental parameters chosen for the measurements. Moreover, the obtained results incorporate the influence of different sources of decoherence, such as spectral and instantaneous diffusion.

Nevertheless, the measured T_m provides insights into the environment where the spins are situated and can serve as a tool to understand alterations in the environment induced by temperature variations. The primary aim of this study is not to determine absolute values, but to comprehend the behavior of the coherence time concerning increasing temperature.

The target lines for performing the 2-pulses sequence are: the core-defect, the L_2, representing the methyl radical and the L_6, representing the 3-lines system. Applying this technique, it was observed that the echo decay exhibits modulations, linked to the interaction with nuclear spins, notably prominent in the initial µs of the measurement (this characteristic will be treated in details in Section 4.11). In this context, the fitting related to the decay may experience disturbances due to this modulation.

In this scenario, three different functions were applied in an attempt to fit the experimental data:
(1) Mono-exponential model: This is the simplest model, describing the decay of the echo with a mono-exponential dependence on time (τ):

$$I(\tau) = I_0 \exp\left(\frac{-2(\tau - 136)}{T_m}\right) \tag{4.17}$$

In this approach we considered the dead time of the spectrometer, set at 136 ns. We observed that fitting the decay through a mono-exponential function showed some discrepancy between the fit and the experimental data. Therefore, we decided to use a second approach, considering a stretched exponential.

(2) Stretched exponential: We employed the stretched exponential, that differs from the mono-exponential by an added parameter n, (<1 n <3), that accounts effects of spectral diffusion in the system. The stretched exponential is given by:

$$I(\tau) = I_0 \exp\left[\left(\frac{-2(\tau - 136)}{T_m}\right)\right]^n \tag{4.18}$$

However, applying this approach, we obtained that the value of n inferior to 1, (n $\approx$ 0.7). This value is unexpected, and its connection to a physical phenomenon becomes

invalidated. Finally, for comparison, we used a bi-exponential model:

$$I(\tau) = I_1 \exp\left(\frac{-2(\tau - 136)}{T_{m1}}\right) + I_2 \exp\left(\frac{-2(\tau - 136)}{T_{m2}}\right) \tag{4.19}$$

The bi-exponential model fits the decay well, but the lack of a physical interpretation to explain the two distinct relaxation times imposes restrictions to the interpretation of the found parameters. Figure 4.35 illustrates the experimental data obtained for the line L_2 at 18K, with the respective models used for the fit.

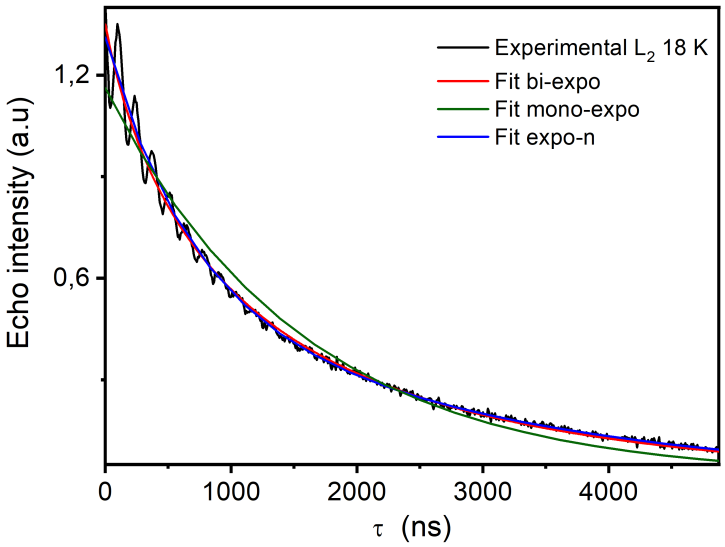

Figure 4.35: *The echo decay of the line L_2, linked to the methyl radical, at 18K. The Figure shows the accuracy of the functions used for the fit.*

Interestingly, despite the divergence observed between models, the behavior in temperature follow a same trend for the methyl radical. For this system, the phase memory time T_m increases with rising temperature, in the studied regime (18 <T< 65 K). As the coherence time is strongly linked to the spin concentration, we can conclude that the concentration of methyl decreases with increasing temperature. Note that this phenomenon begins to be observed from 30 K, in agreement with the results obtained in CW EPR, where we noticed the presence of the vanishment of methyl radicals starting at this temperature. This result is depicted in Figure 4.36, where the three models are compared for the lines related to the methyl radical and the 3-lines system.

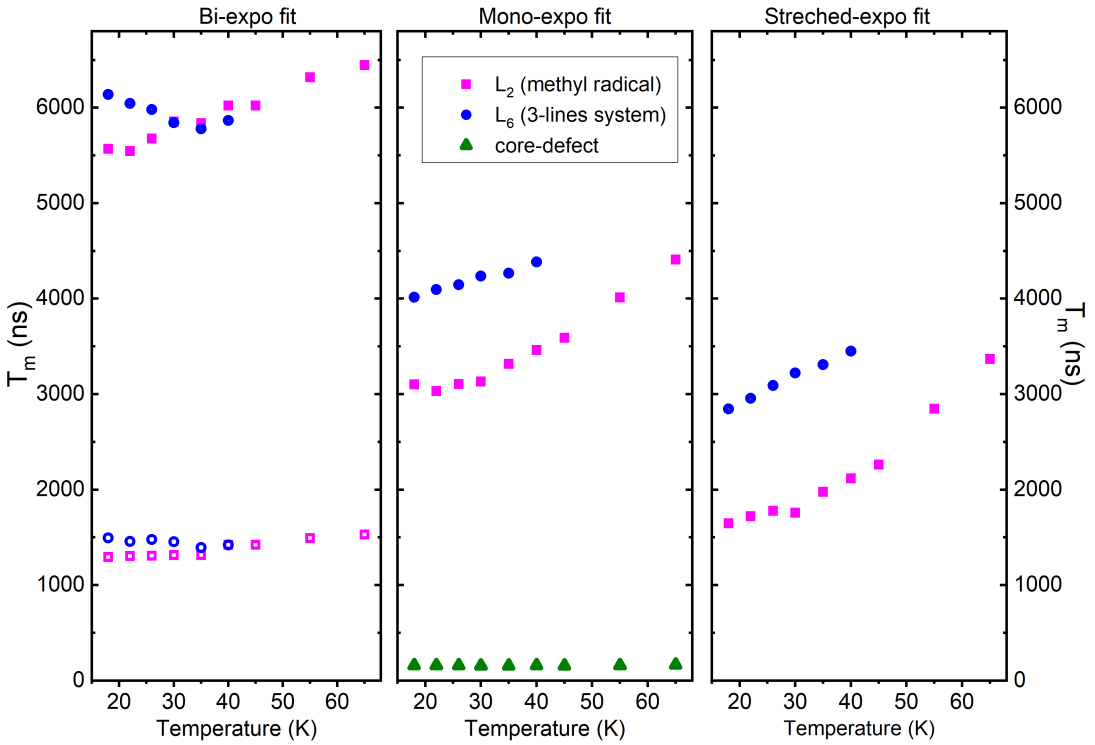

Figure 4.36: *Behavior of the phase memory time T_m measured by 2-pulses echo decay for the different systems. The monoexponential, biexponential and stretched exponential models are considered for the fit of the behavior of the methyl radicals and 3-lines system. For the core-defect, only the monoexponential model was applied. Disregarding the discrepancy between the values obtained for T_m, the trend presented by the methyl radicals is the same for the three models, i.e, T_m increases with increasing temperature.*

For the core-defect, the mono-exponential model appropriately fitted the decay, thus no further supplementary analyses were conducted for this signal. Regarding the 3-lines system, both the mono-exponential and stretched exponential models showed the same trend, which is the increase of T_m with rising temperature. However, the bi-exponential model exhibited the opposite trend.

The signal from the methyl radicals remains detectable until 65K, whereas for the 3-line system, the lines become too weak to be measured at 40K. Beyond these temperatures, the echo signal diminishes significantly, making it challenging to conduct further measurements.

In terms of the relaxation time value for each temperature, there is a significant discrepancy between models. The stretched exponential shows the lowest values among the models, followed respectively by the mono-exponential and the bi-exponential. Despite the divergence in these values, it is possible to access the order of magnitude of this variable, which is in the order of microseconds. This property can be better visualizated in Figure 4.37, that compares the coherence time obtained by each method for each system.

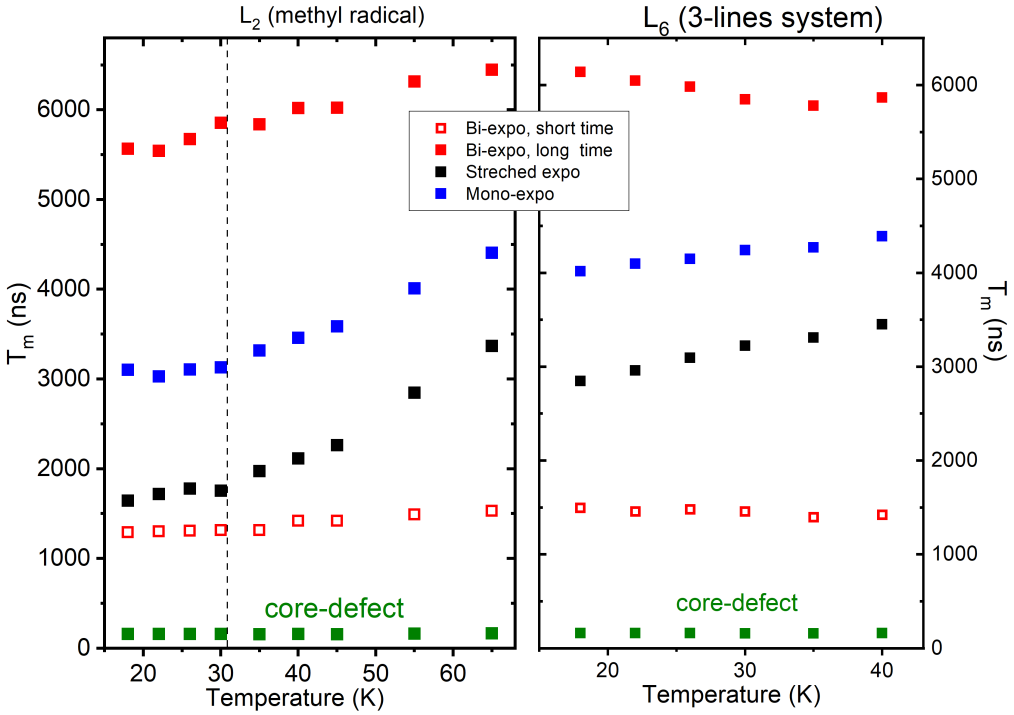

Figure 4.37: *Behavior of the phase memory time T_m measured by 2-pulses echo decay for the different systems. The different models applied for the fit result in different T_m.*

Additionally, it can be observed that the coherence time value for the core-defect is significantly lower than for the organic systems, indicating that this system is embedded in an environment rich in spins, causing its fast decoherence.

For comparison, the values obtained through the monoexponential fit for T_m and the values acquired for T_1 (for the methyl radical and the 3-lines system) are juxtaposed on a log-log scale and presented in Figure 4.38. This comparison allows the observation that the loss of magnetization in the system is primarily due to decoherence. As temperature is increased, T_1 reduces drastically, thus, participating more effectively to the loss of magnetization.

Due to difficulties in establishing connections between the parameters derived from the bi-exponential and negative exponent of the stretched exponential model, the author suggests that the most appropriate fit for describing the system is attained using the mono-exponential model, despite observed discrepancies. Through this mode, it is observable that the value of T_m increases with temperature, in agreement with the previous results obtained in CW EPR. This behavior indicates a a decrease in the number of the spins present in the system as the temperature increases. This is in agreement to the chemical reaction involving the methyl radicals.

To address the present discrepancies, the author proposes conducting additional measurements to incorporate more experimental data into the model. As a result, more comprehensive investigations utilizing supplementary techniques, such as CPMG, are recommended to provide additional complementary sources for comparison.

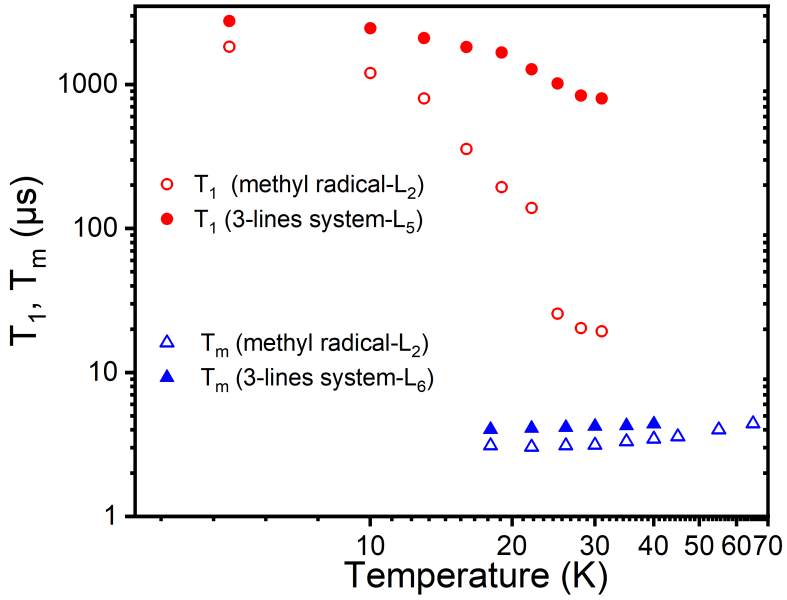

Figure 4.38: *Comparison of T_1 and T_m measured by 2-pulses Hahn's echo decay for the the different organic systems in ZnO nanoparticles.*

4.11 Electron Spin Echo Envelope Modulation (ESEEM)

The presence of modulation in the 2-pulses echo decay experiment was firstly observed by Rowan, Hahn and Mims in 1965 [105]. They observed that the modulation frequency was related to nuclear frequencies. After this observation, the ESEEM was apprimorated for reveal weak hyperfine and nuclear quadrupole interactions present in the system. In Figure 4.35, where the echo decay is presented, it is possible to notice the presence of modulations, that are more pronounced at the initial stage of the decay and persists up to 1200 ns. The presence of these modulations indicates the presence of nuclei in the vicinity of the electronic spins.

The modulation was consistently present for each temperature studied and was observed in the 4-lines of the methyl radicals and also in the lines belonging to the 3-liness system. The oscilations were identical for the two systems. The frequency of oscillation remained constant by increasing the temperature. The primary phase of the decay (t $<$ 1500 ns) measured in the line L_2 for several temperatures is presented in Figure 4.39.

In Section 2.15, it was demonstrated that the ESEEM modulation accounts frequency terms related the nuclear frequency and its sum and difference with the hyperfine interaction. Notably, only one modulation frequency was observed in our system, indicating that the difference between frequencies are so small that are hiden in the linewidht, thus, indicating a weak interaction. The modulation frequency directly corresponds to the Larmor frequency of the associated nuclei. An essential condition for the modulation effect in the two-pulse echo decay experiment is that the system displays either an anisotropy in the hyperfine interaction or the presence of a nuclear quadrupole interaction with the involved nuclei.

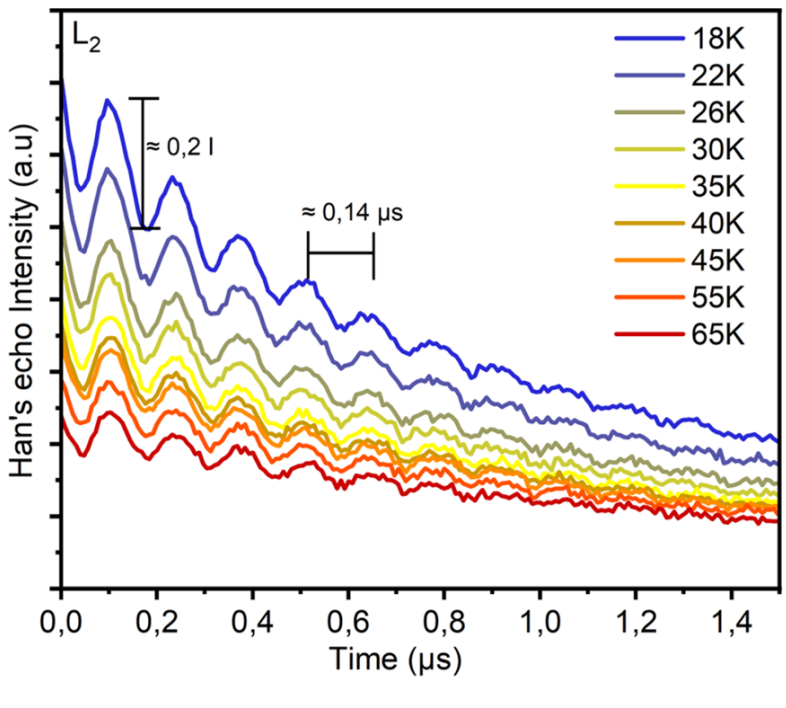

Figure 4.39: *The observation of modulation in the Hahn's echo decay experiment indicates the proximity of nuclei to the electrons.*

As protons possess a nuclear spin of 1/2 and thus lack a nuclear quadrupole, we must consider that the presence of modulations is due to significant anisotropy in the hyperfine interaction [4]. However, the hyperfine coupling of 65 MHz, measured by the CW EPR technique, is excessively strong to solely explain the observed modulation. Therefore, there must be another weak and anisotropic hyperfine interaction involving protons external to the methyl radical molecule.

Considering the hyperfine coupling obtained through CW EPR $A = 65$ MHz, the Larmor frequency of the hydrogen $\omega_I = 15$ MHz and anisotropy $B = 1.5$ MHz, the expected value for the modulation depth (Equation 2.73) is expected to be $k \approx 7\times 10^{-4}$. Remarkably, this value does not correspond at all to the modulation depth observed in our system, k$\approx$ 0.2 (Figure 4.39). Moreover, the predicted modulation frequencies from equation 2.76 are ω_α, ω_β, $\omega_\alpha + \omega_\beta$, $\omega_\alpha - \omega_\beta$, which are respectively 48, 18, 66 and 30 MHz. None of these frequencies are observed in the Fourier Transform analysis of the ESEEM data (Figure 4.40 - b). Indeed, the observed frequency spectra and the depth modulation are much more suggestive of a very weak coupling, with sizeable anisotropy. In this case ($A << \omega_I$) $\omega_\alpha \approx \omega_\beta \approx \omega_I$, and the expected frequencies are only ω_I and $2\omega_I$, compatible with the observed spectra (Figure 4.40 - b). For such a weak coupling case, $k \approx (B/\omega_I)^2$, so that $B = 6$ MHz would reproduce the experimental value $k = 0.2$. We are then led to conclude that, in addition of the strong hyperfine interaction within the methyl radical molecule, a second coupling, significantly weaker must exist with secondary protons, as illustrated in Figure 4.41.

To ascertain if the modulation in the spectrum resulted from neighboring methyl radicals, a study on the deuterated sample was conducted. Through NMR techniques, it was observed the deuterium partially replaced the hydrogens of the methyl group of the sample (observed at room temperature without optical excitation); however, all the methyl

[4]For an isotropic coupling, B=0, implying that the depth of modulation k = 0.

radicals formed upon illumination were deuterated. In this context, if the interaction originates from neighboring radicals, the entire modulation should change, aligning with the shift in the difference between the Larmor frequencies associated with hydrogen and deuterium nuclei.

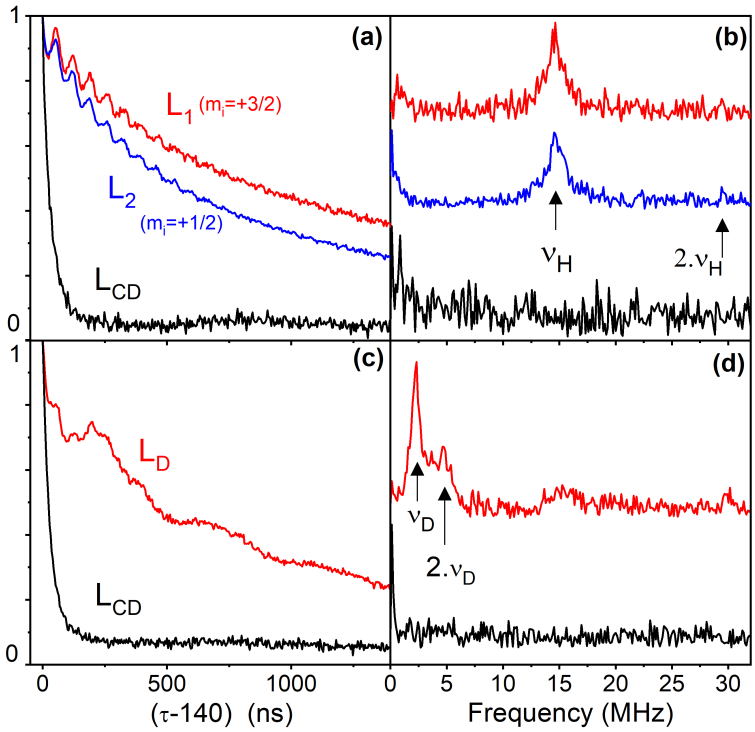

Figure 4.40: *The 2-pulses echo decay reveals modulation in the lines linked to the methyl radical (a). Upon deuteration of the sample, a drastic alteration in the modulation frequency is observed (c). Performing Fourier transform in the signal, distinct Larmor frequencies, corresponding to hydrogen (b) and deuterium (d) nuclei are identified for the as-grown and deuterated samples, respectively. Notably, no modulation is detected in the core-defect.*

The results obtained through this approach show a clear alteration in the modulation presented in the signal. The results are presented in Figure 4.40, where the comparison between the as-grown and deuterated samples is presented. The Fourier transform was performed on both spectra, after properly removal of the baseline and the exponential decay. This approach aims to identify the frequencies associated with the modulation. The analysis revealed the Larmor frequency corresponding to hydrogen nuclei (in the as-grown sample) and deuterium (in the deuterated sample), aligning with our anticipated expectations.

In this scenario, we investigate the potential presence of a superhyperfine coupling. The representation of a superhyperfine coupling for methyl radicals is illustrated in Figure 4.41.

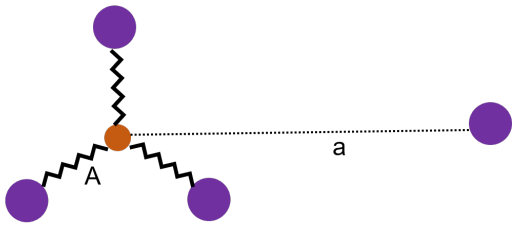

Figure 4.41: *Representation of superhyperfine interaction for the methyl radicals. The electrons belonging to a molecule 1 interact with protons from a molecule 2. This interaction, defined by a is significantly smaller than the hyperfine interaction A.*

Notably, the core-defect did not display any modulation. This outcome affirms its location within the bulk, thus, submitted to a different nuclear environment, where no protons from organic compounds are present. The results conducted for measuring the phase memory time T_m show that the core-defect possess faster relaxation time. This suggests a higher concentration of electronic spins in its proximity, potentially originating from other core-defects, different types of defects, or even residual free electrons within the bulk.

To further investigate the weak nuclear coupling, suggested by the analysis performed with ESEEM, the HYSCOREE technique was employed, as it is designed to discern weak nuclear couplings. For details of the HYSCORE technique, see section 2.16.

4.12 HYSCORE

The HYSCORE technique revealed the presence of hydrogen (in the as-grown sample) and deuterium (in the deuterated sample) nuclei in the proximity of the unpaired electron. This was evidenced by observing peaks corresponding to the hydrogen Larmor frequency (14.8 MHz) in the as-grown sample (Figure 4.42 - a) and the deuterium Larmor frequency (2.4 MHz) in the deuterated sample (Figure 4.42 -b. The experiment was performed at 20K over the line L_2 (346 mT) for the sample as-grown and in the gravity center (347 mT) of the deuterated sample.

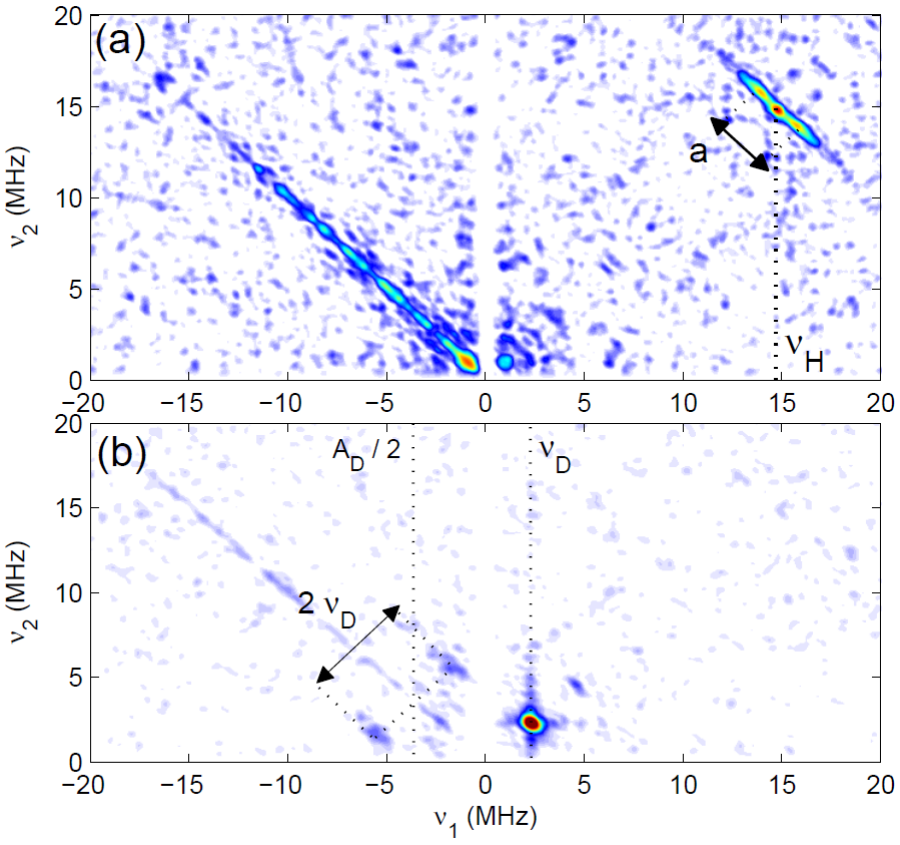

Figure 4.42: *Hyscore spectra for the as-grown (a) and deuterated (b) samples. In the as-grown sample, the Larmor frequency of hydrogen is identified at 14.8 MHz, while a weak coupling of 2.72 MHz is measured through the satellite lines. In the deuterated samples, the Larmor frequency of deuterium is identified at 2.4 MHz and the hyperfine coupling is observed in the strong coupling panel (left).*

In the sample as-grown, satellite peaks are observed around the main peak of hydrogen, corresponding to a weak coupling case ($a < 2\nu_H$). It indicates the presence of an interaction between the electron and nuclei corresponding to a value of 2.72 MHz (approximately 25 times smaller than the hyperfine coupling). In terms of magnetic field, this coupling represents a splitting of 0.1 mT in CW EPR, thus, hide in the linewidht. Importantly, the frequency range spans from 0 to 20 MHz, signaling that couplings beyond 20 MHz remain unobservable.

The prominent signal observed in the negative diagonal does not represent an inherent physical property of the system. Rather, it is likely associated with the formation of anti-echoes, often caused by errors within the pulse sequence.

For the deuterated sample, the situation differs. In this case, we observe a strong regime coupling ($a > \nu_D$), presented in the left panel of Figure 4.42 (b). The measured coupling corresponds to a value of approximately 12 MHz, in agreement with the hyperfine coupling observed in CW EPR.

The absence of hydrogen peaks in the deuterated samples indicates the complete removal of protons from the vicinity of $^{\bullet}CD_3$ radicals. This observation suggests that in the as-grown sample, all the detected protons originate from $^{\bullet}CH_3$ radicals. Consequently, the superhyperfine coupling observed in the as-grown sample can be attributed to ($^{\bullet}CH_3$)–($^{\bullet}CH_3$) interaction.

The HYSCORE technique has also been employed on line L_6, which is part of the 3-lines system, in an effort to detect potential weak nuclear couplings within this system. Whereas the Larmor frequency of hydrogen has been once more identified, no definitive couplings were identified in the spectrum. The broadening of the hydrogen peak in the diagonal could indicate the presence of weak satellite peaks, yet it could also be attributed to experimental artifacts, rendering the results inconclusive.

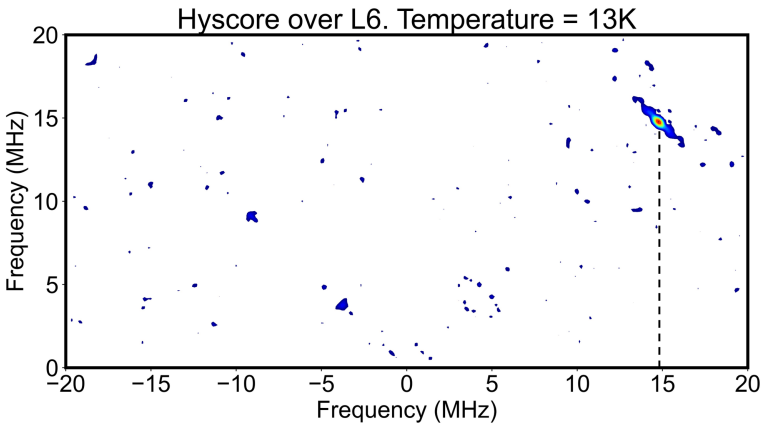

Figure 4.43: *HYSCORE of the L_6 line, belongint to the 3-lines system. The hydrogen Larmor frquency has been identified.*

4.13 Q-band EPR analysis

To explore the correlation among different systems, EPR spectroscopy was conducted at Q-band (MW frequency = 33.73 GHz). Altering the resonance frequency (or the EPR band) enables the differentiation of systems with distinct resonance positions that might overlap within a specific frequency band. In the studied NPs, we observed the overlapping of signals of the methyl radicals, the 3-lines system, and the "elephant" signal in X-band. If these signal are originated from different centers, thus, presenting different g-factor values, the relative position of their lines in the B-field axis are expected to be modified, changing or avoiding the overlapping. The EPR field-sweep echo intensity spectrum for photo-excited NPs (always at 405 nm laser excitation) at Q-band are depicted in Figure 4.44.

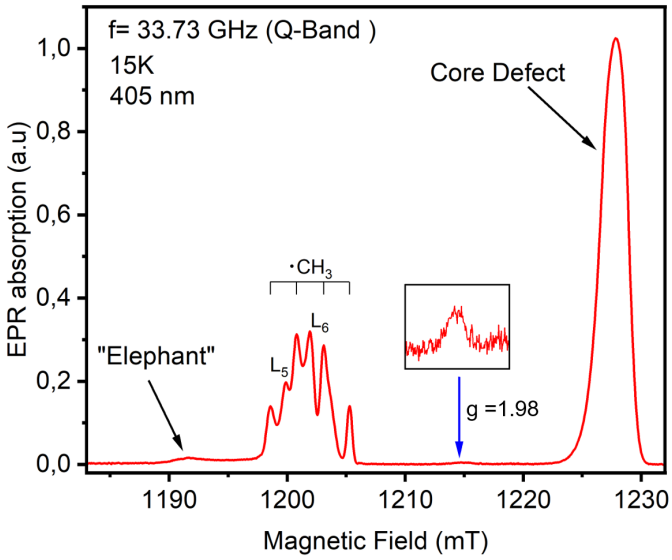

Figure 4.44: *EPR absorption spectrum of photo-excited ZnO NP in Q band. In this regime, the signal associated to the "elephant" and the 7-lines cluster are no longer overlapped. The distance between the 7-lines group and the core-defect is also increased. An adjacent line positioned at the gravity center between the 7-lines cluster and the core-defect is highlighted by the blue arrow (g=1.98). This line was observed in CW EPR in the deuterated sample. In the as-grown sample, this line is present, but it is superposed to the line L_4 of the methyl radical. This signal arises probably from a correlation between the organic shell and the core of the NP, pointing a connection between the core-defect ionization and the formation of methyl radicals.*

As expected, the signals "elephant" and the cluster formed by the 7-lines formed by the organic shell are completely separable, indicating its different nature. This result is in agreement with the CW EPR results, that indicated that the "elephant" signal is not associated to the organic shell, but to a more stable state of the NP, probably another kind of defect in the NP core. Moreover, the "elephant" signal has been observed in samples lacking the organic shell (synthesized via the aqueous precipitation method). A concise description of the "elephant" signal in these nanostructures is provided in Annex D.

Considering the 7-lines group, interestingly, the methyl radicals and the 3-lines system remained coupled in Q band. This suggests that these systems share the same resonance gravity center, further indicating an intimate correlation between these two systems. I also suggest that the origin of the 3-lines system is the same as the methyl radical. The fact that these lines are produced by the same photon, at same temperatures and that they are vanished under similar conditions (annealing), support this hypothesis. In the next chapter, we perform some simulations to demonstrate that the 3-lines system could arise from biradicals formed by the interaction of neighboring methyl radicals.

The core-defect, as as expected, shifted away from the 7-line group. Interestingly, an adjacent line, positioned between the 7-line group and the core-defect, was observed. This particular line is denoted by the blue arrow in Figure 4.44. Additionally, in the deuterated sample, a line was observed in the X-band between the gravity center of the deuterated radical and the core-defect. This line manifests as a deformation of the L_4 line observed in the as-grown sample. It is hypothesized that these two distinct observations are linked

to the same transition, resulting from a Heisenberg interaction indicating an interaction between the core-defect and the methyl radical.

Notably, as the frequency band was changed, this line consistently maintained its position precisely midway between the gravity center of the core-defect and the 7-line group. It is well kwown that if two spin 1/2 with g-factors g_1 and g_2 are coupled by a Heisenberg-like interaction, an additionnal EPR line resonating at $g = (g_1+g_2)/2$ is observed. Indeed the average between the core-defect g-factor (1.96) and the methyl gravity center ($g = 2.005$) give $g = 1.9825$, corresponding to the observed intermediary line in Figures 4.44 and 4.13. If this is the presented case here, it would indicate that methyl radicals and cored-defect are indeed very close to each other, so as to have a substantial overlapping of the wave function. It would then be consistent that the core-defects that are ionized by realesing a hole, are those located very close to the NP surface.

In the next chapter, we demonstrate how the observation of the core-defect and the generation of methyl radicals in the surface is connected. The interaction line, observed between the core-defect and the 7-lines cluster, gives support to the model, demonstrating that the surface and the core of the NP are not completely independent systems.

4.14 Correlation between EPR lines - ELDOR detected NMR

The study of the correlation between adjacent transitions was conducted by employing the double resonance technique. The Electron-Electron Double Resonance (ELDOR) experiment employs two microwave channels to investigate transitions that are electronically forbidden.

In this method, the measurement is conducted using the standard $\pi/2$ - π sequence in channel 1, while excitation with a second microwave (MW) pulse of variable sequence is applied through channel 2. When the MW emitted via the second channel precisely matches the transition line where detection occurs using MW channel 1, it causes a decrease in signal intensity at that particular resonance condition. This decrease results in the formation of the "central hole" in the EPR spectrum. This hole is indicated at Figure 4.45 at 0 detuning.

If the specific targeted transition (being measured in MW channel 1) is associated with another transition that is either fully or weakly allowed, it leads to the creation of additional holes in the spectra. This approach of hole burning is commonly employed to detect nuclear frequencies, which elucidates the term ELDOR-detected NMR. The pulse sequence applied and additional information about the ELDOR-detected NMR technique are elaborated in Section 2.17.1.

To ascertain that the hole burned in the spectrum arises from physical correlations within the system rather than experimental artifacts, different pulse excitation durations were applied, as depicted in Figure 4.45. A comparison is made between a less selective pulse (64ns) and a more selective one (128ns).

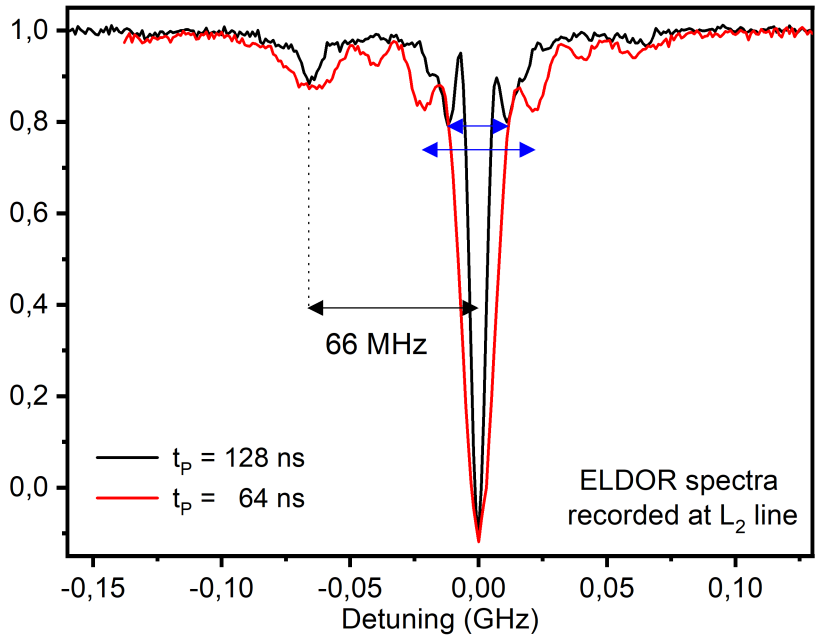

Figure 4.45: *ELDOR spectrum recorder with a selective (128ns) and a non-selective (64ns) MW pulse. In the non-selective pulse, extra holes are present, likely arising from the excitation of more than one line simultaneously.*

The more selective pulse yields better results, revealing the correlation between the line L_2, associated with the methyl group, and its neighboring line L_1, separated by 66 MHz. Conversely, the additional adjacent lines observed in the less selective pulse stem from broader band excitation, which should be disregarded. The satellite holes surrounding the central hole (located at zero detuning) demonstrate an inverse relationship with the duration of the pumping pulse. Essentially, they represent the Fourier transform in the frequency domain of the rectangular 128 nanoseconds pumping pulse, resembling the wings of a cardinal sinusoid.

In Figure 4.46 (a), the plot depicts the field sweep echo intensity, illustrating the four transitions associated with the methyl radicals. However, the observed intensity ratio among these transitions notably deviates from the expected 1:3:3:1 ratio for this particular group. These spectra were recorded at a temperature of 20K. Figure 4.46 (b) displays the ELDOR spectra, individually presented for each transition. At zero detuning, the echo intensity diminishes to zero. Conversely, at multiples of 65MHz (equivalent to 2.3 mT), a slight intensity decrease of approximately 10% is noticeable, indicating a correlation between the transitions. The origin of this correlation is likely linked to cross-relaxation phenomena between different rotational states of a single radical or between two adjacent ones [156]. Further comprehension of these intriguing quantum tunneling relaxation mechanisms would necessitate an extensive temperature study conducted through single and double resonance experiments.

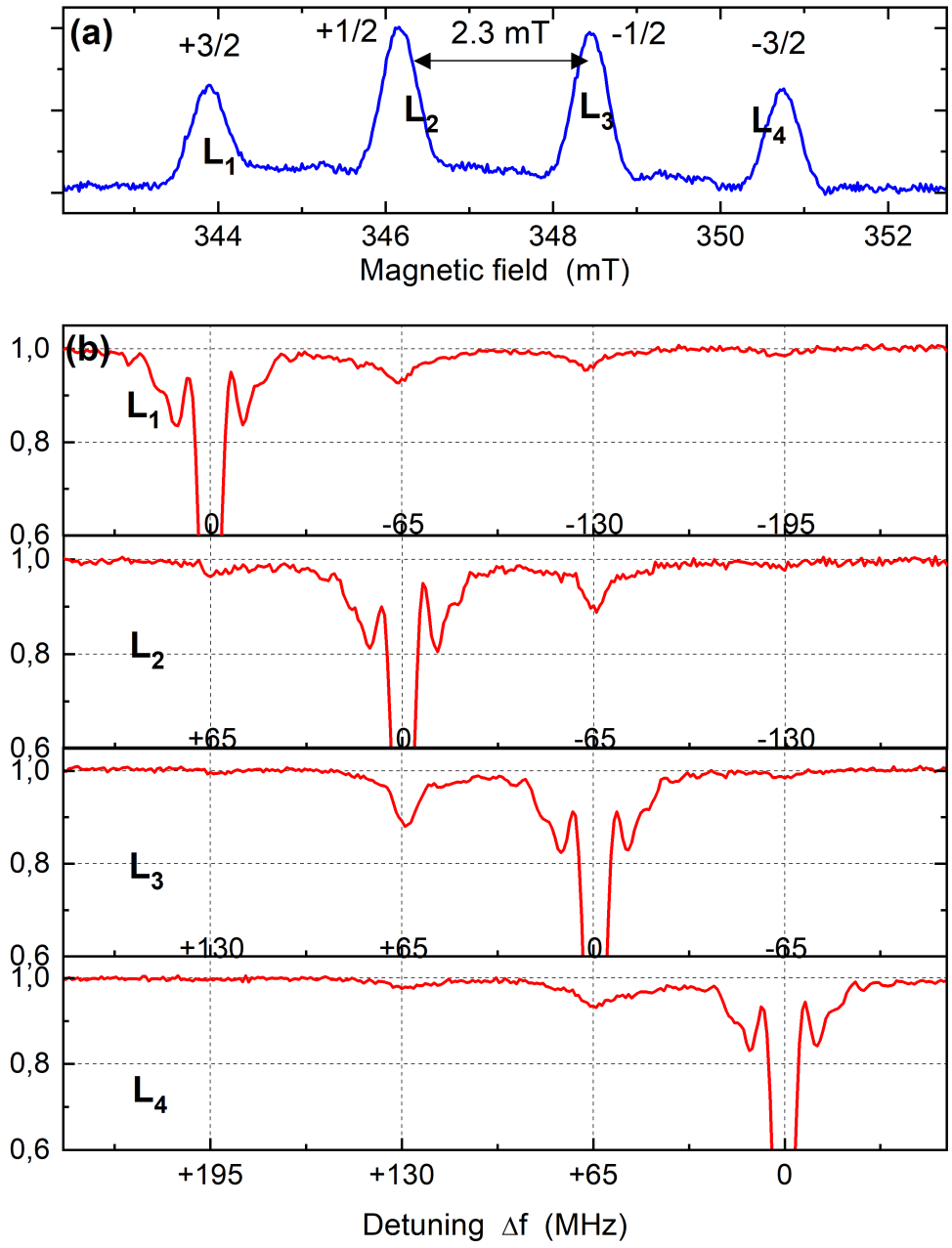

Figure 4.46: *In (a), a field sweep of the 4-lines, associated to the methyl radical. The spin projects are associated to each line. In (b), the ELDOR sequence applied to the lines L_1, L_2, L_3 and L_4, respectively. It is observable that a hole is formed when the detuning correspond to another transition, indicating the correlation between them.*

4.15 Partial conclusions

ZnO NPs synthesized via sol-gel method present different groups of paramagnetic signals when submitted to photo-excitation (photon energy ≈ 3 eV). The observed EPR lines are composed by a core-defect, centered at $g = 1.96$, a group of 4-lines, centered at g=2.005, a group of 3-lines, superposed with the 4-lines and a broad signal, labeled "elephant", also superposed to the 7-lines signal. The ZnO NPs present the wurtzite structure, with high

degree of cristalinilly and an average diameter of 15 nm, presenting an almost spherical geometry.

Analysis performed with FTIR and NMR spectroscopy indicate the presence of a organic shell, containing acetic acid in the NPs surface. Surface functionalization with deuterated acetate demonstrate that the EPR signal presented by the 4-lines group arise from methyl radicals formed on the NP surface. Moreover, through the surface functionalization, the hydrogens presented in the formed methyl radicals were preplaced by deuterium, promoting a change in the EPR spectrum of the NP.

Notably, the energy provided by the photon (3 eV) is not enough for promoting an electron from the VB to the CB (ZnO bandgap = 3.4 eV). This suggests that the core-defect, confirmed to originate from the bulk, represents an intra-band gap state. As ZnO is know for its intrinsic defects, it is anticipated that the core-defect results from the ionization of a defect existing within the crystalline lattice. Furthermore, considering the photo-Kolbe reaction triggered by this ionization, it is expected that the core-defect is associated with an acceptor defect, capable of accepting an electron, thereby generating a hole that initiates the photo-Kolbe reaction.

Upon subjecting the nanoparticles to an annealing process (500°C), a notable effect is observed — the NPs' size increases, displaying an average diameter of 50nm post-annealing. Furthermore, FTIR analysis reveals the disappearance of the organic shell after the annealing procedure. Consequently, both the 4-line and 3-line groups vanish, while the core-defect remains present. The state of the core-defect is changed, and in the annealed samples, it is present even under dark conditions, alongside a surface-defect. However, the "elephant" signal persists and remains activated by illumination, indicating that this signal is not associated with organic compounds situated on the surface of the NP. Preliminary results demonstrates that the "elephant" signal can be activated but also deactivated through optical excitation. Further details of this phenomena should be explored.

Rabi oscillations conducted by simultaneously varying the time and magnetic field (2D Rabi oscillation) revealed that all the electronic spins oscillate with the same frequency, indicating that all systems are characterized by the same electronic spin value, s=1/2.

The study of the EPR intensity of the systems with increasing temperature reveals that the methyl radical possesses a peak of intensity around 36 K. Below this temperature, the lines become more broadened with reduced intensity. This phenomenon is associated with the rotational states of the methyl radical, indicating that the rotor becomes rigid. The change in the intensity ratio in this regime indicates that the states with a projection of s=$\pm$3/2 are less populated. At temperatures above 36K, chemical reactions involving the methyl radicals take place, and the system loses intensity in an irreversible pathway. This feature is highlighted by the change in the behavior related to the linear coefficient of the saturation curves, which present discrepancies from the Curie law. It indicates that the relaxation time T_m undergoes changes in this regime, related to a decrease in the number of spins. The relaxation time T_m was explored by means of PW EPR technique. The evolution of T_m with increasing temperature was investigated, confirming the change in the number of spins when the system undergoes heating.

The analysis of the stability of the optically excited state indicates that among the three systems (core-defect, methyl radicals, and the 3-lines system), the 3-lines system is the most stable under temperature changes, exhibiting complete stability at temperatures below 110K. The core-defect and the methyl radical decay exponentially with temperature. The presence of the 3-lines group is consistently associated with the presence of methyl

radicals, suggesting a relationship between these systems. Moreover, the stability observed at higher temperatures implies that the 3-lines group is likely associated with an organic, less reactive compound.

An additional line observed between the 7-lines system and the core-defect indicates an interaction between the core-defect and the methyl radicals present in the shell of the NP. This line was observed in X-band in the deuterated sample. In the as-grown sample, this line manifests as a deformation in the L_4 line, associated with the methyl radical.

Upon analyzing the system in Q-band, this line shifts while maintaining its position in the exact center between the core-defect and the 7-lines cluster (g=1.98). These results strongly suggest a connection between the core-defect and the methyl radical, demonstrating that the surface and the core of the NP are not completely independent.

Pulsed EPR techniques were employed to access information on the behavior of magnetization with increasing temperatures. Applying the inversion recovery sequence enabled access to the spin-lattice relaxation time T_1. The results indicate that at low temperatures, the core-defect and the 3-lines group relax via a direct process, with Raman contributions starting to gain significance at temperatures beyond 15K. Regarding the methyl radicals, the relaxation phenomenon is characterized by a non-usual Raman process, showing a dependence of $1/T^4$ with temperature.

The phase memory time T_m was measured using the 2-pulse echo decay sequence. This sequence was chosen for its simplicity and to provide initial insights into the behavior of the relaxation time of the system. Measuring the transverse relaxation time is challenging because the measurement itself interferes with the measured time. Further analysis is planned to separate the different mechanisms that affect T_m. In this context, measuring T_m using the Carr-Purcell-Meiboom-Gill (CPMG) technique or employing soft pulses is encouraged.

When applying the 2-pulse sequence, modulation in the decay was observed. These modulations arise from a transfer of polarization from electronic to nuclear transitions, indicating an environment rich in nuclei. The frequency exhibited by the modulation corresponds to the Larmor frequency of hydrogen for the as-grown sample and deuterium for the deuterated sample. Moreover, the existence of electronic-nuclear coupling, characterized by additional frequencies involving the sum and difference of nuclear frequencies with the hyperfine coupling, could be present but hidden in the linewidth. To access this information, the HYSCORE technique was employed for the as-grown sample (in the lines L_2 and L_6) and the deuterated samples. Notably, the Larmor frequency of hydrogen and deuterium was once again observable, and a small coupling was resolved, with a value of 2.72 MHz for the as-grown sample. This coupling is almost 25 times smaller than the hyperfine coupling measured through CW techniques, possibly indicating the interaction between neighboring radicals.

Interestingly, in the deuterium sample, the weak coupling with hydrogen atoms was no longer observed, indicating that the measured interaction does not involve hydrogens from the environment but is directly related to the formed radicals. In this sample, the interaction between deuterated radicals was not identified, but this coupling could be hidden in the linewidth of the deuterium principal peak. Access to this information could be obtained by improving the detection sensitivity of the deuterium or performing the HYSCORE experiment in a different frequency band (preferably band Q), where the Larmor frequency of deuterium is increased, potentially allowing the identification of the coupling.

However, in the deuterated sample, the hyperfine coupling of the deuterated radical

was identified, in agreement with the CW measurements. The HYSCORE performed in the 3-lines system did not provide conclusive results. It's important to note that HYSCORE is a technique that demands a significant amount of time in the spectrometer (more than 12 hours for a single spectrum), which poses a challenge in obtaining multiple spectra with optimized parameters.

Chapter 5

Co-doped ZnO

Contents

5.1 ZnO:Co nanoparticles wet fabrication method 114
5.2 Nanoparticle's characterization 115
5.3 EPR Study 117
5.4 ZnO:Co high-temperature method 120
5.4.1 Nanoparticle's characterization 120
5.4.2 EPR study 123
5.5 Analytical and simulation approaches 129
5.5.1 Matrix interaction 129
5.5.2 Eigenenergies and eigenstates 132
5.5.3 Perturbational treatment of the Zeeman interaction 133
5.5.4 EPR transitions 134
5.5.5 Simulations 135
5.6 Partial conclusions 137

Diluted magnetic semiconductors (DMS) belong to a class of semiconducting materials where atoms or ions with substantial magnetic moments are introduced as impurities into the crystal lattice of the semiconductor host. These materials have attracted considerable interest in the past decades, owing to their distinctive blend of semiconductor and magnetic characteristics encapsulated within a single material[157].

This approach of introducing carefully selected dopants to create new magnetic properties proves immensely advantageous. It offers a pathway to imbue magnetic characteristics into these nanostructures, by coupling the local spin of impurities with that of the charge carriers (electron or hole), which is the basics of spintronic [158].Careful selection of both the impurity ions and the host element can yield significant advancements in information storage [159] and processing technologies [160]. These materials can also apply to the development of solotronic devices [1] [161]. Furthermore, such precisely tailored ion-host combinations can have practical applications in quantum metrology systems [162], [163].

Contemporary advancements round the concept of controlling magnetic states through optical pumps at various frequency ranges. However, a significant challenge lies in surpassing the limitations imposed by the inherent thermal and quantum fluctuations intrinsic to these microscopically localized states.

In this research context, we developed a DMS consisting of cobalt embedded in a ZnO lattice. The benefit of incorporating a transition-metal (TM) ion into a semiconductor crystal lies in the presence of a locally intrinsic high-spin electronic state originating from the TM ion, which resides within the energy band gap below the Fermi level (i.e occupied even when $T \to 0$).

Besides it, cobalt-doped ZnO presents an intense spin-lattice coupling . This characteristic anisotropy presented by cobalt can lead to unconventional phenomena, such as EPR zero-field resonance occurring when two Co^{2+} ions are close enough. Furthermore, research has shown that in bulk materials, thin films, and microwires, apart from the single Cobalt impurity signal, as many as 11 distinct Cobalt pairs can be individually identified through EPR detection.

In the preceding chapter, we explored the magnetic behavior of ZnO attributed to the interaction between defects in the crystalline lattice and organic compounds residing on the surface of the nanoparticles. In this chapter, we present in a first moment, ZnO NPs cobalt-doped synthesized by the same method (sol-gel), with aim to condensate the properties presented by the ZnO with those of the transition ion. Additionally, we investigate the behavior of the core defect upon the introduction of cobalt into the lattice. In this scenario, very low doping amounts were targeted (0 to 1% Co).

At a subsequent stage, nanoparticles with a higher doping level (1 to 10% Co) were synthesized through a solid-state reaction that demands higher temperatures. Unlike the prior scenario, the absence of organic compounds characterizes this setup. The primary objective for these NPs is to investigate the behavior of the cobalt ions within this altered environment, including the examination of cobalt pair formations.

In resume, the two sets of samples explored in this chapter are:

(1) ZnO:Co synthesized via the sol-gel method.

(2) ZnO:Co synthesized using high-temperature methods.

[1] Electronic systems operating on the level of individual atoms or molecules. In semiconductors this approach can be extended to optoelectronic devices based on single dopants or defects.

The specifics of the sample preparation procedures are covered in section 3.1.4. The primary distinction between the samples lies in the nanoparticle size, which is larger for the high-temperature method, and the presence of an organic shell in those produced using the sol-gel method.

5.1 ZnO:Co nanoparticles wet fabrication method

In Chapter 4, we explored the paramagnetic signals that may be present in ZnO nanoparticles produced by the sol-gel method. Under specific light irradiation (405 nm), defects within the nanoparticles become ionized. This ionization process liberates a hole, which can then be captured by molecules on the nanoparticle's surface. This event initiates a photo-Kolbe reaction leading to the formation of methyl radicals and biradicals, detectable through EPR spectroscopy. In a simplified scheme, the steps of this process can be described as follows:

1. The ionization of a defect and liberation of a hole in the bulk:

$$\mathrm{X}^0 \xrightarrow{h\nu} \mathrm{X}^- + \mathrm{h}^+ \text{ (bulk)} \tag{5.1}$$

2. The transfer of the hole from the NP bulk to the surface:

$$\mathrm{h}^+ \text{ (bulk)} \rightarrow \mathrm{h}^+ \text{ (surface)} \tag{5.2}$$

3. The interaction of the hole with the organic molecules aggregated to the surface, leading to the formation of methyl radicals:

$$\mathrm{h}^+ + \mathrm{CH_3COO}^- \rightarrow^{\cdot} \mathrm{CH_3} + \mathrm{COO} \text{ (surface)} \tag{5.3}$$

According to the mechanism above, the final generation of methyl radical $^{\cdot}CH_3$ is subject to three main limitations: (1) the presence of the initial neutral defect X^0, releasing the hole under optical excitation. (2) The possibility for the hole to reach the surface before recombination, and (3) the presence of surface-adsorbed negatively charged acetate CH_3COO^- capturing the hole.

As illustrated in Figure 4.7,in the preceding chapter, we demonstrated that when the nanoparticles are subjected to high temperatures, the organic shell vanishes and the formation of radicals is prevented. In other words, mechanism (3) in the scheme below is impeded, and thus no signal associated to the methyl radicals is observable. Additionally, when thermal energy surpasses a certain threshold (T > 120K), hole recombination occurs instantaneously, impeding hole migration from the bulk to the surface. Consequently, condition (2) is no longer met, resulting in the absence of an EPR signal at elevated temperatures.

In the following sections, we delve into the possibility of suppressing the core defect by doping the ZnO matrix with cobalt. It has been documented that the introduction of an appropriate amount of cobalt into the ZnO lattice leads to the complete elimination of the core defect [121]. In such circumstances, the blockage of methyl generation is anticipated since the hole release involved in reactions (1) - (3) is prevented. Comparable competitive effects have also been noted in Mn-doped ZnO NPs [140].

For this purpose, samples with a gradual incorporation of cobalt into the lattice were prepared using the sol-gel method, as detailed in Section 3.1.4. The doping levels were

0.00, 0.01, 0.1, and 1% in nominal concentration. It's crucial to note that these nominal concentrations do not correspond directly to the actual substitutional cobalt content within the ZnO matrix, which is much lower. However, they are expected to scale with it.

5.2 Nanoparticle's characterization

Similarly to the procedure applied in Chapter 4, part of the samples were annealed in order to vanish the organic shell present in the NPs and separate the behaviors emanating from the organic shell from those associated to the NP by itself. The SEM and TEM images for these NP are presented below.

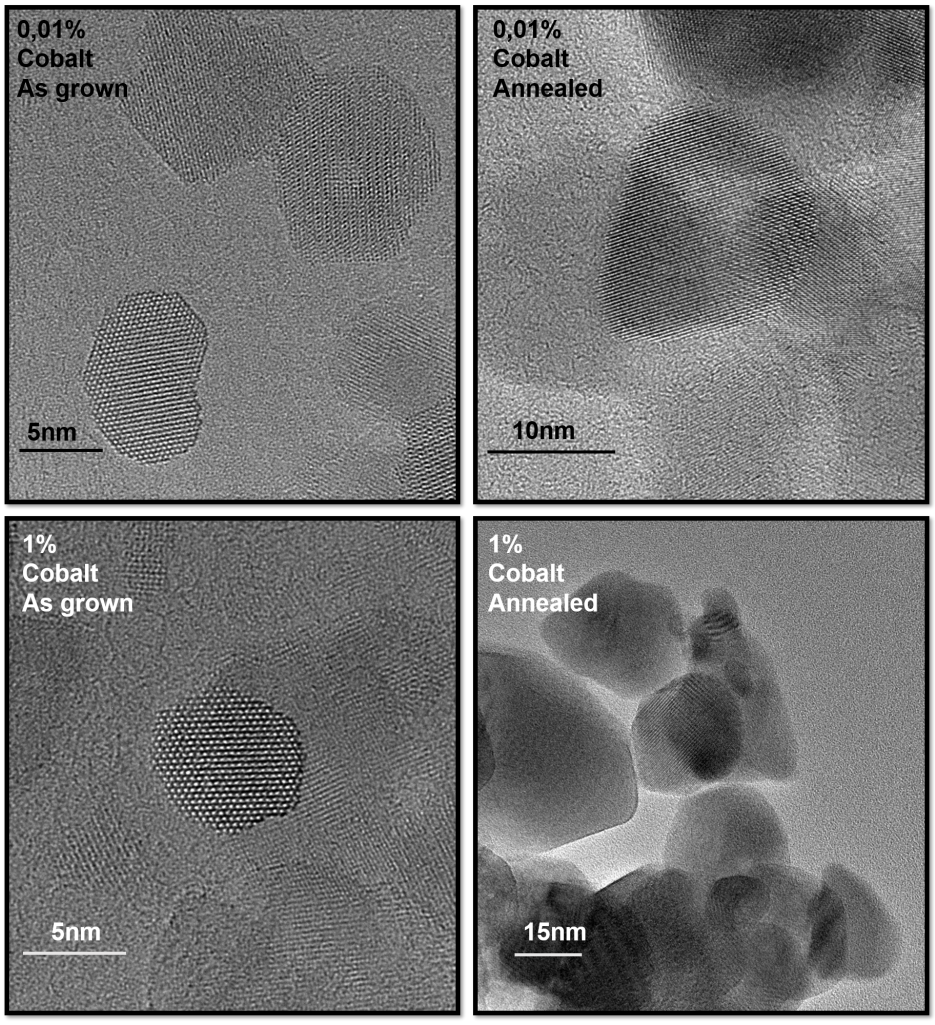

Figure 5.1: *(a) and (b): TEM images for ZnO doped with 0.01% Co in as grown regime and annealed, respectively. (c) and (d) TEM images of ZnO NP with 1% Co doping.*

The doping does not alter the structural characteristics of the nanoparticles, which still maintain the wurtzite structure with exceptional crystalline quality, as observed in TEM images. The annealing process produces a similar effect in the doped nanoparticles as it does in the non-doped ones. Specifically, the nanoparticle diameter increases by a factor of 3, resulting in an average diameter of 50 nm.

X-ray diffraction analysis affirms the quality of the crystal structure by displaying the characteristic (h, k, l) planes of the wurtzite structure. The crystallinity, which reflects the spatial coherence of the material, remains unaltered by the inclusion of cobalt in the lattice. Nevertheless, a notable improvement in crystallinity is evident after the annealing process, as indicated by the sharpening of peaks. This narrowing is consistent with an increase in the size of the nanoparticles. The XRD is presented in figure 5.2.

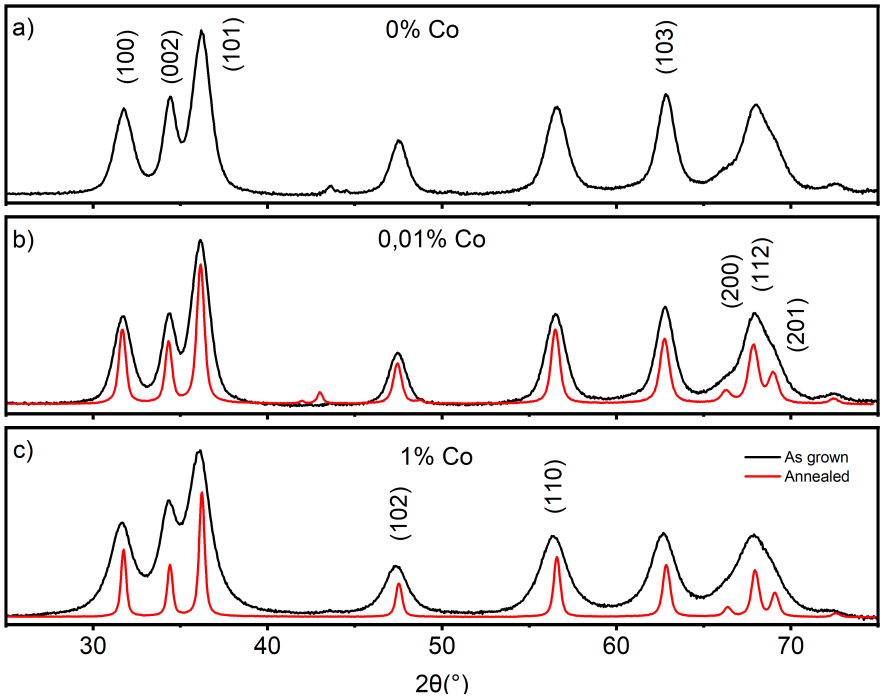

Figure 5.2: *XRD analysis on ZnO:Co samples. In (a), no cobalt is added to the ZnO lattice. (b) and (c) represents nominal doping of 0.01 and 1%, respectively. The black line stands for nanoparticles as grown and red for NP's annealed. Figure adapted from ref [164].*

Insight into the potential organic compounds adsorbed on the nanoparticle surface is acquired through Fourier transform infrared spectroscopy (FTIR). This technique reveals the existence of the same organic groups previously described in section 4.2.1. These results are presented in figure 5.3.

As the concentration of cobalt increases, additional vibration modes become detectable. However, these extra modes disappear when the samples undergo the annealing process. This phenomenon can be attributed to the presence of residual complexes formed by surface-adsorbed cobalt acetate, which evaporate upon heating.

A positive peak at approximately 1100 cm^{-1} has been observed, though no specific vibrational mode can be conclusively attributed to it. Initially considered an artifact in the measurement process, its persistence across all samples and its correlation with cobalt concentration suggest radiative recombination in ZnO. Interestingly, in the measure cobalt is added to the lattice, with the consequent reduction of core defect, the positive peak decreases and is almost completely vanished for the sample containing 1% of Cobalt.

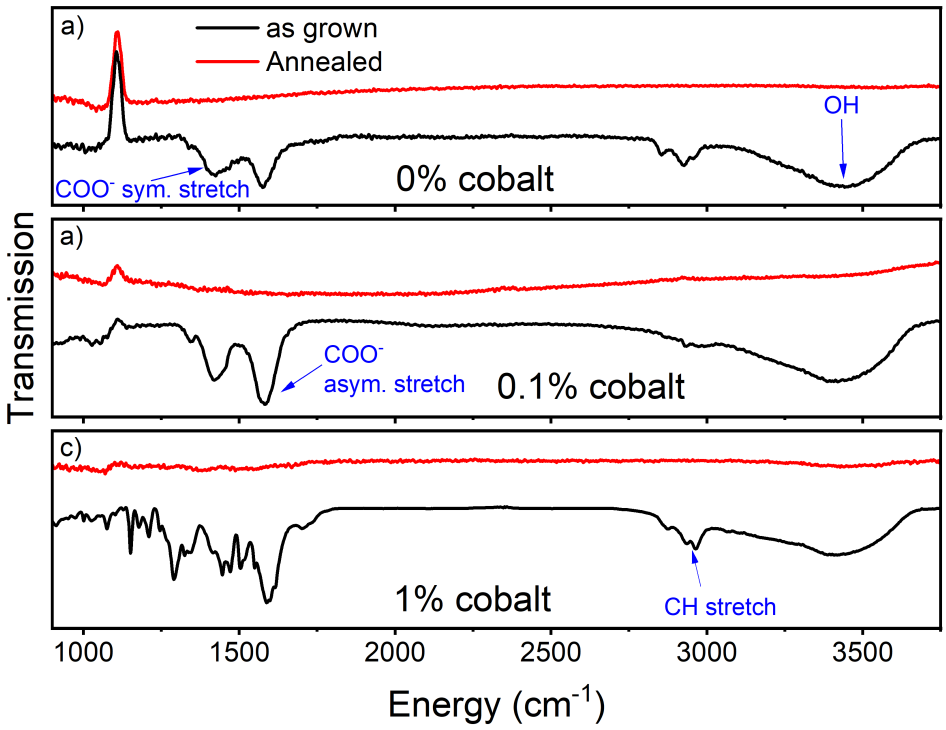

Figure 5.3: *FTIR analysis for ZnO:Co doped with percentage doping: (a)no doping, (b)0.01% and (c)1%. The presence of organic groups is identified in the as grown samples but are vanished when the samples are submitted to annealing procedures. Figure adapted from Figure [164].*

5.3 EPR Study

The EPR spectra of the as grown samples are presented in figure 5.4. In the left panel, the entire spectrum is presented without optical excitation (dark). The characteristic signal arising from the single Co^{2+} ions can be observed. In the right panel, the sample was exposed to optical excitation at a wavelength of 405 nm. Only the region where the organic compounds and the core defect resonate is highlighted. The presence of the core defect and the organic radicals is discernible. These two systems become less pronounced with an increasing concentration of Co^{2+} doping. This suggests a competition between the persistence of the core defect and the incorporation of cobalt into the lattice [121]. This behavior is highlighted in figure 5.6, where the presence of methyl radical in the surface and the core defect are traced as a function of the dopant amount.

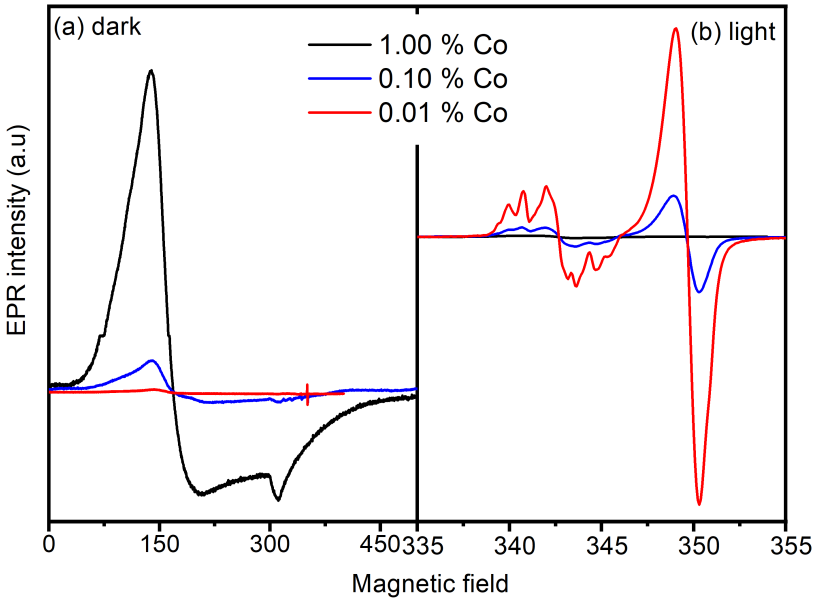

Figure 5.4: *EPR spectra of ZnO:Co as grown for different doping concentrations. In the left panel no optical excitation was applied and the spectrum present the intense signal related to the single Co^{2+} ions. In the right panel, the region where the photoactive signal appears is highlited, the presence of methyl formation decreases with increasing amount of doping. Figure [164].*

In the 0% cobalt case (used as reference), the photo-generated signal is clearly dominated by the four-lines structure of methyl radical around g = 2.003 and by an intense core-defect (g = 1.960). Other weaker lines are visible between those of methyl, likely to arise from surface-defect and/or other type of radicals. With increasing percentage of dopant, these lines decrease progressively and in 1%, they are barely visible. Even in the presence of the photo excitation, the NP's that present higher amount of cobalt in the lattice, have the core defect and the methyl complexes progressively vanished.

The efficiency of the substitutional cobalt doping within the ZnO matrix is examined through EPR conducted on the annealed samples. To facilitate comparison, the various spectra have been normalized as follows: First, using the 1% cobalt signal as a reference, the 0.1% cobalt signal is adjusted to be 10 times weaker. Subsequently, since the surface defect line (g = 2.003) does not exhibit significant variation in these two scaled spectra, it is inferred that this line's intensity remains nearly unaffected by the cobalt content. Consequently, the 0% cobalt sample spectrum is scaled in a manner that aligns its surface-defect intensity closely with that of the 0.1% cobalt sample.

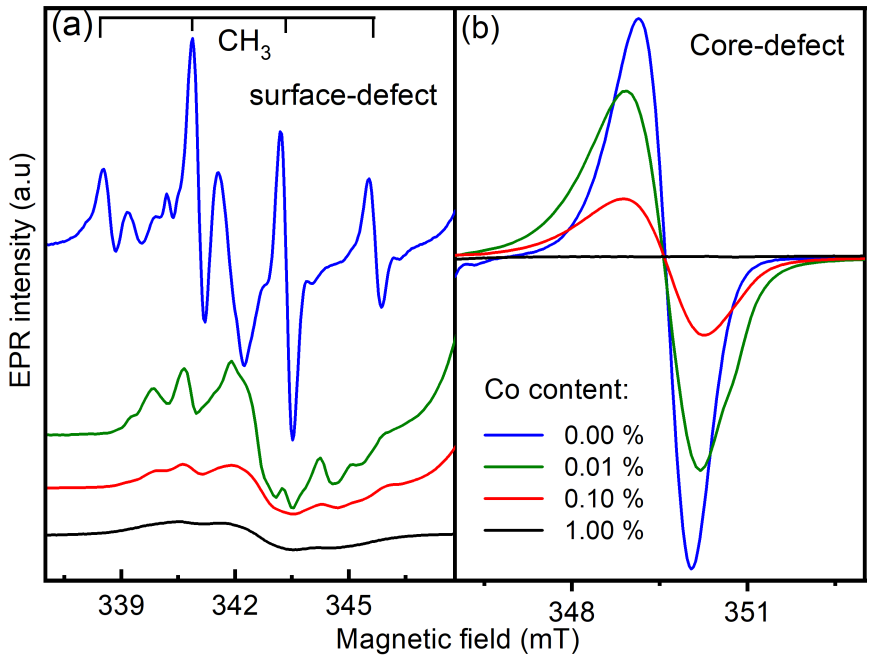

Figure 5.5: *The presence of cobalt ions in the ZnO lattice inhibit the presence of core defect and the formation of organic radicals in the NP surface. NPs were excited with light 405* nm.*Figure [164].*

Similarly to the non-doped NPs, the annealing procedure removes the organic shell and ionize the core defect, present at low concentrations of cobalt. For all the concentrations, a signal resonating at $g = 2.003$ is present, indicating the existence of surface defects in the NPs [127] [128].

In the annealed samples, the crystal quality is improved and the parallel component of the hyperfine coupling is resolved, having the best resolution for 0.1% doping. At higher concentrations, the dipolar broadening start to impact significantly the spectrum quality. The hyperfine interaction is presented in a group of 8 lines spaced by 1.6 mT. With increasing amount of Cobalt in the lattice, complexes Co-Co start to be identifiable, as represented in figure 5.6 (b), where the pairs denoted by J_6 and J_7 are noticeable. The study of these pairs is carried in more details in next section, with the samples containing more important amount of cobalt into the lattice.

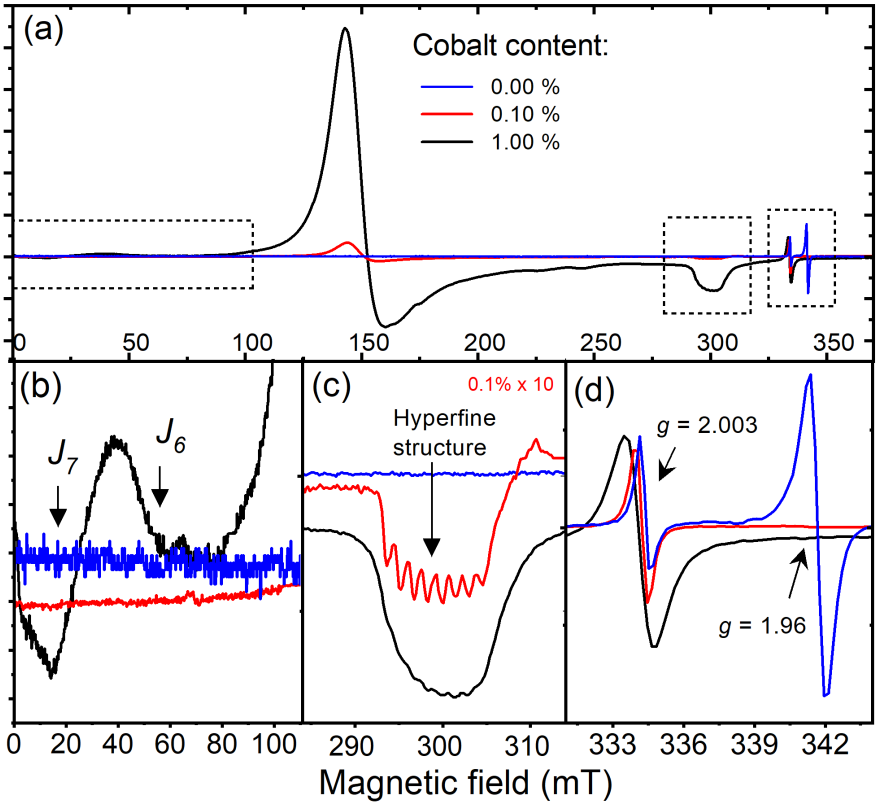

Figure 5.6: *EPR spectra of ZnO:Co annealed. In (a) the entire spectrum is presented. In (b) the presence of cobalt pairs start to be detectable for higher concentrations of Co doping. In (c), the parallel component of the hyperfine coupling is resolved and in (d), the presence of a surface defect at g=2.003 is present for all concentrations. The presence of core defect is only present for low doping concentration.Figure [164].*

5.4 ZnO:Co high-temperature method

5.4.1 Nanoparticle's characterization

The samples are presented in powder form from Co content ranging from 0 to 10%. The grains were observed by Scanning Electron Microscopy (SEM). The images obtained for 1% doping is showed in figure 5.7. Notably, the nanoparticles present heterogeneity in nanoparticle sizes and irregular shapes. The process of high temperature to which these nanoparticles are submitted to promote the doping certainly influences these irregularities.

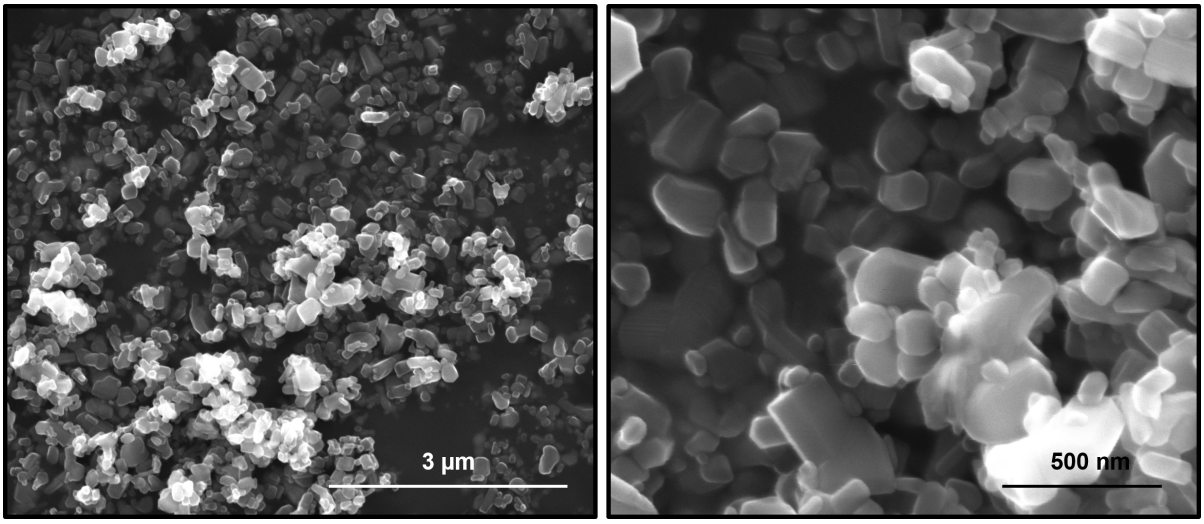

Figure 5.7: *Images obtained by Scanning Electron Microscopy (SEM) for ZnO:Co. The nominal percentage of doping is 1%*

The analysis of the crystalline structure was conducted using X-Ray Diffraction (XRD) spectroscopy. The results indicates that the nanoparticles present the crystalline plans associated to the hexagonal wurtzite structure for all the amounts of Co doping. No secondary peaks related to Co clusters or any other metal oxide or impurity were observed.

Nonetheless, the occurrence of a blue shift in the diffraction peaks as the doping percentage increases indicates the presence of tensile stress. This stress is a result of the mismatch between Zn^{2+} and substitutional Co^{2+} ionic radius. Consequently, the tensile stresses become more pronounced with higher concentrations of Co. The XRD spectra with the associated planes is shown in figure 5.8. The line crossing the (110) plane highlights the blue shift associated to tensille stress in the lattice

With the X-ray diffraction technique, the wurtzite lattice parameters a and c were calculated, using the expression

$$d^{-2} = 4a^{-2}/3 + c^{-2}, \tag{5.4}$$

where the planes (101) and (011) were considered for performing the calculation. The details of the correspondent geometrical representation of these parameters can be seen in details in Figure 1.1. The unit cell's volume, denoted as V was calculated using the formula:

$$V = \sqrt{3}\ a^2 c/2 \tag{5.5}$$

For all the doping amounts, the c/a ratio is smaller than the ideal value $\sqrt{8/3} \approx 1.633$, corresponding to wurtzite structures compressed along the c-axis. The disparities between the calculated values and the typical lattice parameters of ZnO, which are, $a = 3.249$ Å and $c = 5.206$ Å provide further evidence of the strain existing within the lattice [52]. These parameters remain within a narrow range of variation, diverging less than 4% when compared to the 1% nominal concentration.

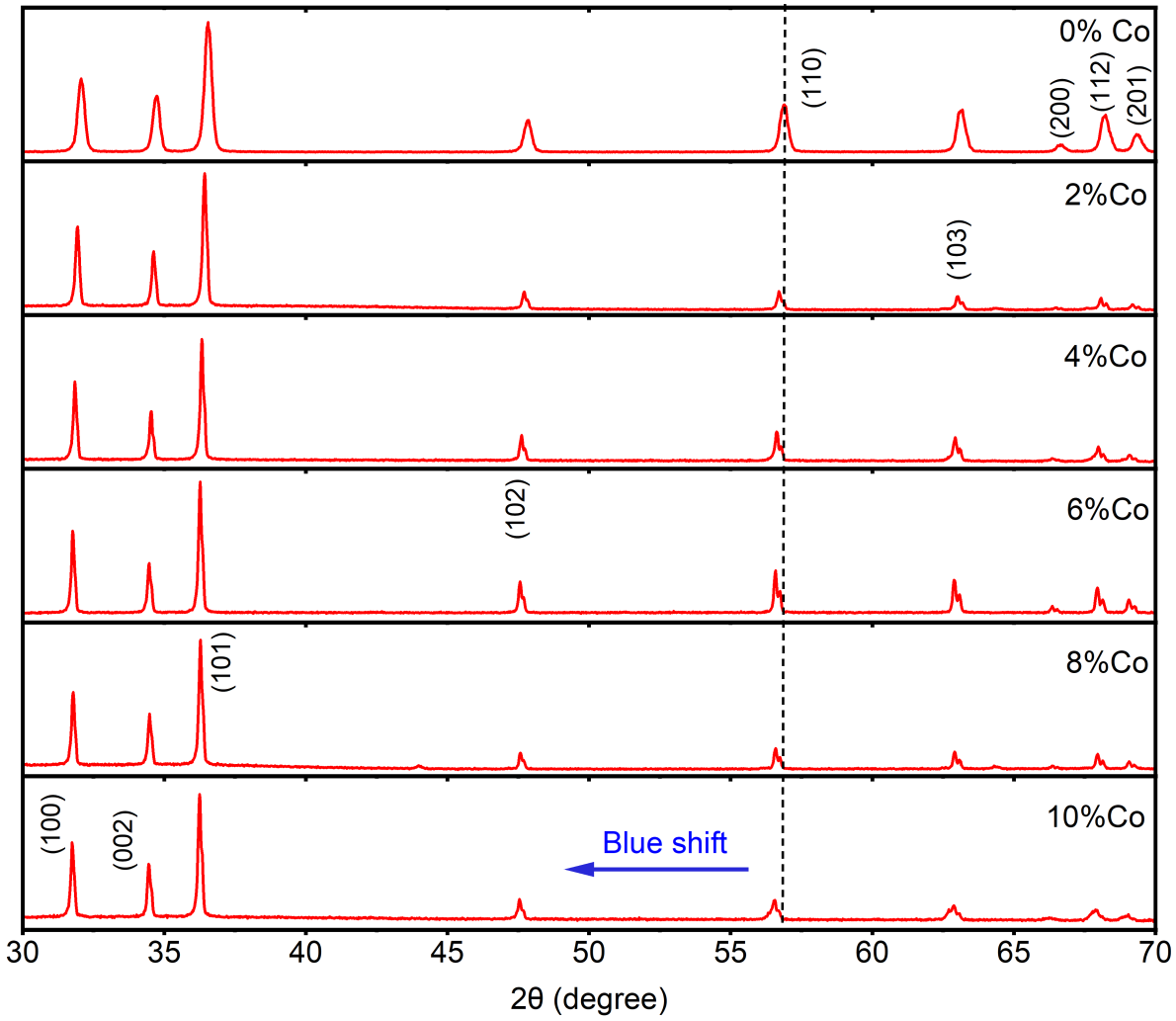

Figure 5.8: *XRD pattern for Co-doped ZnO nanoparticles produced by solid-state technique. The cobalt doping into ZnO lattice does not promote structural transitions. However, a blue shift associated to tensile stress is observed with increasing percentage of cobalt in the lattice.*

The deviation observed in the current values for the lattice parameters compared to those in the literature, where the structure is not subjected to stress, suggests the potential influence of confinement effects within the nanoparticles. The summarized results of all parameters for each concentration are presented in the following table:

The average crystal diameter, denoted as 'r' was determined using the Scherrer formula. This is a widely used method for estimating the size of crystals in powder form by analyzing the broadening of a peak in a diffraction pattern [165]. The relation is given by:

$$r = \frac{0.9\lambda}{\beta cos\theta}, \tag{5.6}$$

where λ stands for the wavelength of X-rays (1.54Å). The parameter β corresponds to the average width of the diffracted peaks, measured as the Full Width at Half Maximum (FWHM) in radians. Lastly, θ represents the angular position of the diffracted peaks in the diffraction pattern.

% Co	V (Å^3)	a (Å)	c (Å)	c/a
1	47.1339	3.2396	5.1857	1.6006
2	46.9444	3.2354	5.1785	1.6006
4	47.3025	3.2438	5.1911	1.6003
6	47.6032	3.2510	5.2008	1.5997
8	47.5618	3.2503	5.1985	1.5994
10	47.6672	3.2529	5.2019	1.5992

Table 5.1: *Lattice parameters for Zno Co-doped produced by solid state method*

Applying this method in the NP spectra, the average crystal size is found to be about 70 nm, in accordance with the results obtained by SEM, where NP's are observed to be averagely bigger than that, hinting at the possible presence of poly crystalline NPs in the sample.

5.4.2 EPR study

The Co^{2+} ions are characterized by a nuclear spin of $I = 7/2$ ^{59}Co in 100% abundance and an electronic configuration of $[Ar]3d^7$. This electronic structure can result in a high spin case $S = 3/2$ or a low spin case $S = 1/2$, depending on the symmetry of the environment, which drives the electrons distribution in the orbitals [166].

In the case of ZnO:Co with wurtzite symmetry, Co^{2+} assumes a high spin state. However, due to the crystal field splitting parameter D, this can be simplified to an "effective" spin of $\tilde{S} = 1/2$. It's important to note that D is approximately equal to 2.5 cm^{-1}. According to the Boltzmann law, the thermal energy required to occupy the state $\tilde{S} = 3/2$ is reached at temperatures around 3.6K, indicating that even at the lowest temperatures achieved in our study, these states were thermally occupied. The energy provided by the X-band microwave radiation is $h\nu \approx 0.3$ cm $^{-1}$, insufficient to couple the states.

This scenario is represented in Figure E.1, where the separation between spin projections $\pm 3/2$ and $\pm 1/2$ and its dependence on D value is illustrated. The effectiveness of the fictitious spin approach improves as the value of D becomes larger.

Figure 5.9 represents the energy levels for the high spin state cobalt ions. The equation in red determines the energy separation for each orientation θ of the crystal for the lower projection state ($m_s = \pm 1/2$). Assuming the two extremes cases, $\theta = 0°$ and $\theta = 90°$, the expression shows that the resonant field for the parallel direction is twice the value for the perpendicular one (assuming $g_{\parallel} \approx g_{\perp}$). Besides it, considering the orientation of the crystal, the easy plane orientation is favored, as expressed by the simulation presented in Figure 5.10.

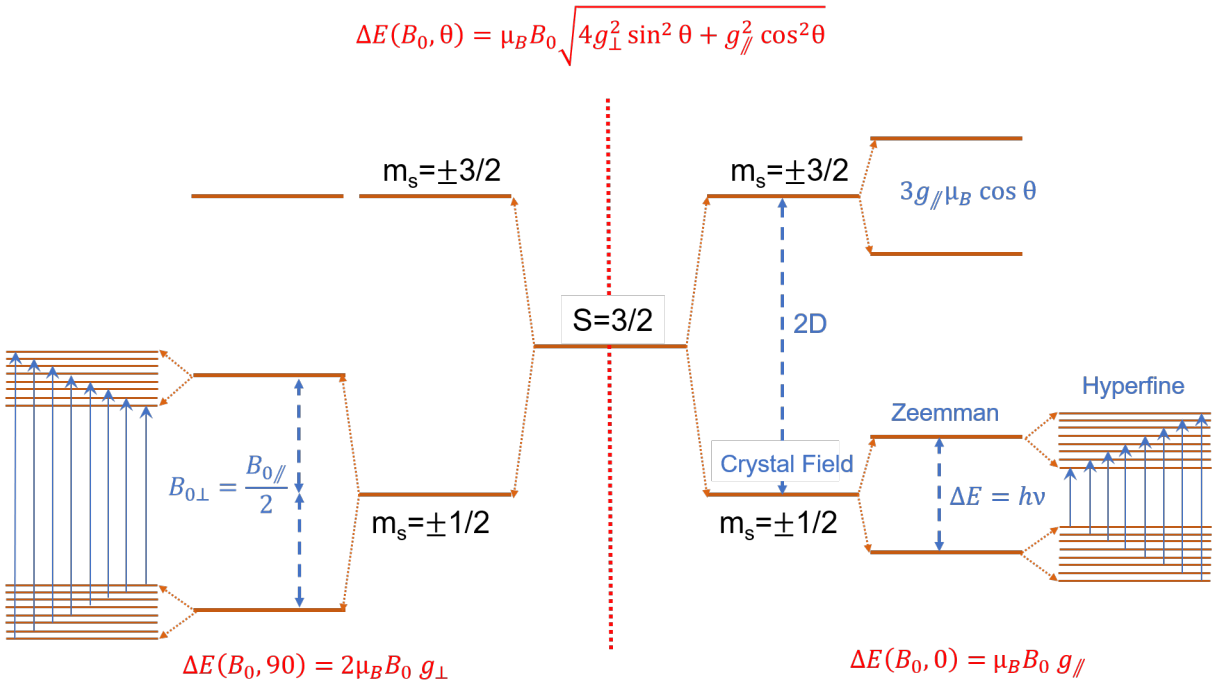

Figure 5.9: *Energy levels for an Co^{2+} ion. The low and high spin states are separated by the Crystal field constant D. The hyerfine splitting due to the interaction zith the $I = 7/2$ nucleus is represented for the lower case.*

In figure 5.10 (a), the distribution of states is presented. The states that have projections in the plane are more abundant, while a minority have projections along the axis. Due to this characteristic, the intensity of the signal originating from the perpendicular projection is considerably higher than that arising from the parallel projection. Taking into account this axial anisotropy, the spin Hamiltonian for a single ion can be explained as the combination of the crystal field contribution, the Zeeman splitting, and the hyperfine coupling:

$$H_1 = DS_z^2 + \mu_B \vec{S} \cdot \tilde{g} \cdot \vec{B} + \vec{S} \cdot \tilde{A} \cdot \vec{I} \tag{5.7}$$

Since the crystals exhibit a hexagonal structure, the orientation of the static magnetic field and the microwave application concerning the crystal's symmetry becomes a crucial factor. The detailed study of all the orientations possible of a crystal in EPR cavity and the exemplification of parallel and perpendicular mode is carried in Annex E. The EPR analysis of the NP powder, that accounts the average of all the possible crystal orientations is presented in Figure 5.11.

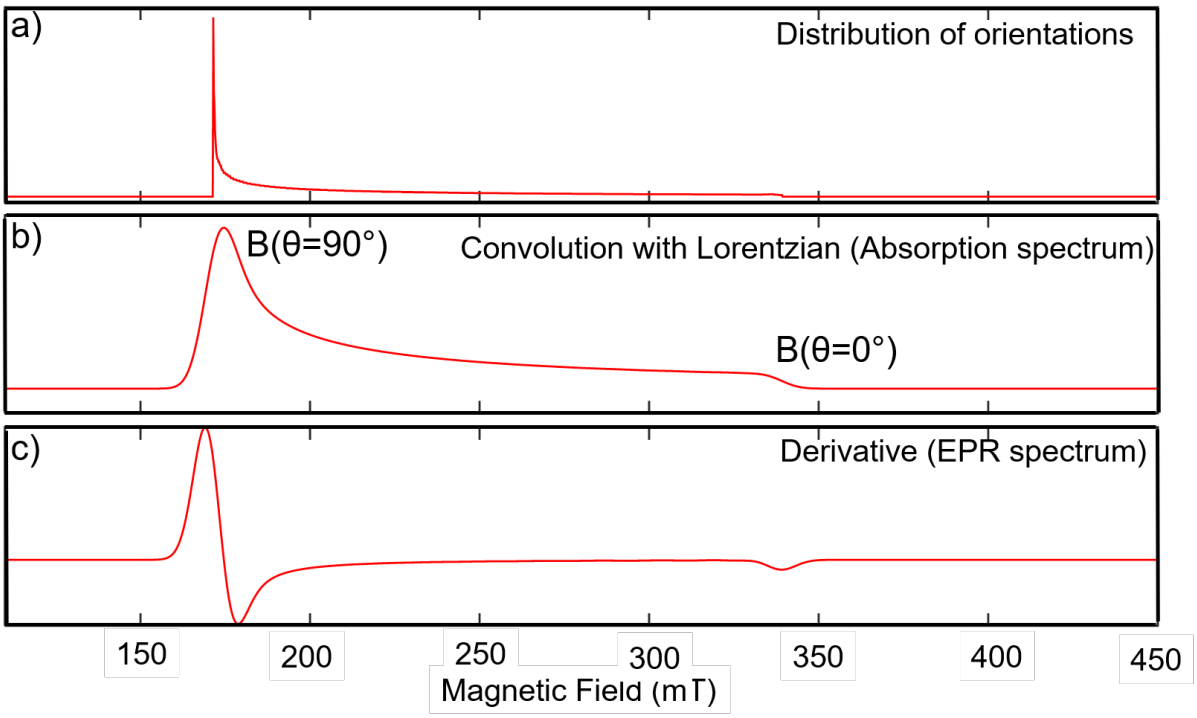

Figure 5.10: *Easyspin simulation for spin 3/2. The easy plane configuration is shown in (a), where the distribution of states that possess projection in the plane is way bigger than of those whom possess projection in the axis. In (b) the convolution with a Lorentzian distribution represents the absorption spectrum and in (c) the derivative simulates the EPR spectrum.*

The effective g factors extracted from the EPR analysis are $g_\perp = 4.479$, resonating at $B = 153.5\ mT$ and $g_\parallel = 2.245$, resonating at $B = 306\ mT$. In the configuration where the static magnetic field B_0 is aligned parallel to the crystallographic axis c, the hyperfine structure of the effective electronic 1/2 spin with the 7/2 spin of the ^{59}Co nucleus is resolved. This reveals a hyperfine coupling constant A of approximately 1.6 mT. It's noteworthy that the perpendicular component of the hyperfine constant is typically around five times smaller than the parallel component [167], and for this, it's not resolved for the powder spectra.

Remarkably, the hyperfine coupling value observed for Co doping in ZnO nanoparticles (NP) matches that of bulk ZnO:Co [168; 169]. This alignment suggests that these ions experience a comparable environment in these two distinct scenarios, since this coupling constant finely depends on the spatial extension of the Co^{2+} 3d wave functions. Furthermore, this resemblance also indicates the crystalline quality exhibited by the nanoparticles in these samples, where linewidths measuring less than 1.6 mT are observed, a rarity in ZnO:Co powders.

Due to the strong spin-lattice coupling of cobalt in ZnO, the system is susceptible to fast relaxation [170], [171] and the EPR signal rapidly decreases in temperatures above 30K. The fast relaxation time is also a limitating factor for pulsed EPR observation, and no detectable spin echo is produced by these samples.

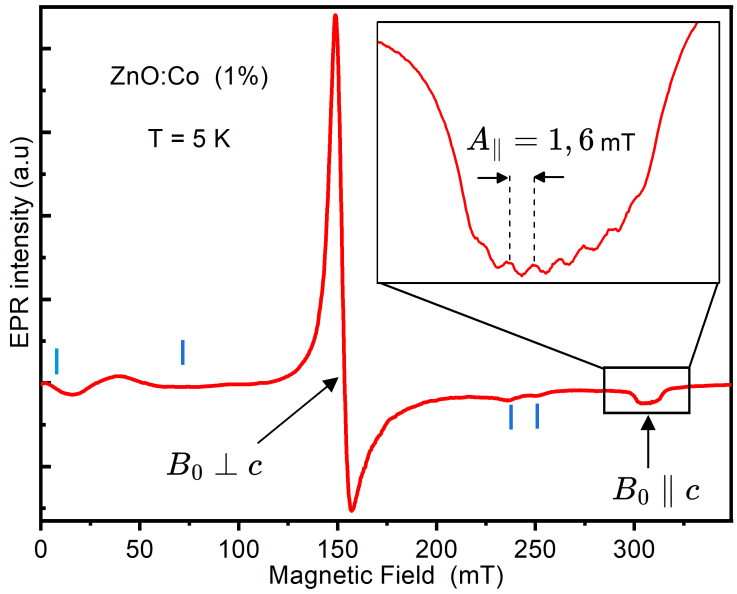

Figure 5.11: *X-band (9.6243 GHz) EPR spectrum of Co-doped ZnO (1 % Co) recorded at 5 K, 9 dB attenuation and 5 G modulation. The frame provides a zoom of the $B \parallel c$ orientation, where the hyperfine splitting is resolved ($A = 1.6mT$). The Blue marks indicate weak EPR lines that are not associated to single Co^{2+}. Figure from ref [172].*

Apart from the single-ion EPR line, there are additional weak lines detected, as indicated by the blue markers in Figure 5.11. These lines do not correspond to any transitions associated with the single ion Co^{2+}. To elucidate the nature of these lines, the same spectrum was recorded for various cobalt concentrations. The spectra were subsequently normalized to the maximum of the single-ion spectrum ($B_0 \perp c \approx 150$ mT) to facilitate the observation of any effects on these lines. This study is presented in Figure 5.12.

In Figure 5.12, a first study analyzing the behavior of the lines with increasing EPR power was performed. At higher power, the shape of the satelline lines is more evidenciated.

Following the condition that for a non-saturated system, by decreasing the power attenuation of 6dB the EPR intensity doubles, it is possible to observe that the cobalt lines start to present light saturation effect at power attenuation (9dB), as presented in Figure 5.13, where all the lines were normalized considering the linear behavior of the EPR intensity with increasing B_1. This behavior indicates a fast relaxation mechanism present in these resonant elements. Moreover, the effect of changing the power attenuation seems to have similar effect in all the satellite lines, indicating that they are incoming from the same system.

In the lower panel pf Figure 5.12, a comparison between different Co doping amount is presented. Notably, the linewidhts are augmented with increasing amount of cobalt. This phenomenon can be attributed to dipolar broadening, which become more intense as the concentration of paramagnetic species increases. Consequently, the resonance fields are progressively shifted away from their usual positions due to small local magnetic fields. These results strongly suggest the presence of a second-order interaction between Cobalt ions. Analytical and simulation treatments corroborate this hypothesis.

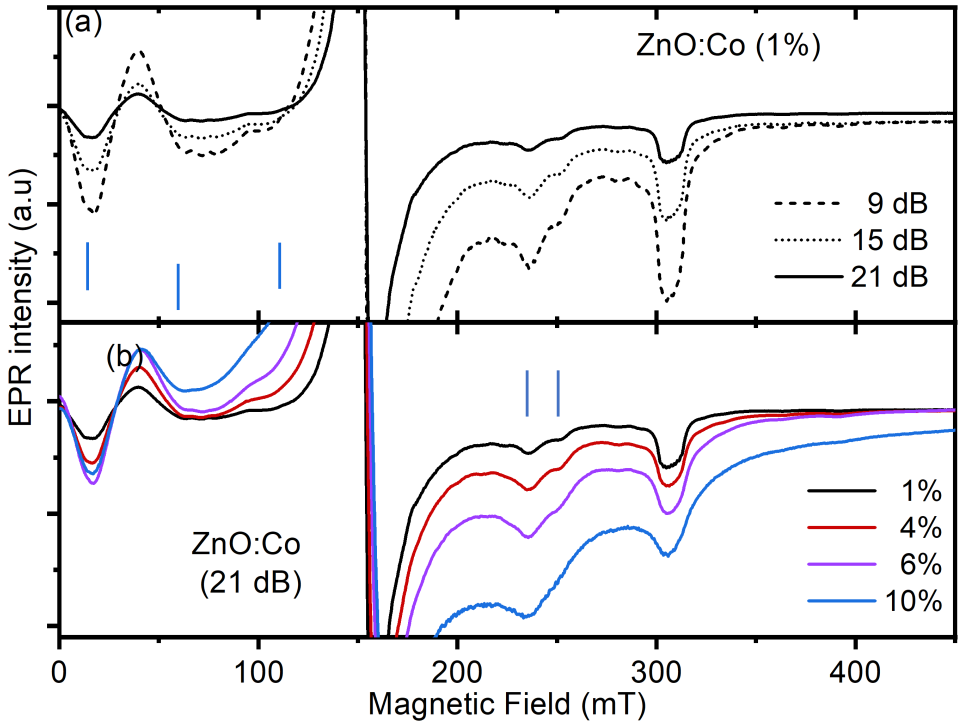

Figure 5.12: *In (a), X-band EPR spectrum of ZnO:Co (1 % Co) is presented. The spectra were recorded at 5K, with modulation of 5G and different mw power, controlled by the mw attenuation factor, from 9 to 21 dB. The presence of the secondary peaks are more accentuated in higher microwave power, showing the fast relaxation exhibited by these resonant elements. In (b), the evolution of the secondary peaks with increasing amounts of nominal cobalt doping. Figure from ref. [172].*

An interesting characteristic of the secondary lines is the presence of lines close to zero magnetic field. To get insight into these transitions and in its nature, EPR spectroscopy was conducted by inverting the static magnetic field B_0, so the lines resonating at the neighborhood of $B = 0$ are highlighted.

Applying this method, the zero-field line is highlighted and the absence of hysteresis phenomena in the origin indicates a full paramagnetic system, with no significant ferromagnetic contributions.

The complete EPR spectra in perpendicular and parallel mode is represented in figure 5.14, where two powers for the MW, where the system is at non-saturated regime. The EPR spectroscopy was performed in two different configurations. In (a) the oscillatory field is perpendicular to the static field and in (b) both fields are aligned in parallel. The details about these two distinct modes are illustrated in Annex E.

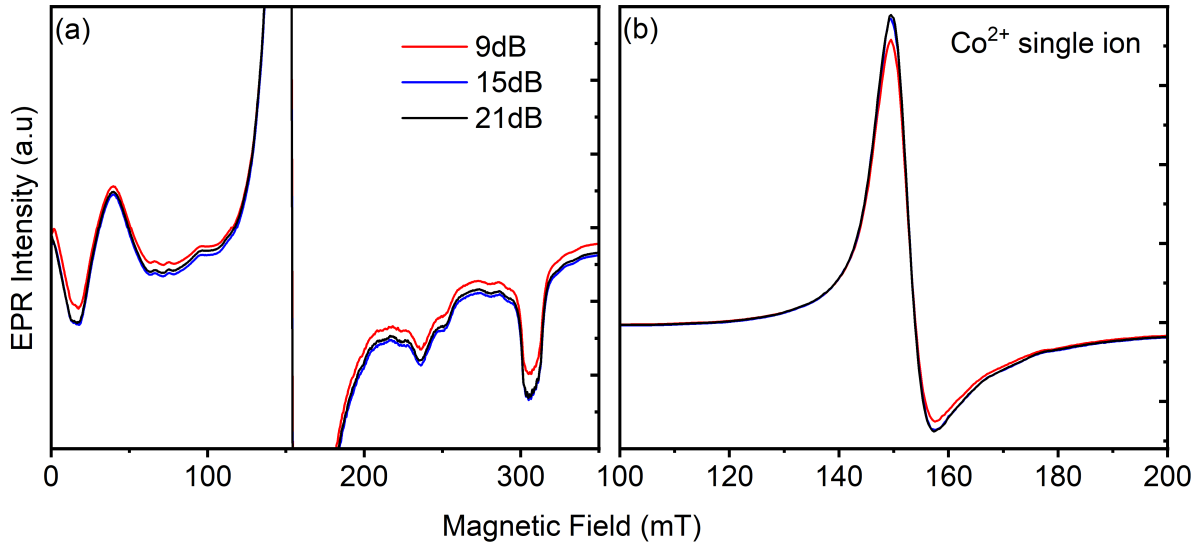

Figure 5.13: *Behavior of the EPR lines, changing the EPR power. All the saturation lines were normalized considering the linear dependence of the Intensity with increasing B_1. In (a) the satellite lines are highlighted and in (b) the single ion.*

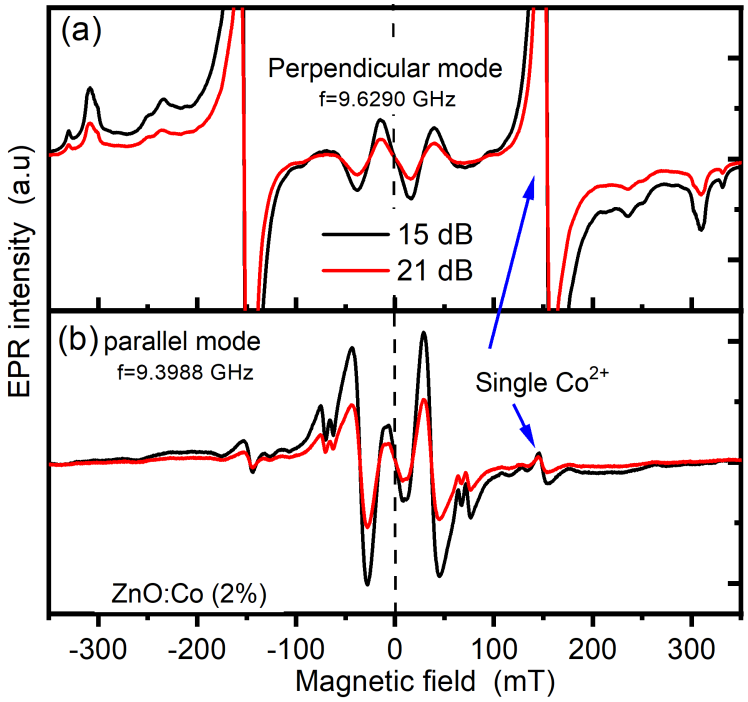

Figure 5.14: *(a) Perpendicular ($B_1 \perp B_0$) mode spectra of ZnO/Co 2%. (b) EPR spectra recorded using the parallel ($B_1 \parallel B_0$) mode of the dual mode cavity. In Both cases, the zero-field transition is present. Figure from ref. [172].*

Employing the parallel mode, the strong signal emanating from the single ion is sup-

pressed, leaving only a minor disturbance in the spectrum. This residual signal is a result of the sample's physical dimensions. Since the sample has a certain spatial extension, a portion of it can still be excited by small perpendicular microwave components, that is totally parallel just in the very center of the cavity. Non-surprisingly, the near zero field transition line still present, once that this transition is almost field independent, and thus, the orientation of the field is irrelevant.

5.5 Analytical and simulation approaches

Analytical and simulation analysis were carried in order to prove that the satellite lines arise from the formation of Co^{2+} pairs. The pairs are assumed to be coupled through isotropic Heisenberg exchange interactions. The key premise is that as the concentration of cobalt ions in the crystal increases, these ions become less isolated and are more prone to interact with one another.

5.5.1 Matrix interaction

The Hamiltonian describing the interaction between two ions is constructed by summing the individual Hamiltonians (H_1 and H_2), coupled with a term representing interactions between the ions. The strength of this coupling is determined by the J_k parameters. In this context, the complete Hamiltonian is given by

$$H = H_1(\vec{S}_1) + H_1(\vec{S}_2) - 2J_k(\vec{S}_1).(\vec{S}_2) \tag{5.8}$$

Each of the individual Hamiltonians (H_1 and H_2) account terms of crystal field, Zeeman and hyperfine interactions specific for each ion, as presented in equation 5.7.

To facilitate the analytical treatment, the hyperfine coupling is omitted as it doesn't impact the pair behavior. Subsequently, the crystal field and exchange interaction are exactly solved, and the Zeeman interaction is considered as a perturbation in a second step. This approach is justified by invoking the low field approximation. The effective transitions are then calculated using the transition Hamiltonian (H_1), considered in the final step. In summary, the approach used to fully describe the system is illustrated in Figure 5.15, where all the considered terms are explicit.

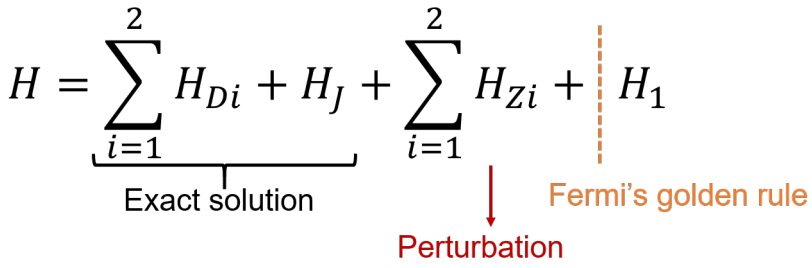

Figure 5.15: *Approaches used to solve the complete Hamiltonian.*

In this context, the part of the Hamiltonian that is exactly solved is given by:

$$H = D(S_{1z}^2 + S_{2z}^2) - 2J_k(S_{1x}S_{2x} + S_{1y}S_{2y} + S_{1z}S_{2z}), \tag{5.9}$$

where the formalism of raising and lowering operators can be used (see Annex C for details), leading the Hamiltonian to the representation

$$H = D(S_{1z}^2 + S_{2z}^2) - J_k(S_1^+ S_2^- + S_1^- S_2^+ + 2S_{1z}S_{2z}). \tag{5.10}$$

The coupling Hamiltonian includes the single-ion anisotropy ($D = 2.76cm^{-1} = 3.97K$) and an isotropic Heisenberg coupling J with values in the range from $J = |0.134|$ to $|0.382|$ K. In the adopted notation, positive values of J indicate the formation of ferromagnetic pairs and negative values antiferromagnetic pairs.

Since that different spin projections are not coupled by the Hamiltonian (Zeeman is not present), the exact solution can be obtained, resulting in a 16-dimensional state space. These states are numerated and presented in the table below, where the spin state for individual ions m_{si} and for the pair $m_{s\ \mathrm{total}}$ are explicit.

$m_{s\ total}$	m_{s1}	m_{s2}	state
+1	+1/2	+1/2	$\|1\rangle$
0	+ 1/2	-1/2	$\|2\rangle$
0	-1/2	+1/2	$\|3\rangle$
-1	-1/2	-1/2	$\|4\rangle$
+2	+3/2	+1/2	$\|5\rangle$
+2	+1/2	+3/2	$\|6\rangle$
-2	-3/2	-1/2	$\|7\rangle$
-2	-1/2	-3/2	$\|8\rangle$
+1	+3/2	-1/2	$\|9\rangle$
+1	-1/2	+3/2	$\|10\rangle$
-1	-3/2	+1/2	$\|11\rangle$
-1	+1/2	-3/2	$\|12\rangle$
+3	+3/2	+3/2	$\|13\rangle$
0	+3/2	-3/2	$\|14\rangle$
0	-3/2	+3/2	$\|15\rangle$
-3	-3/2	-3/2	$\|16\rangle$

Furthermore, all the non-diagonal terms within the matrix arise from the Heisenberg coupling term, specifically the formation of Co^{2+} pairs. Thus, the total spin projection m_s for these states must be conserved. This property leads to a simplification in the treatment, once that the 16-dimensional matrix can be divided into secondary matrixes, each one associated with a specific m_s value. The rearranged system with the respective spin projections is represented by the matrix below:

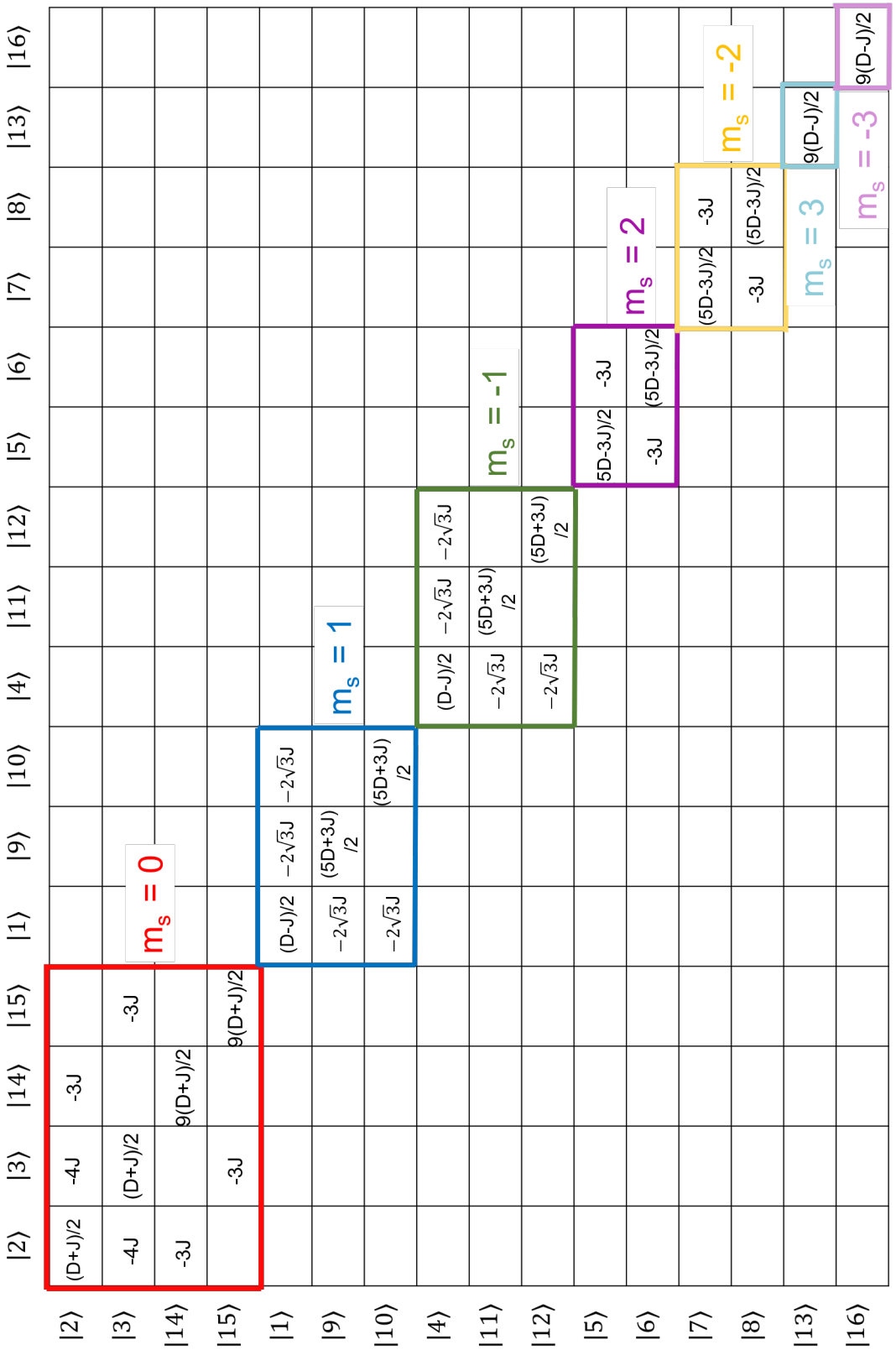

Figure 5.16: *The 16 states can be separated by total spin projection. In this scenario, the system is subdivided in one matrix with dimension 4 corresponding to* $m_s = 0$*, two matrixes with dimension 3 corresponding to* $m_s = \pm 1$*, two matrixes with dimension 2 corresponding to* $m_s = \pm 2$ *and two matrixes with dimension 1 corresponding to* $m_s = \pm 3$*,*

The only states of interest are those with spin projections $m_s = 0, \pm 1$ arising from the lower states. Attention must be taken due to the fact that the higher energy states can also yield these projections and should not be considered.

5.5.2 Eigenenergies and eigenstates

Considering the Hamiltonian presented in the last section and the approach for exact diagonalization, the associated energy for the system, arising from the lower manifold are:

$$\begin{aligned} E_1 &= 1/2(3D + J - \sqrt{X}) \\ E_3 &= 1/2(3D + J - \sqrt{X}) \\ E_2 &= 1/2(5D + 9J - \sqrt{Y}) \\ E_4 &= 1/2(5D + J - \sqrt{Z}). \end{aligned} \tag{5.11}$$

The correspondent eigenstates, composed by the linear sum of the eigenvectors for this projection are

$$\begin{aligned} |v_1\rangle &= \alpha(+|1\rangle + |4\rangle) + \beta(+|9\rangle + |10\rangle + |11\rangle + |12\rangle) \\ |v_2\rangle &= \gamma(-|2\rangle + |3\rangle) + \delta(-|14\rangle + |15\rangle) \\ |v_3\rangle &= \alpha(+|1\rangle - |4\rangle) + \beta(+|9\rangle + |10\rangle - |11\rangle - |12\rangle) \\ |v_4\rangle &= \epsilon(+|2\rangle + |3\rangle) + \xi(+|14\rangle + |15\rangle). \end{aligned} \tag{5.12}$$

The respective coefficients used in the calculus are explicated in Annex F.

In Figure 5.17 the energy levels adopting this simplified calculus is represented. The energies E_1 and E_3 are degenerated. Note that two energy differences are present and are denoted by Δ_1 and Δ_2. Once that Δ_2 is related to a different effective spin, it can not be couplet to other energy levels, thus Δ_2 does not represent a real transition

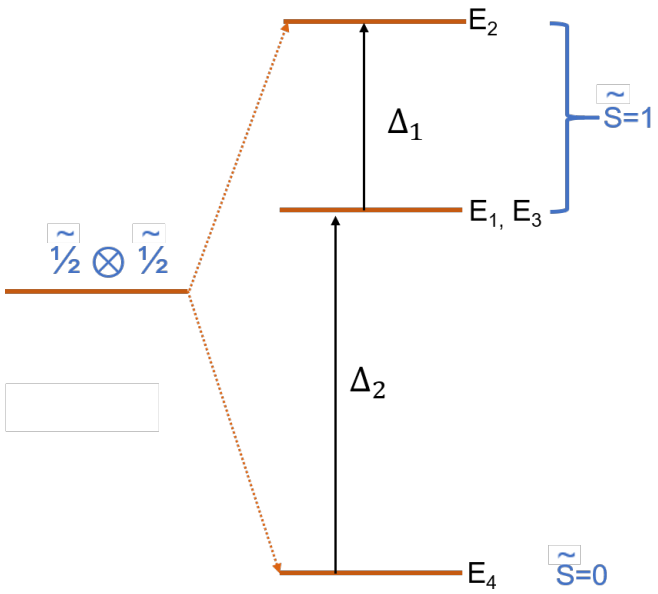

Figure 5.17: *Simplified energy levels for the formation of cobalt pairs. The results are obtained by the calculation of fictitious spins 1/2 coupled by exchange interaction.*

The value of Δ_i are

$$\begin{aligned} \Delta_1 &= |E_2 - E_{1,3}| = |-D + \sqrt{Z} - \sqrt{X}| \\ \Delta_2 &= |E_{1,3} - E_4| = |D + 4J + \sqrt{X} - \sqrt{Y}| \end{aligned} \tag{5.13}$$

The X,Y and Z parameters are explicit in Annex F. Adopting the condition $D >> J$, the value of the transition Δ_1 can be expanded in J/D powers up to second order, simplifying the results:

$$\Delta_1 \simeq 3|J| \left(1 - \frac{13J}{4D} + \frac{5J^2}{2D^2}\right), \tag{5.14}$$

The limit $\Delta_1 = 3|J|$ is achieved considering $D \to \infty$. In this case, the separation of manifolds provided by the crystal field is large enough to eradicate the interaction. No further consideration will be given to the energy difference Δ_2, once that it doesn't present an effective transition and can be disregarded without any lost.

5.5.3 Perturbational treatment of the Zeeman interaction

Up to this point, we have considered the crystal field and exchange coupling, and the Hamiltonian has been exactly diagonalized. At this stage, the Zeeman interaction is introduced as a perturbation to correct the energy levels.

In systems with axial symmetry, where the x and y directions are equivalent, calculations yield the same results when considering the transition Hamiltonian in either the x or y direction. The introduced Zeeman Hamiltonian takes into account the effect on ions 1 and 2:

$$H_z = g_\perp \mu_B (S_x^1 + S_x^2) B_0 \tag{5.15}$$

In the perturbation treatment, the first order correction give zero contribution to the energy levels, in order that the first contributions are given by the second order terms:

$$\epsilon_i = g_\perp^2 \mu_B^2 B_0^2 \frac{\sum_{i \neq j} |\langle v_i| S_x^1 + S_x^2 |v_j\rangle|^2}{E_i - E_j} \tag{5.16}$$

The field-dependent term is highlighted in red, revealing a parabolic dependence characteristic of second-order features. The disparity introduced in the energy levels of the system is evident in Figure 5.18, where the exact solution corresponds to situation (a), and the Zeeman perturbation results in situation (b). The non-linear Zeeman effect is responsible for the presence of zero-field transitions.

The perturbation doesn't couple degenerated states ($\langle v_1| H_Z |v_3\rangle = 0$), in such a way that the perturbation theory for non-degenerated states can be applied. In this sense, the second order perturbation applied to the other states (those related to energies E_2 and E_4). In this case, the correction for the four levels is $\epsilon_2 = \epsilon_3 = 0$, $\epsilon_4 = KB^2$ and $\epsilon_1 = -KB^2$, implementing a parabolic dependence on the energy levels E_1 and E_4, as showed in Figure 5.18. The allowed transitions are represented in red for the perpendicular case and in blue for the parallel one.

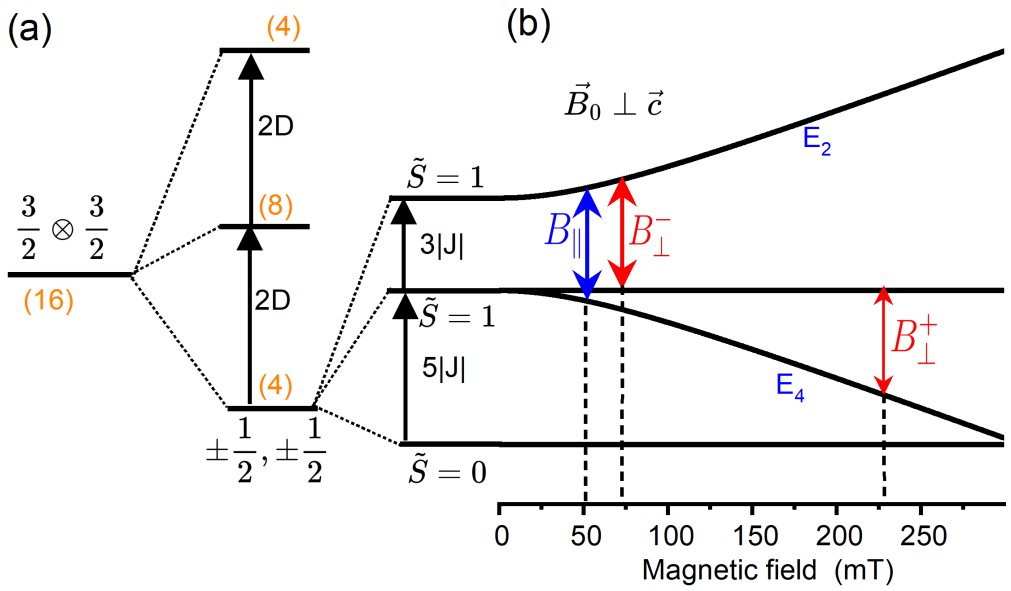

Figure 5.18: *Energy levels for Co^{2+} ions interacting through exchange interaction. Only the lower level of the entire manifold is considered. In (a), the energy levels resulting from the exact solution of the Hamiltonian are provided, while in (b), the perturbative Zeeman interaction is also taken into account. Figure adapted from ref. [172].*

The coefficient K, that corrects the energy levels is given by the expression

$$K = \frac{g_{\perp}^2 \mu_B^2}{\Delta_1} \frac{[2D^2 + 25J^2 + \sqrt{XZ} + 4J(\sqrt{X} + \sqrt{Z}) + D(12J + 2\sqrt{X} + \sqrt{Z})]^2}{[D^2 + D(2J + \sqrt{X}) + J(25J + \sqrt{X})][4D^2 + 2D(8J + \sqrt{Z}) + J(25J + 4\sqrt{Z})]} \tag{5.17}$$

5.5.4 EPR transitions

EPR transitions occur when the transition probability of an electron in an initial state i transitioning to a final state f is non-zero. The coupling between the initial and final states is achieved through the oscillatory field B_1 (MW). The transition probability is mathematically expressed by the transition Hamiltonian, which follows the Fermi's golden rule [173]:

$$T_{i \to f} = \frac{2\pi}{\hbar} |\langle f | H_t | i \rangle|^2 \rho(E_f), \tag{5.18}$$

where i and f stands for initial and final states, respectively. H_t designates the transition Hamiltonian, and ρ is the density of states.

The transition probabilities were calculated in the vicinity of the lower manifold by applying the condition $D \to \infty$ following the method presented in reference [174]. In this simplified approach, only spins with individual projections $m_{is} = \pm 1/2$ are considered, so only states $|1\rangle$ to $|4\rangle$ are taken into account. Within this basis, exact solutions for the Heisenberg coupling and Zeeman interaction are obtained. The transition Hamiltonian is then applied to these states, and the results are directionally dependent:

$$
\begin{aligned}
W_{\parallel}(x) &= \frac{8\pi\rho}{\hbar} g_{\perp}^2 \mu_B^2 B_1^2 \left[1 + \left(\frac{4 g_{\perp} \mu_B B_0}{3J}\right)^2\right]^{-1} \\
W_{\perp}^{\pm}(y) &= \frac{4\pi\rho}{\hbar} g_{\perp}^2 \mu_B^2 B_1^2 \left[1 \mp \left(1 + \left(\frac{4 g_{\perp} \mu_B B_0}{3J}\right)^2\right)\right]^{-1/2} \\
W_{\perp}^{\pm}(z) &= \frac{g_{\parallel}^2}{4 g_{\perp}^2} W_{\perp}^{\pm}(y)
\end{aligned}
\tag{5.19}
$$

Interestingly, the transition probability for a magnetic field B_1 applied parallel to the static field B_0 is non-zero. This is a very rare result that arises from the present anisotropy that generates a nonlinear Zeeman effect. For parallel mode, only one transition is present, and its transition probability is maxima close to zero field. It goes to zero as the field is increased, when the level slope becomes linear.

For y and z directions, two transitions are expected, where the exponent $+$ and $-$ designates high field and low field, respectively. All these features are represented in the figure below

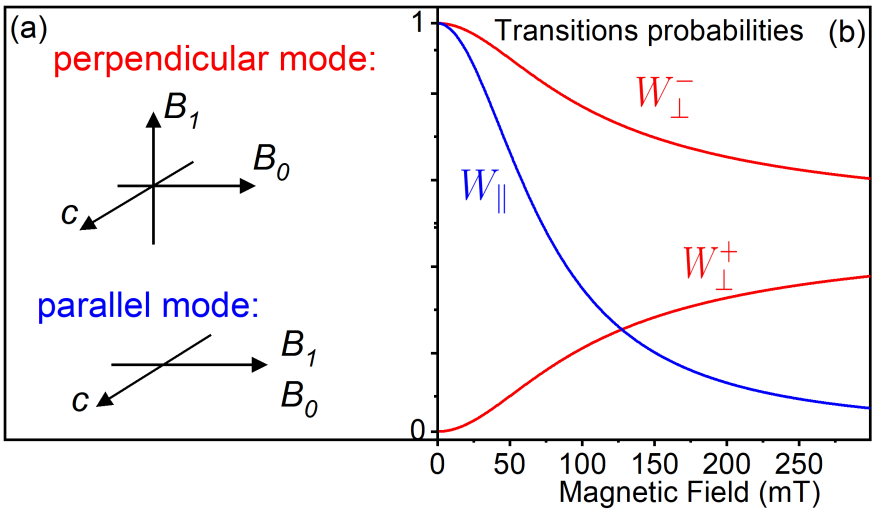

Figure 5.19: *Transition probability for the allowed transitions for Cobalt pairs embedded in ZnO matrix.Figure adapted from ref. [172].*

5.5.5 Simulations

Simulations were conducted using the EasySpin toolbox, and the results corroborate the analytical calculations. Through the simulations, the values of the Heisenberg couplings (J) and the weights associated with the abundance of each pair (w_i) were determined. For all simulations, the single-ion spectrum to pair spectra ratio is 170:w_i. In Table 5.2, the coupling values and its relative abundance obtained in our study with NPs is presented. For comparison, we include results obtained by other authors with nanowires (NW) [175] and in bulk [176] samples.

i	wi	J_i (NP) (K)	J_i (NW) (K)	J_i (Bulk) (K)
4	2	-0.378	-0.379	-0.382
5	6	+0.351	+0.3636	+0.347
6	6	+0.145	+0.170	+0.168
7	3	-0.137	-0.138	-0.134

Table 5.2: *Values of the Heisenberg exchange constant J_k and its associated weight w for Cobalt pairs within ZnO nanoparticles. A positive sign indicates ferromagnetic coupling, while a negative sign indicates antiferromagnetic coupling. The values obtained for nanoparticles (NPs) are the results of this study, while the values for nanowires (NW) and bulk are extracted from references [175] and [176], respectively.*

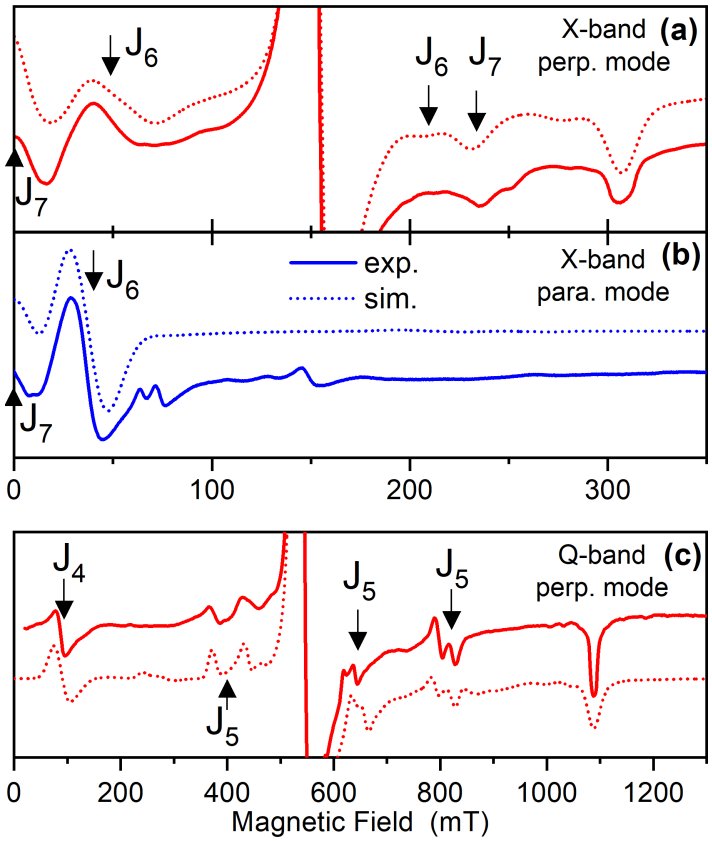

Figure 5.20: *Identification of the cobalt pairs in ZnO nanoparticles. Solid lines represent experimental spectra and dashed lines simulations. The pairs resonate in X band perpendicular (a) and parallel (b) modes and also in Q-band (c). Figure adapted from ref. [172].*

The notation starting by J_4 is adopted for keeping the accordance with other published results carried by other authors who identified Cobalt pairs in bulk samples [175].

The presence of two ferromagnetic pairs (J_5 and J_6) and two antiferromagnetic pairs (J_4 and J_7) are predicted, but only J_6 and J_7 resonate at X-band. The identification of the pairs J_4 and J_5 is possible by conducting EPR in the Q-band regime. The zero-field resonance line arises from the J_7 pair, while the other pairs are responsible for promoting the weak-field line distributed in the spectra. Simulations carried out using the EasySpin

tool in Matlab support this model and indicate that the J_6 pair exhibits a robust signal in the parallel mode.

Figure 5.20 presents all the identified Cobalt pairs in the X-band (both perpendicular and parallel modes) and Q-band. The solid lines correspond to the experimental spectra, while the dashed lines represent simulations. When performing the simulations, all the pairs were considered simultaneously. Consistent with experimental observations, it was noted that the pairs resonating in the X-band did not interfere with the Q-band spectrum, and vice versa.

In previous works conducted by Savoyant et al. [175], the analysis of the physical locations of these pairs within the ZnO lattice was considered, and the conclusions are presented in Figure 5.21. The geometry constraints imposed by the ZnO lattice compel the formation of cobalt pairs that assume a discrete range of values for the J coupling. The separation distance of these pairs is estimated to range from 4 to 6 angstroms.

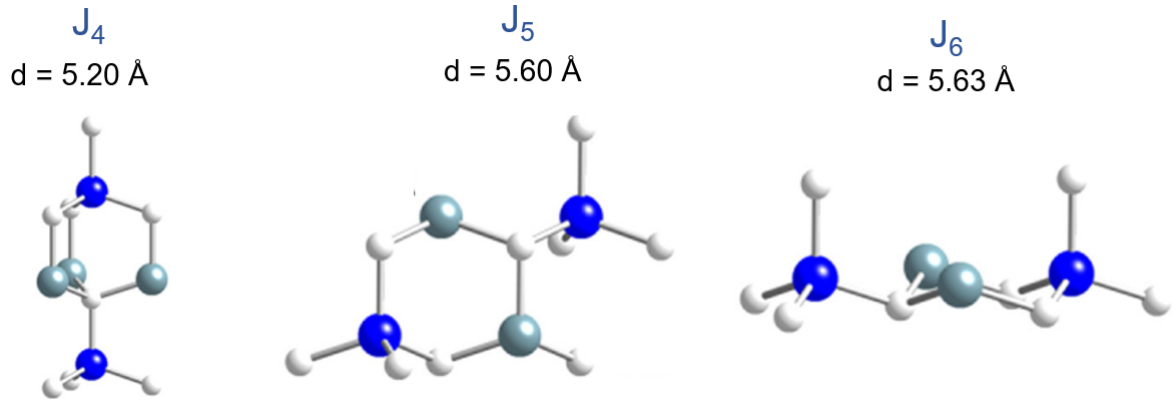

Figure 5.21: *The positions of Cobalt pairs corresponding to the coupling values J_4, J_5, and J_6, along with their respective distances between centers. In the figure, oxygen, zinc, and cobalt ions are represented in light gray, gray, and blue, respectively. This representation is adapted from [175].*

5.6 Partial conclusions

The nanoparticles synthesized via the sol-gel method exhibit an average diameter of approximately 15 nm. The doping process does not impact the size of the nanoparticles. However, subjecting the NPs to an annealing procedure results in an increase in diameter up to 50 nm. The NPs produced by sol-gel method are noticeably smaller than those doped through solid-state reaction, which have an average diameter of 70 nm. Both fabrication techniques result in nanoparticles with high crystallinity. The structural pattern conforms to the wurtzite crystal structure, and there is no discernible formation of Cobalt clusters in the material.

The incorporation of cobalt into the ZnO lattice leads to the elimination of the core defect, suggesting a competitive relationship between these two systems. The generation of methyl radicals on the NP surface, triggered by a photo-Kolbe reaction, is notably reliant on the presence and activation of the core defect. In situations where the core defect is absent, the formation of methyl radicals is inhibited.

The amount of the photo-generated holes can be controlled by increasing the temperature and also by cobalt incorporation in the ZnO NPs. When the amount of cobalt becomes important (more than 1%), the cobalt ions are less isolate and interact by Heisenberg exchange, resulting in detectable Co^{2+} pairs. The values of the coupling constants J_k have been determined, and their presence has been associated with two ferromagnetic and two antiferromagnetic pairs within the EPR spectra, spanning the X and Q bands. The estimated values of the J coupling range from |0.137| to |0.378|K.

In the case of Co^{2+} pairs, their high anisotropy leads to a parabolic relationship in the resonating levels, facilitating the occurrence of EPR transitions in the parallel mode. Finally, the most limiting factors for the use of such paired spins in a quantum technology context is the difficulty controlling their number and nature.

Chapter 6

Physical modelling

Contents

6.1 Origin of the 3-lines system 140

6.2 Polar nanoparticles 148

6.2.1 Non-passivated nanoparticles 150

6.2.2 Passivated nanoparticles 152

In this chapter, we initially focus on the 3-lines system, examining its properties demonstrated in preceding chapters as a means to suggest an origin for this system. Our hypothesis, which centers on the formation of biradicals is supported through simulations using the EasySpin software.

In a second moment, we introduce a physical model grounded in the properties specific to ZnO nanoparticles, as detailed in Chapter 1, aiming to elucidate the formation of the paramagnetic centers described in the preceding chapters. This model relies on the polarization inherent to the ZnO when it exists in the Wurtzite structure. We propose that the polarization generates fictitious charges located on the surface, necessitating the presence of passivation mechanisms to re-establish thermodynamic equilibrium.

Concisely, the primary objectives of this chapter are:

1. To introduce potential origins for the 3-lines system observed in the NPs upon methyl radical formation. Simulations conducted with EasySpin software suggest the possibility that these lines result from the formation of biradicals, emerging from the interaction between two neighboring methyl radicals.

2. To provide an explanation for all the observed results presented in the preceding chapters by qualitatively describing the NP physics. The discussion involves the surface passivation through various mechanisms, including shell and core impurities. This approach successfully accounts for the appearance of the paramagnetic state of the core defect when the NPs undergo photo-excitation. Additionally, it associates the formation of methyl radicals on the NP surface as a consequence of the ionization of the core defect via a photo-Kolbe reaction and explains the presence of acetic acid and acetates at the NP surface.

6.1 Origin of the 3-lines system

In this section, we suggest that the identified 3-lines system in the analyzed samples results from the interaction between two methyl radicals, occurring through exchange interaction potentially accompanied by dipolar interactions. This process results in the creation of biradicals.

In Section 4.6.1, we showed that heating the as-grown sample up to 110 K triggers a chemical reaction leading to the loss of methyl radicals. Before reaching the initial state, these elements go through an intermediate stage that is EPR silent. Despite this reaction involving methyl radicals, all measurements confirm that the 3-lines system does not relax from its optical excited state and does not decrease in quantity when the temperatures are elevated up to 110K. In the following, we reanalyze these results in order to associate the 3-lines group to the formation of biradicals.

Considering the experiment described in Section 4.6.1, where the sample was illuminated at 8K and then subjected to heating cycles with the laser turned off. To recap the experimental procedure: the sample was first illuminated at 8K. Following that, the laser was turned off, and an initial EPR spectrum was recorded. Subsequently, the sample was heated up to 110K and then cooled back down to 8K. Another EPR measurement was conducted. For a clearer representation of this experimental pathway, the described sequence is depicted in Figure 6.1.

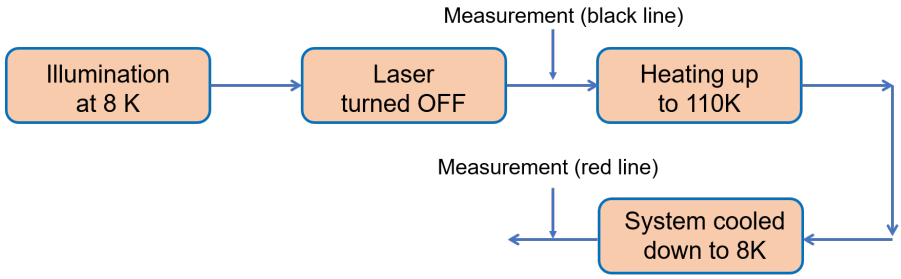

Figure 6.1: *Pathway of the experiment resulting in the behavior depicted in Figure 6.2.*

Figure 6.2 illustrates the comparison between the initial spectrum (dark line), the spectrum recorded at 8K after the heating process (red), and the difference between the initial spectrum and the spectrum after heating (blue). This analysis is performed on the absorption spectra to facilitate a comparison between the findings obtained from CW EPR and PW EPR, alongside simulations executed using the EasySpin software.

In Figure 6.2, we observe that the difference between spectra (blue line) corresponds to the signal of methyl radical, indicating that with the heating cycle, methyl radicals were eliminated from the system, but the 3-lines system remained unchanged after the heating cycle.

The chemical reaction that vanishes the methyl radicals is expected to take place around 30 K and above, causing an abrupt change in the system's behavior that impacts the relaxation time T_m of the system. This characteristic was observed in the analyses conducted in Sections 4.4.4 and 4.10.1.

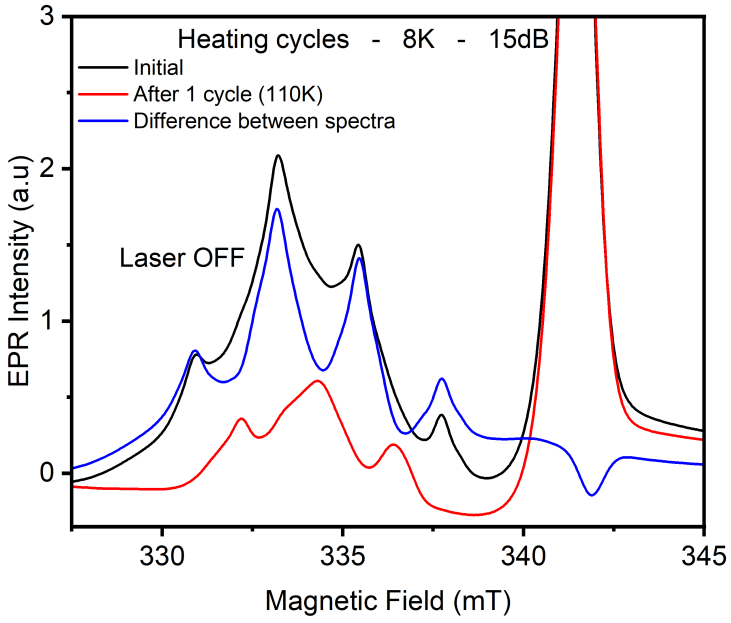

Figure 6.2: *EPR absorption spectra of the sample as-grown. The sample was illuminated at 8K (dark line). After illumination, the system was heated up to 110K (with the laser off) and then cooled down to 8K for a subsequent measurement (red). The discrepancy between these spectra, shown in blue, demonstrates the disappearance of the methyl radicals.*

The results are promising, but the saturation of the methyl EPR transitions and its possible hindered rotation at low temperatures result in broad lines, that difficult the analysis. To overcome this challenge, a new analysis was conducted using spectra

recorded at 60 K from the same experiment. However, following the measurement at 8 K, a subsequent illumination was performed after finishing the cycle. To facilitate the visualization of the experiment, the experimental pathway of this approach is illustrated in Figure 6.3.

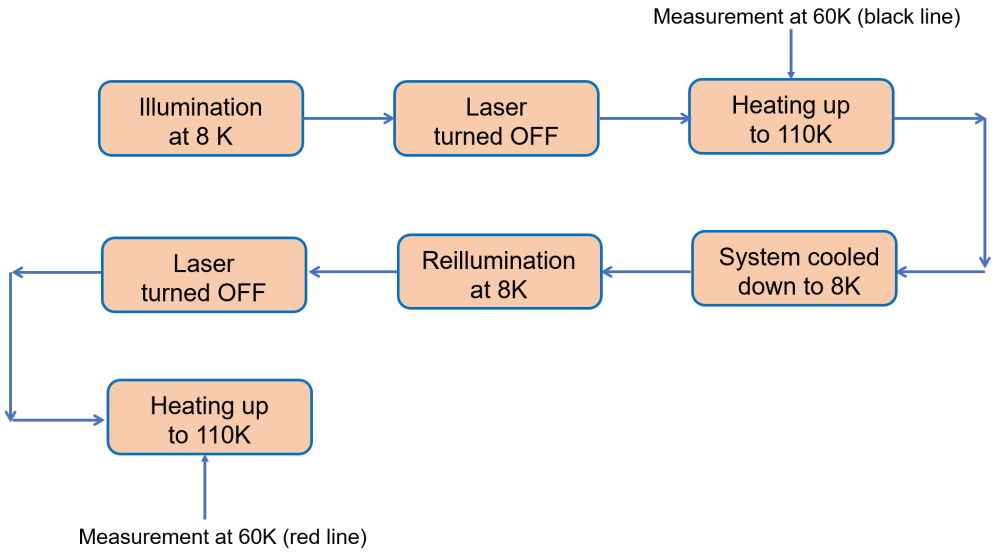

Figure 6.3: *Pathway of the experiment resulting in the behavior depicted in Figure 6.4.*

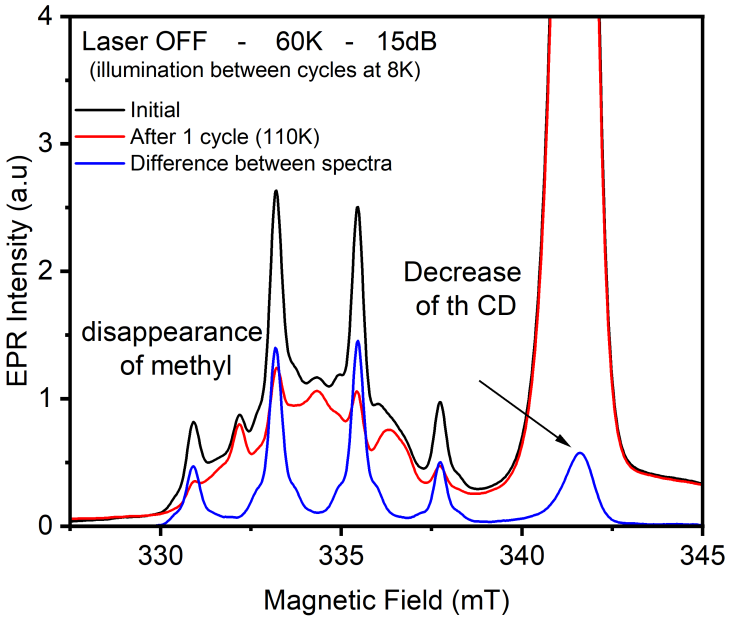

Figure 6.4: *EPR absorption spectra of the as-grown sample. The experimental procedure is the same as Figure 6.2 but recorded at 60K. Subsequently cooled to 8K, the system underwent a second illumination before being heated again to 60K. For a better understanding, refer to Figure 6.3. In dark, we present the initial spectrum at 60K, in red the spectrum after the cycle of heating and in blue the difference between the spectra.*

Through this approach, a small quantity of new methyl radicals is formed during the second illumination. However, the relative amount of methyl formed during this process

is negligible and is not expected to alter the behavior of the 3-lines system. Nevertheless, the number of methyl radicals that disappear due to the thermal reaction is superior to the quantity formed through reillumination. This behavior is observed in Figure 6.4, where the initial spectrum is depicted in black, the spectrum after the heating cycle in red, and the difference between them in blue.

After the heating cycle, we observe a slight decrease in the core defect, as indicated in Figure 6.4. The discrepancy between spectra in the region of the 7-lines is evidently caused by the disappearance of methyl radicals, as highlighted by the 4-lines, that accurately describe the methyl radical (blue line). At 60 K, saturation effects are minimized, and are expected to be the origin of the shoulders present in the spectrum. At this temperature, the methyl rotor is free to rotate, inhibiting possible effects on the EPR spectrum caused by this phenomenon. No observable changes were noted in the 3-lines system, indicating its stability under heating (T<110 K).

The previous results are compared to those obtained after optical extinction (same data of Section 4.6), where no heating cycles were performed. In this particular experiment, the sample was illuminated and maintained at a constant temperature of 85K, while observing the system's evolution over time. The system's behavior was observed for 480 minutes after the laser was turned off, to witness the relaxation of the optically excited state.

The initial spectrum, captured just after the removal of the optical excitation, was compared to the spectrum after 480 minutes. These outcomes are depicted by the black and red lines in Figure 6.5, respectively. The difference between these spectra is represented by the blue line.

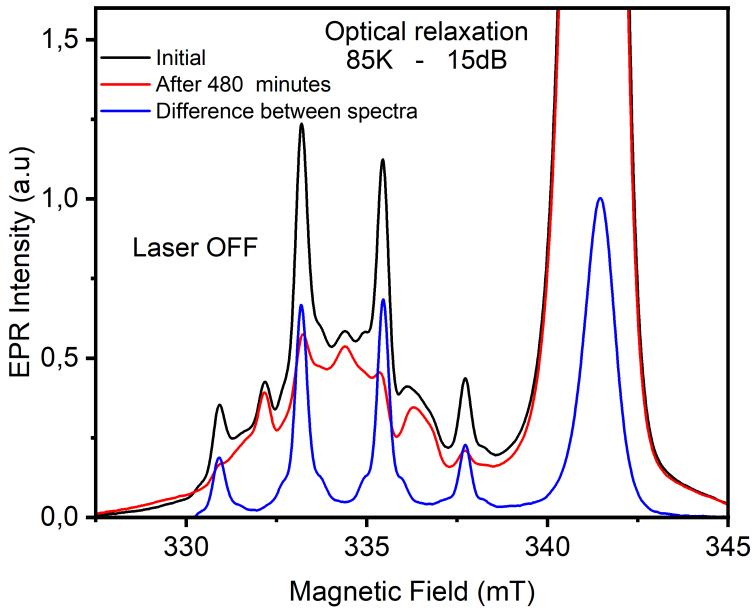

Figure 6.5: *EPR absorption spectra of the as-grown sample after removal of optical excitation. The black line represents the spectrum captured immediately after optical excitation removal. The red line represents the spectrum recorded 480 minutes later, while the blue line illustrates the difference between spectra.*

The results obtained through this approach are similar to those of the heating cycles. Specifically, the 3-lines system shows no alteration under heating cycles and exhibits no relaxation even after 480 minutes at 85K. In both methodologies, the changes in the EPR spectra are due to the decrease of methyl radicals. Simultaneously, the findings

presented in the previous chapters indicate that this group of lines is formed under the same conditions as methyl radicals (same optical excitation) and is also present at 8K, excluding the possibility of arising from subsequent reactions triggered by increasing the temperature.

Moreover, the analysis of the 7-lines group in Q band EPR demonstrates that this group possesses the same gravity center of resonance (g=2.005). While the other systems present in the NP (elephant and core defect) are separated through transitioning from the X to Q band, the 7-lines remains coupled. This result is depicted in Figure 6.6, where the 7-lines group is recorded in X and Q band. The red lines associate the peaks of the methyl radicals, while the blue lines associate the 3-lines group. The consistent separation between the lines independently of the MW band suggest that the 3-lines group originates from a single system (and thus are not 3 independent lines, originating from 3 different centers).

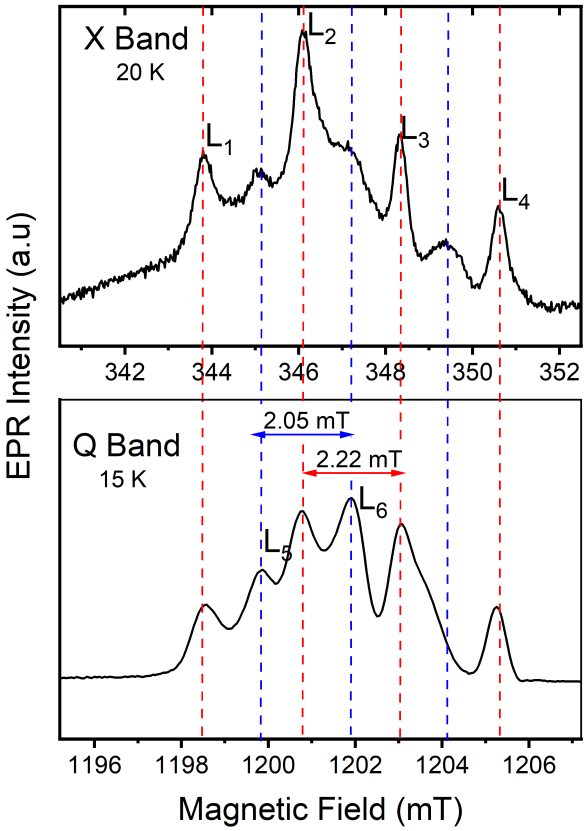

Figure 6.6: *The EPR absorption spectra of the 7-lines group recorded in X band (9.73 GHz) at 20K and Q band (33.73 GHz) at 15K. The distance between the methyl lines measures 2.22 mT, whereas for the 3-lines group, 2.05 mT. Despite the difference in spacings, both systems exhibit the same resonant gravity center, suggesting a probable common origin for these species.*

Based on the above-mentioned properties, we propose that the 3-lines system is formed by the interaction of two neighboring methyl radicals, i.e, that the methyl radicals can form biradicals under appropriate conditions. In this considered scenario, the interaction is assumed to be sufficiently strong to alter the EPR spectrum but not strong enough to transition from a spin 1/2 to a spin 1 configuration (in agreement with Rabi oscillations, which confirmed that the 3-lines system corresponds to spin 1/2).

In this scenario, we consider that the two interactions that can act to promote this coupling are:
(1) The exchange interaction, characterized by the Hamiltonian

$$H_{EX} = J\vec{S_1} \cdot \vec{S_2} \tag{6.1}$$

(2) The dipolar interaction, characterized by the Hamiltonian

$$H_{DIP} = K(r)|\vec{S_1} \cdot \vec{S_2} - 3(\vec{S_1} \cdot \vec{e_{12}})(\vec{S_2} \cdot \vec{e_{12}}))| \tag{6.2}$$

Note that the type of interaction exhibited between radicals depend on the distance between them. The factor $K(r)$ for the dipolar interaction is given by equation 2.29, while the J parameter depend on the wavefunction overlaping. When the distance is sufficiently small to allow an overlap of the wave function of the electrons, it results in the exchange interaction. However, when the electrons are close enough to interact, but there is no wave function overlap, the dipolar interaction occurs. At even superior distances, there is no interaction, and the system is characterized by a single radical.

Simulating a biradical composed of two methyl radicals, each with isotropic hyperfine coupling (A = -63.5 MHz), we examine the impact of incorporating exchange (J) and dipolar (K) couplings between the radicals on the spectrum. The outcomes are depicted in Figure 6.7, where the experimental spectrum following optical decay at 85K (Figure 6.5) is also included for comparison. It is important to note that, in both cases, when considering a coupling equal to zero, the resulting spectrum reverts to that of a single methyl radical.

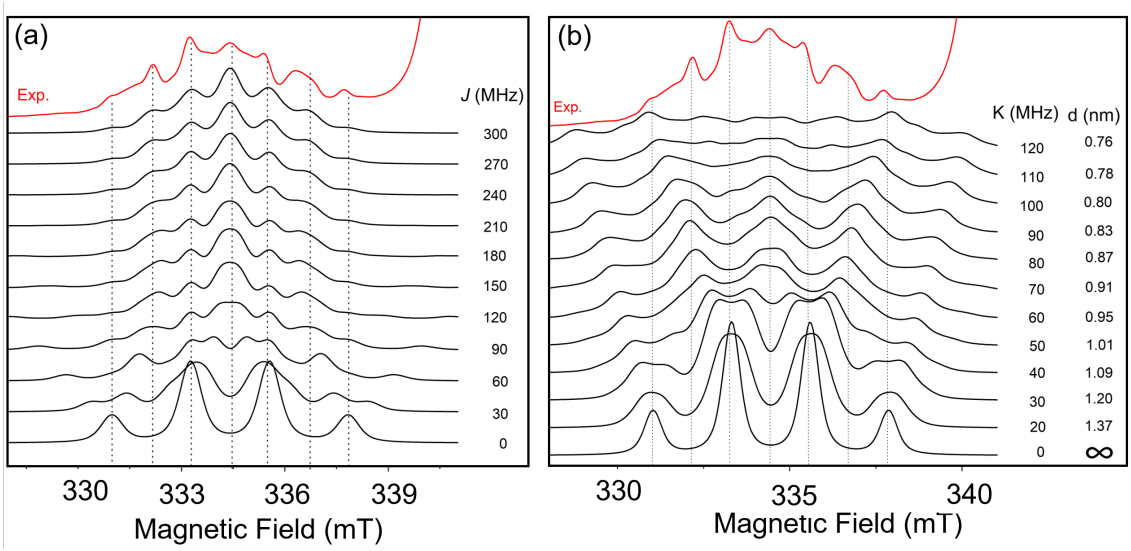

Figure 6.7: *Simulation: Effect of the exchange interaction (a) and dipolar interaction (b) between two methyl radicals in the EPR spectrum of the methyl radical. In red, the experimental results obtained through optical relaxation of the sample as-grown for 480 min. are shown for comparison.*

The impact of introducing and increasing the J interaction in the methyl radical spectrum is illustrated in Figure 6.7 (a). As the value of J increases, the central lines initially become broader, then undergo a splitting, and eventually merge to form a single

broader line, positioned at the center between the methyl lines. This line aligns with the position of the line L_6 observed in the 3-lines system. The first adjacent satellite lines overlap with the lines L_2 and L_4 of the methyl spectrum. However, the second set of satellite lines corresponds to the positions where we identify the lines L_5 and L_7, strongly indicating that this phenomenon is responsible for the appearance of these lines. Beyond 120 MHz, the simulated spectrum remains almost unchanged despite further increments in the interaction intensity.

Analyzing the effects of the dipolar interaction (K) on the spectrum, we observe that the lines initially broaden, then undergo a splitting, and subsequently each line gradually becomes broader. Within the interaction value range of 50 to 100 MHz, the resulting spectrum exhibits lines positioned where the 3-lines system resonates. In contrast to the exchange coupling, increasing the value of the dipolar interaction consistently induces alterations in the spectra, continuously broadening the lines. In the extreme case considered (K = 120 MHz), the lines become so broadened that they are nearly unidentifiable.

Following this initial analysis, where we identified the effects of each interaction on the spectrum, we conducted an optimized simulation aiming to replicate the observed 7-line pattern. To mitigate the substantial contribution of the methyl radical, that mask the contribution of the the 3-lines system, we revisited the spectrum obtained after optical relaxation for 480 minutes at 85 K for comparison.

In this scenario, we initially considered the exchange coupling between methyl radicals. The chosen value for this coupling was J = 350 MHz, although, as previously discussed, a range of J values yields similar results. To reduce the computational time required for the simulation, we employed an isotropic hyperfine interaction for modeling each interacting radical ($A = -63.5$ MHz), despite the experimentally measured methyl radical presenting slight anisotropy. The considered g-factor is g = 2.0064 and the line shape was simulated through a Voigtian shape (convolution of a Gaussian and Lorentzian line shape), of linewidht 3 G. Subsequently, we took into account the contribution from the "elephant" signal since it significantly distorts the spectrum in the region where L_1 and L_5 are located. For the elephant, anisotropy of the g-factor was considered. The values for the perpendicular and parallel component considered were $g_\perp$ = 2.024, $g_\parallel$ = 2.007. A Voigtian line shape with a linewidth of 3.6 G was utilized for the simulated signal. Furthermore, we incorporated the presence of individual methyl radicals, which give rise to the four main lines observed in the spectrum. For this simulation, a g-factor of g = 2.0068 was considered along with anisotropic hyperfine coupling ($A_x = -62.74$ MHz, $A_y = -64.26$ MHz, and $A_z = -65.02$ MHz). A Voigtian line shape with a linewidth of 3G was used in this simulation.

The results obtained accounting the biradicals (weight 53 %), the "elephant" signal (weight 27%) and the single methyl radicals (weight 20%), were accounted together. The resultant spectrum is presented in Figure 6.8, in red. The experimental result of the 7-lines system after optical relaxation for 480 min at 85K is presented in blue, for comparison.

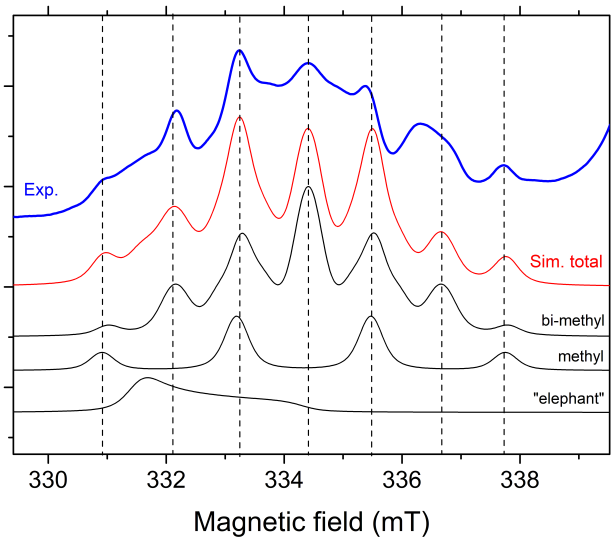

Figure 6.8: *Simulation: sum of different mechanisms for the formation of the 7-lines group observed in EPR. The weight of each system is 0.2 for the "elephant", 0.27 for the methyl radical and 0.5 for the biradicals. The biradicals are coupled through exchange interaction J=350 MHz. The results show a 7-lines patterns that reproduces excellently the position of the experimental spectra. A discrepancy in the shape is observed.*

The discrepancy in the shape presented in the spectrum of the biradicals coupled by an exchange factor J can be resulting from contributions of dipolar interaction. Considering the nanoparticle's surface, it is reasonable to assume that the methyl radicals might be positioned at non-uniform distances from each other.

Furthermore, we propose that the formation of methyl radicals occurs through a surface passivation mechanism (which will be further discussed in the next section). The density of surfacic charges is expected to be non-uniform in the NP, leading to a non-uniform distribution of methyl radicals. Regions of the nanoparticle with higher charge density, such as near the poles, are expected to exhibit a higher density of methyl radicals, resulting in their closer proximity. Conversely, at the equator of the nanoparticle, where a lower charge density is expected, the density of methyl radicals is expected to be reduced. Considering the entire NP, there should exist a distribution of distances between the methyl radicals, leading to a distribution of observed J and K values. At distances smaller than 0.5 nm, the interaction between radicals is expected to be governed by the exchange interaction. For distances ranging between 0.5 and 1.5 nm, the expected mechanism of interaction is the dipolar and at distances higher than 1.5 nm, the methyl radical exists in its single configuration. This scenario is depicted in Figure 6.9 (b), where a Gaussian distribution representing the dipolar regime is illustrated. In Figure 6.9 (a), the spectrum of biradicals interacting via dipolar interaction is considered for various distances within the dipolar regime (within the Gaussian distribution).

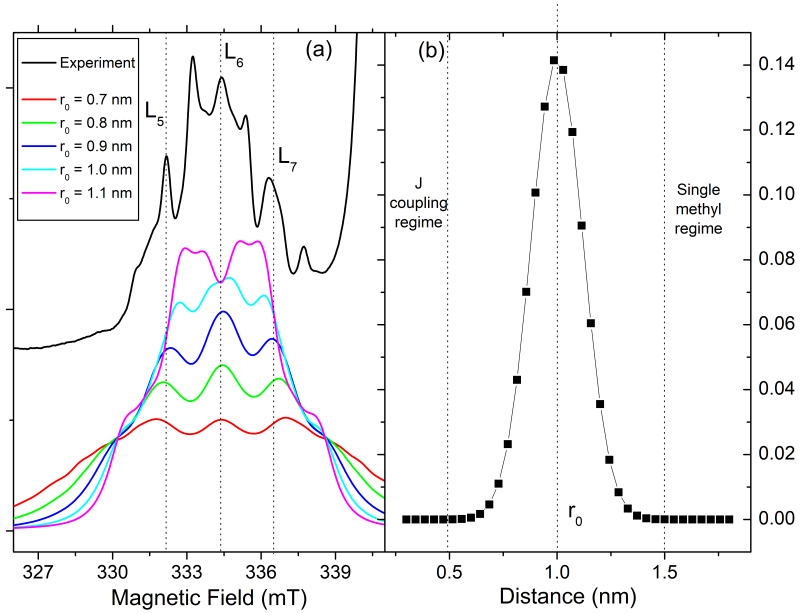

Figure 6.9: *Simulation: Gaussian distribution of the dipolar interaction around a mean distance* r_0.

A final approach, considering the contributions of a distribution of K and J, is envisioned as a future perspective, as it is expected to describe more accurately the amorphous zone of the NP (organic shell), providing definitive evidence for the origin of the 3-lines system.

Other radicals

Studies performed by other authors also identified the 3-lines system appearing simultaneously to methyl radicals [177; 178], but this signal was associate to the formation of carboxymethyl radicals ($^{\cdot}CH_2CO_2^-$) at the oxide surfaces, following the equation

$$^{\bullet}CH_3 + CH_3COO^- \rightarrow^{\bullet} CH_2COO^- + CH_4 \tag{6.3}$$

The principal conflict that we observe in this approach is that the authors indicate that the weight of the carboxymethyl increase at temperatures above 100 K, while we observe by the preceding analysis that the weight of the 3-lines system do not increase, it remains constant an and the difference in the spectrum is made by the loss of methyl radicals. Moreover, we observe that this element is formed together with the methyl radicals, at 8K. Therefore, definitive conclusions for the origin of the 3-lines system are not presented, although we consider that the scenario involving the formation of methyl biradicals is strongly more plausible.

6.2 Polar nanoparticles

The formation of ZnO crystals, comprised of positively charged Zn and negatively charged O, leads to the generation of electrical dipoles within each elementary cell of the crystal [179; 180]. Within a pure and finite crystal, achieving complete charge neutrality at the crystal's edges is unattainable. This restriction results in the creation of a negatively

charged surface on the O side and a positively charged one on the Zn side, which correspond to the hexagonal plane (0001) and (000$\bar{1}$). Consequently, a polarization vector $\vec{P}$ arises within the crystal. The polarization vector is defined by the volumetric electric dipole:

$$\vec{P} = \frac{\vec{d}}{v} \tag{6.4}$$

The polarization within the nanoparticles is linked to the bound charges within the NPs. In classical electromagnetism theory, this finite polarization $\vec{P}$ leads to two kinds of charge density:
(1). A volumetric charge density linked to the divergence of $\vec{P}$:

$$\rho_V = \vec{\nabla} \cdot \vec{P} \tag{6.5}$$

(2). A surfacic charge density linked to the scalar product of $\vec{P}$ with the surface normal vector $\vec{n}$:

$$\rho_S = \vec{n} \cdot \vec{P} \tag{6.6}$$

Assuming a uniform polarization vector inside the NP, only the second kind of charge density is present. The polarization, itself, generates a depolarizing field $\vec{E}$. The combined effect of both fields is defined as the electric displacement $\vec{D}$. Within the nanoparticle, where the polarization exists, the constitutive relation holds :

$$\vec{D_i} = \varepsilon_0 \vec{E} + \vec{P}, \tag{6.7}$$

where ε_0 is the vacuum permittivity.

Outside the nanoparticle, where there is an absence of polarization, the displacement vector is:

$$\vec{D_o} = \varepsilon_0 \vec{E} \tag{6.8}$$

At the interface between the interior and exterior, the electric field encounters a discontinuity in its normal component (perpendicular to the surface). This process is visually depicted in Figure 6.10.

The presence of charged surfaces generates a system out of thermodynamic equilibrium, once that the electrical potential is non-uniform within the NP. It leads the system to the necessity of capturing or generating charges from either the inside or the outside of the nanoparticle, in order to restore the equilibrium.

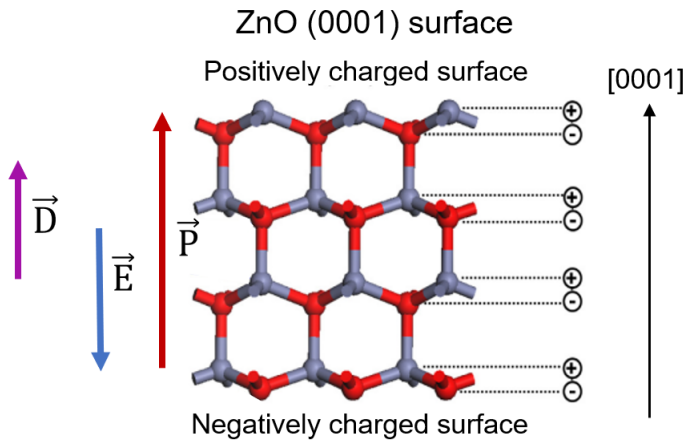

Figure 6.10: *Representation of the formation of the polar surfaces in ZnO. Adapted from [181]*

Considering the ZnO, a pure electrostatic model accounting the $+2e$ and $-2e$ charges per elementary cell corresponding to the Zn^{2+} and O^{2-} atoms, leads to a surfacic charge density of 0.25 C/m^2. This must represent an upper limit because complete ionization cannot occur, and all charge delocalization effects will tend to decrease this value. Indeed, ab initio calculations estimate the surface charge density to be approximately 0.05 C/m^2 [182], a reasonable value that will be utilized in the subsequent analysis.

6.2.1 Non-passivated nanoparticles

Considering a spherical nanoparticle of radius R, we examine the influence of polarization within the interior, exterior, and surface regions of the nanoparticle. As previously mentioned, polarization arises from a density of dipoles. This polarization results in the formation of a charged surface, where the charge density can be expressed as the product of the surface's normal vector and the polarization vector, i.e $\rho_s = \vec{n} \cdot \vec{P}$. It's important to note that the charge density at the surface of the sphere is non-uniform (maximum at the top, zero at the equator, and minimum at the bottom), and when integrated over the entire surface of the nanoparticle, the total charge equals zero ($Q = 0$), as the nanoparticle is globally neutral:

$$Q = \oint_S \rho_s dS = PR^2 \oint_S \cos\theta \sin\theta d\theta d\phi = 0 \tag{6.9}$$

where the spherical coordinate system (r, θ, ϕ) has been used to describe the element of surface. The polar NP consists of two hemispheres, one bearing a positive charge and the other a negative charge. Regarding the positive surface (which holds an equal number of charges as the negative surface but with opposite polarity), the quantity of charges on this surface is given by

$$Q_+ = \int_{S+} \rho_s dS = PR^2 \int_0^{\pi/2} \int_0^{2\pi} \cos\theta \sin\theta d\theta d\phi. \tag{6.10}$$

This simplifies to:

$$Q_+ = \pi PR^2 \tag{6.11}$$

Considering a NP with a radius of 8 nm (average size presented by the NPs synthesized via sol-gel mehtod), considering the estimated polarization of 0.05 C/m^2 = 0.312 e/nm^2 [182], we find that the quantity of charges in the positive surface is $Q_+ \approx 20$ e[1]. It means that for this NP, the charge of approximately 20 elementary charges need to be neutralized in each hemisphere for the system to achieve electrical equilibrium.

Electrical potential and electrical field generated by the NP

The charge distribution induced by the polarization produce an electrical potential inside and outside the nanoparticle (with continuity on the surface). For the interior of the NP, the potential is given by

$$V_{int}(r,\theta) = \frac{Pr\cos\theta}{3\varepsilon_0}, \tag{6.12}$$

where r is the position in which the potential is considered (r<R) and ε_0 is the electrical permittivity of the vacuum. The potential on the outside of the NP (r>R) is:

$$V_{ext}(r,\theta) = \frac{PR^3\cos\theta}{3\varepsilon_0 r^2}, \tag{6.13}$$

On the surface, the potential depends solely on the angle θ:

$$V(R,\theta) = \frac{PR\cos\theta}{3\varepsilon_0} \tag{6.14}$$

and its continuity at the surface is verified. Giving the relation $\vec{E}=-\nabla V$, the electric field is calculated:

$$\vec{E}_{int} = -\frac{\vec{P}}{3\varepsilon_0} \tag{6.15}$$

Thus, for the simple spherical geometry, the depolarizing field is exactly one third of the polarization vector, directed in the opposite sens. By employing Equation 6.7, the resultant field inside the nanoparticle is expressed as $\vec{D} = 2/3\ \vec{P}$. In simpler terms, the depolarization vector diminishes the polarization field by 1/3. The electrical field inside the sphere is uniform; however, this is not the case for the external electric field, given by

$$\vec{E}_{ext}(\theta) = \frac{PR^3}{3\varepsilon_0 r^3}(2\cos\theta\hat{e_r} + \sin\theta\hat{e_\theta}) \tag{6.16}$$

The representation of the internal and external electric field presented by a polarized NP is presented in Figure 6.11.

[1]e = absolute value of the elementary charges

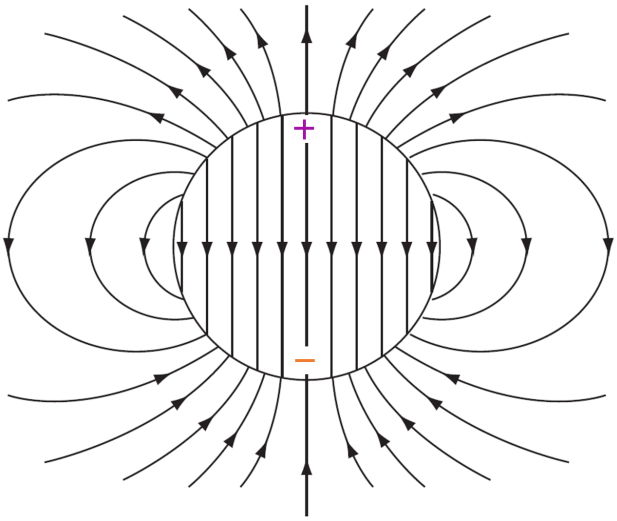

Figure 6.11: *Electrical field inside and outside a polarized sphere. Figure adapted from [183].*

Finally, it's evident that the non-passivated NP is not in thermodynamic equilibrium (which requires uniformity in all intensive variables within the system). This lack of equilibrium is attributed to the non-uniform electrical potential, resulting in a potential difference between two distinct regions of space. The resultant non-zero electrical field, present both inside and outside the NP (Figure 6.11), offers opportunities for capturing electrical charges from the interior and/or the exterior of the NP to restore thermodynamic equilibrium.

In the subsequent sections, we explore the process of capture of charges, that leads to surface passivation in the case of ZnO nanoparticles.

6.2.2 Passivated nanoparticles

The non passivated NP constitute a mechanism out of thermodynamic equilibrium. Consequently, the system tends to seek methods to attain equilibrium. This quest for equilibrium drives the NP to evolve or adapt towards a more stable configuration.

The mechanisms responsible for effectively passivating the NPS must consider both internal and external factors. Internally, these mechanisms should address the defects within the lattice of the ZnO. Externally, they should involve interactions with molecules present in the organic shell surrounding the NP. Inside the NP, the defects present in ZnO lattice can include point charges, that can interact with the existing electric field. The defects also act as charge traps, where acceptor levels can trap holes (by accepting an electron) and donors can trap electrons (by ejecting them to the conduction band). Consequently, the rapid charge separation due to the $\vec{D}$ vector efficiently prevents the recombination of electrons and holes. This is the reason for the notable existence of stable exciton at room temperature in ZnO.

Outside the NP, the organic shell adhered to the NP's surface forms a complex semi-amorphous region that potentially accommodates various types of molecules [184]. These molecules are connected to the surface through electrical forces and/or chemisorption.

The chemisorption, or chemical adsorption, is a process characterized by strong interactions between the surface of an adsorbent and adsorbates. Specific functional groups,

such as amine (-NH_2), carboxylic acid (-COOH), hydroxyl (-OH), and thiol (-SH) groups, are renowned for their ability to covalently couple with inorganic nanoparticles [185]. In nanomaterials, this process becomes increasingly crucial as chemisorption intensifies with the augmented surface area of the adsorbent. The same holds true for physical adsorption [186].

Within this context, organic compounds present during synthesis aggregate onto the NP surface, remaining stable even after the NPs are dried. The results obtained through FTIR (see Fig. 5.3) and NMR spectroscopy (see Fig. 4.3) indicate the presence of simple organic chains, including ethanoic acid (CH_3COOH), commonly known as acetic acid. This polar molecule exhibits a dipole moment of 1.7 D [187]. When subjected to ionization, it leads to the formation of acetate ions as a product, releasing a proton in the following reaction:

$$CH_3COOH \longleftrightarrow CH_3COO^- + H^+ \tag{6.17}$$

To ensure an effective passivation process for nanoparticles (NPs), candidates capable of passivating both negative and positive surfaces are crucial. Below are the candidates identified for passivating each surface:

Positive surface

The negatively charged elements that can be presented for the passivation are:

- Conduction electrons (e^-);
- Negatively ionized point defect (X^-);
- Acetates (Ac^-) originating from the ionization of acetic acid;
- Hydroxyl group (OH^-),residues from the synthesis involving KOH, NaOH, and MeOH.

Negative surface

The positively charged elements that can be presented for the passivation are:

1. Valence hole (h^+);
2. Positively ionized point defect (Y^+);
3. cation part of catalyst (Na^+ or K^+);
4. Protons (H^+) from acetic acid or global environment.

Besides the passivation that can occur through the elements mentioned above, other mechanisms may act to passivate the surface. Notably, surface reconstruction is a significant process wherein, in the absence of impurities, crystal atoms reorganize themselves to minimize energy. In the case of ZnO, no such reconstruction has been observed. This absence is likely attributed to its strong ionic nature, which imparts a high degree of rigidity to the lattice. Another conceivable process involves macroscopic passivation, where a group of nanoparticles could self-organize in an alternating orientation, akin to an antiferroelectric arrangement. However, this particular order hasn't been observed in our

sample. These two cited mechanisms are less favorable and, would probably take place if absolutely none of the other previously mentioned mechanisms were possible.

ZnO material is known for decades to be a naturally n-type semiconductor, with difficulty to achieved p-type doping or even a full charge compensation. Main electrons donor candidate are interstitial hydrogen atom and ionized oxygen vacancy, although this latte has been calculated to be a relatively deep donor. Nevertheless, as for every semiconductor, the conductivity of ZnO must decrease as the temperature is lowered [130] due to the phenomenon where electrons, released by shallow defects into the conduction band, return to their original sites when the thermal energy is insufficient to keep them in an excited state. This characteristic leads to the consideration of three distinct regimes:

1. Room temperature regime: Where the behavior of ZnO nanoparticles is observed at standard operating temperatures, with substantial free electron density.

2. Low-temperature regime: Investigating the behavior of ZnO nanoparticles at reduced temperatures where free electron density is notably affected.

3. Low-temperature regime with photoexcitation: Exploring the NP behavior at low temperatures while subjecting them to photoexcitation, potentially altering their conductivity characteristics.

Each of these regimes demands meticulous examination to understand how ZnO nanoparticles behave in response to temperature variations and when subjected to photoexcitation. Understanding their internal and external behaviors under these conditions is crucial. Undoubtedly, the actual situation is likely to be very complex, with various mechanisms interplaying together. In the subsequent analysis, we aim to delineate the most probable and predominant mechanisms occurring in different regimes.

Room temperature regime

At room temperature, shallow donors possess sufficient energy to promote an electron to the conduction band. The presence of shallow donors is well-established and is attributed to the n-type conductivity of ZnO.

In this specific regime, the passivation of nanoparticles (NPs) primarily involves the shallow defects within the ZnO lattice. The donor defects release electrons, that act as passivators for the positive charged surface. Conversely, the ionized defect (after releasing the electron and becoming positively charged) is responsible for passivating the negative surface. This mechanism is referred to as the electron/donor passivation and its mechanism is represented in Figure 6.12.

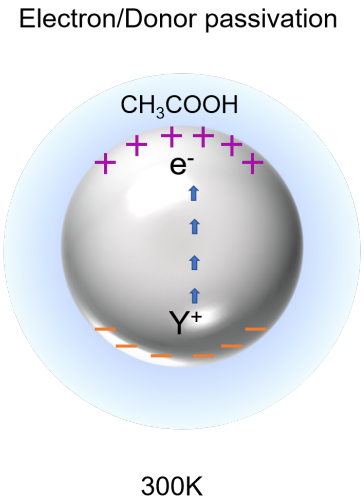

Figure 6.12: *At room temperature, the surface passivation of the nanoparticles occurs via shallow donors that release electrons into the conduction band, thereby passivating the positively charged surface. The defect itself becomes positively charged and is responsible for passivating the negative surface. The nanoparticle is capped by acetic acid, that is situated in the shell (transparent blue).*

The electron and the donor are characterized by very high and very low mobility, respectively. Assuming fixed donors (zero mobility) randomly distributed within the NP, it implies that only the donors localized in the negative hemisphere, primarily those in close proximity to the bottom, will ionize to Y+ and release an electron. Subsequently, this released electron rapidly reaches the positive surface.

This mechanism is anticipated to be the predominant method of passivation at room temperature. However, it might also work in conjunction with the chemisorption of compounds onto the surface. Specifically, it is possible for some OH- and Na+ (or K+) ions to exist at the positive and negative surfaces, respectively.

This primary electron/donor passivation aligns with the n-type characteristic of ZnO and correlates with the observation of CH_3COOH at room temperature. Nevertheless, the photo-Kolbe reaction, identified as the mechanism responsible for producing the observed $^{\cdot}CH_3$ at low temperatures (<120K), involves the acetate anion CH_3COO^-. This discrepancy is explained in the following sections, where a change in the passivation mechanism occurs as the temperature decreases.

Low temperature regime

At low temperatures, the mechanism should change, once that the conductivity of the NPs change, becoming more insulator in the measure the temperature decrease. As presented by Savchenko et al. [130], the decrease of the conductivity of ZnO is observed below 100K, indicating that electrons released by shallow donors return to their respective sites and are no longer able to passivate the NP. Here, we attribute to the decrease in conductivity the change from CH_3COOH to CH_3COO^-.

Without the charges e^- and Y^+ that passivate the NP surface, the external electric field produced by the NPs intensifies, possibly becoming strong enough to ionize the acetic acid situated on the surface [183].

However, the non observation of acid ionization at room temperature implies that

this phenomenon cannot be solely attributed to thermal energy at low temperatures (if the release of protons does not occur at room temperature, there is no reason to expect it to happen at lower temperatures.) Instead, it suggests that the mechanism is likely facilitated by the electric field generated by the nanoparticles. If the ionization of acetic acid is regarded as an endothermic chemical reaction, it will not occur if the thermal energy is insufficient. However, in lower temperatures, the electron/donor passivation vanishes, promoting an increase in the electric field generated by the NP. Considering the existence of the electric field, in order to demonstrate the potential for an electric-field-induced endothermic reaction, we have developed a simplified thermochemistry model, including the main parameters relevant to this demonstration.

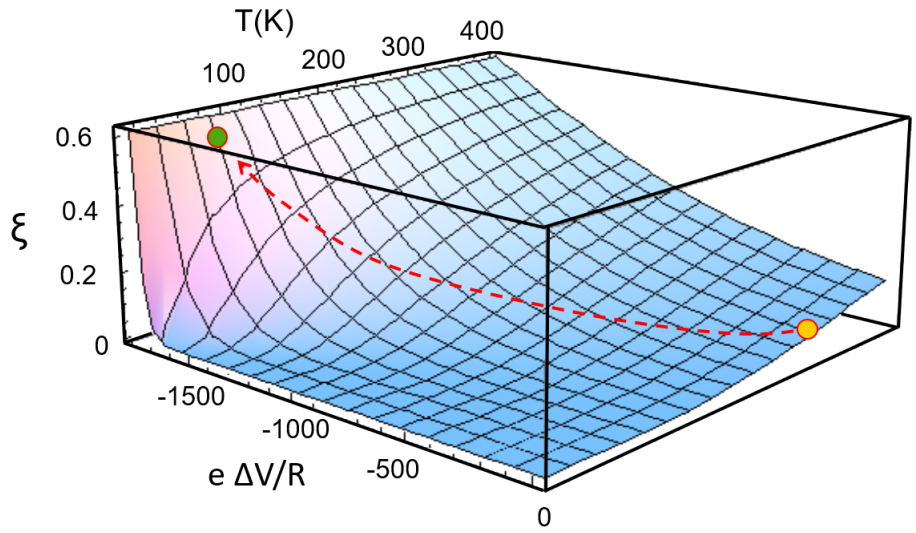

Figure 6.13: *Thermochemical calculations demonstrate that at room temperature (yellow point), the reaction progress ξ shows a non-zero value, suggesting a partial dissociation of acetic acids into acetates and the release of a proton. Upon decreasing the temperature (dotted arrow), the reduced thermal energy becomes inadequate to sustain the reaction. However, the electric potential escalates. Consequently, at 85K (green point), the elevated potential intensifies the reaction progress, leading to increased dissociation of acetic acid.*

As a result, the reaction progress ξ, is finally a function of the temperature and the electrical potential, linked by the following relation:

$$\xi(T, \Delta V) = \frac{K}{2}\left(\sqrt{1 + \frac{4}{K}} - 1\right) \tag{6.18}$$

where

$$K = e^{-\frac{-\Delta_r G^0}{RT}}(1 + e^{-\frac{e\Delta V}{RT}}) \tag{6.19}$$

where ΔV represents the difference of potential, the R is the universal gas constant (R=8.31 J/K) and $\Delta_r G^0$ is the Gibbs free energy of reaction. Conducting some calculations, it is observed the electrical potential favors the reaction. These results are depicted in Figure 6.13.

In the presented model, it implies that although the dissociation of Acetic acid $\rightarrow Ac^-$ + H^+ is not possible at room temperature and below, the reaction becomes feasible when the electric potential gains significance due to reduced conductivity (the electrons are trapped in their donor sites). Under these conditions, acetic acid undergoes ionization,

releasing a proton that passivates the negative surface. Consequently, the resulting acetate, being negatively charged, passivates the positive surface. This process is expected to be more pronounced at the poles of the NPs, where the electric field is stronger. This mechanism is represented in Figure 6.14.

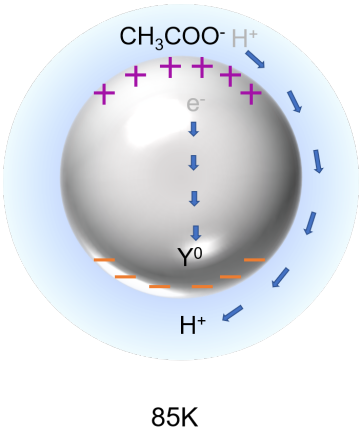

Figure 6.14: *At low temperatures (T < 100K), the conductivity of ZnO decreases due to the recombination of conduction electrons with their original centers. In this scenario, the external electric field surrounding the NP intensifies, potentially ionizing the acetic acids. This ionization process generates negatively charged acetates and releases protons. The resulting acetates passivate the positively charged surface, while the protons passivate the negatively charged one.*

Photo excitation at low temperatures

At low temperatures, as mentioned earlier, most of defects within the ZnO lattice are in their neutral state, as the passivation is mainly ensure by acetate and proton. However, upon photo-excitation in the NPs, sufficient energy (3eV) is supplied to promote an electron from the valence band to an intraband-gap state created by an acceptor defect, leaving a hole in the VB.

$$X^0 \xrightarrow{h\nu} X^- + h^+ \text{ (bulk)} \tag{6.20}$$

This ionized defect is associated to the signal that we observe in EPR, at g=1.96, the core defect. In a second moment, the photo generated holes can be transported to the NP surface, provided that X acceptor is not too far from the positive surface.

$$h^+ \text{ (bulk)} \rightarrow h^+ \text{ (surface)} \ , \tag{6.21}$$

The photo-generated holes are potential reactive oxidant species [2], and can interact with the acetates present in the surface [188]. In this context, the role is transferred from the nanoparticle to the acetate, leading to the formation of methyl radicals and CO_2 as products of the reaction.

$$h^+ + CH_3COO^- \rightarrow^{\bullet} CH_3 + COO \text{ (surface)} \tag{6.22}$$

The formation of radicals through this process has been observed by other authors [26]. Referred to as the photo-Kolbe reaction, this reaction has been extensively documented

[2] A molecule or atom capable of accepting electrons during a redox reaction.

on oxidized surfaces [189; 178; 190; 191]. The mechanism of this process is illustrated in Figure 6.15.

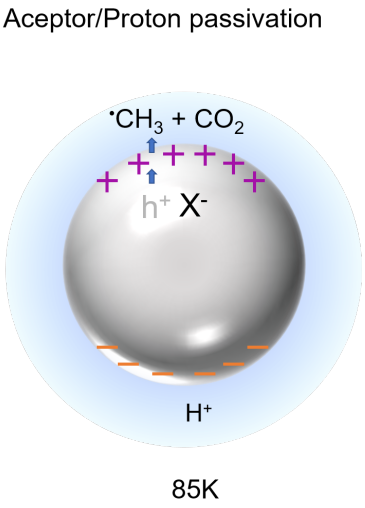

Figure 6.15: *At low temperatures, upon exposure to photo-excitation (405 nm), electrons from the valence band are elevated into intra band-gap states formed by acceptor defects. This action results in the liberation of a hole, which moves to the NP surface and is transferred to the acetates adhering to the surface. This initiates a photo-Kolbe reaction, producing methyl radicals and CO_2 as reaction products.*

This intricate passivation mechanism is particularly crucial due to the prominence of surface states in nanostructures, where the surface-to-volume ratio increases as the nanoparticle size reduces. The photo-generated holes, which interact with the acetates, are anticipated to be formed in proximity to the surface, ensuring a non-negligible probability of their presence over the acetate. The identification of the weak line observed in Q-band experiments supports this assertion. The photo-activated Zn and O vacancies within the ZnO lattice are indicated as crucial elements in the catalytic properties exhibited by this material [26]. This suggests that the ionized acceptor responsible for the photo-Kolbe reaction is likely associated with Zinc vacancies present in the lattice. However, additional analysis is necessary to reach a definitive conclusion.

Finally, the entire mechanism explaining the emergence of methyl radicals and the occurrence of the core defect at low temperatures following optical excitation is depicted in Figure 6.16. This process can be seen as a change in the positive surface passivation, from acetate anion (Ac^-) to negatively charge acceptor (X^-).

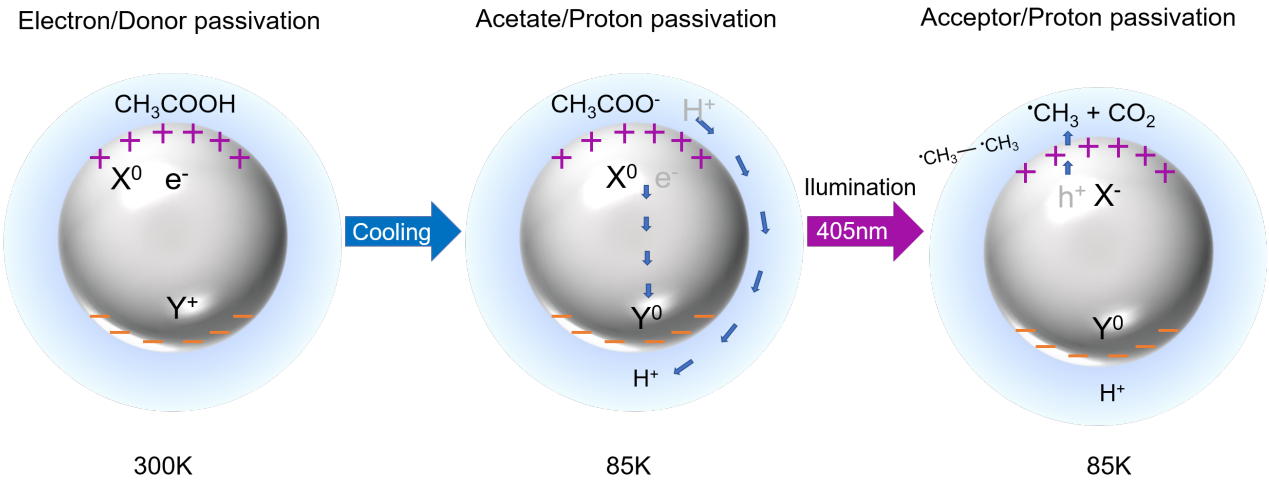

Figure 6.16: *At room temperature, the NP surface is passivated via shallow donors. With decreasing temperature, the electrons revert to their original centers, prompting surface passivation through the ionization of acetic acid molecules located on the NP surface. Upon optical excitation, the photo-Kolbe reaction takes place, resulting in the formation of methyl radicals detectable through EPR.*

The photo-Kolbe reaction is anticipated to exhibit a reversible nature. This assumption stems from Chapter 4, where observations indicated that when the samples are allowed to rest at room temperature for approximately 1 hour, the system reverts to its initial state. This observation strongly suggests the existence of a chemical reaction driving the system back to its original state. Additionally, in Section 4.6.1, the presence of an EPR-silent intermediate state was noted, emerging when the samples were heated up to 110K. This suggests a probable phase wherein the methyl radicals transform into other chemical entities before reassembling into acetates.

When the sample is annealed, the organic shell is removed from the surface. Consequently, during the sample's cooling phase, the decrease in conductivity is no longer compensated by the acetic acid dissociation. Instead, it is directly compensated by acceptor ionization without the need for illumination. The observation of this phenomenon is illustrated in Figure 6.17.

When cobalt ions are introduced into the ZnO lattice, a noticeable reduction and complete suppression of the core defect signal are observed, as the doping levels increase. The core defect is completely absent at doping level 1%. Previous investigations conducted on ZnO nanorods indicate that this phenomenon occurs even when the core defect is initially observed under dark conditions [121] (no light sensitivity). These observations lead to two potential conclusions: either the defect responsible for generating the core defect signal is no longer present (possibly substituted by cobalt ions) or the presence of cobalt inhibits the ionization of this defect. In both cases, the absence of ionization of the core defect results in the prevention of subsequent reactions, as observed experimentally. Our experimental findings corroborate this, indicating that in the absence of the core defect signal, methyl groups are not identified within the system.

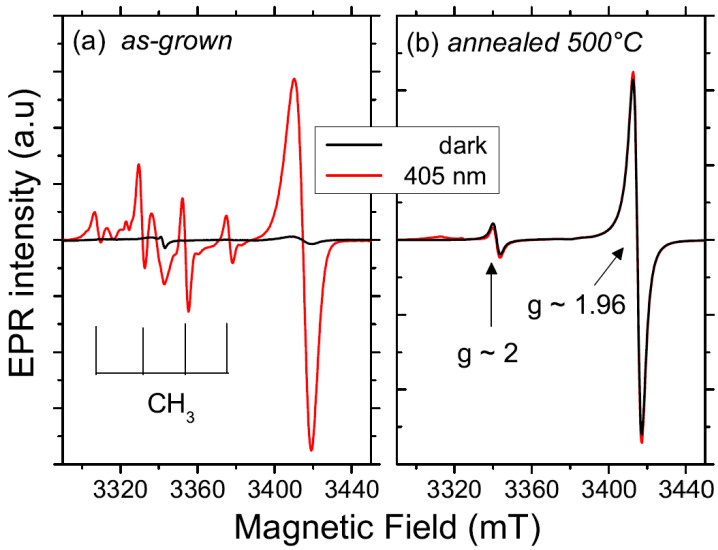

Figure 6.17: *Comparison of the EPR spectra at T=35K and 15dB attenuation of the samples as-grown and annealed in dark (black) and illuminated (red) conditions. After the annealing, the organic shell that entourages the NP is no longer present. Consequently, the surface passivation is made through acceptor ionization when the temperature of the system is decreased.*

Moreover, understanding this characteristic of ZnO open new possibilities for the application of this material, once that new approaches be implemented to passivate or modify the surface of ZnO nanostructures by interesting organic and inorganic materials [192].

Conclusion

Regarding the morphology of the studied samples, all the examined ZnO NPs, whether doped or undoped, exhibit the hexagonal wurtzite structure with a notably high level of crystallinity. The introduction of cobalt ions as dopants does not alter the lattice structure. However, NPs generated via a solid-state reaction show structural stress. This characteristic is evidenced by the deviation from the expected a and c parameters for the Wurtzite structure. Upon exposure to high temperatures (500 °C), the size of the NPs increases from an average diameter of 15 nm to 50 nm.

The NPs synthesized through the sol-gel method, both doped and undoped, demonstrate an intriguing interaction between their organic and inorganic constituents. These NPs display photo-activated paramagnetic signals that are discernible through EPR spectroscopy. The observed signals consist of an inorganic core-defect ($g = 1.96$), originating from the bulk of the NPs, along with methyl radicals formed on the NP surface via a photo-Kolbe reaction, thus forming a shell state. Additionally, a system characterized by 3-lines is observed, likely associated with the formation of methyl biradicals. Both the methyl radicals and the 3-lines system share the same resonance center at $g = 2.005$. A photo-excited signal is observed superposed to the 7-lines group, due to its anisotropic form, this signal was named "elephant".

To gain insights about the electronic spin of each system, the Rabi oscillation sequence was applied, simultaneously varying the time and the magnetic field (2D Rabi oscillations). This technique revealed that all the systems respond identically to the applied MW, oscillating with the same frequency, indicating that all systems are characterized by the same electronic spin value, s=1/2.

Concerning the core-defect, in the samples that contain the organic shell (as-grown and deuterated), this signal is only present under photo-excitation. Notably, the energy provided by the photon (3 eV) is not enough to promote an electron from the VB to the CB (ZnO bandgap = 3.4 eV). This suggests that the core-defect, confirmed to originate from the bulk, represents an intra-band gap state. As ZnO is known for its intrinsic defects, it is anticipated that the core-defect results from the ionization of a defect existing within the crystalline lattice. Furthermore, considering that the photo-Kolbe reaction is triggered by this ionization, it is expected that the core-defect is associated with an acceptor defect, capable of accepting an electron, thereby generating a hole that initiates the photo-Kolbe reaction.

The identification of the origin of the 4-lines system was possible due to the combination of different techniques. The identification of organic groups was accomplished using FTIR and NMR techniques, conducted at room temperature. The results revealed the presence of acetic acid within the ZnO NPs. Performing a surface functionalization with deuterated acetate, some hydrogen atoms present in the organic molecules were replaced by deuterium. Under photo-excitation, the functionalized NPs presented a signal characteristic of deuterated radical ($^{\bullet}CD_3$), proving that the observed 4-lines signal in the

as-grown samples arises from the formation of methyl radicals on the NP surface. The distance between adjacent lines in this system is related to the hyperfine coupling, which corresponds to approximately 65 MHz.

Upon subjecting the NPs to an annealing process (500 °C), a notable effect is observed — the NPs' size increases, displaying an average diameter of 50 nm post-annealing. Furthermore, FTIR analysis reveals the disappearance of the organic shell after the annealing procedure. Consequently, both the 4-lines and 3-lines groups vanish, while the core-defect remains present. The state of the core-defect is changed, and in the annealed samples, it is present even under dark conditions. In this scenario, due to the vanishment of the organic shell, the core-defect changes its charge state, acting as a mechanism of surface passivation. In annealed samples, a surface defect centered at $g = 2.003$ is also present.

The signal labeled as "elephant" is present in all the samples, persisting even after the annealing procedure. It indicates that this signal is not associated with organic compounds situated on the surface of the NP. This signal only emerges under optical excitation. Preliminary results demonstrate that the "elephant" signal can be activated and deactivated through optical excitation. Further investigation into these phenomena is necessary for a better understanding and for potential technological applications.

Comparing the different samples, it is possible to conclude that the synthesis method employed for the NP fabrication significantly alters the surface states, thereby influencing the observed EPR signals present in the NPs.

Concerning the characterization of the dynamics of methyl radicals, the results indicate that above 30 K, these elements undergo a chemical reaction, transitioning through an intermediate EPR-silent state before returning to their initial state (achieved by letting the sample rest at room conditions for approximately 1 hour). This characteristic is observed through the deviation from the Curie's model for paramagnetic materials, suggesting that at temperatures higher than 30 K, the chemical reaction alters the concentration of spins, leading to a change in the transverse relaxation time T_2. The change in the spin concentration of methyl radicals with increasing temperature is also observed using pulsed wave EPR techniques. The variation in the quantity of electronic spins induces changes in the coherence time (T_m), inherently linked to the concentration of spins. Consequently, the spin-spin relaxation time measured by 2-pulses echo decay T_m of the methyl radicals increases with rising temperature, in agreement with predictions derived from results obtained in CW EPR. Nevertheless, optically-generated methyl radicals remain detectable at temperatures up to 120K. For the other systems (core-defect and 3-lines system), the behavior of T_m remains nearly constant, suggesting that the quantity of these entities remains unchanged with increasing temperature. However, the core-defect exhibits significantly shorter T_m, implying that this element is embedded in an environment with a higher concentration of electronic spins, leading to quicker decoherence.

When applying the 2-pulse sequence, modulation in the decay was observed. These modulations arise from a transfer of polarization from electronic to nuclear transitions, indicating an environment rich in nuclei. The frequency exhibited by the modulation corresponds to the Larmor frequency of hydrogen for the as-grown sample and deuterium for the deuterated sample. Moreover, the existence of electronic-nuclear coupling, characterized by additional frequencies involving the sum and difference of nuclear frequencies with the hyperfine coupling, could be present but hidden in the linewidth. To access this information, the HYSCORE technique was employed for the as-grown sample (in the lines L_2 and L_6) and the deuterated samples. Notably, the Larmor frequency of hydrogen and deuterium was once again observable, and a small coupling was resolved, with a value of

2.72 MHz for the as-grown sample. This coupling is almost 25 times smaller than the hyperfine coupling measured through CW techniques, possibly indicating the interaction between neighboring radicals protons.

Interestingly, in the deuterium sample, the weak coupling with hydrogen atoms was no longer observed, indicating that the measured interaction does not involve hydrogens from the environment but is directly related to the formed radicals. In this sample, the interaction between deuterated radicals was not identified, but this coupling could be hidden in the linewidth of the deuterium principal peak. Access to this information could be obtained by improving the detection sensitivity of the deuterium or performing the HYSCORE experiment in a different frequency band (preferably band Q), where the Larmor frequency of deuterium is increased, potentially allowing the identification of the coupling.

However, in the deuterated sample, the hyperfine coupling of the deuterated radical was identified, in agreement with the CW measurements. The HYSCORE performed in the 3-lines system did not provide conclusive results. It's important to note that HYSCORE is a technique that demands a significant amount of time in the spectrometer (more than 12 hours for a single spectrum), which poses a challenge in obtaining multiple spectra with optimized parameters.

A line localized between the gravity center of the methyl radical and the core-defect ($g = 1.98$) is observed in Q-band EPR. This line is also present in X-band EPR but is obscured by the line L_4 of the methyl radical. This line suggests a coupling between the surface states (methyl radicals) and the core-defect, indicating that the core-defects responsible for transferring the hole to the organic shell are situated very close to the surface. This proximity is necessary because this coupling indicates a Heisenberg interaction, characterized by the overlap of the electronic wavefunctions.

Concerning the 3-lines system, its presence is consistently associated with the presence of methyl radicals, suggesting a relationship between these systems. Moreover, this signal exhibits higher optical stability, remaining unchanged under temperatures up to 110 K. This indicates greater stability of this system compared to the methyl radicals. The analysis in Q-band also indicates that the 3-lines system and the methyl radicals share the same gravity center, implying a probable similarity in their origins. This scenario suggests the possibility of the 3-lines system originating from biradicals, formed by the interaction of two methyl radicals through exchange and/or dipolar interaction. Simulations conducted in the EasySpin software, considering this possibility, indicate that by adjusting appropriate values of exchange and dipolar couplings, the pattern presented by the 3-lines group could be reproduced. However, a more comprehensive analysis is necessary to conclusively attribute this signal to the formation of biradicals. This comprehensive analysis should involve consideration of anisotropic J and K values, along with a distribution of distances between centers, to confirm this hypothesis. This inhomogeneity of distances is expected because the NPs do not exhibit a constant potential. This suggests that the formation of methyl radicals should be more efficient at the poles and nearly nonexistent at the equator of the NP.

Analyzing the behavior of T_1 for the different systems using the inversion recovery technique, we observe that at low temperatures (T$<$ 10K), the spin-lattice relaxation time is over 100 times longer than the coherence time for the organic systems. However, as the temperature rises, leading to an increase in the density of phonons within the system, this difference is significantly reduced. The results indicate that at low temperatures, the relaxation of the core-defect and the 3-lines group occurs via a direct process, with

Raman contributions starting to become significant at temperatures beyond 15 K. As for the methyl radicals, the relaxation phenomenon is characterized by a non-usual Raman process, exhibiting a dependence of $1/T^4$.

Doping ZnO NPs with cobalt by changing the precursor during the sol-gel synthesis results in NPs that retain the aforementioned surface properties, alongside properties introduced by cobalt ions. We have observed that with an increase in the percentage of cobalt doping, the signal linked to the core-defect decreases progressively until it completely disappears. This suggests that the introduction of cobalt into the ZnO lattice either eliminates the defect attributed to the core-defect or hinders this defect from undergoing ionization. Consequently, without the observation of the core-defect, the signals originating from the methyl radical and the 3-lines system are no longer detected. This indicates that these latter signals can only arise through charge transfer facilitated by the ionization of the core-defect. Furthermore, with a substantial increase in the quantity of cobalt doping, additional adjacent lines are observed in the EPR spectrum, which are associated with the formation of cobalt pairs interacting through exchange interaction.

Higher doping levels (ranging from 1 to 8%) are investigated in samples produced via the solid-state method, which involves high-temperature processes, resulting in samples without the organic shell. In these samples, adjacent lines are observed in the EPR spectrum, indicating the formation of cobalt pairs interacting through exchange interaction. These states are particularly intriguing due to the generation of resonant lines near zero magnetic field.

Regarding the near-zero field transition, we conducted an analytical calculation treating the Zeeman effect as a perturbation. Through this approach, we identified the emergence of EPR transitions occurring between levels that display a parabolic dependence on the magnetic field, providing an explanation for this phenomenon. Additionally, this transition is observed in the parallel mode, wherein the static magnetic field and the microwave are applied in a parallel configuration. This geometry offers advantages as, in this configuration, the prominent signal originating from the single ion is almost completely eliminated.

Finally, all the aforementioned results are consolidated to propose a physical model for the NPs, elucidating the reactions occurring on the surface. In this model, we propose that the characteristic polarization of ZnO generates charged surfaces in the NP and, consequently, a non-uniform electric potential within the NP. In this context, the system is out of the thermodynamic equilibrium and utilizes available elements to passivate the surfaces. The passivation mechanism adopted by the system depends on the temperature range. At room temperature, where electrons donated by donor defects are available, passivation occurs through the simple ionization of donor defects (turning them positive and passivating the negative surface) and by the electrons themselves (passivating the positive surface). This model aligns with the well-known n-type conductivity exhibited by ZnO. At low temperatures, electrons are drawn back towards their centers, since the system lacks sufficient thermal energy to keep them separated. Consequently, the NP experience an increase in the electric potential with decreasing temperature. This rise in the potential leads to the ionization of acetic acids present on the surface of the NP. The ionization of the acetic acid generated acetates, negatively charged, that are able to passivate the positive surface, while the released protons (out coming from the ionization of the acetic acid) passivate the negative surface. When the system is photo-excited, light induces the ionization of an acceptor defect, capturing an electron from the valence band. This process releases a hole, which interacts with the acetates located on the surface,

through a photo-Kolbe reaction, generating methyl radicals.

The presence of core-defects at dark condition in particles derived from solid-state reaction or exposed to high temperatures implies that in the absence of an organic shell, the system experiences charge separation to stabilize its polar surfaces. This stabilization process involves the ionization of neutral acceptor defects localized near the (Zn^{2+})-terminated surface, transforming them into negatively charged states. Consequently, this alteration results in the observation of a core-defect signal ($g = 1.96$) under dark conditions.

An additional line observed between the 7-lines system and the core-defect indicates an interaction between the core-defect and the methyl radicals present in the shell of the NP. This line was observed in X-band in the deuterated sample. In the as-grown sample, this line manifests as a deformation in the L_4 line, associated with the methyl radical. Upon analyzing the system in Q-band, this line shifts while maintaining its position in the exact center between the core-defect and the 7-lines cluster ($g = 1.98$). These results strongly suggest a connection between the core-defect and the methyl radical, demonstrating that the surface and the core of the NP are not completely independent.

Future Perspectives

Some future perspectives for the continuity of this work are:

- The presence of surface states identified in the NPs suggests that this material, when produced via the sol-gel method, has the ability to stably aggregate molecules from its surroundings. Our work also demonstrated that these molecules can be replaced (as in the case of deuterium substitution) and maintained stably, opening the possibility of exchanging these molecules for substances that might be interesting for technological applications.

- In the context of studying the chemical transformations of compounds present in NPs, further studies are encouraged to clarify the intermediate reaction through which methyl undergoes before returning to its initial state. Investigations confirming the origin of the 3-lines system are also sought after.

  itemMeasurements regarding the change in the conductivity of ZnO in the regime where our model proposes that passivation is accomplished through the ionization of acetic acid would be a pivotal point for validating the model.

- The reduction in the size of the Co-doped NPs can induce confinement effects, as the NPs may become smaller than the distance between Co-pairs. This characteristic is aimed to be further explored.

- Preliminary results suggest that the "Elephant" signal observed in NPs produced by aqueous coprecipitation can be both activated and deactivated by exposure to light with varying photon energies. This newly discovered characteristic warrants further exploration, as the photo-activation and deactivation signals could potentially form a binary system, holding promising technological applications.

- To improve the HYSCORE detection of the possible couplings between deuterated radicals, HYSCORE measurements in Q-band for the deuterated sample are aspirated.

Appendix A

ZnO NP synthesis

In a glove box:

Separate 2 volumetric balloons (250ml and 125ml), wash both with the solvent that will be used in the reaction to be sure that no impurities remain.

Put **4,1 g** of Zinc acetate in the big volumetric balloon, add **210 ml** of methanol anhydrous and an agitator inside the baloon. Seal it with a rubber stopper.

Put **2,2 g** of KOH in the small balloon. Add **115 ml** of methanol anhydrous and seal it with a rubber stopper.

Make sure that the balloons are well closed. Shake them for some minutes to mix well the substances.

Put the balloons in ultrasound until the substances are well dissolved. The temperature must not exceed **60 °C**.

Put **1,25 ml** of distilled water in the big balloon. Do attention to perform this stage fast, the balloon must not be open for long time.

Close the column and seal it to the big balloon with grease (just a little bit is enough)

Submerge the big balloon in stirring oil at **60°C** and 1000 rpm.

Close the column and utilize a needle and a balloon with Argon to remove the O2 from the tube. Let the key opened in this first procedure.

Close the key, put the KOH in the column and redo the procedure for removing the O2.

Wait 5 minutes and open the dropper. In 30 minutes, all the KOH must be dropped in the Zinc acetate.

After all the KOH is deposed, let the solution in the oil for **3h15**. During this time, the solution will assume a white coloration, after it will be clean again and, in the end, it will be white-blue and finally white again.

Remove the balloon with the solution from the column and separate the solution in 8 falcon tubes.

Put the tubes in the centrifuge for 12 minutes and with rotation 7800 rpm.

Remove the residue from the solution after centrifuge

In the glove box: Put 8 – 10 ml of methanol inside each Falcon tube in such a way that ZnO will return in solution.

Put the falcon tubes in ultrasound once again until all the solution is dissolved

For driving the powder, centrifygate the solution again, remove the solution's residue and let the concentrate dry in an oven at **100°C** for **10 minutes** .

Appendix B

Fourier Transform Infrared Spectroscopy (FTIR)

To elucidate the structure of the matter at molecular scale, Infrared Spectroscopie (IR) is a very useful technique, furthermore when organic compounds are present once that the chemical composition and the bonding arrangements can be extract by this technique. The basic principle of IR spectroscopy is to apply an infrared radiation into the sample and measure the reflexion or transmission (depending on the operation mode) of the radiation through the sample. If the sample contains molecular groups whose vibrational frequency corresponds to that of the radiation, energy will be asorbed, and a "hole" will be seen in the spectra[193] [194]. It's important to reinforce that in IR spectroscopy, the energy given by the radiation is strong enough just to cause vibrational excitation but not to promote an electron to an excited state. The type of vibration that can occur in a molecule are separated in two types: stretching (more energetic) and bending (low energetic) and these vibrational modes can be symetric or assymetric. The schematic representation of these vibrational modes are represented in figure B.1

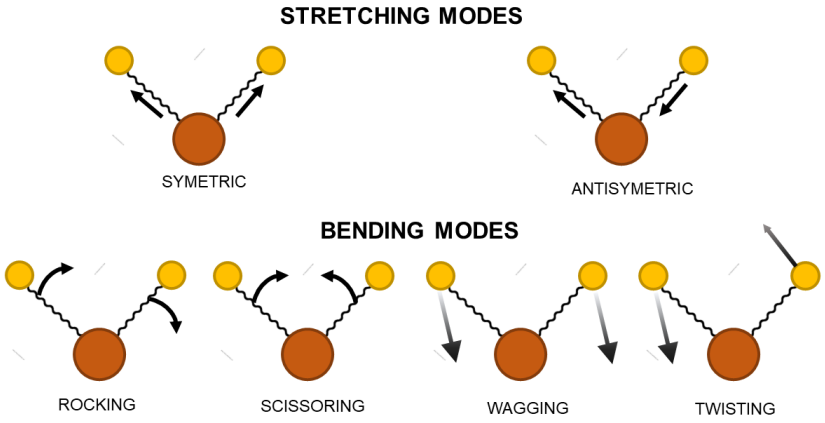

Figure B.1: *Caption*

For organic chemistry, the range of absorption will happen in the mid-infrared region (4000 - 400 cm^{-1}).

A more sofisticated technique is the Fourier Transform Infrared Spectroscopy (FTIR) that relies in apply IR radiation in the form of a complex frequency interferogram into

the sample and identify the missing frequencies after Fourier Transform. In this way the frequencies in which the sample absorbs will be well characterized by dips.

The current utilisation of Infrared Spectroscopy relies in compare the measured absorption of the sample with a well-known table that associates the region of the absorbed spectra with a determined molecular vibration mode. A complete table that associes the absorption range to a specific molecular vibration is presented in the next pages.

Table 1. Characteristic IR Absorption Peaks of Functional Groups*

Vibration	Position (cm^{-1})	Intensity*	Notes
Alkanes			
C-H stretch	2990 – 2850	m to s	
Alkenes			
=C-H stretch	3100 – 3000	m	
C=C stretch	1680 – 1620 (sat.) 1650 – 1600 (conj.)	w to m	
=C-H bend	995 – 685	s	See Table 2 for detail
Alkynes			
≡C-H stretch	3310 – 3200	s	
C≡C stretch	2250 – 2100	m to w	
Aromatic Compounds			
C-H stretch	3100 – 3000	m to w	
C=C stretch	1625 – 1440	m to w	Hidden in fingerprint region
C-H bend	900 – 680	s	See Table 2 for detail
Alcohols**			
O-H stretch	3550 – 3200	br, s	Hydrogen bonded (typical)
Amines			
N-H stretch	3550 – 3250	br, m	Primary (two bands) Secondary (one band)
Nitriles			
C≡N stretch	2280 – 2200	s	
Aldehydes			
C-H stretch	2900 – 2800 & 2800 – 2700	s	H-C=O Fermi doublet
C=O stretch	1740 – 1720 (sat.) 1715 – 1680 (conj.)	s	
Ketones			
C=O stretch	1750 – 1705 (sat.) 1700 – 1665 (conj.)	s	
Esters**			
C=O stretch	1765 – 1735 (sat.) 1730 – 1715 (conj.)	s	
Carboxylic Acids**			
O-H stretch	3200 – 2500	br, m to w	
C=O stretch	1725 – 1700 (sat.) 1715 – 1680 (conj.)	s	
Amides			
N-H stretch	3500 – 3150	m	Primary (two bands) Secondary (one band)
C=O stretch	1700 – 1630	s	

Table 1 cont'd

Vibration	Position (cm^{-1})	Intensity	Notes
Anhydrides**			
C=O stretch	1850 – 1800 & 1790 – 1740	s	
Acid Chlorides			
C=O stretch	1815 – 1770	s	
Nitro Compounds			
NO_2 stretch	1570 – 1490 & 1390 – 1300	s	
Thiols†			
R-S-H stretch	2550 – 2600		
Alkyl & Aryl Halides†			
C-F stretch	1000 – 1400		Hidden in fingerprint region
C-Cl stretch	< 600 – 840		
C-Br stretch	< 700		
C-I stretch	< 600		

* Abbreviations: s = strong; m = medium; w = weak; br = broad; sat. = saturated; conj. = conjugated
** Alcohols, Esters, Carboxylic Acids, and Anhydrides also absorb in the fingerprint region due to the C-O stretch (1300 – 1000, s).

Table 2. Out-of-Plane C-H Bending Vibrations in Alkenes and Aromatics

Alkene Structure	Position (cm^{-1})	Phenyl Structure	Position (cm^{-1})
Mono-substituted 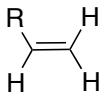	997 – 985 & 915 – 905	Mono-substituted 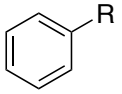	770 – 730 & 720 – 680
Disubstituted, *trans* 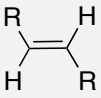	980 – 960	Disubstituted, *ortho* 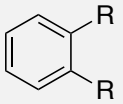	770 – 735
Disubstituted, *cis* 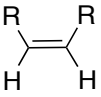	730 – 665	Disubstituted, *meta* 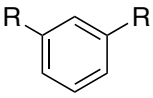	810 – 750 & 725 – 680
Disubstituted, symm. 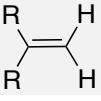	895 – 885	Disubstituted, *para* 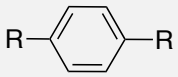	860 – 800
Trisubstituted 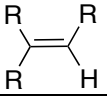	840 – 790		

[*] Adapted from…Mohrig, J. R.; Hammond, C. N.; Schatz, P. F. "Infrared Spectroscopy" in *Techniques in Organic Chemistry*. Freeman: New York, 2006.
[†] Palleros, D. R. "Infrared Spectroscopy" in *Experimental Organic Chemistry*. Wiley: New York, 2000. p. 688.

Appendix C

Raising and lowering operators formalism

Assuming the quantization of the spin, which can assume only values $\pm\frac{\hbar}{2}$, the matrix operators for the components S_x, S_y and S_z are written in terms of the Pauli spin matrices. Defining the direction z as the direction in which a magnetic field is placed, we have

$$\begin{aligned} S_x &= \frac{\hbar}{2}\sigma_x = \frac{\hbar}{2}\begin{pmatrix} 0 & 1 \\ 1 & 0 \end{pmatrix} \\ S_y &= \frac{\hbar}{2}\sigma_y = \frac{\hbar}{2}\begin{pmatrix} 0 & -i \\ i & 0 \end{pmatrix} \\ S_z &= \frac{\hbar}{2}\sigma_z = \frac{\hbar}{2}\begin{pmatrix} 1 & 0 \\ 0 & -1 \end{pmatrix} \end{aligned} \tag{C.1}$$

in which σ_x,σ_y and σ_z are the Pauli matrices, that obey the comutation relations:

$$\begin{aligned} \sigma_y\sigma_z - \sigma_z\sigma_y &= 2i\sigma_x \\ \sigma_z\sigma_x - \sigma_x\sigma_z &= 2i\sigma_y \\ \sigma_x\sigma_y - \sigma_y\sigma_x &= 2i\sigma_z \end{aligned} \tag{C.2}$$

From the Pauli matrices, the relation $|S|^2 = S_x^2 + S_y^2 + S_z^2 = s(s+1)\hbar^2[I]$ can be obtained, and the similarity with the relations for the angular momentum $|L|^2 = m(m+1)\hbar^2[I]$ is explicit.

From the relation C.1, the following properties can be extracted:

$$\begin{aligned} [S_x, S_y] &= ihS_z \\ [S_y, S_z] &= ihS_x \\ [S_z, S_x] &= ihS_y \\ [S^2, S_i] &= 0, for i = 0, 1, 2... \end{aligned} \tag{C.3}$$

Defining the raising and lowering operators, respectively as

$$\begin{aligned} S_+ &= S_x + iS_y \\ S_- &= S_x - iS_y \end{aligned} \tag{C.4}$$

or, from the Pauli matrixes

$$\begin{aligned} \sigma_+ &= \sigma_x + i\sigma_y = 2\begin{pmatrix} 0 & 1 \\ 0 & 0 \end{pmatrix} \\ \sigma_+ &= \sigma_x - i\sigma_y = 2\begin{pmatrix} 0 & 0 \\ 1 & 0 \end{pmatrix} \end{aligned} \tag{C.5}$$

Appendix D

"Elephant" signal

Initial investigations were conducted on the signal identified as "Elephant." This signal is consistently present in all ZnO samples produced through wet fabrication methods. However, it appears superimposed on the signals corresponding to the methyl radical and the 3-line system.

Another fabrication method, known as aqueous coprecipitation (3.1.3), was employed to synthesize nanoflakes. This method effectively prevents the formation of radicals on the surface, enabling separate analysis of the "Elephant" signal, even in X-band EPR. The morphology displayed through this synthesis approach showcases nanoflakes, resembling salt flowers, as depicted in Figure D.1.

It's important to note that the "elephant" line is also photosensitive and only manifests under illumination. This signal is activated using the same wavelength employed for generating methyl radicals (405nm).

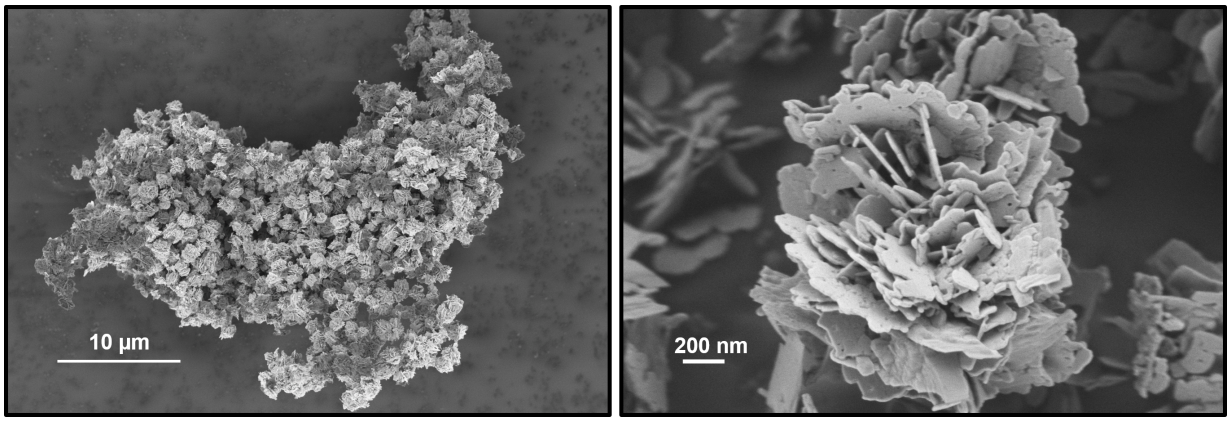

Figure D.1: *Nanoflakes of ZnO synthesized via aqueous coprecipitation method.*

The EPR spectrum of the nanoflakes is displayed in Figure D.3. Additionally, the core defect, associated with the bulk of the nanoflakes, is also present and exhibits high sensitivity to light exposure.

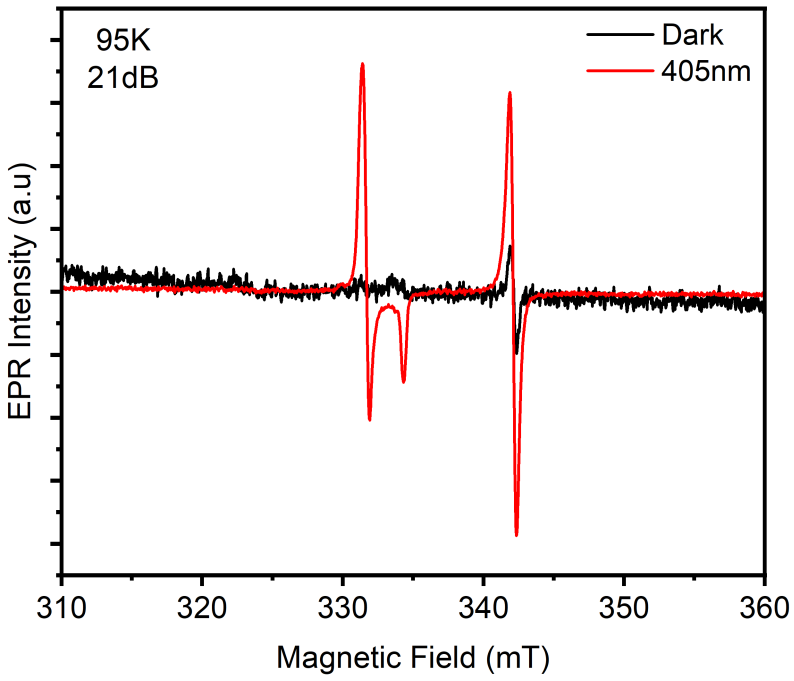

Figure D.2: *EPR spectra of the nanoflafles produced via aqueous coprecipitation method. The core defect is present, together with the "elephant" signal.*

The "Elephant signal" in the EPR spectrum manifests as two distinct lines, with a separation of 2.67 mT. Upon closer examination, the analysis reveals a splitting of 0.15 mT in the second line.

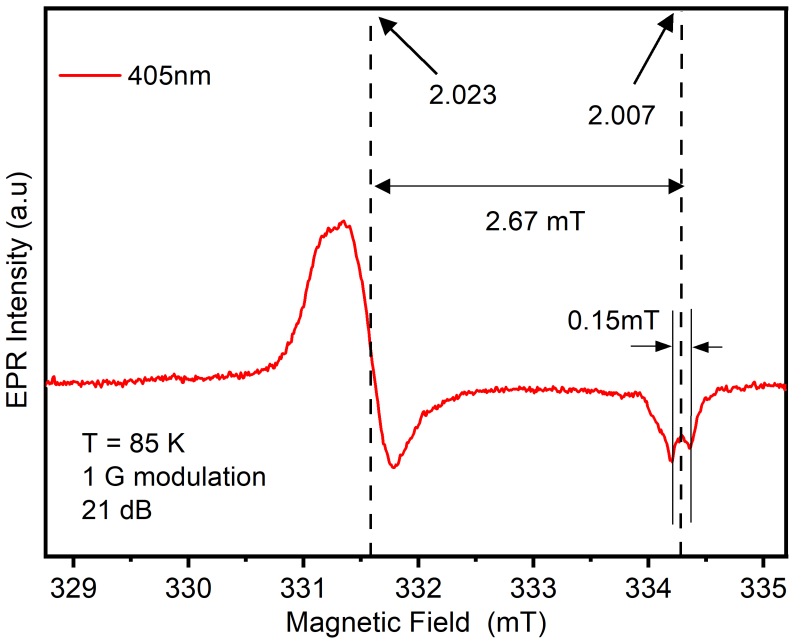

Figure D.3: *Splitting of the lines belonging to th e"Elephant" signal*

Appendix E

Orientation of an anisotropic crystal in EPR

In the context of an anisotropic crystal, the crystal's orientation within the EPR cavity is of crucial importance because different directions do not resonate in the same way.

For axial anisotropy, as presented in the Wurtzite structure, the crystal can adopt two extreme cases within the resonator. The intermediate states are linear combinations of these primary orientations. The possible orientations are illustrated in Figure E.1:

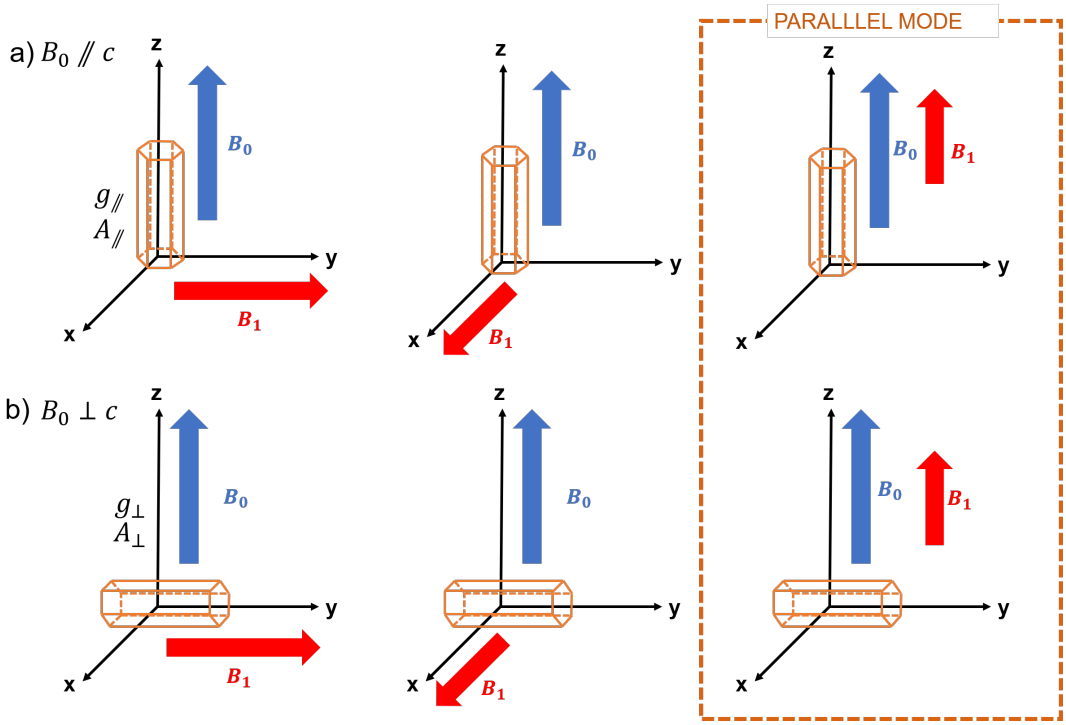

Figure E.1: *All the possible orientations of a crystal and the magnetic fields in the EPR cavity. in a) The axis c of the crystal is parallel to the static magnetic field B_0 . In b) the axis c is perpendicular to the static magnetic field B_0. for each case, the oscillatory field can be applied in two perpendicular and one parallel orientations. The associated quantities g and A are associated for each direction.*

In scenario (a), the c-axis of the crystal structure aligns parallel to the static magnetic

field. This alignment is responsible for the determination of the quantities $g_{\parallel}$ and $A_{\parallel}$.

In this configuration, the oscillatory magnetic field B_1 can be applied in three different directions, resulting in two perpendicular cases and one parallel case with respect to the static magnetic field.

In scenario (b), the static magnetic field is oriented perpendicular to the c-axis. In this context, the quantities $g_{\perp}$ and $A_{\perp}$ are determined. Similarly, the oscillatory magnetic field can be applied in two perpendicular modes and one parallel mode. It's worth noting that the (b) configuration is more abundant in powder spectra.

Appendix F

Analytical coefficients

The analytical coefficients obtained for describing the energy levels presented by cobalt pairs in ZnO lattice are:

$$\begin{aligned} X &= D^2 + 2DJ + 25J^2 \\ Y &= 4D^2 + 9J^2 \\ Z &= 4D^2 + 16DJ + 25J^2 \end{aligned} \tag{F.1}$$

and those related to the eigenstates are:

$$\begin{aligned} \alpha &= \frac{D + J + \sqrt{X}}{\sqrt{2}\sqrt{(D + J + \sqrt{X})^2 + 24J^2}} \\ \beta &= \frac{2\sqrt{3}J}{\sqrt{2}\sqrt{(D + J + \sqrt{X})^2 + 24J^2}} \\ \gamma &= \frac{2D + \sqrt{Y}}{\sqrt{2}\sqrt{(2D + \sqrt{Y})^2 + 9J^2}} \\ \delta &= \frac{3J}{\sqrt{2}\sqrt{(2D + \sqrt{Y})^2 + 9J^2}} \\ \epsilon &= \frac{2D + 4J + \sqrt{Z}}{\sqrt{2}\sqrt{(2D + 4J + \sqrt{Z})^2 + 9J^2}} \\ \xi &= \frac{3J}{\sqrt{2}\sqrt{(2D + 4J + \sqrt{Z})^2 + 9J^2}} \end{aligned} \tag{F.2}$$

Bibliography

[1] A. Savoyant, M. Rollo, M. Texier, R. Adam, S. Bernardini, O. Pilone, O. Margeat, O. Nur, M. Willander, and S. Bertaina, Nanotechnology **31**, 095707 (2019).

[2] R. Laiho, D. Poloskin, Y. P. Stepanov, M. Vlasenko, L. S. Vlasenko, and V. Zakhvalinskii, Journal of Applied Physics **106** (2009).

[3] J. Bao, I. Shalish, Z. Su, R. Gurwitz, F. Capasso, X. Wang, and Z. Ren, Nanoscale research letters **6**, 1 (2011).

[4] J. R. Harbour, V. Chow, and J. R. Bolton, Canadian Journal of Chemistry **52**, 3549 (1974).

[5] A. Lipovsky, Z. Tzitrinovich, H. Friedmann, G. Applerot, A. Gedanken, and R. Lubart, The Journal of Physical Chemistry C **113**, 15997 (2009).

[6] F. Kayaci, S. Vempati, I. Donmez, N. Biyikli, and T. Uyar, Nanoscale **6**, 10224 (2014).

[7] Y. Tang, H. Zhou, K. Zhang, J. Ding, T. Fan, and D. Zhang, Chemical Engineering Journal **262**, 260 (2015).

[8] T. Butkhuzi, T. Chelidze, A. Georgobiani, D. Jashiashvili, T. Khulordava, and B. Tsekvava, Physical Review B **58**, 10692 (1998).

[9] P. Rodnyi and I. Khodyuk, Optics and Spectroscopy **111**, 776 (2011).

[10] A. Chatterjee, P. Stevenson, S. De Franceschi, A. Morello, N. P. de Leon, and F. Kuemmeth, Nature Reviews Physics **3**, 157 (2021).

[11] K. Vanheusden, C. Seager, W. t. Warren, D. Tallant, and J. Voigt, Applied physics letters **68**, 403 (1996).

[12] A. Bera and D. Basak, Applied Physics Letters **94** (2009).

[13] V. Titov, A. Lisachenko, I. K. Akopyan, M. Labzowskaya, and B. Novikov, Journal of Luminescence **195**, 153 (2018).

[14] X. Meng, Y. Zhou, X. Zeng, X. Chen, and Y. Chu, Journal of Luminescence **195**, 201 (2018).

[15] J. Lv, C. Li, and Z. Chai, Journal of Luminescence **208**, 225 (2019).

[16] Bruker, EPR 101: An Introduction to Electron Paramagnetic Resonance (2023).

[17] P. H. Kasai, Physical Review **130**, 989 (1963).

[18] D. Galland and A. Herve, Physics Letters A **33**, 1 (1970).

[19] D. Galland and A. Herve, Solid State Communications **14**, 953 (1974).

[20] W. Carlos, E. Glaser, and D. C. Look, Physica B: Condensed Matter **308**, 976 (2001).

[21] L. S. Vlasenko, Physica B: Condensed Matter **404**, 4774 (2009).

[22] L. Vlasenko, Applied Magnetic Resonance **39**, 103 (2010).

[23] S. Nadupalli, S. Repp, S. Weber, and E. Erdem, Nanoscale **13**, 9160 (2021).

[24] J. Lambe, J. Baker, and C. Kikuchi, Physical Review Letters **3**, 270 (1959).

[25] W. Holton, J. Schneider, and T. Estle, Physical Review **133**, A1638 (1964).

[26] T.-T. Chen, I.-C. Chang, M.-H. Yang, H.-T. Chiu, and C.-Y. Lee, Applied Catalysis B: Environmental **142**, 442 (2013).

[27] M. Atzori and R. Sessoli, Journal of the American Chemical Society **141**, 11339 (2019).

[28] E. Knill, R. Laflamme, and G. J. Milburn, nature **409**, 46 (2001).

[29] R. Blatt and D. Wineland, Nature **453**, 1008 (2008).

[30] N. A. Gershenfeld and I. L. Chuang, science **275**, 350 (1997).

[31] R. Maurand, X. Jehl, D. Kotekar-Patil, A. Corna, H. Bohuslavskyi, R. Laviéville, L. Hutin, S. Barraud, M. Vinet, M. Sanquer, *et al.*, Nature communications **7**, 13575 (2016).

[32] J. Weber, W. Koehl, J. Varley, A. Janotti, B. Buckley, C. Van de Walle, and D. D. Awschalom, Proceedings of the National Academy of Sciences **107**, 8513 (2010).

[33] D. D. Awschalom, L. C. Bassett, A. S. Dzurak, E. L. Hu, and J. R. Petta, Science **339**, 1174 (2013).

[34] J. J. Pla, K. Y. Tan, J. P. Dehollain, W. H. Lim, J. J. Morton, D. N. Jamieson, A. S. Dzurak, and A. Morello, Nature **489**, 541 (2012).

[35] S. Nakazawa, S. Nishida, T. Ise, T. Yoshino, N. Mori, R. D. Rahimi, K. Sato, Y. Morita, K. Toyota, D. Shiomi, *et al.*, Angewandte Chemie International Edition **51**, 9860 (2012).

[36] H. J. Queisser and E. E. Haller, Science **281**, 945 (1998).

[37] S. Parashar, B. Murty, S. Repp, S. Weber, and E. Erdem, Journal of Applied Physics **111** (2012).

[38] A. Pöppl and G. Völkel, physica status solidi (a) **121**, 195 (1990).

[39] A. Pöppl and G. Völkel, physica status solidi (a) **125**, 571 (1991).

[40] V. Nikitenko, Journal of Applied Spectroscopy **57**, 783 (1992).

[41] D. Marin, G. Gerbaud, O. Margeat, F. Ziarelli, F. Ferrer, O. Ouari, A. Campos, S. Bertaina, and A. Savoyant, The Journal of Chemical Physics **158** (2023).

[42] A. Savoyant, C. Sebastiao, and O. Margeat, physica status solidi (RRL)–Rapid Research Letters **14**, 2000176 (2020).

[43] I. Ayoub, V. Kumar, R. Abolhassani, R. Sehgal, V. Sharma, R. Sehgal, H. C. Swart, and Y. K. Mishra, Nanotechnology Reviews **11**, 575 (2022).

[44] R. S. Rai and V. Bajpai, Adv. Nano Res **11**, 37 (2021).

[45] B. Weintraub, Z. Zhou, Y. Li, and Y. Deng, Nanoscale **2**, 1573 (2010).

[46] E. Roduner, Chemical society reviews **35**, 583 (2006).

[47] V. I. Korepanov, S.-Y. Chan, H.-C. Hsu, and H.-o. Hamaguchi, Heliyon **5** (2019).

[48] S. Singh, P. Thiyagarajan, K. M. Kant, D. Anita, S. Thirupathiah, N. Rama, B. Tiwari, M. Kottaisamy, and M. R. Rao, Journal of Physics D: Applied Physics **40**, 6312 (2007).

[49] H. S. Kang, B. D. Ahn, J. H. Kim, G. H. Kim, S. H. Lim, H. W. Chang, and S. Y. Lee, Applied Physics Letters **88** (2006).

[50] H. Mathieu and H. Fanet, *Physique des semiconducteurs et des composants électroniques-6ème édition: Cours et exercices corrigés* (Dunod, 2009).

[51] C. F. Klingshirn, A. Waag, A. Hoffmann, and J. Geurts, (2010).

[52] M. Sowjanya, M. Shariq, Y. Alajlani, D. Pamu, R. Chowdhury, R. Jayaganthan, and S. Taqiullah, Acta Physica Polonica, A. **137** (2020).

[53] F. Li, *Fabrication and characterization of ZnO-based microcavities working in the strong coupling regime: polariton laser*, Ph.D. thesis, Université Nice Sophia Antipolis (2013).

[54] Ü. Özgür, Y. I. Alivov, C. Liu, A. Teke, M. A. Reshchikov, S. Doğan, V. Avrutin, S.-J. Cho, Morkoç, and H, Journal of applied physics **98** (2005).

[55] H. Karzel, W. Potzel, M. Köfferlein, W. Schiessl, M. Steiner, U. Hiller, G. Kalvius, D. Mitchell, T. Das, P. Blaha, *et al.*, Physical Review B **53**, 11425 (1996).

[56] M. Catti, Y. Noel, and R. Dovesi, Journal of physics and Chemistry of Solids **64**, 2183 (2003).

[57] M. De Jong, W. Chen, H. Geerlings, M. Asta, and K. A. Persson, Scientific data **2**, 1 (2015).

[58] A. Dal Corso, M. Posternak, R. Resta, and A. Baldereschi, Physical Review B **50**, 10715 (1994).

[59] O. Dulub, U. Diebold, and G. Kresse, Physical review letters **90**, 016102 (2003).

[60] S. Pal, T. Jasper-Tönnies, M. Hack, and E. Pehlke, Physical Review B **87**, 085445 (2013).

[61] M. Zobel, *Nanoparticle crystallization and solvent interface restructuring especially for ZnO nanoparticles in organic solvents*, Ph.D. thesis, Friedrich-Alexander-Universität Erlangen-Nürnberg (FAU) (2016).

[62] C. Klingshirn, H. Priller, M. Decker, J. Brückner, H. Kalt, R. Hauschild, J. Zeller, A. Waag, A. Bakin, H. W. K. Thonke, *et al.*, Advances in Solid State Physics , 275 (2006).

[63] S. Choi, M. R. Phillips, I. Aharonovich, S. Pornsuwan, B. C. Cowie, and C. Ton-That, Advanced Optical Materials **3**, 821 (2015).

[64] M. Cardona and Y. Y. Peter, *Fundamentals of semiconductors*, Vol. 619 (Springer, 2005).

[65] K. Nagpal, E. Rauwel, E. Estephan, M. R. Soares, and P. Rauwel, Nanomaterials **12**, 3546 (2022).

[66] A. Janotti and C. G. Van de Walle, Physical Review B **76**, 165202 (2007).

[67] L. Liu, Z. Mei, A. Tang, A. Azarov, A. Kuznetsov, Q.-K. Xue, and X. Du, Physical Review B **93**, 235305 (2016).

[68] F. Oba, M. Choi, A. Togo, and I. Tanaka, Science and Technology of Advanced Materials (2011).

[69] A. B. Djurišić, W. C. Choy, V. A. L. Roy, Y. H. Leung, C. Y. Kwong, K. W. Cheah, T. Gundu Rao, W. K. Chan, H. Fei Lui, and C. Surya, Advanced Functional Materials **14**, 856 (2004).

[70] E. Ahmed, S. Mazumder, and K. Senthilkumar, Solid State Communications **339**, 114501 (2021).

[71] K. Senthilkumar, M. Tokunaga, H. Okamoto, O. Senthilkumar, and Y. Fujita, Applied physics letters **97** (2010).

[72] S. Chichibu, T. Onuma, M. Kubota, A. Uedono, T. Sota, A. Tsukazaki, A. Ohtomo, and M. Kawasaki, Journal of applied physics **99** (2006).

[73] R.-A. Eichel, E. Erdem, P. Jakes, A. Ozarowski, J. Van Tol, R. C. Hoffmann, and J. J. Schneider, Functional Materials Letters **6**, 1330004 (2013).

[74] M. Gerhard, B. Louis, R. Camacho, A. Merdasa, J. Li, A. Kiligaridis, A. Dobrovolsky, J. Hofkens, and I. G. Scheblykin, Nature Communications **10**, 1698 (2019).

[75] T. Goudon, V. Miljanović, and C. Schmeiser, SIAM Journal on Applied Mathematics **67**, 1183 (2007).

[76] X. Wang and S. Xu, Applied Physics Letters **102**, 181909 (2013).

[77] B. K. Meyer, H. Alves, 1, D. Hofmann, W. Kriegseis, D. Forster, F. Bertram, J. Christen, A. Hoffmann, M. Straßburg, M. Dworzak, *et al.*, physica status solidi (b) **241**, 231 (2004).

[78] M. Garcia, J. Merino, E. Fernández Pinel, A. Quesada, J. De la Venta, M. Ruíz González, G. Castro, P. Crespo, J. Llopis, J. González-Calbet, *et al.*, Nano letters **7**, 1489 (2007).

[79] R. L. Carlin and A. J. van Duyneveldt, *Magnetic properties of transition metal compounds* (Springer, 1977).

[80] Y. Yafet, in *Solid state physics*, Vol. 14 (Elsevier, 1963) pp. 1–98.

[81] P. A. M. Dirac, Proceedings of the Royal Society of London. Series A, Containing Papers of a Mathematical and Physical Character **117**, 610 (1928).

[82] J. Fu and M. Wu, Journal of Applied Physics **104**, 093712 (2008).

[83] C. E. Pryor and M. E. Flatté, Physical review letters **96**, 026804 (2006).

[84] J. A. Weil and J. R. Bolton, *Electron paramagnetic resonance: elementary theory and practical applications* (John Wiley & Sons, 2007).

[85] A. Schweiger and G. Jeschke, *Principles of pulse electron paramagnetic resonance* (Oxford University Press on Demand, 2001).

[86] G. R. Eaton, S. S. Eaton, D. P. Barr, and R. T. Weber, *Quantitative Epr* (Springer Science & Business Media, 2010).

[87] J.-M. Spaeth and H. Overhof, *Point defects in semiconductors and insulators: determination of atomic and electronic structure from paramagnetic hyperfine interactions*, Vol. 51 (Springer Science & Business Media, 2003).

[88] P. Bertrand, *Electron Paramagnetic Resonance Spectroscopy* (Springer, 2020).

[89] C. Gorter and J. Van Vleck, Physical Review **72**, 1128 (1947).

[90] J. H. Van Vleck, Physical Review **74**, 1168 (1948).

[91] P.-W. Anderson and P. Weiss, Reviews of Modern Physics **25**, 269 (1953).

[92] A. Bencini, D. Gatteschi, *et al.*, .

[93] A. Ginsberg, Journal of the American Chemical Society **102**, 111 (1980).

[94] S. S. Eaton and G. R. Eaton, Distance measurements in biological systems by EPR , 29 (2000).

[95] N. W. Ashcroft and N. D. Mermin, *Solid state physics* (Cengage Learning, 2022).

[96] L. Gu and R. Wu, Physical Review B **103**, 014401 (2021).

[97] L. P. Soriano, *Etude par Résonance Paramagnétique Electronique de la cohérence de spin dans les composés organiques (o-DMTTF) 2X (X= Cl, Br, I NO2 and NO3)*, Ph.D. thesis, Aix-Marseille Université (2022).

[98] R. Orbach, Proceedings of the Royal Society of London. Series A. Mathematical and Physical Sciences **264**, 458 (1961).

[99] M. Briganti, F. Santanni, L. Tesi, F. Totti, R. Sessoli, and A. Lunghi, Journal of the American Chemical Society **143**, 13633 (2021).

[100] E. Dikarov, O. Zgadzai, Y. Artzi, and A. Blank, Physical Review Applied **6**, 044001 (2016).

[101] W. Mims, K. Nassau, and J. McGee, Physical Review **123**, 2059 (1961).

[102] M. A. Hemminga and L. Berliner, *ESR spectroscopy in membrane biophysics*, Vol. 27 (Springer Science & Business Media, 2007).

[103] E. L. Hahn, Physical review **80**, 580 (1950).

[104] Nobel Media AB, The nobel prize in physics 1944 (1944).

[105] L. Rowan, E. Hahn, and W. Mims, Physical Review **137**, A61 (1965).

[106] A. Schweiger, Angewandte Chemie International Edition in English **30**, 265 (1991).

[107] S. A. Dikanov and Y. Tsvetkov, *Electron spin echo envelope modulation (ESEEM) spectroscopy* (CRC press, 1992).

[108] J. McCracken, Applications of Physical Methods to Inorganic and Bioinorganic Chemistry , 57 (2007).

[109] R. Merks and R. De Beer, Journal of Physical Chemistry **83**, 3319 (1979).

[110] P. Höfer, A. Grupp, H. Nebenführ, and M. Mehring, Chemical physics letters **132**, 279 (1986).

[111] C. Pacholski, A. Kornowski, and H. Weller, Angewandte Chemie International Edition **41**, 1188 (2002).

[112] J. Hasnidawani, H. Azlina, H. Norita, N. Bonnia, S. Ratim, and E. Ali, Procedia Chemistry **19**, 211 (2016).

[113] F. Giovannelli, A. N. Ndimba, P. Diaz-Chao, M. Motelica-Heino, P. Raynal, C. Autret, and F. Delorme, Powder technology **262**, 203 (2014).

[114] B. Cheetham, A. Cheetham, P. Day, *et al.*, *Solid state chemistry: techniques*, Vol. 1 (Oxford University Press, 1987).

[115] I. Žutić, J. Fabian, and S. D. Sarma, Physical Review B **64**, 121201 (2001).

[116] J. Kikkawa and D. Awschalom, Nature **397**, 139 (1999).

[117] Y. S. Didosyan, H. Hauser, G. A. Reider, and W. Toriser, Journal of applied physics **95**, 7339 (2004).

[118] D. C. Look, Materials science and engineering: B **80**, 383 (2001).

[119] Z. Chen, J. Wang, H. Wu, J. Yang, Y. Wang, J. Zhang, Q. Bao, M. Wang, Z. Ma, W. Tress, *et al.*, Nature Communications **13**, 4387 (2022).

[120] S. D. Birajdar, A. R. Saraf, A. P. Maharolkar, K. P. Gattu, N. G. Patil, R. B. Chavan, M. V. Jamkar, Y. S. Mundhe, R. N. Kambale, R. C. Alange, *et al.*, Journal of Alloys and Compounds **929**, 167272 (2022).

[121] A. Savoyant, H. Alnoor, O. Pilone, O. Nur, and M. Willander, Nanotechnology **28**, 285705 (2017).

[122] S. B. Orlinskii, J. Schmidt, P. G. Baranov, D. M. Hofmann, C. de Mello Donegá, and A. Meijerink, Physical review letters **92**, 047603 (2004).

[123] S. Orlinskii, H. Blok, E. Groenen, J. Schmidt, P. Baranov, C. de Mello Donegá, and A. Meijerink, Magnetic Resonance in Chemistry **43**, S140 (2005).

[124] H. Noei, H. Qiu, Y. Wang, E. Löffler, C. Wöll, and M. Muhler, Physical Chemistry Chemical Physics **10**, 7092 (2008).

[125] J. Schaefer and E. Stejskal, Journal of the American Chemical Society **98**, 1031 (1976).

[126] A. Umar, R. Kumar, G. Kumar, H. Algarni, and S. Kim, Journal of Alloys and Compounds **648**, 46 (2015).

[127] H. Kaftelen, K. Ocakoglu, R. Thomann, S. Tu, S. Weber, and E. Erdem, Physical Review B **86**, 014113 (2012).

[128] E. Erdem, Journal of alloys and compounds **605**, 34 (2014).

[129] I. Elhamdi, H. Souissi, O. Taktak, J. Elghoul, S. Kammoun, E. Dhahri, and B. F. Costa, RSC advances **12**, 13074 (2022).

[130] D. Savchenko, A. Vasin, O. Kuz, I. Verovsky, A. Prokhorov, A. Nazarov, J. Lančok, and E. Kalabukhova, Scientific Reports **10**.

[131] E. Cerrato, M. C. Paganini, and E. Giamello, Journal of Photochemistry and Photobiology A: Chemistry **397**, 112531 (2020).

[132] R. L. Carlin, A. van Duyneveldt, R. L. Carlin, and A. van Duyneveldt, Magnetic Properties of Transition Metal Compounds , 1 (1977).

[133] F. J. Adrian, Journal of Colloid and Interface Science **26**, 317 (1968).

[134] M. Chiesa, E. Giamello, and M. Che, Chemical reviews **110**, 1320 (2010).

[135] S. Stoll and A. Schweiger, Journal of magnetic resonance **178**, 42 (2006).

[136] P. G. Baranov, S. B. Orlinskii, C. de Mello Donegá, and J. Schmidt, Applied magnetic resonance **39**, 151 (2010).

[137] K. Toriyama, K. Nunome, and M. Iwasaki, The Journal of Chemical Physics **64**, 2020 (1976).

[138] M. Danilczuk, J. Sadło, A. Lund, H. Yamada, and J. Michalik, Nukleonika **50**, 51 (2005).

[139] A. Lund, E. Sagstuen, A. Sanderud, and J. Maruani, Radiation research **172**, 753 (2009).

[140] T. Ruf, S. Repp, J. Urban, R. Thomann, and E. Erdem, Journal of Nanoparticle Research **18**, 1 (2016).

[141] R. D. Yang, S. Tripathy, Y. Li, and H.-J. Sue, Chemical physics letters **411**, 150 (2005).

[142] R. Frost and J. Kloprogge, Journal of Molecular Structure **526**, 131 (2000).

[143] V. I. Feldman, EPR of Free Radicals in Solids II: Trends in Methods and Applications , 25 (2012).

[144] R. L. Morehouse, J. J. Christiansen, and W. Gordy, The Journal of Chemical Physics **45**, 1751 (1966).

[145] M. Šimėnas, D. Klose, M. Ptak, K. Aidas, M. Mączka, J. Banys, A. Pöppl, and G. Jeschke, Science advances **6**, eaba1517 (2020).

[146] T. Yamada, K. Komaguchi, M. Shiotani, N. P. Benetis, and A. R. Sørnes, The Journal of Physical Chemistry A **103**, 4823 (1999).

[147] N. P. Benetis, I. A. Zelenetckii, and Y. A. Dmitriev, Low Temperature Physics **45**, 427 (2019).

[148] E. Popov, T. Kiljunen, H. Kunttu, and J. Eloranta, The Journal of chemical physics **126** (2007).

[149] C. Jen, S. Foner, E. Cochran, and V. Bowers, Physical Review **112**, 1169 (1958).

[150] A. Horsewill, Progress in nuclear magnetic resonance spectroscopy **35**, 359 (1999).

[151] X. Linpeng, T. Karin, M. Durnev, R. Barbour, M. Glazov, E. Y. Sherman, S. Watkins, S. Seto, and K.-M. C. Fu, Physical Review B **94**, 125401 (2016).

[152] W. F. Beck, J. B. Innes, J. B. Lynch, and G. W. Brudvig, Journal of Magnetic Resonance (1969) **91**, 12 (1991).

[153] J. R. Harbridge, S. S. Eaton, and G. R. Eaton, The Journal of Physical Chemistry A **107**, 598 (2003).

[154] S. S. Eaton, G. R. Eaton, and L. J. Berliner, *Biomedical EPR-Part B: methodology, instrumentation, and dynamics*, Vol. 24 (Springer Science & Business Media, 2004).

[155] J. Klauder and P. Anderson, Physical Review **125**, 912 (1962).

[156] J. R. Harbridge, S. S. Eaton, and G. R. Eaton, Journal of Magnetic Resonance **159**, 195 (2002).

[157] L.-T. Tseng, *Nanostructured diluted magnetic semiconductors*, Ph.D. thesis, UNSW Sydney (2016).

[158] A. Savoyant, H. Alnoor, S. Bertaina, O. Nur, and M. Willander, Nanotechnology **28**, 035705 (2016).

[159] G. Balasubramanian, P. Neumann, D. Twitchen, M. Markham, R. Kolesov, N. Mizuochi, J. Isoya, J. Achard, J. Beck, J. Tissler, *et al.*, Nature materials **8**, 383 (2009).

[160] V. Dobrovitski, G. Fuchs, A. Falk, C. Santori, and D. Awschalom, Annu. Rev. Condens. Matter Phys. **4**, 23 (2013).

[161] J. Kobak, T. Smoleński, M. Goryca, M. Papaj, K. Gietka, A. Bogucki, M. Koperski, J.-G. Rousset, J. Suffczyński, E. Janik, *et al.*, Nature communications **5**, 3191 (2014).

[162] J. Salfi, M. Tong, S. Rogge, and D. Culcer, Nanotechnology **27**, 244001 (2016).

[163] G. Wolfowicz, A. M. Tyryshkin, R. E. George, H. Riemann, N. V. Abrosimov, P. Becker, H.-J. Pohl, M. L. Thewalt, S. A. Lyon, and J. J. Morton, Nature nanotechnology **8**, 561 (2013).

[164] Z. Jradi, D. Marin, A. Campos, M. O'byrne, O. Margeat, S. Bertaina, and A. Savoyant, physica status solidi (RRL)–Rapid Research Letters (2023).

[165] A. Patterson, Physical review **56**, 978 (1939).

[166] D. Piwowarska, P. Gnutek, and C. Rudowicz, Applied Magnetic Resonance **50**, 797 (2019).

[167] A. Savoyant, O. Pilone, S. Bertaina, F. Delorme, and F. Giovannelli, Superlattices and Microstructures **125**, 113 (2019).

[168] T. Estle and M. De Wit, Bull. Am. Phys. Soc **6**, 110 (1961).

[169] A. Hausmann, Physica Status Solidi B Basic Research **31**, K131 (1969).

[170] F. Acosta-Humánez, R. C. Pitalúa, and O. Almanza, Journal of Magnetism and Magnetic Materials **329**, 39 (2013).

[171] T. Castro, P. Rodrigues, A. Oliveira, F. Nakagomi, J. Mantilla, J. Coaquira, A. Franco Junior, H. Pessoni, P. Morais, and S. Da Silva, Journal of Applied Physics **121** (2017).

[172] D. Marin, S. Tiwari, S. Bertaina, and A. Savoyant, Physical Review B **105**, 035424 (2022).

[173] C. Cohen-Tannoudji, B. Diu, and F. Laloë, *Quantum mechanics, volume 3: fermions, bosons, photons, correlations, and entanglement* (John Wiley & Sons, 2019).

[174] R. Aasa *et al.*, Journal of Magnetic Resonance (1969) **19**, 308 (1975).

[175] A. Savoyant, F. Giovannelli, F. Delorme, and A. Stepanov, Semiconductor Science and Technology **30**, 075004 (2015).

[176] S. d'Ambrosio, V. Pashchenko, J.-M. Mignot, O. Ignatchik, R. Kuzian, A. Savoyant, Z. Golacki, K. Grasza, and A. Stepanov, Physical Review B **86**, 035202 (2012).

[177] I. A. Shkrob, S. D. Chemerisov, and T. W. Marin, Astrobiology **10**, 425 (2010).

[178] S. Bouhadoun, C. Guillard, S. Sorgues, A. Hérissan, C. Colbeau-Justin, F. Dapozze, A. Habert, V. Maurel, and N. Herlin-Boime, Science and Technology of advanced MaTerialS **18**, 805 (2017).

[179] D. Mora-Fonz, T. Lazauskas, M. R. Farrow, C. R. A. Catlow, S. M. Woodley, and A. A. Sokol, Chemistry of Materials **29**, 5306 (2017).

[180] S. Massidda, R. Resta, M. Posternak, and A. Baldereschi, Physical Review B **52**, R16977 (1995).

[181] Y. Chen, H. Zhao, B. Liu, and H. Yang, Applied Catalysis B: Environmental **163**, 189 (2015).

[182] P. Gopal and N. A. Spaldin, Journal of Electronic Materials **35**, 538 (2006).

[183] D. J. Griffiths, Introduction to electrodynamics (2005).

[184] K. Kähler, M. C. Holz, M. Rohe, J. Strunk, and M. Muhler, ChemPhysChem **11**, 2521 (2010).

[185] S. K. Verma and A. K. Das, (No Title) .

[186] D.-S. Park, H. Wang, S. K. Vasheghani Farahani, M. Walker, A. Bhatnagar, D. Seghier, C.-J. Choi, J.-H. Kang, and C. F. McConville, Scientific reports **6**, 18449 (2016).

[187] E. R. D. J. III, NIST Computational Chemistry Comparison and Benchmark Database (2022), NIST Standard Reference Database Number 101 Release 22.

[188] A. R. González-Elipe and J. Soria, Journal of the Chemical Society, Faraday Transactions 1: Physical Chemistry in Condensed Phases **84**, 3961 (1988).

[189] E. Giamello, Catalysis today **41**, 239 (1998).

[190] M. Schmitt, Macromolecular Chemistry and Physics **213**, 1953 (2012).

[191] M. Schmitt, S. Kuhn, M. Wotocek, and R. Hempelmann, Zeitschrift für Physikalische Chemie **225**, 297 (2011).

[192] A. Bazargan, F. Sharif, S. Mazinani, and N. Naderi, Journal of Materials Science: Materials in Electronics **27**, 8221 (2016).

[193] R. J. Anderson, D. J. Bendell, and P. W. Groundwater, *Organic spectroscopic analysis*, Vol. 22 (Royal Society of Chemistry, 2004).

[194] L. M. Harwood and T. D. Claridge, *Introduction to organic spectroscopy* (Oxford University Press New York, 1997).

Keywords : Electron paramagnetic resonance, spin dynamics, ZnO NPs, photoexcitation, methyl radicals, polar surface, photo-Kolbe reaction.

.